Exploring past and present ice-sheet dynamics with geophysically-derived temperature and crystal orientation fabric

Benjamin Hills

A dissertation
submitted in partial fulfillment of the
requirements for the degree of

Doctor of Philosophy

University of Washington

2023

Reading Committee:

Knut Christianson, Chair

Dale Winebrenner

T.J. Fudge

Program Authorized to Offer Degree:
Earth and Space Sciences

University of Washington

Abstract

Exploring past and present ice-sheet dynamics with geophysically-derived temperature and crystal orientation fabric

Benjamin Hills

Chair of the Supervisory Committee:
Dr. Knut Christianson
Earth and Space Sciences

The greatest physical uncertainty for projections of future sea-level rise is in ice-sheet flow dynamics and the potential realization of theorized instabilities (IPCC, AR6). While knowledge on the precise fate of Earth's ice sheets is still out of reach, looking to past states provides insight on their potential evolution. Past ice-sheet states, and particularly their flow dynamics, are preserved in present-day ice temperature (Robin, 1955) and preferred crystal orientation fabric (COF) (Alley, 1988); moreover, the future ice dynamics are governed by those same properties through the ice viscosity (Glen, 1955) and the tendency to slide over a temperate bed (Weertman, 1957). Theoretically, ice temperature and COF can both be inferred using ice-penetrating radar measurements, but prior work shows that it is difficult to disentangle these intrinsic properties of the ice column from each other or even from interface properties, such as reflectivity between layers and at the ice-sheet bed. Here, I contribute to the development of methods for ice-penetrating radar power and phase interpretation. I use those methods alongside mathematical models to infer both present-day and historical ice-sheet dynamics for three areas of the Antarctic Ice Sheet: Siple Coast, South Pole Lake, and Hercules Dome. Each of the three regional studies is formulated around a separate scientific problem, and the results for each drive physical interpretation of ice-sheet processes. At the Siple Coast I calculate spatial variations in radar attenuation and use them to show that ice-stream temperatures are colder than previously thought because of their upstream sourcing. At South Pole Lake, I calculate spatial variations in ice-bed reflectivity, depth variations in radar attenuation, and develop a novel ice-

temperature model to show that the ice-bed interface is regionally thawed and has been stable at least since the last glacial period, in contradiction to prior studies. At Hercules Dome, I use measurements of the present-day ice dynamics, both surface and englacial velocities, to constrain a model of COF evolution. I then compare the modeled COF against measurements from radar polarimetry to infer stability in the regional ice dynamics since the last glacial period. Together, these three studies demonstrate novel and innovative radar analysis used to theorize dynamic evolution of the Antarctic Ice Sheet. Looking forward, these types of radar measurements will be incorporated into continent-wide modeling studies to constrain ice-sheet dynamics and projections of future sea-level rise.

Dedication

to Dani, on the eve of our wedding

Acknowledgments

The work presented in this dissertation would not have been possible without significant contributions from a long list of individuals. In particular, I want to thank my primary research advisor, Knut Christianson, and my dissertation committee: Dale Winebrenner, TJ Fudge, Eric Steig, Bonnie Light, and Nicholas Holschuh. Each of them have kept their door open for not only research-specific advise, but also career and personal mentorship. Robert Jacobel and Howard Conway are not technically on my committee but have each offered significant support throughout my research.

The field measurements critical to this research depended on many separate groups. First, those scientists who did the fieldwork: Annika Horlings, Andrew Hoffman, Gemma O'Connor, John Christian, Emma Erwin, Liam Kirkpatrick, Erika Schreiber. One tangential dataset was collected by the COLDEX geophysics team which has been used to shape some of the findings presented here. We received significant field support from the US Antarctic Program, with particular dedication from our implementers, Bija Sass and Jenny Cunningham. We were entirely reliant on two flight teams, Kenn Borek Air and the US Air National Guard.

There are several additional groups who helped shape my thinking on the topics presented herein. I have been continuously supported by those building community within the WAIS Workshop: Matthew Siegfried, Ryan Venturelli, Dustin Schroeder, Brooke Medley, Lauren Simkins, Peter Neff, and many others. The undergraduate researchers who I have worked with have been fantastic, extending beyond their learner role into becoming a research colleague, Joshua Driscol, Raphael Sauvage, Jonathan Ortiz-Candelaria. Stephanie Harrington fought tirelessly for me as a student in times when I was confronted with institutional barriers to doing my work.

This research was funded by NSF grants #1643353 and #1744649. I want to thank the manager of the Glaciology and Ice Core Science Programs at NSF, Paul Cutler. He has gone far beyond his role, supporting me personally as a scientist and as a person.

Software and Data Availability

Original Geophysical Datasets:

- *Siple Coast Geophysics*

  Chapter 3 uses previously published radar datasets from Jacobel et al. (2009) available at https://doi.org/10.7265/N5ZC80SH, Conway et al. (2002) available at https://doi.org/10.7265/N5736NTS, and Christianson et al. (2016) available at https://doi.org/10.7265/N54J0C2W.

- *South Pole Lake Geophysics*

  The profiling radar data used in Chapter 4 were first published in Hills et al. (2020); those, as well as the surface velocity measurements, ApRES acquisitions, and associated vertical velocities are all archived at https://www.usap-dc.org/view/project/p0010160.

- *Hercules Dome Geophysics*

  The profiling radar and ApRES acquisitions used in Chapter 5 are still being archived. A preliminary data project has been published at https://www.usap-dc.org/view/project/p0010359, and more will be added there over time.

Original Software Repositories:

- *ImpDAR* - **Imp**ulse ra**dar** processing toolkit (Lilien et al., 2020)
  https://github.com/dlilien/ImpDAR
  and *ImpDAR Tutorials*
  https://github.com/benhills/impdar-tutorials

- *iceotherm* - Analytical and numerical models of ice-sheet temperature
  https://github.com/benhills/iceotherm

- *effmed-ice* - Electromagnetic wave propagation in anisotropic ice
  https://github.com/benhills/effmed-ice

Notable External Software Repositories Used Here:

- *specfab* - Spectral fabric model (Rathmann et al., 2021)
  https://github.com/nicholasmr/specfab

- *tamm* - Transfer matrix model (Rathmann et al., 2022)
  https://github.com/nicholasmr/tamm

- *GPT-4* - Used as a writing assistant.

Leveraged Borehole Datasets:

- Borehole temperatures used in Chapter 3 were published by Harrison et al. (1998) and Engelhardt (2004b), available at https://doi.org/10.7265/N5PN93J8.

- South Pole Ice Core
  https://spicecore.org/data/

Leveraged Ice-Sheet Model Output:

- Paleo ice-sheet model ensemble (Albrecht et al., 2020a, 2020b)
  https://doi.pangaea.de/10.1594/PANGAEA.909727

- Paleo ice-sheet model scenario (Pollard, personal communication)

- Last Glacial Maximum ice-sheet model (Golledge et al., 2012)
  https://osf.io/qtfdk/

Table of Contents

List of Figures

List of Tables

List of Symbols

A list of symbols that appear in equations throughout the text. To avoid overly repetitive variable explanations, they are not always defined where they are presented in the text. Some symbols are excluded from this table, those which are only used once and are not central to the context of the dissertation (in those instances, the variable is defined in the text).

Square brackets around variables represent electrical properties measured in decibels.

Variable	**Name**	**Value**	**Units**
Geometric Variables			
t	Time		s
Δt	Time step		s
x	Longitudinal distance		m
y	Lateral distance		m
z	Depth below surface (range of radar wave propagation)		m
h	Height above bed		m
ℓ	Characteristic length		m
H	Ice thickness		m
ζ	Normalized depth below surface		-
S	Ice surface elevation		m
θ	Azimuthal angle		rad
ϕ	Polar angle		rad
Creep Deformation Variables			
$\dot{\varepsilon}$	Strain rate		s^{-1}
τ	Stress		Pa
A	Rate factor		s^{-1} Pa^{-n}
n	Glen (1955) creep exponent	3	-
ρ	Density	917	kg m^{-3}
E	Activation energy	60000	J mol^{-1}
R	Gas constant	8.315	J mol^{-1} K^{-1}
g	Gravitational constant	9.81	m s^{-2}
Flow Variables			

$\mathbf{u}$	Macroscopic velocity field	m s^{-1}
u	Longitudinal velocity	m s^{-1}
v	Lateral velocity	m s^{-1}
w	Vertical velocity	m s^{-1}
$\dot{a}$	Mass balance rate	m s^{-1}
$\mathscr{g}$	Rezvanbehbahani (2019) exponent	-
p	Lliboutry (1979) shape factor	-

Crystal Orientation Fabric Variables

ψ	c-axis distribution	N rad^{-1}
c	c-axis orientation	rad
$\dot{c}$	c-axis velocity	rad s^{-1}
$\mathbf{W}$	Macroscopic spin	s^{-1}
ι	Rigid-body to basal-glide ratio	-
Ω	Rotational diffusivity	s^{-1}
Γ	Recrystallization rate factor	s^{-1}
Γ_0	Recrystallization prefactor	s^{-1}
$\mathscr{D}$	Deformability	-

Temperature Variables

T	Temperature		°C
c	Specific heat capacity	2097	J kg^{-1} K^{-1}
k	Thermal conductivity	2.1	J $m^{-1}K^{-1}s^{-1}$
κ	Thermal diffusivity	$1.09x10^{-6}$	m^2 s^{-1}
L	Latent heat of fusion	$3.33x10^{5}$	J kg^{-1}
Ξ	Melting point depression constant	$-7.42x10^{-8}$	K Pa^{-1}
Q	Heat source		J $m^{-3}s^{-1}$
$\dot{m}$	Melt rate		m s^{-1}

Non-Dimensional Numbers

Pe	*Peclet* number	-
Λ	Horizontal *Peclet*-like number	-
Br	*Brinkman* number	-

Electrical Variables

γ	Propagation constant	m^{-1}
α	Electrical absorption coefficient (real component of γ)	m^{-1}

β	Phase constant (imaginary component of γ)	m^{-1}
i	Imaginary number, $i \equiv \sqrt{-1}$	-
ω	Angular frequency	rad s^{-1}
ε	Permittivity	V m^{-1}
μ	Magnetic permeability	H m^{-1}
σ	Electrical conductivity	S m^{-1}
$\mathscr{m}$	Molar conductivity	S m^{-1} M^{-1}
M	Molarity	M

Radar Power Variables

N	Radar attenuation	dB m^{-1}
$[P_r]$	Received radar power	dB
$[P_c]$	Received radar power (corrected)	dB
$[P_t]$	Transmitted radar power	dB
$[G]$	Antenna gain	dB
$[R]$	Radar reflectivity	dB
$[F]$	Refractive focusing	dB
$[B]$	Birefringent power losses	dB
$[S]$	Radar system power (total power correction for instrument)	dB

Effective Medium Model Variables

$\mathscr{S}$	Scattering matrix	dB
$\mathscr{s}$	Scattering array for an individual polarization	dB
$\mathbf{R}$	Rotation matrix	-
$\mathbf{T}$	Transmission matrix	dB
$\mathscr{R}$	Reflectivity matrix	dB
D	Free space spreading losses	dB
$\mathscr{k}$	wave vector	m^{-1}
C	Phase coherence	-
Φ	Phase angle	rad

Chapter 1

Introduction

1.1 Motivation

Water is unique as an Earth material in that all three phases are present and stable at the Earth surface. For any given climate state, there exists an equilibrium between the three phases, with warmer climates leading to more liquid/gaseous water and less solid ice (including no ice in the warmest climates). Today, ~26.6 million gigatons of ice (~65.6 m of sea-level equivalent, 'SLE') are stored amongst the numerous alpine glaciers (~0.3 m SLE) (Farinotti et al., 2019) and the two polar ice sheets, Antarctica (~57.9 m SLE) (Morlighem et al., 2020) and Greenland (~7.4 m SLE) (Morlighem et al., 2017). There is evidence that the relative volume of frozen ice to ocean water has varied dramatically through Earth history (e.g. Bintanja et al., 2005; Elderfield et al., 2012; Kopp et al., 2009). Likewise, we should expect that future climate trends will lead to a change in the global ice volume and therefore future sea level.

The idea that a climate state should give some predictable ice/water equilibrium volume is intuitive based on simple energy-accounting physics. However, the challenge of research in glaciology is to know *how large* a change in equilibrium volume might be and *how long* it may take to transition between states. For example, if we assume that by year 2100 the global air temperature will be 1.5°C above preindustrial levels (the optimistic target established in the Paris Agreement (United Nations, 2015)), then we can ask how much the global ice volume will shrink in response and how many years beyond 2100 it will take to do so.

Ice sheets change size by exchanging water mass with the atmosphere, ocean, and to a lesser

Figure 1.1:
Projections of future sea-level rise from the IPCC's sixth Assessment Report. Projections are for five emissions scenarios and one extraordinarily high-impact scenario which includes ice-sheet instabilities. A) Global mean sea level change relative to 1900 plotted from 1950-2100. B) Same as (A) but for projections to 2300. This figure is taken directly from the report.

Citation: Figure SPM.8 in IPCC, 2021: Summary for Policymakers. In: Climate Change 2021: The Physical Science Basis. Contribution of Working Group I to the Sixth Assessment Report of the Intergovernmental Panel on Climate Change [Masson-Delmotte, V., P. Zhai, A. Pirani, S.L. Connors, C. Péan, S. Berger, N. Caud, Y. Chen, L. Goldfarb, M.I. Gomis, M. Huang, K. Leitzell, E. Lonnoy, J.B.R. Matthews, T.K. Maycock, T. Waterfield, O. Yelekçi, R. Yu, and B. Zhou (eds.)]. Cambridge University Press, Cambridge, UK and New York, NY,USA, pp. 3-32, doi: 10.1017/9781009157896.001.

extent land-water and subsurface storage. They grow when solid ice precipitates out of the atmosphere, and they shrink either by sublimation, surface melt and runoff, melt at the ice-ocean interface, or direct discharge of ice into the ocean (iceberg calving). We generally combine precipitation, sublimation, and surface melt into a single variable called the 'surface mass balance' which is most heavily dependent on the atmospheric conditions, notably the air temperature, humidity, and precipitation rate.

The timescale for glacier response to a change in atmospheric conditions is dependent on the glacier thickness, H, and the mass-balance rate, $\dot{a}$, $t = \frac{H}{-\dot{a}}$ (Johannesson et al., 1989). This timescale was established for alpine glaciers where response times are order 10^1-10^2 years. Considering ice sheets, response to atmospheric changes would take longer, order 10^3 years. However, we now know that ice sheets can change significantly faster than this millennial timescale, largely because of their propensity to rapidly lose mass to the *ocean* through the third and fourth mechanisms mentioned above, melting and iceberg calving. Here, a different timescale is more appropriate, one that is dependent on the characteristic length of the glacier or ice sheet, ℓ, and the speed of ice flow, u, $t = \frac{\ell}{u}$ (Nye, 1960). Then, the ice dynamics (ice flow) become the driving process and response times are again shorter, order 10^2 years (~human lifetime).

The faster, dynamic, timescale for ice-sheet response (~centennial) was emphasized in the most recent assessment report from the International Panel on Climate Change (IPCC AR6, Fox-Kemper et al. (2021)). They highlight two ice-dynamic instabilities which could lead to rapid draw down, in particular of the West Antarctic Ice Sheet, the 'marine ice-sheet instability' (Weertman, 1974) and the 'marine ice cliff instability' (Bassis et al., 2021). Including those instabilities and dynamic ice sheets in future projections can lead to scenarios with up to 15 m of sea-level rise (SLR) by year 2300 (Figure 1.1).

While the end-member scenario of 15 m SLR is far from certain, even the more optimistic scenario (SSP1-2.6) predicts ~50-300 cm SLR by 2300 (Figure 1.1) which would be devastating for coastal communities. Hundreds of millions of people live in these vulnerable coastal areas (Hooijer & Vernimmen, 2021; Kulp & Strauss, 2019) as well as ports and other critical global infrastructure. We know that sea level is rising today (Frederikse et al., 2020) and that it will continue to rise into the future, but the uncertainty on *how high* it could rise and *how quickly* makes preparation and adaptation extremely challenging.

The broad goal of the glaciology community, and the motivation for this dissertation, is to assign better constraints on the uncertainty for future sea-level rise in an effort to better equip the global population for adaptation. Since it is difficult to predict the future before it arrives, one way to understand the range of *possible* futures is to look at past states. This has been my approach, focusing primarily on past states of the Antarctic Ice Sheet in particular. Next, I review the broad ice-sheet history to contextualize discussion that will come in later chapters.

1.2 Ice-Sheet History

As a glaciologist, I typically think on timescales of hundreds to thousands of years because, as explained in the prior section, those are the approximate response timescales for glaciers and ice sheets. For completeness, I describe a fuller history here, starting with deep geologic time and moving toward the more recent history which is most relevant to human interaction with the climate system.

Ice on Earth can be traced to the Proterozoic Eon (2.5-0.5 billion years ago) when there was a series of global glaciations collectively known as the 'Snowball Earth' events (Harland, 1964). A Snowball Earth is in a climate equilibrium far from today's, with the entire globe (including oceans) covered in ice. Such an event is triggered by the runaway feedback between sea-ice and the global radiation balance (Budyko, 1969), and the only way out is through significant volcanic emission of greenhouse gases (CO_2).

During the subsequent eon, the Phanerozoic (0.5 billion years ago to present day), the climate has fluctuated between warm periods ('climate optima') and partial glaciations (although no Snowball Earth events). These fluctuations have happened over 10's to 100's of millions of years, being driven by the *long-term* geologic carbon cycle (Archer et al., 1997) where more volcanic activity tends to lead to warmer climates and more rock weathering to colder. The most recent climate optimum was in the early Cenozoic Era (~50 million years ago) where temperatures were ~10-15 °C warmer than present day and there was likely no solid ice on Earth's surface. Around that time, the Indian Plate collided with the Eurasian Plate and uplifted the Himalaya. Exposure of igneous rocks increased the rate of carbonate weathering (pulling carbon out of the atmosphere) and caused a slow descent into colder global temperatures over 10's of millions of years.

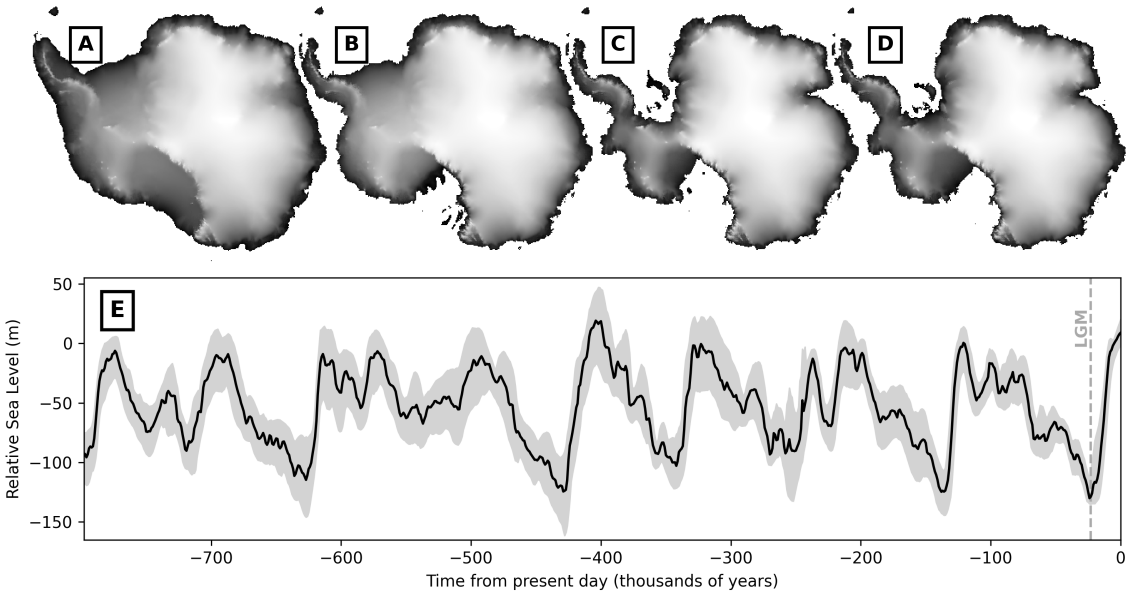

Figure 1.2: A-D) Modeled history of ice-sheet geometry from LGM (A) to today (D) (Albrecht et al., 2020b). D) Estimated history of global sea level from various proxies, with uncertainty shown as the grey band (Spratt & Lisiecki, 2016).

From 2.6 million to 10 thousand years ago there have been a series of smaller glacial/interglacial cycles grouped into the Pleistocene Epoch. These smaller and faster glaciations are driven by the *short-term* carbon cycle which is connected to patterns in the Earth's orbit around the Sun (Imbrie & Imbrie, 1980). The climate fluctuations during this epoch are less extreme and more familiar, with the interglacials being similar to present-day climate and glacials ('ice ages') having enough ice to lower sea level by ~100 m (Figure 1.2). During glacial periods, ice sheets covered significant portions of North America, Europe, and Asia, and their advance and retreat shaped the planet's topography, carving out valleys, fjords, and other geologic features.

The most recent Pleistocene glacial cycle reached its height ~20 thousand years ago at the 'Last Glacial Maximum' (LGM). Since then, the Earth has entered an interglacial period (the Holocene), marked by the retreat of ice sheets and a warmer global climate in which humans have flourished. With no influence from human activity, the history suggests that Earth would soon begin another gradual cooling period over 10's to 100's of thousands of years into glaciation. However, an external force on the delicate carbon cycle could easily push the climate toward a new equilibrium, one not

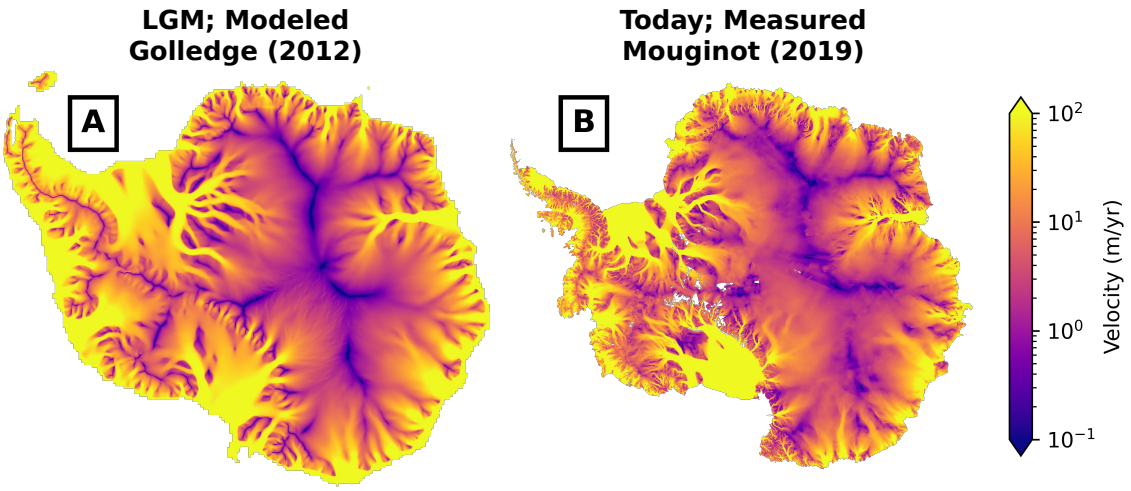

Figure 1.3: A) Modeled ice velocity in a past ice-sheet state (LGM) (Golledge et al., 2012). B) Present-day ice velocity from satellite measurements (Mouginot et al., 2019).

seen for millions of years.

One outstanding question in glaciology, and one important to this dissertation, is how different the ice dynamics could be in the various ice-sheet states. The modeled surface velocity in paleo-ice-sheet models is relatively similar to what we measure today (Figure 1.3). Of course, the *size* of the ice sheet changes based on the input climate variables, but the dynamic nature is relatively consistent, with ice streams in the same general locations. It is not clear whether these models are over fit to present-day conditions. In particular, the resistive stresses at the ice-sheet bed and within the ice (e.g. ice stream shear margins) are parameterized in a way that could vary depending on the ice and bed properties. If those dynamic parameterizations can change with the ice-sheet state, the response times for dynamic areas could be faster (or slower) than currently understood.

1.3 A Note on Organization

This dissertation is organized into five additional chapters (2-6) beyond this introductory chapter. Chapter 2 provides a thorough background on the physics of ice with particular emphasis on the physical models used in subsequent chapters. The background also includes some novel develop-

ment of methods for both modeling and ice-penetrating radar interpretation. Chapters 3, 4, and 5, are all original research in physical glaciology, leveraging the physics in Chapter 2 to interpret past and present ice-flow dynamics of the Antarctic Ice Sheet. Finally, Chapter 6 is the dissertation conclusion, giving a broader outlook on what the main takeaways are from this body of work and contextualizing how it fits into the broader development of research in physical glaciology.

Each of the three 'research' chapters (3-5) have either already been published or will soon be submitted as standalone articles. Additionally, much of the material from the background and appendices come from prior publications, either accompanying the material from chapters 3-5 or as their own articles. In all cases, I note the journal in which the material has been published (or where it will be submitted) beneath the chapter or section heading. In chapters which were written with coauthors, I use the plural 'we'.

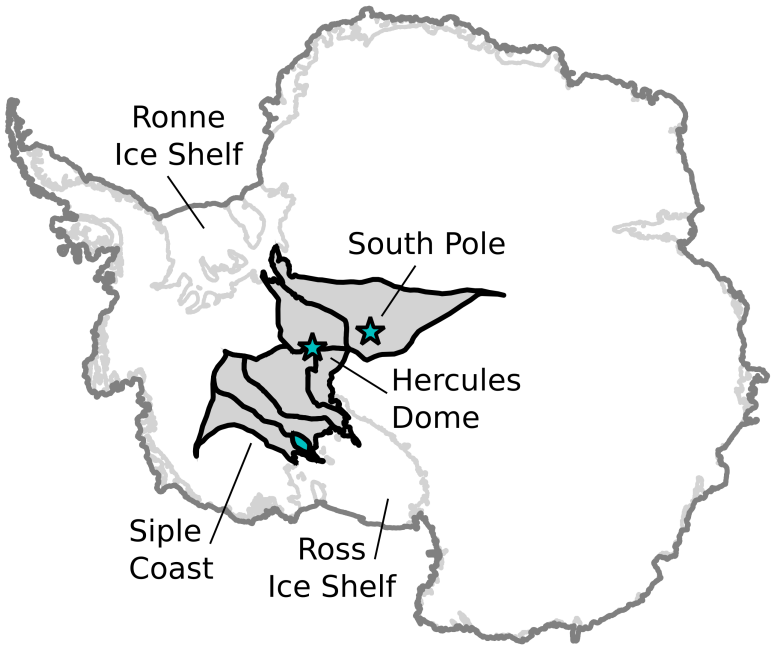

Figure 1.4: An overview map for the regions of interest in this dissertation. The continental outlines are the coastline (darker) and the grounding line (lighter) from Rignot et al. (2011). Dark regions outlined in black are drainage basins for the ice streams of interest. Blue icons show South Pole, Hercules Dome, and Siple Dome, all discussed thoroughly in the coming chapters.

Chapter 2

Background and Methods Development

Chapter Abstract.

Historical ice flow can be preserved within the present-day ice sheets. Most commonly, this is expressed in and interpreted from the ice stratigraphy. That is, isochronal layers deposited at the ice surface have varying chemistry depending on atmospheric conditions at the time of deposition. Those layers can be distinguished by their electrical properties; for instance, direct measurements of ice-core electrical conductivity are used to date recovered ice samples (K. Taylor, 1992). Dated layers are extrapolated away from ice-core drilling sites by connecting the electrical conductivity measurements to imaged stratigraphy in ice-penetrating radar profiles (e.g. Ashmore et al., 2020; MacGregor, Fahnestock, et al., 2015; A. Winter et al., 2019). The distortions and deflections of these layers in the radar stratigraphy can be mapped onto past ice flow (Dowdeswell & Evans, 2004).

Beyond the shape of the stratigraphy, ice-flow history is also preserved in ice properties such as englacial temperature (MacGregor, Li, et al., 2015; Schroeder, Seroussi, et al., 2016), basal-thermal state (Christianson et al., 2014; Schroeder, Grima, et al., 2016), and crystal orientation (T. M. Jordan et al., 2022; Young et al., 2021). The resolvable timescales and ice-sheet settings where history is preserved will be different for each ice property and for the specific site setting, so all are important aspects of deciphering the full history. In this dissertation I focus on these ice properties, englacial ice temperature, basal ice temperature, and crystal orientation, using them to better understand the ice sheet of the recent past, since the Last Glacial Maximum, as well as what that means for today's

ice sheet and that of the future.

In the following sections I give an overview of the relevant physics. Sections 2.1 and 2.2 focus on the mechanical and thermal properties of ice, respectively, addressing the mechanisms and timescales on which these properties change and how they can preserve past ice-sheet states. In Section 2.3, I discuss the electrical properties of ice. Importantly, I focus on how the thermal and mechanical states discussed in 2.1 and 2.2 are related to electrical properties and can therefore be measured remotely (i.e. without drilling into the ice) using ice-penetrating radar methods.

2.1 Mechanical Properties of Ice

2.1.1 Crystal Structure

Water molecules tessellate in a tetrahedral structure to form crystalline ice (Figure 2.1). A perfect ice crystal follows the Bernal-Fowler (1933) rules: 1) each water molecule has one oxygen atom and two hydrogen (protons); 2) each water molecule is connected to all four neighbors through hydrogen bonds; 3) each hydrogen bond has exactly one proton. Even within those limitations, many crystalline phases of ice are possible, and more are being discovered (Hansen, 2021). The only ice phase present on Earth's surface and therefore the only of interest here is ice Ih (hexagonal). Ice Ih crystallizes in hexagonal sheets, with three of the four bonds for any molecule being on the hexagonal plane (basal plane) and the fourth between planes. The ice crystal is therefore strongly anisotropic with the c axis, pointing perpendicular to the basal plane, having different mechanical (described below) and electrical (Section 2.3) properties than the a and b axes which point along the basal plane.

Like many crystalline materials, natural ice crystals contain defects, or molecular dislocations, which are exceptions to the Bernal-Fowler rules stated above. Ice-crystal dislocations come in two varieties (Figure 2.2). Ionic defects are the presence of more (H_3O^+) or less (OH^-) than two hydrogen atoms in a single water molecule. Orientational defects are the presence of two (or zero) hydrogen atoms in a single hydrogen bond (Bjerrum, 1951).

Crystal dislocations are unstable. When placed under an applied stress, a dislocation will tend propagate through the crystal (Weertman & Weertman, 1964). When dislocations propagate along the basal plane (as is most common) the process is referred to as 'basal glide'. Following Cuffey and Paterson (2010), the theoretical strain rate by basal glide of an individual crystal is

$$\dot{\varepsilon}_c = l^* \rho_d u_d \tag{2.1}$$

where l^* is the lattice offset of a single dislocation, ρ_d is the dislocation density, and u_d is the dislocation velocity. The density and velocity of dislocations are both dependent on the applied stress, τ, so

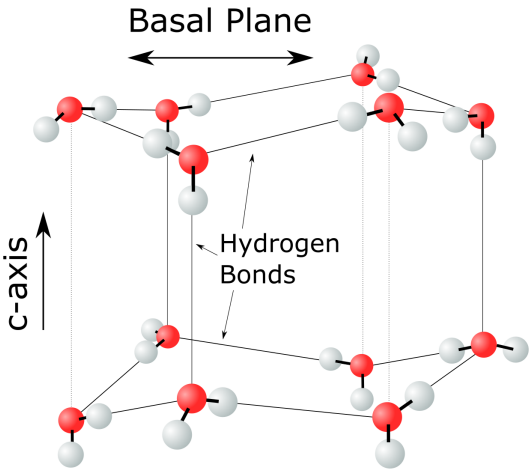

Figure 2.1: Crystal structure of ice. Each water molecule is made up of one oxygen (red) and two hydrogen (white) atoms.

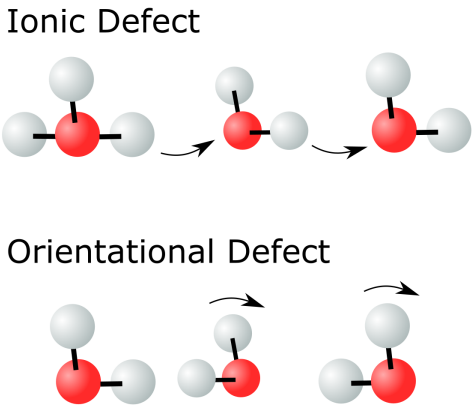

Figure 2.2: The two types of crystalline defects in ice and their propagation between molecules within the crystal.

$$\dot{\mathscr{E}}_c \propto \tau^{r+q} \tag{2.2}$$

Dislocation velocity is generally assumed linear with stress, so $q = 1$. Dislocation density, is less well constrained, with r ranging from 0 (constant) in low stress states (Harper & Dorn, 1957) to 2 at the high stresses commonly seen in an ice sheet (Alley, 1992). Equation 2.2 is commonly reduced to (Glen, 1955)

$$\dot{\mathscr{E}} = A\tau^n \tag{2.3}$$

where n is the combined creep exponent and A is a prefactor which is dependent on temperature among other properties (discussed below). Based on this theory, ice creep by basal glide is a power-law relation with creep exponent, $n = 3$. However, measurements have shown that $n > 3$, especially in extraordinarily high stress settings (Millstein et al., 2022). Alternative creep mechanisms such as dislocation climb (between basal planes) and grain-boundary sliding become important in those cases (Goldsby & Kohlstedt, 2001).

Up to now, I have discussed the mechanical properties of individual ice crystals only; however, ice sheets are made up of many crystals which together determine the bulk properties. Crystals are deposited as snowflakes at random orientation on the ice-sheet surface, so the ice polycrystal is initially isotropic (Figure 2.3). Over time, crystals can grow, shrink, and rotate in a way that they align themselves with the macroscopic stress/strain setting in the ice, forming a crystal 'orientation fabric' (COF). Then, the bulk properties can be anisotropic, in the most extreme case mirroring that of the individual crystal. In the next sections, I review the mathematical framework for COF evolution under an applied stress/strain regime and discuss the importance of COF for interpretation of historical ice dynamics.

2.1.2 Crystal Orientation Fabric and Evolution

COF is represented mathematically as a continuum distribution of c axes, ψ. Here, I follow Rathmann et al. (2021), using spherical coordinates, so

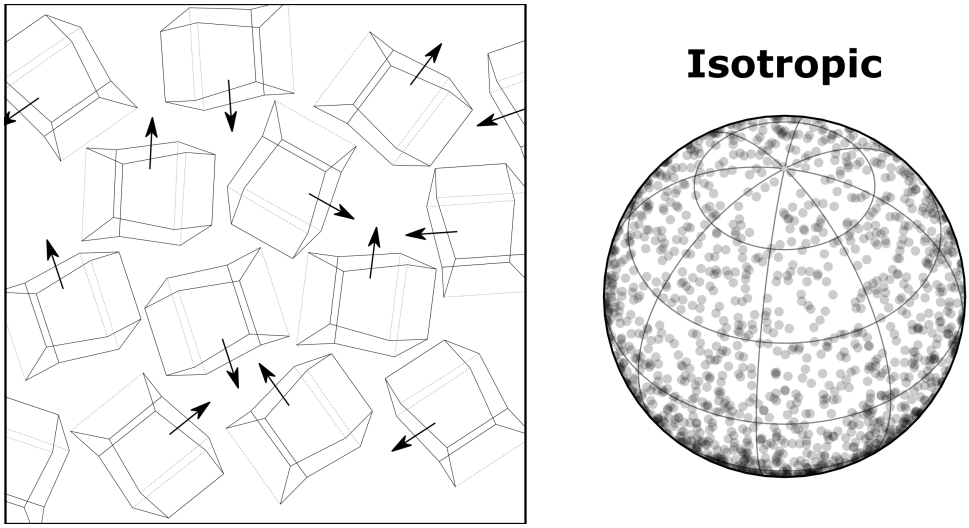

Figure 2.3: An illustration of isotropic ice. Left) Many individual ice crystals with c axes (arrows) pointing in different directions. Right) A spherical projection of ice crystal distribution with individual dots representing crystals evenly spread out through spherical space (pointing in all directions).

$$\psi = \psi(\theta, \phi, t) \tag{2.4}$$

The time rate of change of the c axes distribution (COF evolution) is (Placidi et al., 2010; Rathmann & Lilien, 2021; Richards et al., 2021)

$$\frac{D\psi}{Dt} = -\nabla_{S_2} \cdot (\psi \dot{c}) + \Omega \nabla_{S_2}^2 \psi + \Gamma \psi \tag{2.5}$$

where $\dot{c}$ is the c-axis orientation of an arbitrary ice crystal and the remaining variables are described in turn below. The term on the left is the standard material derivative, where

$$\frac{D}{Dt} = \frac{\partial}{\partial t} + \mathbf{u} \cdot \nabla_{S_1} \tag{2.6}$$

and $\mathbf{u}$ is the macroscopic velocity field within the ice-sheet domain, S_1. The three terms on the right-hand side of equation 2.5 represent lattice rotation, rotational recrystallization, and dynamic recrystallization. These processes all act at the microscopic scale, so I define S_2 as the microscopic orientation space in which individual ice crystals evolve.

Lattice Rotation

The first COF evolution process, $-\nabla_{S_2} \cdot (\psi \dot{c})$, is lattice rotation. Considering only this process, crystals preserve their shape and size but can be rotated. Rotation is generally grouped into two subprocesses ($\dot{c} = \dot{c}_1 + \dot{c}_2$); first, is rotation at the macroscopic scale,

$$\dot{c}_1 = \mathbf{W} \cdot c \tag{2.7}$$

where $\mathbf{W}$ is the spin in the macroscopic velocity field

$$\mathbf{W} = \frac{\nabla \mathbf{u} - (\nabla \mathbf{u})^T}{2} \tag{2.8}$$

Second, is rotation at the microscopic scale (Gödert & Hutter, 1998; Rathmann et al., 2021; Svendsen & Hutter, 1996)

$$\dot{c}_2 = (-\dot{\boldsymbol{\varepsilon}} \cdot c\,c + c\,c \cdot \dot{\boldsymbol{\varepsilon}}) \cdot c \tag{2.9}$$

where the macroscopic stretching (strain rate) is again defined by the velocity field

$$\dot{\boldsymbol{\varepsilon}} = \frac{\nabla \mathbf{u} + (\nabla \mathbf{u})^T}{2} \tag{2.10}$$

Together, the macroscopic and microscopic rotation define the c-axis velocity field (Rathmann et al., 2021)

$$\dot{c} = \mathbf{W} \cdot c + \iota(-\dot{\boldsymbol{\varepsilon}} \cdot c\,c + c\,c \cdot \dot{\boldsymbol{\varepsilon}}) \cdot c \tag{2.11}$$

where ι is an empirical parameter which defines the trade off between rigid-body rotation and that by creep within individual crystals.

Rotational Recrystallization (Polygonization)

Rotational recrystallization, $\Omega \nabla^2_{S_2} \psi$, acts as a diffusive process in equation 2.5 with diffusivity Ω. Sometimes called 'polygonization', this process is a breakdown of one crystal into two or more subcrystals and the outward rotation of those subcrystals away from one another. Some authors have stated that polygonization itself has little effect on COF evolution (Alley et al., 1995), since the subdivided crystals point in the same direction when they first break from the parent crystal. I include this process in the formalization and discuss its effectiveness, in terms of the magnitude of the diffusivity, below.

Dynamic Recrystallization

Dynamic recrystallization, $\Gamma \psi$, is the growth and decay of crystals. Molecules tend to move from high energy states toward lower energy states within the polycrystal. They move from convexities to concavities (rounding or sintering) and down a temperature gradient (facet forming). Importantly for COF evolution, recrystallization is also dependent on the stress state, with molecules moving from high stress environments toward lower. Molecule movement between crystals is called

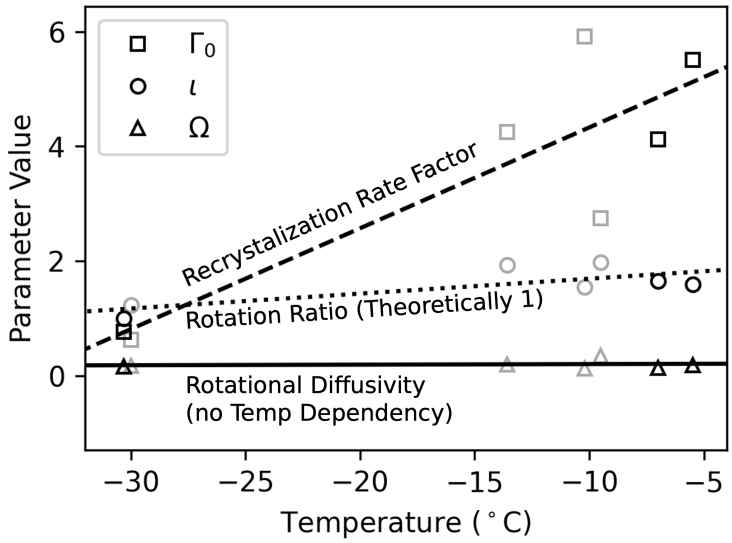

Figure 2.4: Values for the three uncertain parameters of COF evolution discussed in this section. Values are from a model inversion, constrained by measured COF evolution in a laboratory setting. The faded markers are for experiments in uniaxial compression, and the solid markers are for experiments in a simple-shear. This figure is a direct reproduction of Figure 4 from Richards et al. (2021).

Figure 2.5: Modeled COF evolution through time in a strain regime for unconfined uniform compression. Top row) The ordinary distribution function of crystal *c* axes plotted at three stages of cumulative strain. Subsequent rows show the instantaneous contribution to fabric evolution at the given stage (associated with timing in the top row) for three processes: lattice rotation (top), rotational recrystallization (middle), and migration recrystallization (bottom).

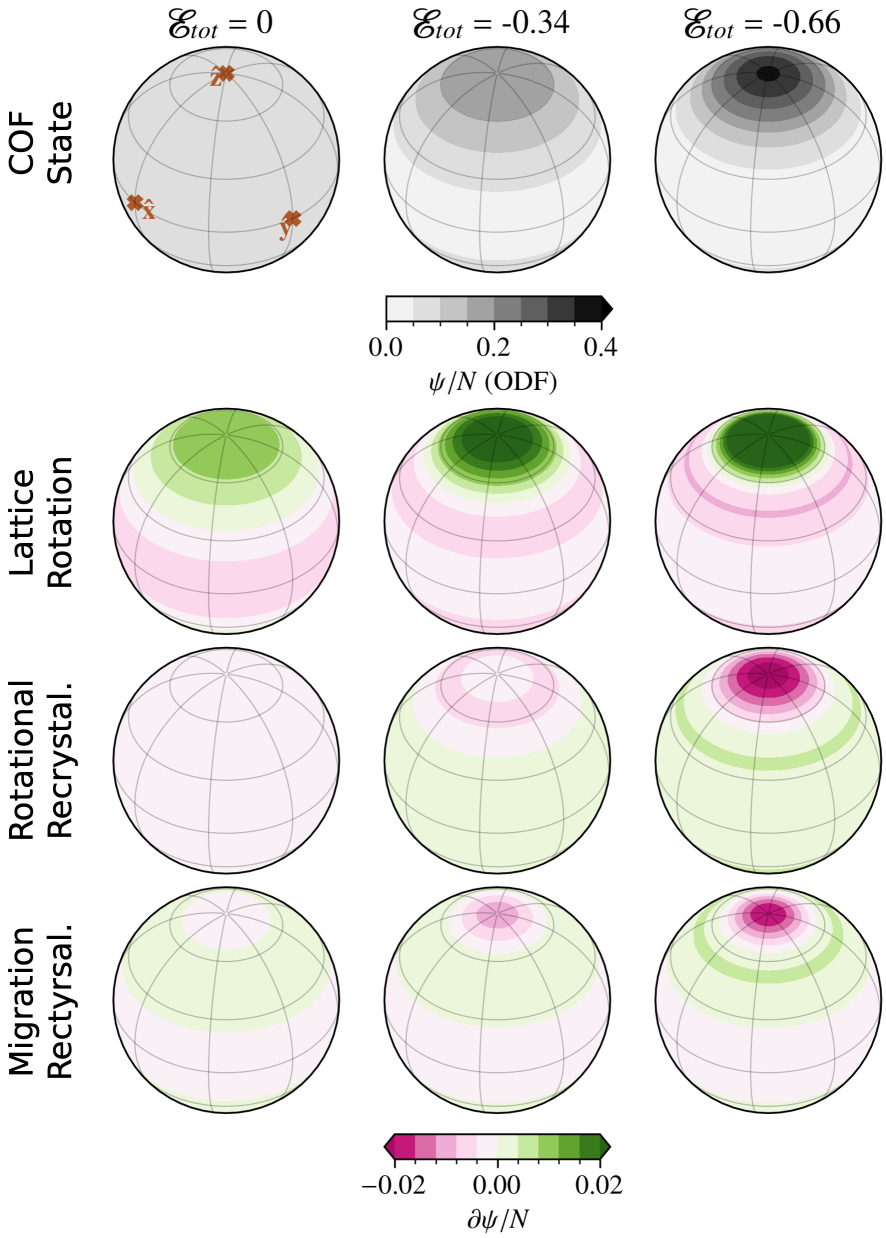
$\mathscr{E}_{tot}$ = 0
$\mathscr{E}_{tot}$ = -0.34
$\mathscr{E}_{tot}$ = -0.66
COF State
Lattice Rotation
Rotational Recrystal.
Migration Rectyrsal.
z
x
y
0.0
0.2
0.4
ψ/N (ODF)
−0.02
0.00
0.02
$\partial\psi/N$

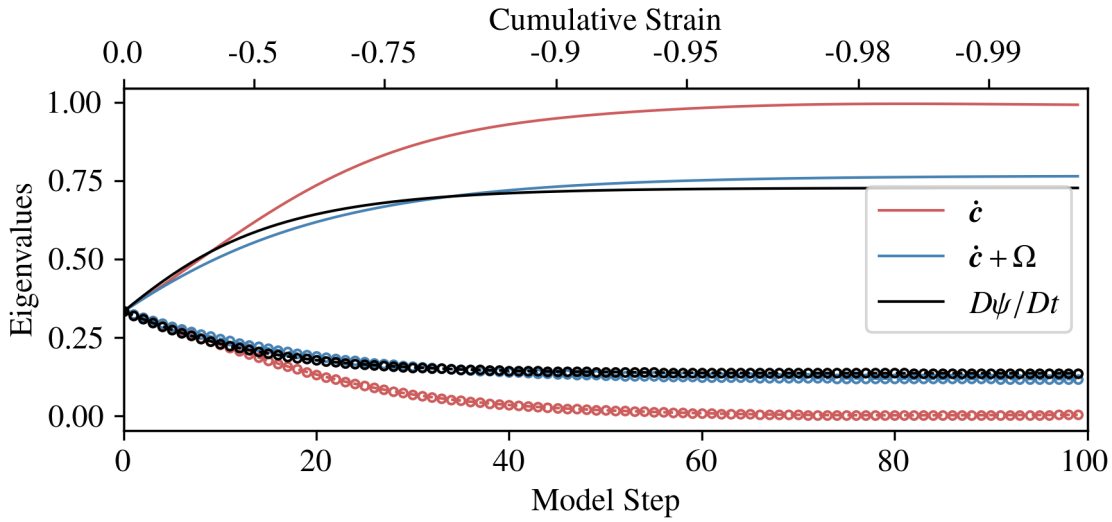

Figure 2.6: Principal eigenvalues for modeled COF evolution in unconfined uniform compression (as in Figure 2.5 above). Here, I show three scenarios of increasing complexity: 1) lattice rotation only (red); 2) lattice rotation and rotational recrystallization (blue); 3) lattice rotation, rotational recrystallization, and dynamic recrystallization (black). The third scenario is equivalent to the top row in Figure 2.5.

'migration recrystallization'. Given a persistent high-stress state, a crystal can eventually be consumed entirely. New crystals can also spawn, called 'grain nucleation', and typically with an orientation favorable to basal glide. The dynamic recrystallization decay rate is

$$\Gamma = \Gamma_0(\mathscr{D} - \langle\mathscr{D}\rangle) \tag{2.12}$$

where Γ_0 is a recrystallization rate factor which depends on temperature, dislocation density, and stress state. The deformability is

$$\mathscr{D} = \frac{(\tau\cdot\tau)\cdot\cdot c^2 - \tau\cdot\cdot c^4\cdot\cdot\tau}{\tau\cdot\cdot\tau} \tag{2.13}$$

and $\langle\mathscr{D}\rangle$ is the average deformability. At orientations where deformability is below average, $\mathscr{D} < \langle\mathscr{D}\rangle$, crystals decay, and at orientations above average deformability crystals grow.

For each of the three processes discussed above, there is one variable which is largely uncon-

strained: the ratio between rigid-body rotation and basal-glide rotation, ι, the rotational diffusivity, Ω, and the recrystallization rate factor, Γ_0. Each of these parameters can be expected to have some dependence on ice properties like temperature, grain size, dislocation density, and stress state. However, determining these dependencies from ice-core COF would require knowing a full history of the ice properties, and the limited laboratory experiments are still too few to constrain the parameters confidently. Below I discuss the temperature dependency, based mainly on a single study, but highlight the need for additional experiments in future work.

Richards et al. (2021) use laboratory COF experiments (e.g. Journaux et al., 2019; Qi et al., 2019) alongside their physical model (similar to that described above) to invert for the three parameters, ι, Ω, and Γ_0 (Figure 2.4). They find that the recrystallization rate factor is strongly temperature dependent. They assign a linear dependence, but I argue that based on the physics it is more likely to have an exponential temperature dependence with some activation energy, like the creep rate factor (see Chapter 2.2) and the electrical conductivity (see Chapter 2.3). The rotational diffusivity and the rotation ratio have significantly weaker temperature dependence, and with so few experiments it is hard to say whether the estimated dependence is significant or a result of uncertainty. The rotation ratio has a theoretical value of one if ice deformation is purely by basal glide. Some studies have found that $\iota \neq 1$ (e.g. Placidi et al., 2006). At high temperatures and high stress states, alternative deformation mechanisms become important, like grain-boundary sliding and dislocation climb. In those cases, it is likely true that $\iota \neq 1$ but more laboratory experiments are necessary to constrain the parameter.

To demonstrate the partitioning between processes, I simulate a synthetic COF evolution for uniform vertical compression (Figure 2.5) using an open-source spectral fabric model, *specfab*, which implements the mathematical formulation above (Rathmann et al., 2021; Rathmann & Lilien, 2021). The initial state is isotropic with uniform distribution of c axes. Through time, crystal c axes rotate toward the compression axis (z in this case), forming a single maximum COF. Crystals rotate upward primarily by lattice rotation. Considering that process alone (Figure 2.6 red), all crystals will eventually align with the axis of compression (by $\mathscr{E} \approx 0.95$). On the other hand, both recrystallization processes, migration and rotational recrystallization, act to counter the upward lattice rotation. Since the compressional stresses are extraordinarily high along the vertical axis, the recrystallization processes are encouraging some outward migration. When considering recrystallization, the equi-

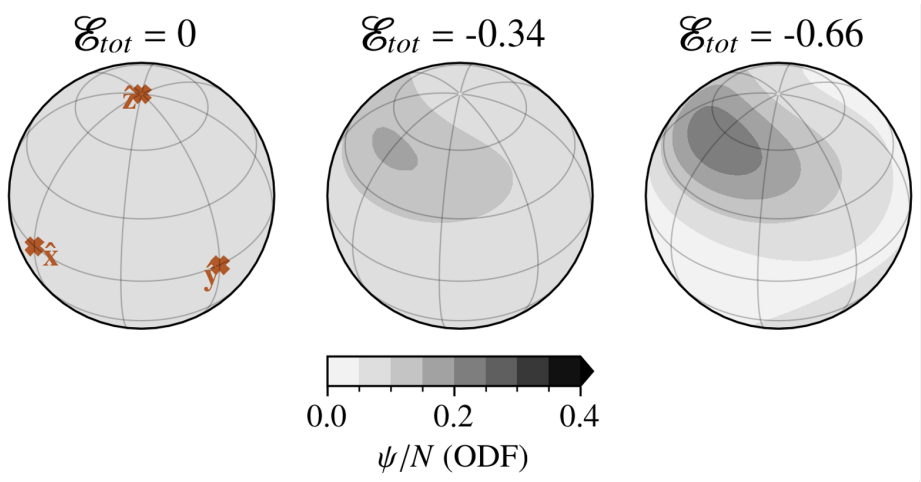

Figure 2.7: COF Evolution as in Figure 2.5 except in simple shear, $\dot{\mathscr{E}}_{xz}$.

librium state is still a single-maximum fabric but with some continuous growth of off-axis crystals.

Vertical compression is the simplest strain regime in terms of the COF evolution. In an analogous simulation to that above, I now prescribe a slightly more complicated strain regime but one that is relevant to this dissertation, simple shear ($\dot{\mathscr{E}}_{xz}$), to demonstrate the evolving COF state (Figure 2.7). Now, the COF maximum is not aligned with a single axis and instead forms a partial vertical girdle.

2.1.3 Crystal Fabric Processes and Timescales in an Ice Sheet Setting

As ice flows, crystal *c* axes tend to rotate away from the primary extensional axis and toward compression (Alley, 1988). Single-pole fabrics with upward-pointing *c* axes (Figure 2.5) develop at an ice dome where flow is by uniform vertical compression and outward extension in all directions from the dome. Along an ice divide, where there is one prominent extensional direction, a vertical girdle develops perpendicular to the axis of extension (e.g. Fitzpatrick et al., 2014). The center of an ice-stream is similar, with extension in the direction of ice flow (E. C. Smith et al., 2017). A partial horizontal girdle develops in an ice-stream shear margin where transverse shear dominates, and a partial vertical girdle in areas where vertical shear dominates (Figure 2.7).

The degree to which a COF is developed depends on the total strain accumulated over time. Both the strain rate in a given setting and the timescale over which that strain setting has persisted in the ice are important for knowing and understanding the COF state. As an order of magnitude

estimate for the time to some initial COF anisotropy in a steady strain setting, laboratory studies show a steadying of the creep characteristics (i.e. convergence to tertiary creep) by cumulative strain ~0.1 (Budd & Jacka, 1989). Therefore, vertical strain rates at an ice dome or ice divide, approximately 10^{-5} to $10^{-4} yr^{-1}$, would develop some noticeable COF on the order of thousands to tens of thousands of years. In areas with much higher strain rates such as an ice-stream shear margin, approximately 10^{-2} to $10^{-1} yr^{-1}$, the COF develops much faster, even on the order of years.

During tertiary creep, the COF continues to evolve, becoming more anisotropic through time as long as the strain regime remains consistent. Eventually, the COF converges to a state that is steady in time, with the time to steadiness depending on the effectiveness of each process: lattice rotation, rotational recrystallization, and dynamic recrystallization (Figure 2.6). Ignoring recrystallization, the COF continues to evolve until perfect anisotropy which is approached as $\mathscr{E} \to 1$. Considering both recrystallization processes, the COF converges by $\mathscr{E} \approx 1 - \frac{1}{e} \approx 0.6$ (at time $t = \frac{1}{\dot{\mathscr{E}}}$). Of course, the precise timing will change depending on the rotational diffusivity, Ω, and the recrystallization rate factor, Γ_0, which are both still poorly constrained.

In addition to its use case for interpreting past ice flow, knowing the COF is also important for understanding present and future ice flow. Since most ice deformation is by glide along the basal plane (especially in cold ice), ice crystals are relatively soft to shear across the c axis and hard to compression along that axis. This becomes important to ice-sheet flow when a COF develops. For instance, a vertical single pole at an ice dome hardens to additional vertical compression, and old ice is preserved near the bed (C. F. Raymond, 1983). Similarly, an established COF in a shear margin can soften the ice and promote faster flow (M. Jackson & Kamb, 1997), with ice being up to two orders of magnitude softer depending on crystal orientation (Shoji & Langway, 1988).

2.2 Thermal Properties of Ice

Executable Jupyter Notebooks to reproduce selected figures from this section are available at github.com/benhills/iceotherm.

The thermal properties of ice used in discussion below can be derived from microscopic properties of the crystal as I did for the mechanical properties in Section 2.1. For example, the heat capacity and latent heat are directly related to the energy of a hydrogen bond. However, an explicit description of the microscopic thermodynamics is less important for discussing macroscopic heat flow than it is for the mechanical (Section 2.1) and electrical (Section 2.3) properties. Here, I focus on macroscopic heat flow and direct the reader toward other texts for derivations of the thermal constants discussed (Fletcher, 1970; Petrenko & Whitworth, 1999).

Ice-sheet temperatures are a result of the climate history, ice-flow history, and upward heat flow from the solid Earth below. Ice temperature evolution is modeled by the heat equation which, in its most general form, is

$$\rho c \frac{DT}{Dt} = k\nabla^2 T + Q \tag{2.14}$$

The relevant physical processes expressed in this equation are illustrated in Figure 2.8. Thermal diffusion, $k\nabla^2 T$, is commonly considered only in the vertical dimension. As for the COF evolution (equation 2.5), the left-hand side here is a material derivative containing the macroscopic velocity field, $\mathbf{u}$, which advects ice of a given temperature through the ice-sheet domain. Because of the way ice flows, it is natural to break advection into a vertical component (dominant near an ice divide) and longitudinal/lateral components (dominant in an ice stream). Lastly, Q is a heat source. Common heat sources in an ice sheet are from the work done by strain and from the latent heat of fusion. In each of the subsections below, I make assumptions to reduce the general heat equation for specific cases relevant to an ice sheet. I discuss analytical solutions for each of those cases and compare to a general numerical implementation which I describe in detail.

2.2.1 Pure Diffusion

Taking no velocity field, $\mathbf{u} = 0$, and no heat source, $Q = 0$, equation (2.14) reduces to pure diffusion.

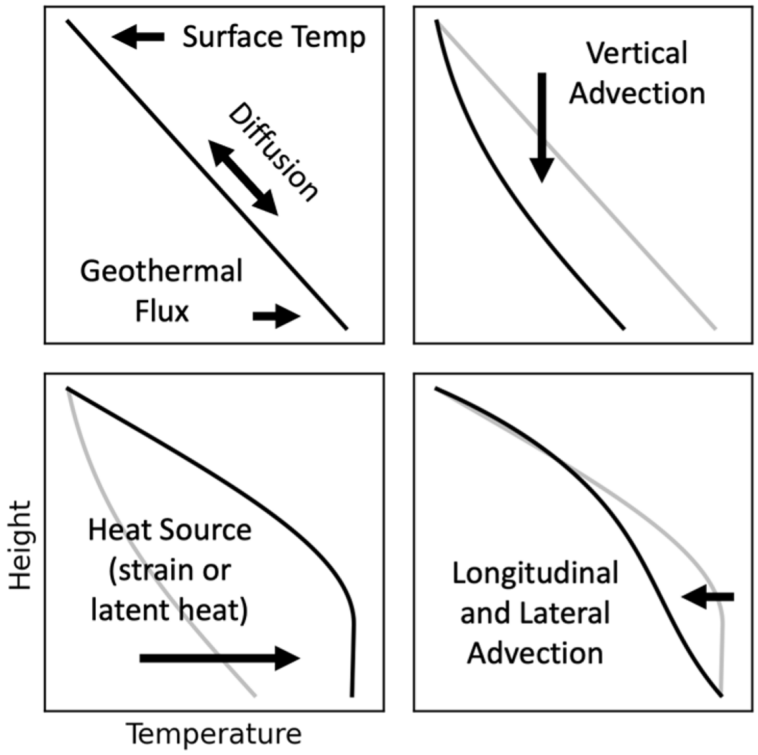

Figure 2.8: Illustration of thermal processes in an ice sheet setting. Processes are added sequentially, so the grey line in each is the previous state (previous panel).

$$\frac{\partial T}{\partial t} = \kappa \nabla^2 T \tag{2.15}$$

where thermal diffusivity $\kappa = \frac{k}{\rho c}$. Earth materials, including ice, can commonly be approximated as a half space, where variations in two dimensions are negligible compared to the third. In those cases, the spatial derivative reduces to one dimension $\nabla^2 = \frac{\partial^2}{\partial z^2}$ simplifying equation 2.15 even further. While ice-sheet temperature gradients cannot always be considered negligible in the horizontal (Hills et al., 2017, e.g.) it is useful to make this approximation for now in order to discuss diffusion timescales in the vertical.

Considering one-dimensional pure diffusion in a half space, many analytical solutions exist (Carslaw & Jaeger, 1959). Two particularly relevant solutions are considering warming/cooling with a fixed surface boundary condition

$$T(z,t) = \Delta T erfc\left(\frac{z}{2\sqrt{\kappa t}}\right) \tag{2.16}$$

and with an oscillating surface boundary condition

$$T(z,t) = \Delta T e^{-z\sqrt{\frac{\omega}{2\kappa}}} sin\left(\omega t - z\sqrt{\frac{\omega}{2\kappa}}\right) \tag{2.17}$$

The former represents some discrete change in the air temperature, ΔT, and how that thermal signature propagates down into the ice, the latter represents an oscillating air temperature with period $t_{period} = \frac{2\pi}{\omega}$. In both cases, a representative length scale appears

$$\ell = 2\sqrt{\kappa t} \tag{2.18a}$$

$$\ell = \sqrt{\frac{2\kappa t_{period}}{\pi}} \tag{2.18b}$$

sometimes called the e-folding depth or, especially for the harmonic case, skin depth. A relevant case for Earth materials is with a 1-year period (the seasonal changes in air temperature). For ice/firn thermal diffusivity, the skin depth of an annual oscillator is ~10 m, often used as a practical estimate of the mean annual air temperature (Hooke, 1976). At longer timescales, it becomes apparent how slow thermal diffusion is and why a thermal signature of historical climate or ice flow could be

preserved in thick ice (Figure 2.9). At the typical thickness of a glacier (~10^2 m) or ice sheet (~10^3 m), the response timescale for diffusion of a temperature change at the surface boundary is 10^2-10^3 years and 10^4 years, respectively.

2.2.2 1-Dimensional Advection-Diffusion

Ice sheets are not static masses of ice, they move. Thus, while pure diffusion is a useful representation to conceptualize the timescales for that individual process, it is not an adequate model to predict ice-sheet temperature for most realistic settings. As new snow is deposited at the ice-sheet surface each year it buries that from previous seasons and pushes the older snow/ice downward toward the bed. This vertical motion is the primary component of ice flow for much of the inland accumulation area. In many such cases, considering advection of heat in only the vertical is sufficient to predict ice temperature. I discuss some relevant analytical solutions under these conditions below.

For steady-state ice velocity only in the vertical, $\mathbf{u} = w(z)$, and ignoring any heat source, equation 2.14 reduces to the steady one-dimensional advection-diffusion equation

$$\kappa \frac{\partial^2 T}{\partial z^2} = w \frac{\partial T}{\partial z} \tag{2.19}$$

In the case of a constant vertical velocity, another useful parameter can be derived. The *Peclet* number

$$Pe = \frac{w\ell}{\kappa} \tag{2.20}$$

is a non-dimensional number which represents the relative importance of advection and diffusion. In an ice sheet, the vertical velocity is approximately equal to the surface accumulation rate, order 10^{-1} m/yr. The representative length scale, ℓ, is the ice thickness in this case, order 10^3. For those approximations, $Pe \approx 3$, so advection is much faster than diffusion. In other words, cold ice from the surface is pushed downward to depths that would otherwise be warmed by the geothermal flux at the ice-sheet base. Of course, realistic ice-sheet settings span a range of *Peclet* numbers.

As for pure diffusion, the utility of prescribing a constant vertical velocity is only to parameterize the process effect. The true ice velocity must decrease with depth since ice does not penetrate the

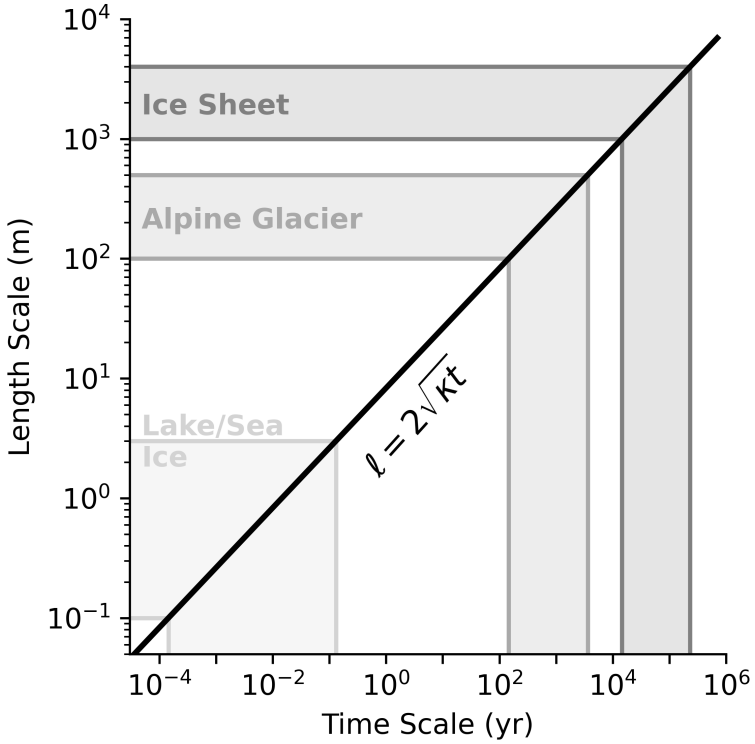

Figure 2.9: Timescale for thermal diffusion in ice of various forms as it exists on Earth's surface.

substrate bedrock. Next, I describe two analytical solutions which make different assumptions about the vertical velocity. Each of which can be used to predict ice-sheet temperatures in settings where vertical velocity dominates the ice-flow regime.

Robin (1955) Solution

The Robin (1955) analytical solution for ice-sheet temperature is by far the most widely used in the glaciology literature. It assumes that the vertical velocity is linear with height above the bed

$$w(h) = -\dot{a}\frac{h}{H} \tag{2.21}$$

where $h = H - z$, so the velocity equals the specific mass balance rate, $\dot{a}$, at the surface, $h = H$, and is zero at the bed, $h = 0$. Then the steady-state temperature with depth is

$$T(h) = T_S + \frac{Q_{geo}\sqrt{2\pi\kappa H}}{2k\sqrt{\dot{a}}}\left[erf\left(h\sqrt{\frac{\dot{a}}{2\kappa H}}\right) - erf\left(H\sqrt{\frac{\dot{a}}{2\kappa H}}\right)\right] \tag{2.22}$$

Once again, the length scale for thermal diffusion (equation 2.18a) shows up here. A modified version of this solution includes the basal melt rate in the vertical velocity, $w \propto \dot{a} + \dot{m}$ (van der Veen, 2013), where

$$\dot{m} = \frac{1}{\Delta t}\frac{\rho c}{\rho_w L}\int_0^H (T - T_{pmp})dz \tag{2.23}$$

The pressure-dependent depression of the melting-point temperature is given by

$$T_{pmp} = \Xi\rho g z \tag{2.24}$$

In this modified version, the analytical solution must be solved iteratively since the melt rate depends on the temperature itself (equation 2.23).

Rezvanbehbahani (2019) Solution

An updated and more comprehensive analytical solution was proposed by Rezvanbehbahani et

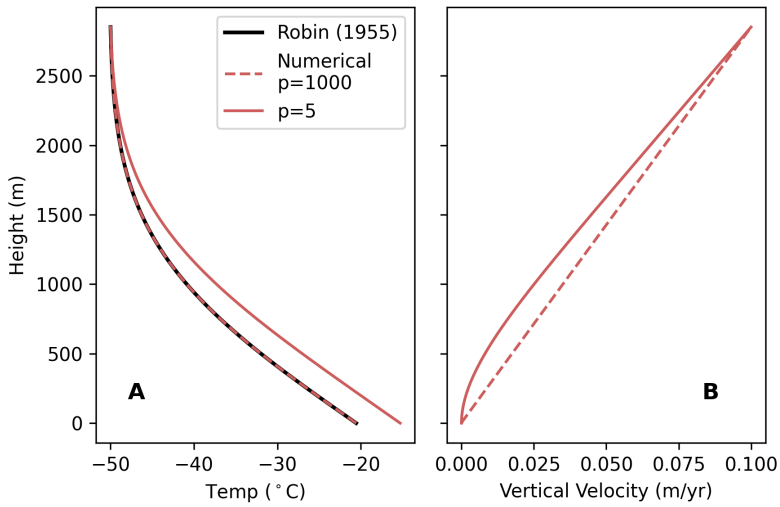

Figure 2.10: Reproduction of the Robin (1955) analytical solution for ice temperature with parameters from Siple Dome and comparison to the numerical solution.

al. (2019) (see (Talalay et al., 2020) for a similar solution). It allows for nonlinear vertical velocity

$$w(h) = -\dot{a}\left(\frac{h}{H}\right)^{\mathcal{G}} \tag{2.25}$$

Then the analytical solution for ice temperature is

$$\begin{aligned} T(z) = \\ T_S + \frac{Qgeo^{\frac{-1}{\mathcal{G}+1}}}{\kappa(\mathcal{G}+1)}\Bigg[& Gamma\left(\frac{1}{\mathcal{G}+1}, \left(\frac{\dot{a}}{\kappa H^{\mathcal{G}}(\mathcal{G}+1)}\right)h^{\mathcal{G}+1}\right) \\ & -Gamma\left(\frac{1}{\mathcal{G}+1}, \left(\frac{\dot{a}}{\kappa H^{\mathcal{G}}(\mathcal{G}+1)}\right)H^{\mathcal{G}+1}\right)\Bigg] \end{aligned} \tag{2.26}$$

where *Gamma* is the Euler integral of the second kind (I reserve Γ to denote dynamic recrystallization as in Section 2.1.2). Compared to Robin (1955), this analytical solution has slower vertical velocities (Figure 2.11A). Therefore, less cold ice penetrates to depth, and the resulting ice-temperature profile is warmer (more realistic for the ice-sheet divide scenario).

As I will discuss below, the true vertical velocity profile in an ice sheet is not the simple expo-

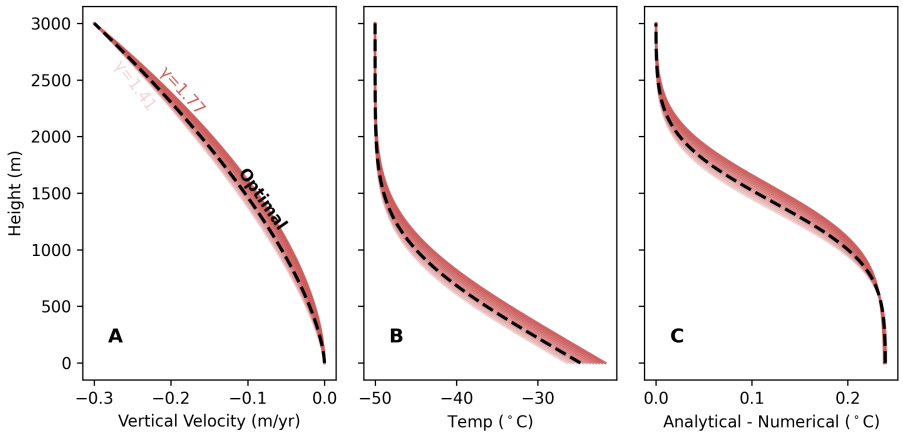

Figure 2.11: Reproduction of the Rezvanbehbahani et al. (2019) analytical solution and comparison to the numerical solution.

nential given in equation 2.26. Still, this form is convenient since it has an analytical solution and can be reduced to other forms above. In the case where $\gamma = 0$ the vertical velocity is constant, and for $\gamma = 1$ it is linear (as in equation 2.22). In reality γ will be greater than 1 and the precise value which most closely approximates ice flow will depend on the setting. Rezvanbehbahani et al. (2019) give significant consideration to this parameter, but I will not discuss it further.

2.2.3 1.5-Dimensional Advection-Diffusion with a Heat Source

Away from the ice divide, streaming ice becomes dominated by flow in the horizontal. Horizontal flow speeds are up to ~10^4 m/yr (Joughin et al., 2018; Mouginot et al., 2019) so can be ~5 orders of magnitude faster than the vertical in these cases. Now, consider a three-dimensional velocity field, $\mathbf{u} = u^*(x^*) + v^*(y^*) + w(z)$, and heat sources, Q, that may arise from shear strain or latent heat

$$\frac{\partial T}{\partial t} = \kappa \frac{\partial^2 T}{\partial z^2} - u^* \frac{\partial T}{\partial x^*} - v^* \frac{\partial T}{\partial y^*} - w \frac{\partial T}{\partial z} + \frac{Q}{\rho c} \tag{2.27}$$

Here, I align the domain with ice flow so that x^* is the longitudinal (along-flow) direction and y^* is the lateral (across-flow) direction. Next, I describe two solutions to the above equation. First, a steady-state analytical solution specific to ice-sheet shear margins. Second, a numerical solution which has more general applications.

Meyer and Minchew (2018) Solution

Shear strain is a significant heat source in ice-stream shear margins. In that setting, the steady temperature profile represents a trade off between heat production by strain and the advective heat sink of cold ice moving through the shear margin. Meyer and Minchew (2018) make two critical assumptions in order to compare these processes with an analytical solution. First, they assume that the velocity field is constant in the vertical, $w = -\dot{a}$, and that horizontal advection is dominated by lateral flow through the shear margin as opposed to longitudinal advection along the ice stream (i.e. $u^* = 0$). Second, they assume that all ice properties are constant, including the rate factor, A, from equation 2.3 which is known to be temperature dependent (Glen, 1955).

Three non-dimensional numbers are used to describe the following analytical solution from Meyer and Minchew (2018). The vertical *Peclet* number, *Pe*, is as above in equation 2.20. The advective heat sink is parameterized by a horizontal *Peclet* number

$$\Lambda = \frac{H}{\kappa(T_b - T_S)} \int_0^H v^* \frac{\partial T}{\partial y^*} dz \tag{2.28}$$

The heat source is parameterized with the *Brinkman* number

$$Br = \frac{QH^2}{k(T_b - T_S)} \tag{2.29}$$

where the heat source is from x^*-y^* plane shear

$$Q = 2\dot{\varepsilon}_{x^*y^*} \tau_{x^*y^*} \tag{2.30}$$

and from Glen's Law (equation 2.3)

$$\tau_{x^*y^*} = \left(\frac{\dot{\varepsilon}_{x^*y^*}}{A} \right)^{1/n} \tag{2.31}$$

Again, the rate factor, A, is constant for this analytical solution. The plane strain rate, $\dot{\varepsilon}_{x^*y^*}$, is prescribed based on ice flow conditions at the site of interest. With the above assumptions and parameterizations, Meyer and Minchew (2018) define a steady-state analytical solution for shear-margin temperature

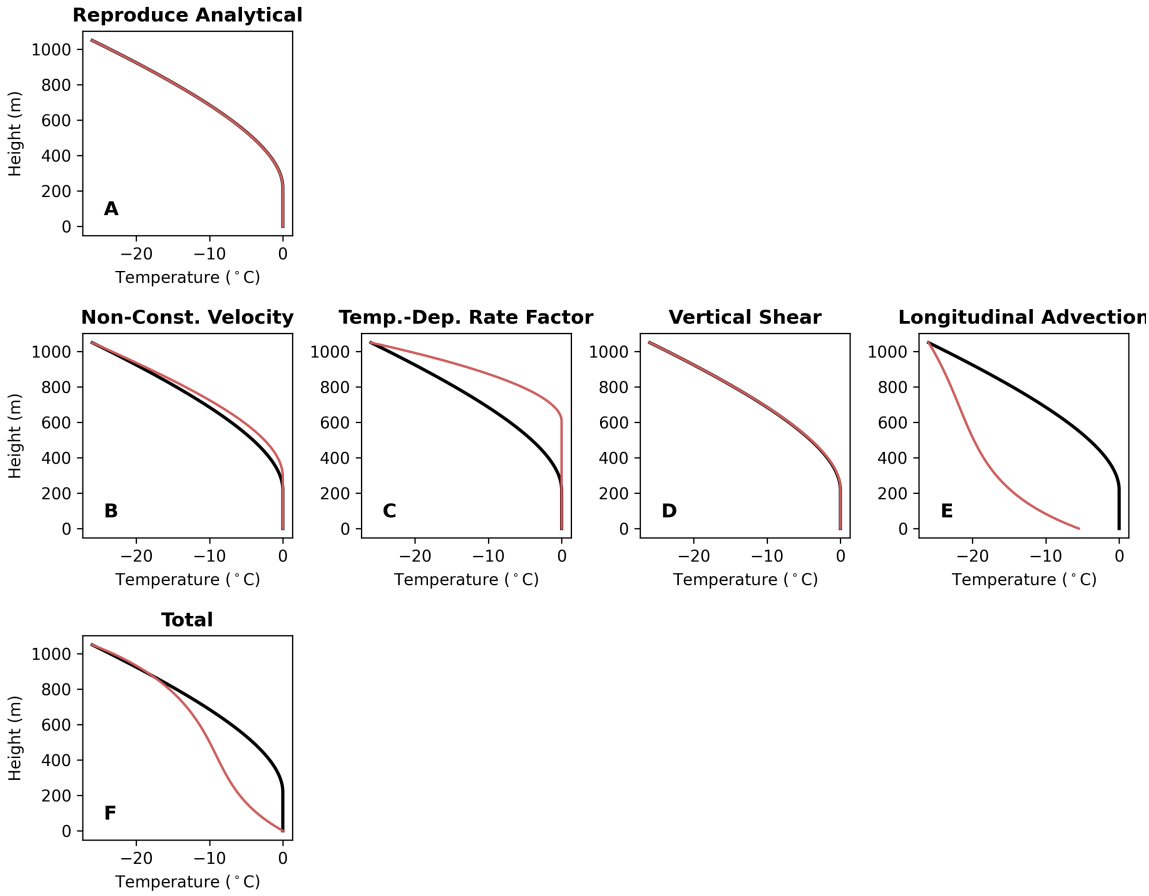

Figure 2.12: Reproduction of the Meyer and Minchew (2018) analytical solution (black) for ice temperature with parameters from the Dragon Shear Margin, Whillans Ice Stream. (A) Direct reproduction of the analytical solution with the numerical model (red). (B-E) Isolated temperature effect of each physical process. (F) Effective temperature solution in a theoretical shear margin (all processes together).

$$T = T_S + (T_B - T_S)\frac{Br - \Lambda}{Pe}\left[1 - \frac{h}{H} + \frac{1}{Pe}e^{Pe\left(\frac{\hbar}{H}-1\right)} - \frac{1}{Pe}e^{Pe\left(\frac{\hbar-h}{H}\right)}\right] \tag{2.32}$$

where $\hbar$ is the height of temperate ice, so any portion of the ice column below that height, $0 \leq z \leq \hbar$, is temperate, $T = T_m$. While prior work had discussed the relative strength of advection and heat generation in ice stream shear margins (Perol & Rice, 2015; Suckale et al., 2014) this analytical solution was a critical step forward to consider ice temperatures and temperate ice thicknesses at the continental scale (Meyer & Minchew, 2018).

Numerical Solution

> *Originally published as supplementary material in Geophysical Research Letters (Hills, Christianson, Hoffman, et al., 2022).*

Here, I outline a more generalized solution to equation 2.27. While it can only be solved numerically, not analytically as above, it applies to a wider variety of ice-sheet settings (including all the above and many more) and with more sophisticated variable dependencies which become especially important at the long timescales considered at an ice divide. The numerical model is resolved in only the vertical dimension but incorporates an advective heat sink to represent longitudinal (and optionally lateral) ice flow.

For vertical velocity, w, I use the Lliboutry (1979) shape factor

$$w = \dot{a}\left(1 - \frac{p+2}{p+1}\zeta + \frac{1}{p+1}\zeta^{p+2}\right) + \dot{m} \tag{2.33}$$

where $\zeta = \frac{z}{H}$ is a normalized depth below surface. $p \gg 1$ in the sliding case, where the vertical velocity should be approximately linear, and in the non-sliding (divide-flow) case (Parrenin et al., 2007, eq. 4)

$$p = n - 1 + \frac{E}{RT_b^2}\frac{\partial T}{\partial z}\Big|_0 \tag{2.34}$$

If the ice sheet is thin relative to the length scale considered for ice flow (shallow ice), then the longitudinal temperature gradient can be approximated as (Weertman, 1968)

$$\frac{\partial T}{\partial x^*} = \frac{\partial T_S}{\partial x^*} + \frac{T - T_S}{2}\left(\frac{1}{H}\frac{\partial H}{\partial x^*} - \frac{1}{\dot{a}}\frac{\partial \dot{a}}{\partial x^*}\right) \tag{2.35}$$

This longitudinal temperature gradient is commonly discarded but is important in fast-moving ice streams. In those cases, cold ice deposited in the accumulation area is rapidly transported into a warmer environment, faster than the ice can warm by diffusion (this is the focus of Chapter 3).

The heat source, Q, has three components,

$$Q = Q_{x^*z} + Q_{x^*y^*} + Q_L \tag{2.36}$$

where $Q_{x^*y^*}$ is heat from plane-shear strain as in equation 2.30. The heat source from vertical-shear strain, Q_{x^*z}, is

$$Q_{x^*z} = 2\dot{\mathscr{E}}_{x^*z}\tau_{x^*z} \tag{2.37}$$

and the vertical shear stress is defined by assuming a local stress equilibrium

$$\tau_{x^*z} = \rho g z \frac{\partial S}{\partial x^*} \tag{2.38}$$

where S is the surface elevation. Again, Glen's Law (equation 2.3) is used to remove one variable, so the heat source from vertical shear is

$$Q_{x^*z} = 2A\tau_{x^*z}^{n+1} \tag{2.39}$$

For this numerical solution, the rate factor can be temperature dependent,

$$A = A_* e^{\frac{-E}{R}\left(\frac{1}{T} - \frac{1}{T_r}\right)} \tag{2.40}$$

I calculate A_* iteratively in a way to maximally conserve energy. That is, the column integrated heat source $\int_0^H Q_{x^*z} dz$ should be equal to the driving stress multiplied by the deformational component of the surface velocity. The final heat source is latent heat from refreezing of liquid water

$$Q_L = L\dot{m}\rho_w \tag{2.41}$$

The boundary conditions are: 1) the surface boundary is fixed to a prescribed air temperature, and 2) the bottom boundary is

$$\left.\frac{\partial T}{\partial z}\right|_0 = Q_{geo} + u_b^* \tau_b \tag{2.42}$$

Unlike the analytical solutions above, this numerical solution is transient, so both boundaries can change in time.

The thermal properties of ice described in this model are not constant, as was assumed in the analytical solutions. Thermal conductivity, k, is dependent on both temperature and density (Cuffey & Paterson, 2010). At ice density,

$$k_i(T) = 9.828 e^{-.0057T} \tag{2.43}$$

and at firn densities (Schwerdtfeger, 1963),

$$k = \frac{2k_i(T)\rho}{3\rho_i - \rho} \tag{2.44}$$

Heat capacity, c, is dependent on temperature as well (Cuffey & Paterson, 2010),

$$c = 152.5 + 7.122T \tag{2.45}$$

This is a specific heat capacity (per unit mass), and the small percent by mass of air in the firn column (<0.1%) does not significantly affect the bulk heat capacity, so we do not consider any density dependence.

In Figures 2.10, 2.11, and 2.12, I compare this numerical model to the above analytical solutions. For both the Robin (1955) and Meyer and Minchew (2018) solutions, the numerical model matches exactly. The Rezvanbehbahani (2019) solution varies slightly from the numerical model because of assumptions made for the nonlinear vertical velocity profile. In Figure 2.12, I show steady-state temperature profiles of increasing complexity in order to demonstrate the effect of each additional physical process.

2.2.4 Thermal Processes and Timescales in an Ice Sheet Setting

As for COF in Section 2.1.2, present-day ice temperature is a result of the ice and climate history, and it also influences subsequent ice flow. Here, I discuss typical ice-sheet temperature patterns, both modeled and measured results, how those patterns can be used to interpret historical conditions, and how ice temperature is important for future ice flow.

Ice temperature at an ice-flow divide is commonly measured in ice cores after they are drilled (Cuffey et al., 2016; Dahl-Jensen & Johnsen, 1986). At these locations, ice flow is only in the vertical direction and is relatively slow and uniform, most closely approximating the 1-dimensional advection-diffusion case explored in Section 2.2.2. Since the timescale for diffusion is long, paleo-air temperatures are preserved within the ice-temperature profile. The difference between measured ice temperatures and a model prediction indicate how past air temperatures were different from today (Cuffey et al., 2016; Dahl-Jensen & Johnsen, 1986).

Fast-flowing ice streams can produce substantial heat, both throughout the ice column by work done to strain the ice as well as at the bed due to friction associated with basal sliding. In these fast-flowing areas, thermal-drilling methods (as opposed to mechanically-drilled holes) have been used to access the ice column. Within streaming ice, the bed is generally thawed. Ice-stream shear margins are difficult to access directly, so our understanding of ice temperature there has improved through data-informed thermal modeling using measurements of surface velocity (Suckale et al., 2014) and ice-temperature measurements from other areas of the ice sheets. Due to strain heating, thermal models often indicate thick temperate ice columns in shear margins, but observational verification remains elusive.

In the ice-sheet ablation area, surface melting leads to supraglacial streams and lakes which eventually drain into the ice. That water brings latent heat deep into the ice column which is released when the water refreezes, warming the ice (M. P. Lüthi et al., 2015; Phillips et al., 2010). Water movement through the englacial system is much faster than ice advection/diffusion, so can act to warm the ice near instantaneously. With enough water, the full ice column should trend to the melting point. The only direct observations of thick temperate ice in an ice-sheet are in western Greenland (Harrington et al., 2015).

I showed in equation 2.40 that ice viscosity is exponentially temperature dependent. Ice-flow

dynamics are therefore dependent on the thermal history of the ice. In the ablation zone, ice may be warm near the upper and lower boundaries where water can infiltrate, but stiffness from the cold core could drive regional ice flow (Ryser et al., 2013). At a shear margin, both strain and potentially water infiltration can soften the ice and stabilize the shear margin boundary (Iken et al., 1993). In this way, ice warming can lead to faster flow and to additional warming. In an extreme end-member scenario one could consider a thermal viscous collapse (Colgan et al., 2015).

2.3 Electrical Properties of Ice

In a similar manner to the mechanical properties discussed in Section 2.1, the electrical properties of ice are made unique by the hydrogen bond, the mobility of protons within the ice lattice, and the polarity of the water molecule. A feature which is of particular importance to this body of work is the near transparency of ice to radio waves. Ice-penetrating radar is effective because radio frequencies are in an absorption gap between Debye relaxation at the low (kHz) frequencies (Fujita et al., 2000) and lattice vibrations (heat) at higher microwave frequencies (Warren, 2019). Radio sounding (ice-penetrating radar) can therefore be used to survey ice for the geometry, stratigraphy, and to interpret ice properties, as I do in subsequent chapters (3, 4, and 5). Here, I provide a detailed background on 1) radar attenuation, and 2) radar birefringence in ice. I choose these two processes because each can be used to interpret ice-penetrating radar for englacial properties. Radar attenuation is dependent on conductivity which is subsequently dependent on the ice temperature (important for Section 2.2). Birefringence (electrical anisotropy) is dependent on the COF (important for Section 2.1.2).

2.3.1 A Theoretical Model for Radar Attenuation

In this section, I derive the radar attenuation rate in ice, N, and discuss its dependence on temperature and ice impurities. For the sake of clarity and simplicity, it is easiest to discuss attenuative losses in terms of the plane-wave equation,

$$\mathscr{A}(z,t) = \mathscr{A}_0 e^{-i\omega t} e^{-\gamma z} \tag{2.46}$$

where $\mathscr{A}$ is the amplitude of the wave which had initial amplitude, $\mathscr{A}_0$, moves in time, $e^{-i\omega t}$, and decreases with propagation, $e^{-\gamma z}$, into the attenuating material. γ, the propagation constant, is defined

$$\gamma = \alpha + i\beta \tag{2.47}$$

where the important term here is the real component, α, which is the absorption coefficient. The imaginary component, β, is the phase constant, which represents the change in phase, both terms are per unit length along the path travelled by the wave, z. Below, I discuss in more detail ex-

actly where the energy lost to attenuation goes, but for now it is sufficient to know that the energy/power/amplitude of the wave decreases with distance traveled. α has units m^{-1} and its inverse, $\ell = 1/\alpha$, is an important length scale, commonly called the e-folding length or sometimes the skin depth (similar to that for temperature in Section 2.2). Physically, this e-folding length scale is the distance at which the wave amplitude has decayed to $1/e$ of the transmitted amplitude, $\mathscr{A}_0$.

Now, I define the propagation constant in terms of dielectric properties following J. D. Jackson (1999)

$$\gamma^2 = i\omega\mu(\sigma + i\omega\varepsilon) \tag{2.48}$$

where ω is the angular frequency, μ is the magnetic permeability, σ is the electrical conductivity, and ε is the permittivity. Solving for the real (attenuation constant) and imaginary (phase constant) components,

$$\alpha = \omega\sqrt{\frac{\mu\varepsilon}{2}\left[\sqrt{1+\left(\frac{\sigma}{\omega\varepsilon}\right)^2}-1\right]} \tag{2.49}$$

$$\beta = \omega\sqrt{\frac{\mu\varepsilon}{2}\left[\sqrt{1+\left(\frac{\sigma}{\omega\varepsilon}\right)^2}+1\right]} \tag{2.50}$$

where the parenthetical term, $\frac{\sigma}{\omega\varepsilon}$, is commonly referred to as the loss tangent, $tan\delta$. Generally, the attenuation constant, α, is reduced further under certain assumptions:

Good Conductors, $tan\delta \gg 1$

$$\alpha = \sqrt{\frac{\omega\mu\sigma}{2}} \tag{2.51}$$

Poor Conductors, $tan\delta \ll 1$

$$\alpha = \frac{\sigma}{2}\sqrt{\frac{\mu}{\varepsilon}} \tag{2.52}$$

The physical mechanism for electrical conductivity in ice is by moving protonic defects through the crystalline lattice (Figure 2.13). Proton mobility is relatively low compared to electrons in a

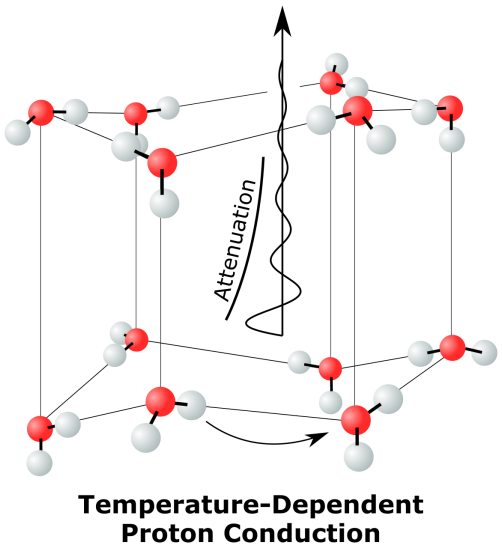

Figure 2.13: Illustration of radar attenuation in an ice crystal. Electrical conduction (by the movement of protons through the lattice) takes energy from the applied electric field, reducing the energy of the electromagnetic wave as it propagates through the ice.

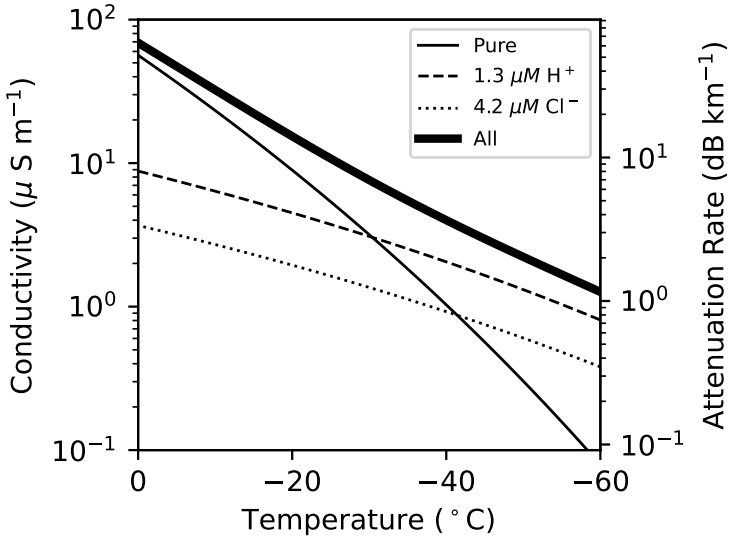

Figure 2.14: Theoretical model for radar attenuation in ice from equation 2.56. The assumed molarities for acids and salts (given in the figure legend) are from MacGregor et al. (2007).

metal conductor, for example, so ice is considered a poor conductor. We can therefore use the simplified attenuation constant in equation 2.52. Assuming that ice is not magnetic, $\mu_r = 1$, and has constant permittivity, ε, then the attenuation is independent of frequency and can be written as only a function of conductivity and some known constants. Now, I separate and recombine terms to mirror the form used by MacGregor et al. (2007),

$$\alpha = \frac{\sigma}{2c_0\varepsilon_0\sqrt{\varepsilon_r}} \tag{2.53}$$

where $\varepsilon = \varepsilon_0\varepsilon_r$ (permittivity of free space, and relative for ice) and $c_0 = \frac{1}{\sqrt{\mu_0\varepsilon_0}}$ is the wave speed in free space. Finally, the one-way attenuation rate, in dB/m, is defined (Winebrenner et al., 2003)

$$N = [e^{2\alpha}] = \alpha 20 log_{10}(e) \tag{2.54}$$

where $[X] = 10log_{10}(X)$ and I square the exponential term to convert to power. Combining equation 2.53 and 2.54 shows that attenuation rate is proportional to conductivity

$$N = \frac{10log_{10}(e)}{c_0\varepsilon_0\sqrt{\varepsilon_r}}\sigma = 921\sigma \tag{2.55}$$

The predominant conductivity model for ice is from MacGregor et al. (2007),

$$\sigma = \sigma_{pure}e^{\frac{-E_{pure}}{R}\left(\frac{1}{T}-\frac{1}{T_r}\right)} + \sum_{i=1}^{n} m_i M_i e^{\frac{-E_i}{R}\left(\frac{1}{T}-\frac{1}{T_r}\right)} \tag{2.56}$$

where E_i is the activation energy, m_i is the molar conductivity, and M_i is the molarity all for a given chemical species. Here we see that the conductivity is temperature dependent, but also that there are i independent chemical species, generally taken with: 0) pure ice; 1) $[H^+]$ the concentration of acids; and 2) $[Cl^-]$ the concentration of salts (Figure 2.14).

2.3.2 An Empirical Framework for Radar Attenuation

Originally published in Annals of Glaciology (Hills et al., 2020).

In this section we describe methods commonly used for measuring radar attenuation in ice (as derived in Section 2.3.1 above) empirically, using ice-penetrating radar data. Specifically, these

methods are targeted toward common-offset type data. Every empirical attenuation method described here is based on some type of regression for diminishing radar power with depth. Measured radar power can be broken into its constitutive components using the radar power equation (Bogorodsky et al., 1985) which we linearize by converting power to decibels, [dB],

$$[P_r] = [P_t] + 2[G] + [R] + [F] - \left[4\pi(2z)^2\right] - [B] - 2Nz \tag{2.57}$$

where $[P_r]$ is the returning power measured at the receiver, $[P_t]$ is the transmitted power, $[G]$ is antenna gain, $[R]$ is the reflection coefficient (which depends on the magnitude of the permittivity contrast across the interface, the incidence angle of the wave, and the interface specularity (Schroeder et al., 2015)), $[F]$ is refractive focusing (Bogorodsky et al., 1985, equation 3.8), z is the reflector depth, $4\pi(2z)^2$ is a spherical spreading term (assuming the target is large relative to the first Fresnel zone), $[B]$ is birefringence loss, and N is the attenuation coefficient derived above. It is worth noting that the plane-wave approximation, necessary to implement equation 2.57, is only accurate for depths well below the antenna separation distance (Arcone, 1995). In the rare cases where near-surface power interpretations are desired, alternative spreading and refractive focusing corrections could be made for a more specific radiation pattern and firn density profile.

To simplify equation 2.57, we correct the received power for spreading and refractive focusing,

$$[P_c] = [P_r] + \left[4\pi(2z)^2\right] - [F] \tag{2.58}$$

group all the system properties into one term,

$$[S] = [P_t] + 2[G] \tag{2.59}$$

and rewrite as

$$[P_c] = [S] + [R] - 2Nz \tag{2.60}$$

ignoring any effects of birefringence, $[B]$, for which corrections require polarimetric data (Fujita et al., 2006; K. Matsuoka et al., 2009). Birefringence losses only need to be considered when there is substantial phase lag between propagating waves of different polarizations, a phenomenon that

requires both a well-developed crystal orientation fabric in ice and a relatively high frequency radar system (more on this in Section 2.3.3 below).

To solve for N, the depth derivative is carried out by linear regression of equation 2.60, with the regression slope being equal to the depth-averaged attenuation rate over the chosen sampling window. This procedure ignores any source or reflectivity changes with depth. Typically, the regression is done by either ordinary least squares (Jacobel et al., 2009) or weighted least squares using the uncertainty of the reflected power as weights (MacGregor, Li, et al., 2015); however, problems which have two measured variables (i.e. depth and power both subject to uncertainty) can also be solved by regression with errors in variables and reporting the uncertainty to some confidence interval, as we do here (Appendix A).

In principle, empirical attenuation calculations all follow this same standard derivation, where some set of observations for the measured power and depth are isolated in equation 2.60 and regressed to calculate the attenuation rate (Figure 2.15). In practice, the precise methods for arriving at a calculated value change in order to sufficiently isolate the depth-power relationship by satisfying the critical assumptions that $\frac{\partial[S]}{\partial z} = \frac{\partial[S]}{\partial x} = 0$, and $\left|\frac{\partial[R]}{\partial z}\right| \ll \left|\frac{\partial[P_c]}{\partial z}\right|$. The validity of these assumptions is site and survey dependent. For some studies, a single coherent reflector is identified in many traces. If the reflector has spatially uniform reflectivity $\left(\frac{\partial[R]}{\partial z} \approx 0\right)$ and has high relief $(\frac{\partial z}{\partial x})$, it can justifiably be matched across many traces to calculate attenuation. In other studies, when multiple reflectors in one trace are assumed to have nearly the same reflectivity $\left(\frac{\partial[R]}{\partial z} \approx 0\right)$, they are used together to calculate attenuation for that trace individually. Lastly, in the select few surveys where a secondary bed reflection can be observed, it is compared directly to the primary reflection to calculate attenuation. We detail the methodology for each of these three groups below.

Single-Reflector Attenuation Methods

Method 1 – Single-reflector spatially-averaged attenuation. This is the most common method for calculating attenuation using a single reflector. A reflector is selected that can be easily identified across many traces, typically the ice-bed interface, and is used in a regression of reflected bed power as a function of ice thickness (i.e. equation 2.60) over a spatial domain with minimal basal reflectivity variations $\left(\left|\frac{\partial[R]}{\partial z}\right| \ll \left|\frac{\partial[P_c]}{\partial z}\right|\right)$ (Jacobel et al., 2009; Winebrenner et al., 2003). The

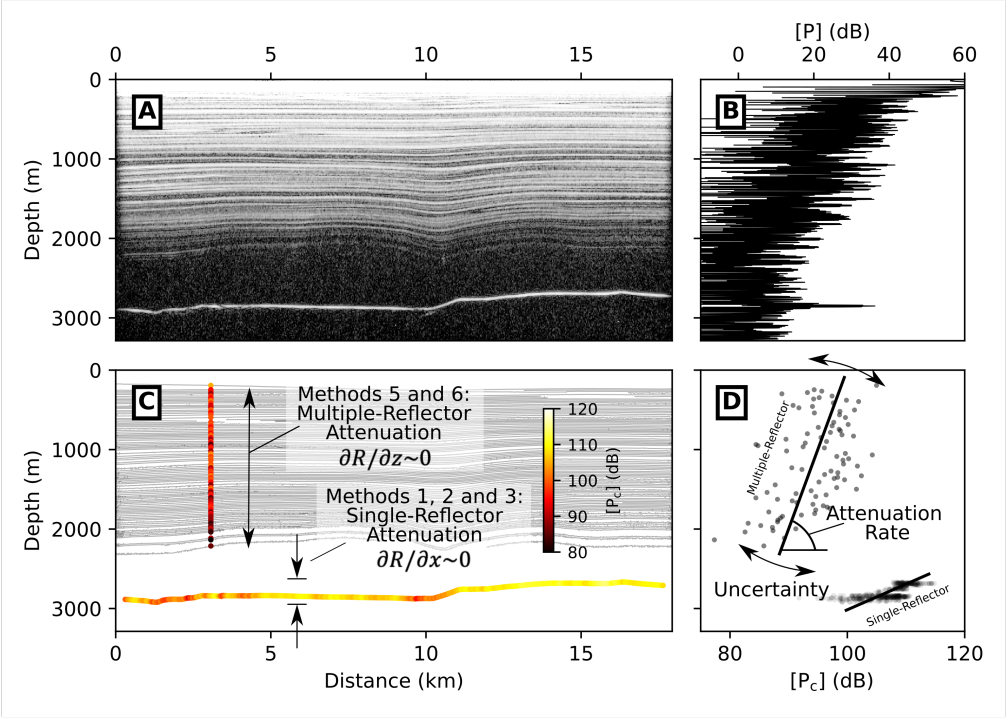

Figure 2.15: A) An along-flow radar profile from South Pole Lake (see Chapter 4), with ice flowing from left to right. B) Uncorrected power for a single A-scope trace from the profile in (A). C) Reflector interpretation for the along-flow profile shown in (A), with gray lines as internal reflectors. The colored points show corrected power for a single reflector over many traces (at the ice-bed interface) and for multiple reflectors from a single trace. D) Corrected power for every sample from colored points in (C). The black line represents the depth-power regression from equation 2.60, with the slope of the line equal to the average attenuation rate over the depth spanned by the reflector(s).

Table 2.1: A framework for empirical attenuation methods. Note that in all cases where the interface reflectivity is unknown (*Methods 1*, *2*, *3*, *5*, and *6*), the critical criteria to be met is $\left|\frac{\partial[R]}{\partial z}\right| \ll \left|\frac{\partial[P_c]}{\partial z}\right|$. To meet this criteria, single-reflector methods (*1*, *2*, and *3*) require an assumption that reflectivity changes along the reflector are small and that the reflector has sufficient relief $\left(\frac{\partial z}{\partial x}\right)$ for the regression. Multiple-reflector methods require an assumption that reflectivity changes between reflectors are small.

Applied at SPL		Well-Suited For	Assume $\frac{\partial[R]}{\partial z} \approx 0$	Assume $\frac{\partial[R]}{\partial x} \approx 0$	Assume $\partial[S] \approx 0$	Assume $[R]$ is known	Assume $[S]$ is known	Reference
→	*Method 1*: Single-Reflector Spatially-Averaged	Large Survey Area High Relief		X	X			(Jacobel et al., 2009) (Winebrenner et al., 2003)
→	*Method 2*: Single-Reflector Depth-Resolved	Large Survey Area High Relief		X	X			(Holschuh et al., 2016)
	Method 3: Single-Reflector Spatially-Resolved	Large Survey Area High Relief		X	X			(Schroeder, Grima, et al., 2016) (Schroeder, Seroussi, et al., 2016)
	Method 4: Single-Reflector Known-Reflectivity	Small Survey Area				X	X	(Bentley et al., 1998) (Shabtaie et al., 1987)
→	*Method 5*: Multiple-Reflector Depth-Averaged	Surveys with Internal Reflections	X		X			(MacGregor, Li, et al., 2015) (K. Matsuoka, Morse, et al., 2010)
→	*Method 6*: Multiple-Reflector Depth-Resolved	Resolving Depth Variations	X		X			(K. Matsuoka, Morse, et al., 2010)
	Method 7: Secondary-Reflection Spatially-Averaged	Small Survey Area				X		(Christianson et al., 2016) (MacGregor et al., 2011)
	Method 8: Secondary-Reflection Spatially-Resolved	Small Survey Area				X		

permittivity contrast between ice and the glacial substrate is large, so the measured power typically has a high signal-to-noise ratio (SNR). This method is limited by the assumption that spatial variations in bed roughness and/or permittivity contrast (i.e., wetness) and that spatial variations in the attenuation rate are small $\left(\left|\frac{\partial N}{\partial x}\right| \ll 0\right)$ in the domain selected for regression. The resulting attenuation rate from this method is commonly reported as a depth-averaged value for the full ice column; however, using the bed reflector preferentially samples power changes due to more or less deep ice, far from the ice-sheet surface which acts as a fixed (cold) thermal boundary. Assuming that spatial variations in attenuation rate are small, the attenuation rate above the shallowest bed reflection is uniform, and the regression of bed power against changes in range represents the attenuation rate of the deepest ice only. In most real cases, some amount of spatial variation in the depth-temperature profile biases the calculated attenuation rate, violating the method's assumptions and resulting in an ill-posed problem. Importantly, the bias can just as easily be in either direction depending on the glaciological conditions (i.e. toward or away from the depth-averaged interpretation which has commonly been used) (see Appendix B).

Method 2 – Single-reflector depth-resolved attenuation. This method is similar to *Method 1* in that it regresses power as a function of depth over many traces, but it uses all the internal reflectors observed throughout the ice column. The value from each reflector represents an interval attenuation rate, so taken together the result is a depth-attenuation profile. This method is analogous to that used for common-midpoint surveys (Holschuh et al., 2016). Unlike the bed, internal reflectors are typically specular, and are less likely to have spatially variable electrical properties over short wavelengths, so the $\left|\frac{\partial [R]}{\partial z}\right| \ll \left|\frac{\partial [P_c]}{\partial z}\right|$ assumption (also required for *Method 1*) is more likely valid. Unfortunately, the measured power from internal reflectors generally has a much lower SNR, and specular reflectors exhibit stronger slope-dependent changes in returned power than do rough reflectors (Holschuh et al., 2014). Without corrections (e.g. MacGregor, Li, et al., 2015), both the lower SNR and slope effects make it difficult to correctly calculate the attenuation rate, but these effects can easily be overlooked by the formal uncertainty metric.

Method 3 – Single-reflector spatially-resolved attenuation. This method uses the bed reflector to adaptively constrain attenuation over a spatial window of varying size, optimizing the window so that it is large enough to capture a sufficient depth range but small enough to minimize variations in reflector properties that introduce uncertainty into the calculation (Schroeder, Grima, et al.,

2016; Schroeder, Seroussi, et al., 2016). By iteratively moving the window through the survey domain, this method can be used to constrain spatial variation in attenuation. In the description of this methodology, Schroeder, Seroussi, et al. (2016) define the optimal attenuation rate as that which most sufficiently decorrelates the attenuation-corrected power from the observed ice thickness. Their derivation is analogous to that which we laid out above; they compute values of N such that $\frac{\partial[P_c]+2N_z}{\partial z} = 0$, again assuming that $\frac{\partial[S]}{\partial z}$ and $\frac{\partial[R]}{\partial z}$ are negligible. They perform a grid search through physically realistic attenuation rates instead of computing N through inversion as we do here. As in the case of *Method 1*, we assert that under the given assumptions this method represents an interval result over the thickness of ice that is spanned by the bed reflector (see Appendix B).

Method 4 – Known reflectivity. This final single-reflector method uses an interface of known reflectivity (e.g. an ice-seawater interface) to calculate the average attenuation rate through the full ice column by constraining all of the correction terms in equation 2.57 (Bentley et al., 1998; Shabtaie et al., 1987). Implementing this method requires high confidence in the measured, inferred, or assumed values of the transmit power as well as the corrections: $[S]$, $[R]$, $[F]$, $[4\pi(2z)^2]$, and $[B]$. The greatest uncertainty is generally associated with the reflectivity correction; for example, even for an ice-seawater interface the reflectivity can be greatly reduced by roughness effects (Christianson et al., 2016).

Multiple-Reflector Attenuation Methods

Method 5 – Multiple-reflector depth-averaged attenuation. This method uses many reflectors within one trace for a regression of reflector power and depth, again using equation 2.60. Normally, a majority of the ice column is included in a single regression, excluding only reflectors very near the surface or bed (MacGregor, Li, et al., 2015). Using this method, attenuation rates can be calculated for each individual trace, resulting in a sense for spatial variation in depth-averaged attenuation. It should be noted that this method heavily relies on the assumption of constant reflectivity between reflectors. However, previous work has shown that the magnitude of internal reflections can vary substantially, as they represent various dielectric contrasts across interfaces in the ice column (Bingham & Siegert, 2007; Eisen et al., 2003b). Corrections can be made to account for each source of reflectivity variation; for example, MacGregor, Li, et al. (2015, Appendix A) use dielectric profiles

from nearby ice cores to estimate the reflectivity within the ice column and correct the attenuation rate.

Method 6 – Multiple-reflector depth-resolved attenuation. This method uses many reflectors over a depth-constrained vertical window that does not span the entire ice column (K. Matsuoka, Morse, et al., 2010); thus, the result is an interval attenuation rate as opposed to a depth-averaged value. This method can be implemented for each individual trace, as in *Method 5*, but is more effective for resolving depth variations when many traces are considered together. Theoretically, an adaptive window-fitting technique, as in *Method 3*, could be used here. Practically though, the window size is effectively constant because it is constrained by the limited thickness of the ice column. Violations in the depth-reflectivity assumption have induced large uncertainties in previous applications of this method. For example, depth-varying attenuation rates computed by K. Matsuoka, Morse, et al. (2010) showed decreasing attenuation rate with depth, opposite to that expected based on the increasing ice temperature with depth.

Secondary-Reflection Attenuation Methods

Method 7 – Secondary-reflection spatially-averaged attenuation. This method uses the power difference between the primary and secondary bed reflections to calculate attenuation through the full ice column (Christianson et al., 2016; MacGregor et al., 2011). The 'secondary reflection', often called the 'multiple' reflection, is a repeated instance of the bed in a single trace. As the initial reflected wave is recorded by the receiver, a secondary wave is generated at the ice surface by reflecting off of the firn-air interface, propagating back into the subsurface and producing a second reflection of the bed that is imaged at the surface after twice the travel time. Attenuation is calculated by comparing the measured power between these two reflections. Secondary reflection methods, often called 'multiple-echo methods', require knowledge of both the ice-bed and firn-air reflectivities, but, unlike all prior methods, do not require any assumption about the system characteristics. When the reflectivities are assumed to be well known (i.e. a smooth ice-seawater interface) and attenuation calculations are spatially averaged over many traces, high confidence can be assigned to the result.

Method 8 – Secondary-reflection spatially-resolved attenuation. In exactly the same manner as

Method 7, this method uses the primary and secondary bed echoes to calculate attenuation. Here though, attenuation results are reported on a trace-by-trace basis and contrasted between locations.

A Framework for Method Selection

The necessary assumptions for each method (summarized in Table 2.1) provide a basis for attenuation method selection. Information about the survey design, instrument characteristics, and the glaciological environment can provide a basis for selecting a method a priori, as different assumptions are likely to be violated for surveys in fast-flowing ice versus slow-flowing ice, for surveys with data predominantly collected along-flow versus across-flow, and in surveys that cover a large spatial area versus those that are more spatially confined. Below, we outline the typical characteristics that can either enable the use of certain methods in the case of a calibration surface, or inhibit the use of certain methods due to a violation of the central assumptions in cases of reflectivity variations associated with geometric effects, paleoclimate variations, or low SNR.

Methods 4, *7*, and *8* each utilize a calibration surface of known reflectivity. While these are among the best constrained methods available, they require unusually uniform glacial environments. These cannot be used without data either focused on a region containing floating ice (on an ice shelf or over previously known subglacial lakes with spatially uniform basal reflectivity) (Christianson et al., 2016; MacGregor et al., 2011), or surveys that deliberately connect to one of these regions before going to their true target. Applicable to the narrowest range of environments, *Methods 4*, *7*, and *8* are most useful for small surveys nearby a known reflector, and generally less useful for large surveys over which reflectivity changes are expected or small surveys focused in the ice-sheet interior where no calibration surface can be expected.

Even for surveys without an obvious ice-water interface, the bed reflector is still the most widely used for attenuation calculations (*Method 1*; Jacobel et al. (2009)). Unfortunately, the bed is also the reflector with the highest likelihood of substantial reflectivity variations. This is especially true in cases where heterogeneous water systems are present at the bed, or where unresolvable bed roughness reduces coherent scattering (Christianson et al., 2016; T. M. Jordan et al., 2017; Schroeder et al., 2014). If bed roughness is inversely correlated with bed depth, such that shallower sections of a profile reflect less power back toward the instrument receiver, the assumption to minimize reflec-

tivity changes along the reflector $\left(\frac{\partial [R]}{\partial x} \approx 0\right)$ is violated, leading to an erroneously low attenuation rate. Where power losses due to roughness are expected, corrections can be made; for example, using an aggregated bed-returned power (T. M. Jordan et al., 2016; Oswald & Gogineni, 2008) or by Kirchhoff Theory (MacGregor et al., 2011; Ogilvy, 1991; M. E. Peters et al., 2005). With no correction though, single-reflector methods (i.e. *1*, *2*, and *3*) are not well suited for surveys where reflectivity changes are likely along the reflector. These cases will show an attenuation bias toward the reflectivity gradient. Surveys that span a larger area are better suited for *Methods 1*, *2*, and *3*, as the effect of heterogeneity in reflector property is reduced with more spatial averaging. Additionally, for these surveys that span a large area, reflectors will generally sample a larger depth range, leading to a more robust regression that represents the attenuation rate over more of the ice column. Both of these advantages are displayed in the correlation metric that underlies Method 3, which often requires a large area to meet the correlation strength minimums.

Dipping internal reflectors cause decreases in measured power for geometric rather than attenuative reasons (Holschuh et al., 2014). Deeper reflectors conform more closely to the bed topography and will therefore have greater dips (Hindmarsh et al., 2006). In addition, layers imaged along-flow tend to be smoother than layers imaged across-flow, as their shared strain history limits the steepness of layer folds to those that can be produced by englacial vertical velocities (Holschuh et al., 2017). Because dip and power are both depth dependent, geometric losses interfere with attenuation calculations and steeply dipping reflectors cannot be used for attenuation calculations unless corrections are made (MacGregor, Li, et al., 2015). Unfortunately, the environments where spatial changes in attenuation can be expected are often those where the layers are most distorted, such as ice-stream shear margins (Holschuh et al., 2019). Thus, in fast flowing ice, *Methods 2*, *5*, and *6* are best applied to data collected along-flow, and in areas with relatively low shear-strain rates.

Paleoclimate transitions can create strong reflectivity changes between reflectors within the ice column. As the atmospheric composition changes, the dust content in depositional snow layers changes which can greatly affect the bulk reflectivity of an interface (Eisen et al., 2003b). For example, in Greenland the Holocene-glacial transition represents a stark change in reflector character, separating bright reflectors near the surface and dimmer glacial layers near the bed (Karlsson et al., 2013; MacGregor, Li, et al., 2015). Using data with such a depth-trend will produce attenuation

Table 2.2: Reported attenuation results and associated uncertainty from this and prior studies.
~Value taken from graph.
* Reported uncertainty does not include error in variables.
**High attenuation rates associated with geometric effects of the common-midpoint survey.
***Many of the reported uncertainty values from this study are lower (in the approximate range 1-10 dB/km).

Method (Error Calculation)	**Site Location**	**Survey and System**	**Att. Rate dB/km (Error)**	**Reference**
Method 1 (std. dev. of unweighted regression)	Kamb Ice Stream Siple Dome (~10,000 km^2)	3 MHz Ground Based Common Offset	11.7-29.5 (0.2-1.2)*	Jacobel et al. (2009)
Method 1 (std. dev. of unweighted regression)	Siple Dome (~150 line-km)	3 MHz Ground Based Common Offset	25.3 (1.1)*	Winebrenner et al. (2003) Revised by MacGregor et al. (2007)
Method 1 (errors-in-variables regression)	South Pole Lake (400 km^2)	3 MHz Ground Based Common Offset	16.7 (0.2)	Appendix D
Method 2 (most uncertainty from antenna pattern)	Kamb Ice Stream NEGIS (Common Midpoint)	3 MHz Ground Based Common Midpoint	~10-90** (~0-25)	Holschuh et al. (2016)
Method 2 (errors-in-variables regression)	South Pole Lake (400 km2)	3 MHz Ground Based Common Offset	-20.9-16.7 (0.1-0.3)	Appendix D
Method 3 (correlation minimum half-widths and cross-over error)	Thwaites Glacier (~200,000 km^2)	52.5-67.5 MHz Airborne, HiCARS Common Offset	~0-20 (~2-8)	Schroeder, Seroussi, et al. (2016)
Method 4 (no reported uncertainty)	Kamb Grounding Zone (Single Trace)	35-50 MHz Airborne Common Offset	17.3 12.2-14.6	Bentley et al. (1998) Shabtaie et al. (1987)
Method 5 (std. dev. of weighted regression)	Greenland Ice Sheet (1,700,000 km^2)	Airborne various CReSIS Common Offset	~0-30 (~0-5)	MacGregor, Li, et al. (2015)
Method 5 (errors-in-variables regression)	South Pole Lake (400 km^2)	3 MHz Ground Based Common Offset	0.9-6.7 (0.2-1.6)	Appendix D
Method 5 (no reported uncertainty)	Kamb Ice Stream NEGIS (Common Midpoint)	3 MHz Ground Based Common Midpoint	~-0.2-22	Holschuh et al. (2016)
Method 6 (std. dev. of unweighted regression)	WAIS Divide (~40,000 km^2)	60 MHz Airborne Common Offset	~8-13 (~0.5-3)*	K. Matsuoka, Morse, et al. (2010) reported as two-way rate
Method 6 (errors-in-variables regression)	South Pole Lake (400 km^2)	3 MHz Ground Based Common Offset	-0.5-9.1 (0.01-0.06)	Appendix D
Method 7 (std. dev. of unweighted regression)	Kamb/Whillans Gndg. Zone (~500 line-km)	2 MHz Ground Based Common Offset	20.8-28.1 (0-89.9)***	MacGregor et al. (2011)
Method 7 (95th percentile confidence intervals)	Whillans Grounding Zone (~20 line-km)	3 MHz Ground Based Common Offset	16.4-19.9 (0.06-0.09)	Christianson et al. (2016)

rates that are anomalously high. *Methods 5* and *6* are best used in ice deposited during a single climate regime, in ice that preserves many distributed climates with depth, or in regions where changes in dust and salt concentrations do not drive large changes in ice acidity. Using *Methods 5* and *6* with radar data that spans a single climate transition would require carefully correcting the reflectivity, as is shown by MacGregor, Li, et al. (2015, Appendix A). The shallowest reflections, from within the firn, are generally associated with density rather than chemical contrasts, so reflectivity variation is expected between those and deeper reflections. Moreover, the magnitude of density contrasts fall as the background density approaches that of solid ice; thus, the reflectivity changes with depth throughout the firn column as well.

Finally, reflectors deep in the ice column are often close to the system noise floor (low SNR) and can therefore show anomalously high variation in measured power. When considered together with other reflectors in the same trace, noisy reflectors can then introduce what looks like an anomalously bright (dim) reflection low in the ice column and lead to a lower (higher) calculated value that is not representative of the true attenuation rate. For *Methods 5* and *6*, other authors have generally excluded very deep reflectors (MacGregor, Li, et al., 2015) and we recommend doing the same.

2.3.3 Electromagnetic Anisotropy and Radar Birefringence

Executable Jupyter Notebooks to reproduce selected figures from this section are available at github.com/benhills/effmed-ice.

Since there are more hydrogen bonds within the basal plane than along the crystal *c* axis (see Section 2.1.2), there is more for an electromagnetic wave to interact with along that plane. Therefore, waves polarized parallel to the *c* axis have a higher permittivity (slower wave speed) than those polarized perpendicular (Figure 2.16). The full permittivity tensor for a single ice crystal is

$$\varepsilon = \begin{bmatrix} \varepsilon_{\perp} & 0 & 0 \\ 0 & \varepsilon_{\perp} & 0 \\ 0 & 0 & \varepsilon_{\parallel} \end{bmatrix} \tag{2.61}$$

where $\varepsilon_{\perp}$ is the relative permittivity of a wave polarized perpendicular to the *c* axis, and $\varepsilon_{\parallel}$ parallel. Permittivity is a complex number, but I do not consider the imaginary component here since it is nearly isotropic (T. Matsuoka et al., 1997), and most of the attenuative losses are from electrical

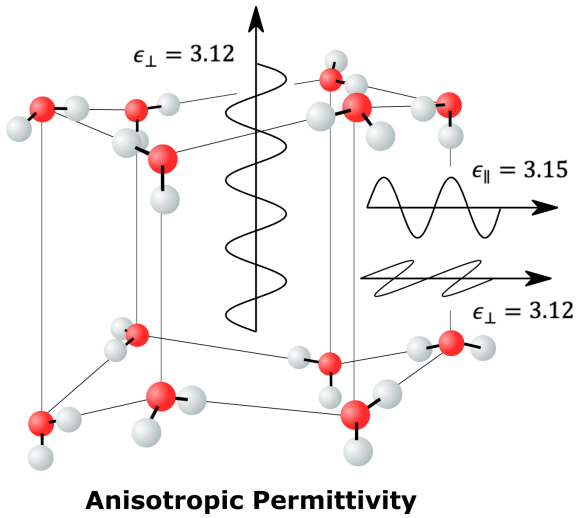

Figure 2.16: Illustration of polarization dependence for permittivity in the anisotropic ice crystal. The wave polarized perpendicular to the *c*-axis travels faster (lower permittivity) than that polarized parallel.

conduction (Section 2.3.1). I consider only the real part of the permittivity and will discuss values as 'relative' to the permittivity of free space. The real permittivity anisotropy

$$\Delta\varepsilon = \varepsilon_\parallel - \varepsilon_\perp \tag{2.62}$$

for an individual crystal at radio frequencies is ~0.034 ($\varepsilon_\parallel - \varepsilon_\perp = 3.173\text{-}3.139$) (Fujita et al., 1993; T. Matsuoka et al., 1997). In other words, pure ice is $\sim$1% anisotropic when considering ice-penetrating radar. Anisotropy is dependent on both wave frequency and ice temperature (Fujita et al., 2000), neither of which are considered here (I assume constant $\Delta\varepsilon = 0.034$).

For polycrystalline ice, the expressed anisotropy is always less than or equal to the anisotropy of an individual crystal since crystals point in different directions. At wavelengths significantly longer than the crystal size, the polycrystal acts as an 'effective medium', so the expressed (or 'effective') anisotropy is proportional to that of an individual crystal but scaled by the COF in the polarization plane.

To understand the birefringent effect, it is useful to first consider a scenario with the antenna array in alignment with a vertical girdle fabric. In this case, the wave polarization remains constant

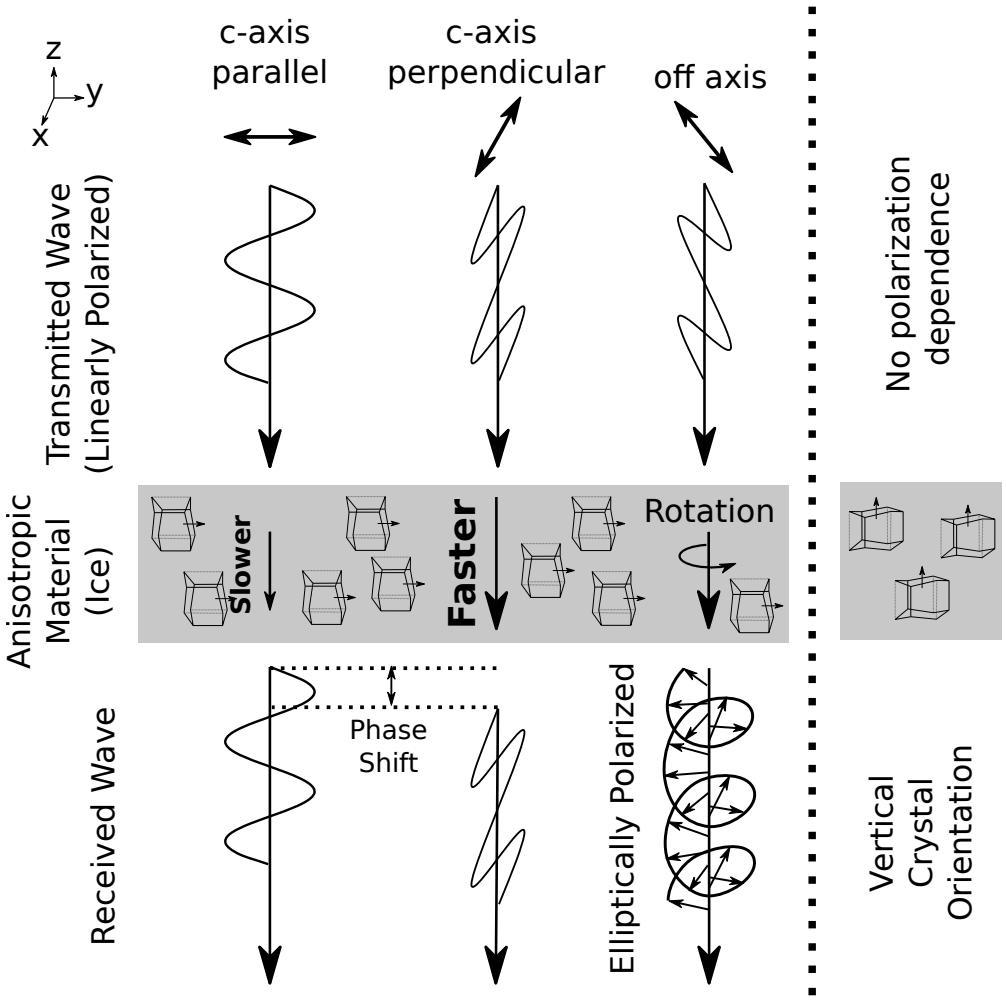

Figure 2.17: Wave propagation through anisotropic ice. The large, dashed line separates the horizontal COF (girdle fabric) from vertical COF (single pole, where vertically propagating waves do not have any polarization dependence).

(linearly polarized transmit) as it propagates through the ice, but the wave speed depends on whether the wave is polarized 'horizontally' (H; with the electric field vector in line with the girdle axis) or 'vertically' (V; perpendicular to the girdle axis). As above, the wave most aligned with crystal c axes (horizontally polarized in this case) travels slower. A measurable phase delay is expected between H and V polarizations based on the difference in wave speed, and therefore directly related to the strength of the vertical girdle.

When misaligned with the vertical girdle, a propagating wave will 'depolarize', turning from linearly polarized to circularly or elliptically polarized, and effectively rotating the wave around its propagation axis. If the receive antenna is oriented perpendicular to the transmit (cross-polarized) it may pick up some of this 'rotated' energy. In the situation discussed above, with a simple vertical girdle fabric and perfect antenna alignment to the girdle, there is no depolarization (no rotation) so a cross-polarized acquisition will theoretically measure no returned power. Therefore, this 'cross-polarized extinction' (XPE) axis can theoretically be used to identify the azimuthal orientation of a vertical girdle (Ershadi et al., 2022). In practice, there is always *some* measured power at the receive antenna, so I pick out the azimuth of minimal returned power in the cross-polarized power image (Figure 2.19B).

For non-uniform COF, especially with girdle rotations, using the XPE to identify the girdle orientation may be ineffective since the wave will depolarize at the girdle rotation. Instead, a numerical model can be used which takes COF as input and outputs the expected birefringent effect. Three such models have been published in the glaciology literature already. First, Fujita et al. (2006) describe a layered matrix method for vertically propagating waves through a girdle fabric. Many more recent studies use the Fujita model (Brisbourne et al., 2019; T. M. Jordan et al., 2019; Young et al., 2021) and some in novel applications, for instance, an inversion for the vertically aligned COF component (Ershadi et al., 2022). Still, I consider all those studies under the same model classification. Second, K. Matsuoka et al. (2009) added oblique orientation dependency to Fujita's matrix model to allow for arbitrary wave propagation (i.e. not necessarily vertical) through either girdle or single-pole COF. The third is most recent and most generalizable (Rathmann et al., 2022) allowing arbitrary COF and modeled in spherical coordinates. In what follows, I describe the details of the Fujita et al. (2006) model, focusing on it in particular because it is still the most widely used in the literature and is the simplest to explain.

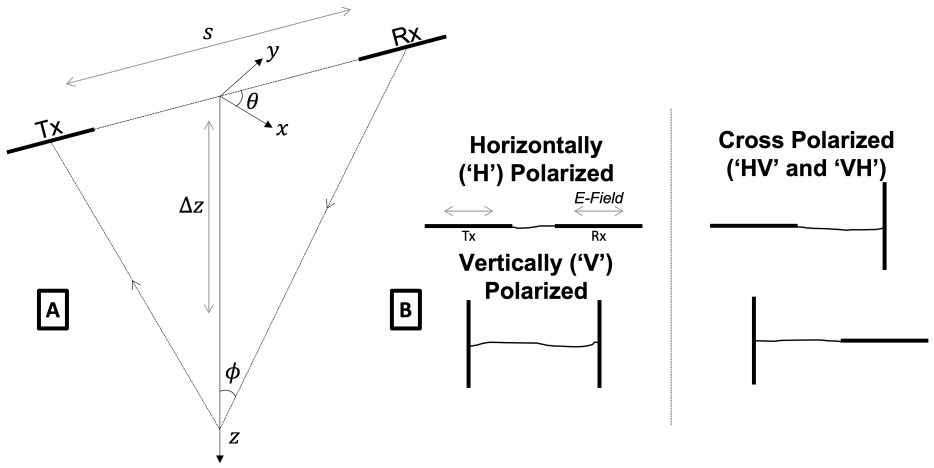

Figure 2.18: Illustration of experimental design for a radar polarimetry acquisition. A) Antenna array orientation with respect to the ice with the two indicated angles, θ is between the optical (COF) axis and the measurement axis, and ϕ is the polar angle of incidence at the reflection interface. B) Antenna polarizations in all four acquisitions.

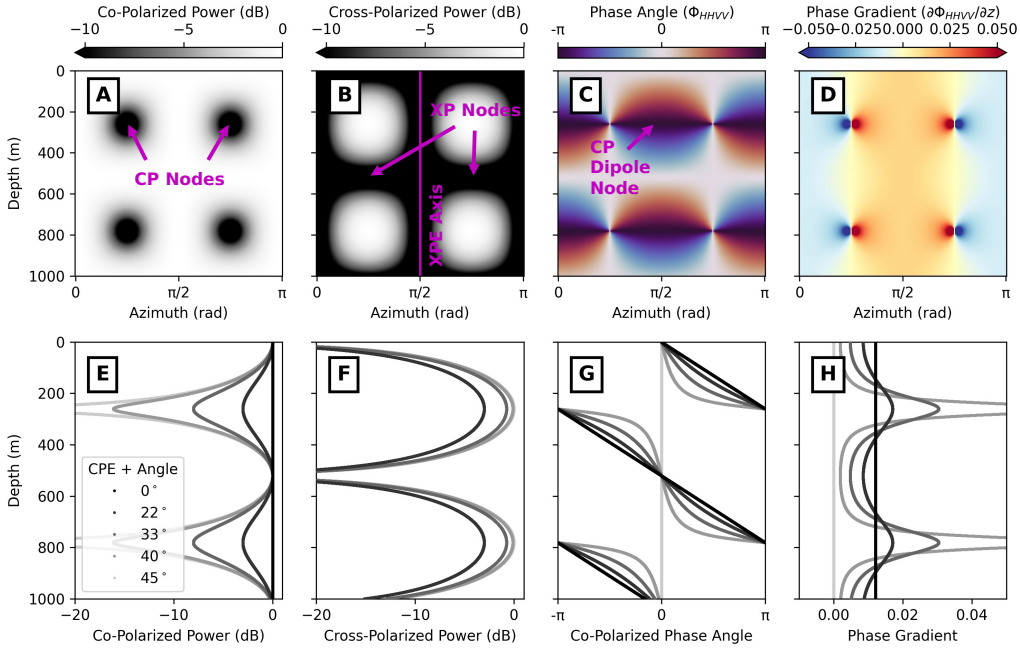

Figure 2.19: Modeled polarimetric radargram for a uniform vertical girdle. A) Power returned to the receive antenna for a co-polarized acquisition (HH or VV) for all azimuths. B) As in (A) but for a cross-polarized acquisition (HV or VH). C) Co-polarized phase angle calculated with equation 2.73. D) Co-polarized phase gradient calculated with equation 2.74. E-H) Profiles extracted from corresponding images (A-D) at the azimuths listed in (E).

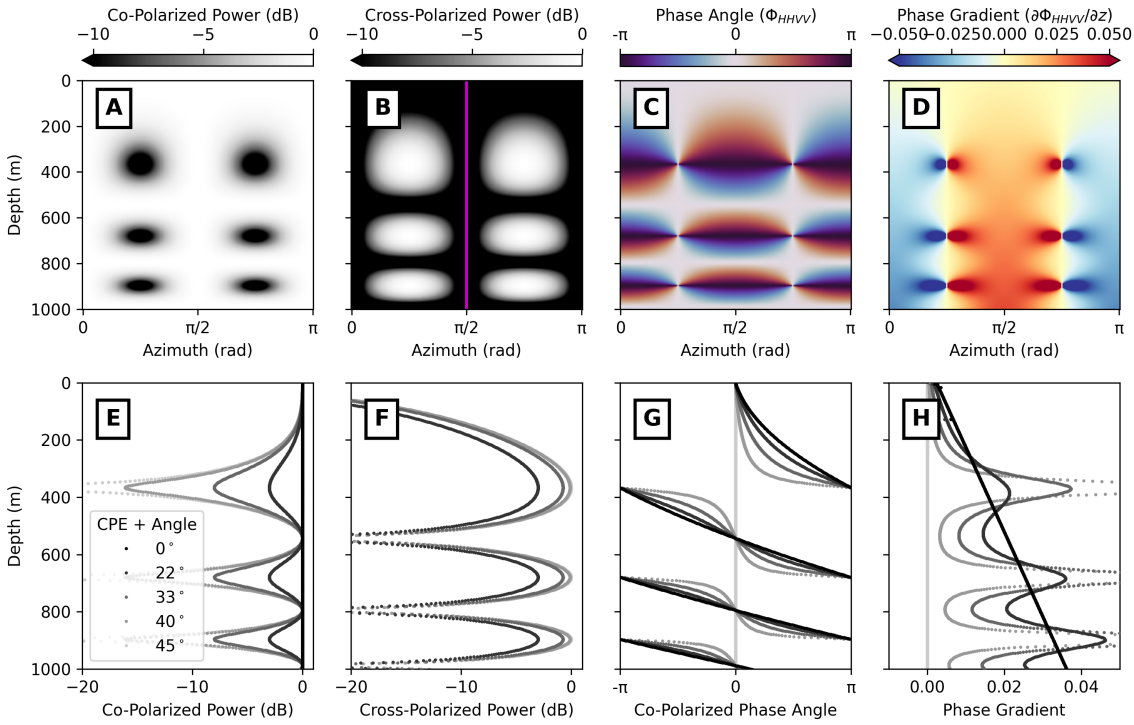

Figure 2.20: Results from the effective medium model as in Figure 2.19, now for the case of linearly increasing girdle strength with depth.

A radar wave measured at the receive antenna is a 2×1 vector (H and V polarizations)

$$\mathbf{E_R} = \boldsymbol{\mathcal{S}}_N \mathbf{E_T} \tag{2.63}$$

where $\mathbf{E_T}$ is the transmitted wave, again a 2×1 vector, and $\boldsymbol{\mathcal{S}}_N$ is the scattering matrix

$$\boldsymbol{\mathcal{S}}_N = \begin{bmatrix} \mathcal{S}_{HH} & \mathcal{S}_{VH} \\ \mathcal{S}_{HV} & \mathcal{S}_{VV} \end{bmatrix}_N \tag{2.64}$$

for layer N. The scattering matrix depends on transmission and rotation through the ice column (in both directions) as well as scattering at the reflection interface

$$\begin{aligned}\mathcal{S}_N = D^2(z_N)\times & \\ & \prod_{i=1}^{N}[\mathbf{R}(\theta_{N+1-i})\mathbf{T}_{N+1-i}\mathbf{R}'(\theta_{N+1-i})]\times \\ & \mathbf{R}(\theta_i)\mathscr{R}_i\mathbf{R}'(\theta_i)\times \\ & \prod_{i=1}^{N}[\mathbf{R}(\theta_i)\mathbf{T}_i\mathbf{R}'(\theta_i)]\end{aligned} \tag{2.65}$$

The first term, D, is wave propagation in free space (i.e. spreading losses)

$$D(z) = \frac{e^{i\mathscr{k}_0 z}}{4\pi z} \tag{2.66}$$

squared in equation 2.65 since it propagates both downward and upward. Then, $\prod$ is an iterative matrix product over all layers, $i = 1$ to N. For each layer, there is some rotation

$$\mathbf{R}(\theta_i) = \begin{bmatrix} cos(\theta_i) & -sin(\theta_i) \\ sin(\theta_i) & cos(\theta_i) \end{bmatrix} \tag{2.67}$$

and some transmission

$$\mathbf{T}_i = \begin{bmatrix} T_{i\text{-}x} & 0 \\ 0 & T_{i\text{-}y} \end{bmatrix} \tag{2.68}$$

where

$$T_{i\text{-}x} = e^{-i\mathscr{k}_0\Delta z + i\mathscr{k}_{i\text{-}x}\Delta z} \tag{2.69a}$$

$$T_{i\text{-}y} = e^{-i\mathscr{k}_0\Delta z + i\mathscr{k}_{i\text{-}y}\Delta z} \tag{2.69b}$$

and

$$\mathscr{k}_{i\text{-}x} = \sqrt{\varepsilon_0\mu_0\varepsilon_{i\text{-}x}\omega^2} \tag{2.70a}$$

$$\mathscr{k}_{i\text{-}y} = \sqrt{\varepsilon_0\mu_0\varepsilon_{i\text{-}y}\omega^2} \tag{2.70b}$$

The permittivity anisotropy shows up here, where the transmission matrix depends on the effec-

tive permittivity for each polarization direction, $\varepsilon_{i\text{-}x}$ and $\varepsilon_{i\text{-}y}$. At the reflection interface, there is a reflectivity matrix which can be considered isotropic as well

$$\boldsymbol{\mathscr{R}}_i = \begin{bmatrix} \mathscr{R}_{i\text{-}x} & 0 \\ 0 & \mathscr{R}_{i\text{-}y} \end{bmatrix} \tag{2.71}$$

where $\mathscr{R}_{i\text{-}x}$ and $\mathscr{R}_{i\text{-}y}$ may be different depending on interface properties. See Fujita et al. (2006) for more details on this model.

A phase delay is expected between the two co-polarized terms. Coherence between the 'H' co-polarized acquisition and the 'V' is

$$C_{HHVV} = \frac{\mathscr{S}_{HH} \cdot \mathscr{S}^*_{VV}}{\sqrt{|\mathscr{S}_{HH}|^2}\sqrt{|\mathscr{S}_{VV}|^2}} \tag{2.72}$$

where $*$ is the complex conjugate. Then, the phase delay is

$$\Phi_{HHVV} = arg\,(C_{HHVV}) \tag{2.73}$$

The phase gradient in depth is directly related to the phase velocity difference between 'H' and 'V' polarized waves (i.e. the effective anisotropy), and can be calculated by

$$\frac{\partial \Phi_{HHVV}}{\partial z} = \frac{C_R \frac{\partial C_I}{\partial z} - C_I \frac{\partial C_R}{\partial z}}{C_R^2 + C_I^2} \tag{2.74}$$

where C_R and C_I are the real and imaginary components of C_{HHVV}.

To illustrate the model behavior, I run four model experiments: 1) uniform vertical girdle (Figure 2.19), 2) vertical girdle with increasing magnitude in depth (Figure 2.20), 3) three variations of vertical girdles with azimuthal rotations in depth (Figure 2.21, 2.22, and 2.23), and 4) single-pole COF with increasing antenna separation ('move-out' survey) (Figure 2.24). Model experiments 1 and 2 have been shown in previous studies (e.g. Ershadi et al., 2022) and demonstrate the expected behavior. That is, the uniform girdle leads to a steady phase gradient, and the strengthening girdle leads to an increasing phase gradient with depth.

Experiment 3 has a less intuitive result than the first two. Azimuthal rotations of a vertical girdle have been discussed (e.g. Brisbourne et al., 2019; T. M. Jordan et al., 2022) but the results here demonstrate that those rotations are difficult to interpret directly. First, I rotate the girdle by exactly

90 degrees (Figure 2.21) so the wave does not depolarize but the birefringent effect is reversed. As expected, the phase gradient changes sign, with co-polarized dipole nodes flipping their polarity across the girdle rotation.

Next, I rotate the girdle by less than 90 degrees, both abruptly (Figure 2.22) and gradually (Figure 2.23). In both cases, the maximum co-polarized phase gradient and the selected XPE axis (magenta) have notably different behavior from the 'true' girdle axis (green) and continue to rotate even below the maximum depth of the true girdle rotation. The reason for this behavior is that the radar wave transforms from the transmitted linearly polarized wave to elliptically polarized when it moves through the off-axis girdle (Figure 2.17). The interaction of the now elliptically polarized wave with the new girdle axis is never such to bring it back to the original linear polarization. In these examples, one can see that the XPE is no longer representative of the girdle axis orientation; however, there is no perfect alternative method for extracting the girdle orientation. Other studies have used an optimization algorithm to maximize the azimuthal symmetry in the phase gradient (T. M. Jordan et al., 2022), but that gives similar results to the XPE axis. I suggest interpreting the COF based on the full phase image, as shown in these examples, and testing the expected behavior against a model as done here. In some cases, a full model inversion to the measured phase image may be appropriate (Ershadi et al., 2021).

Experiment 4 has been discussed in the literature (e.g. Rathmann et al., 2022) but as far as I know has not been demonstrated in the way I do here. The Fujita et al. (2006) model described above and used in the first three experiments is only suitable for vertical wave propagation in a girdle COF. For this experiment, I instead adapt the K. Matsuoka et al. (2009) model with the single-pole indicatrix in order to simulate a move-out polarimetry survey. I do not provide the model details here, but it is similar to the above and the code is publicly available (see Data and Software Availability). With no antenna separation, there is no birefringent effect on the vertically-propagating wave since there is no x-y anisotropy. Hence, the co-polarized power is maximally bright (Figure 2.24A), there is no cross-polarized power (Figure 2.24B), and no phase gradient (Figure 2.24C and 2.22D). As the antenna separation increases, the wave propagation vector moves off vertical and a component of the wave polarization lines up with the vertical c axes. The modeled phase gradient therefore increases with increased antenna separation. As a field experiment, this would be more challenging than the conventional polarimetry acquisition (both in implementation and interpretation), but it should give

a measure of the full 3-component COF.

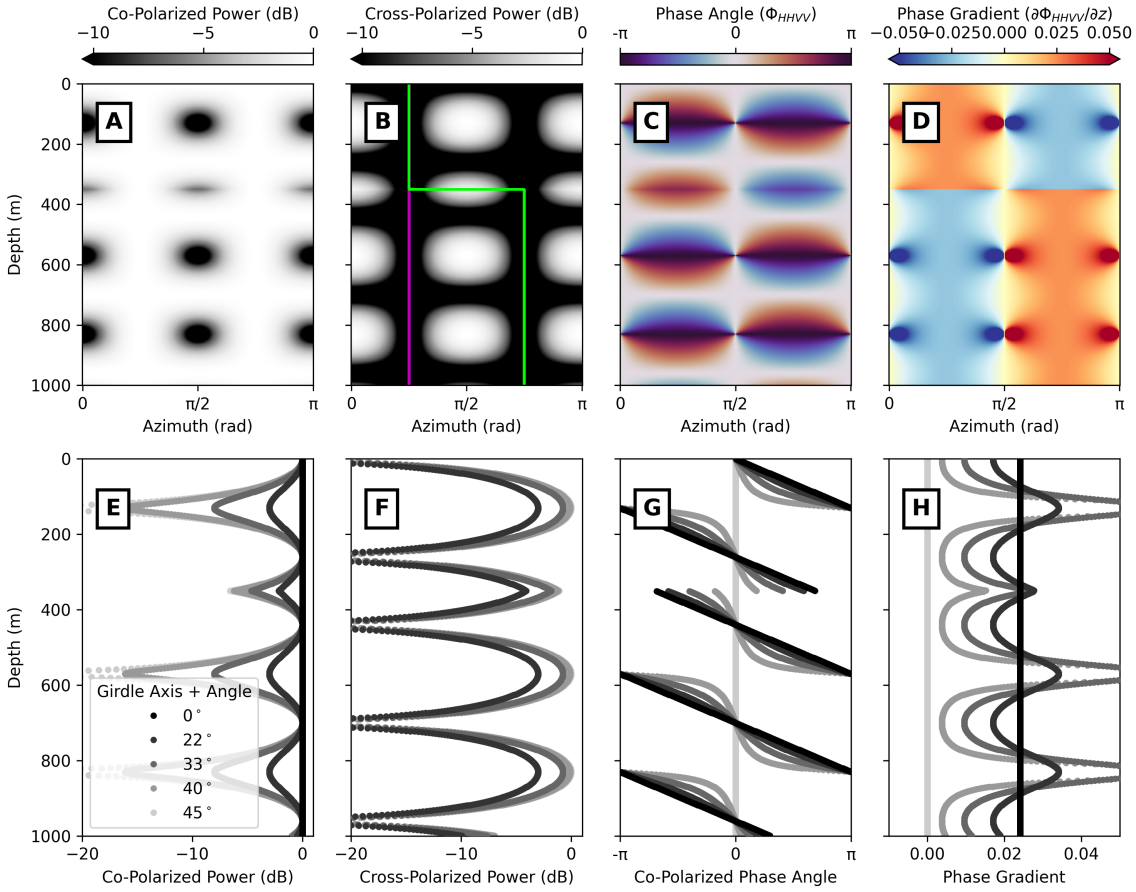

Figure 2.21: Results from the effective medium model as in Figure 2.19, now for the case of an abrupt 90-degree girdle rotation at 350 m depth. The green line in (B) is the true girdle axis and magenta line is the selected XPE axis. Now, profiles in (E-H) are taken from along the true girdle axis (green line)

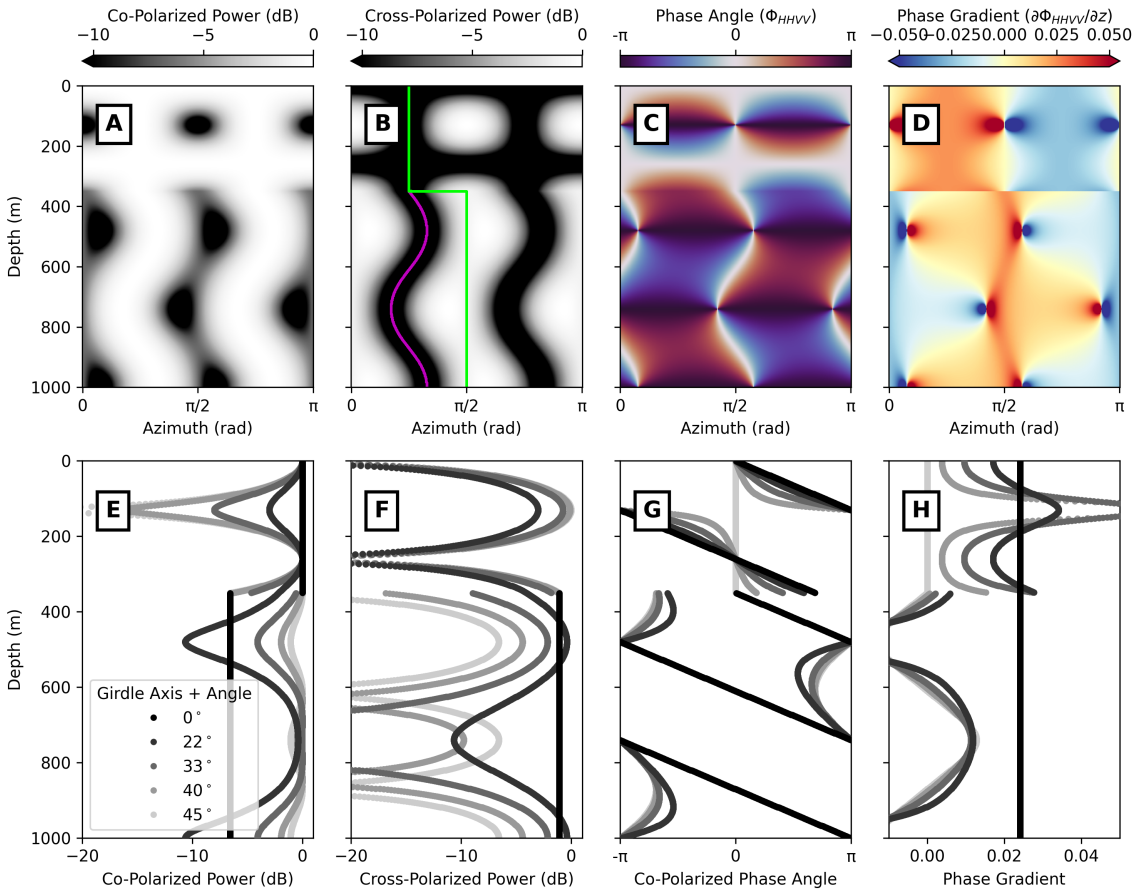

Figure 2.22: Results from the effective medium model as in Figure 2.21, now for the case of an abrupt 45-degree girdle rotation at 350 m depth.

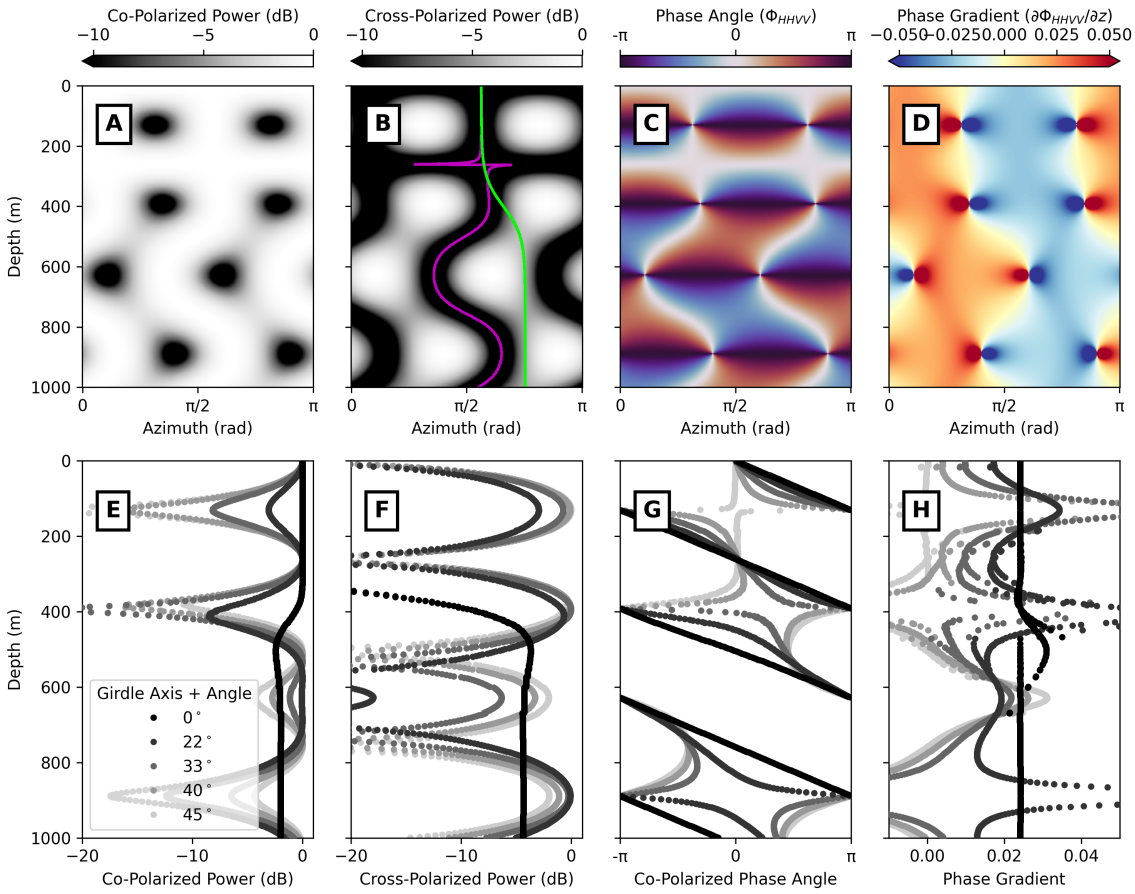

Figure 2.23: Results from the effective medium model as in Figure 2.21, now for the case of a gradual girdle rotation between 200-500 m depth.

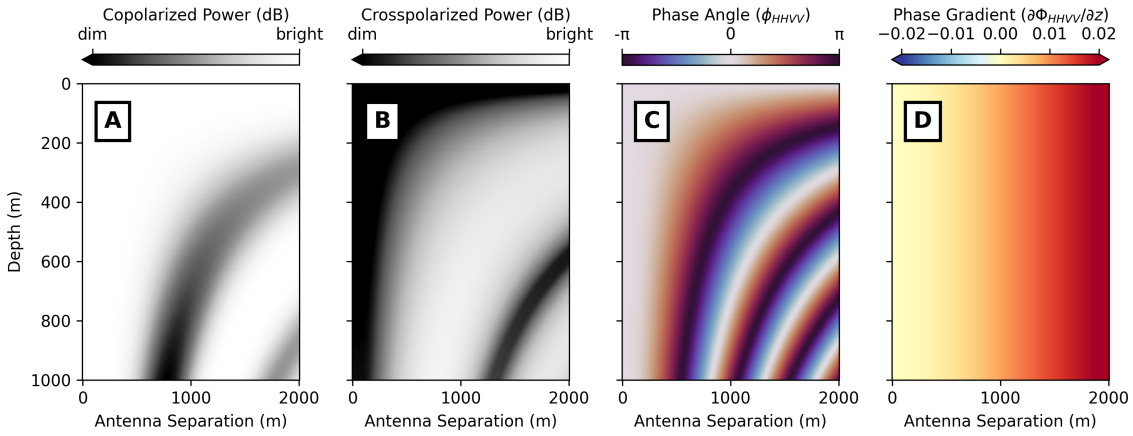

Figure 2.24: Results from the effective medium model as in Figure 2.19 but for a move-out survey with increasing antenna separation (no azimuthal rotation). Here, the COF is an upward pointing single pole.

Chapter 3

Radar Attenuation Indicates Thermal Persistence of Upstream Sourcing in the Siple Coast Ice Streams

Originally published in Journal of Glaciology (Hills, Christianson, Jacobel, et al., 2022).

Chapter Abstract.

Ice-streams are warmed by shear strain, both vertical shear near the bed and lateral shear at the margins. Warm ice deforms more easily, establishing a positive feedback loop where fast flow leads to warm ice and then to even faster flow. Here, we use radar attenuation measurements to show that the Siple Coast ice streams are colder than previously thought which we hypothesize is due to along-flow advection of cold ice from upstream. We interpret the attenuation results within the context of previous ice-temperature measurements from nearby sites where hot-water boreholes were drilled. These in-situ temperatures are notably colder than model predictions, both in the ice streams and in an ice-stream shear margin. We then model ice temperature using a 1.5-dimensional numerical model which includes a parameterization for along-flow advection. Compared to analytical solutions, we find depth-averaged temperatures that are colder by 0.7°C in the Bindschadler Ice Stream, 2.7°C in the Kamb Ice Stream, and 6.2-8.2°C in the Dragon Shear Margin, closer to the borehole

measurements at all locations. Modelled cooling corresponds to thermal hardening by 3-3.5 times compared to the warm-ice case, suggesting some other softening mechanism in ice-stream shear margins, such as material damage or ice-crystal fabric anisotropy.

3.1 Introduction

Understanding ice-stream dynamics is critical for constraining ice-sheet mass balance (Fox-Kemper et al., 2021; Hanna et al., 2013). In ice streams, basal shear stresses are generally low, so gravitational flow is resisted by longitudinal (along-flow) stresses and especially by lateral stresses in the ice-stream shear margins (C. Raymond, 1996). Due to strain heating, material damage in crevasse fields, and crystal reorientation, ice in shear margins may soften by several orders of magnitude compared to adjacent cold, stagnant ice. Current understanding of the partitioning between strain heating and other softening processes in shear margins is observationally limited (Minchew et al., 2018). Here we use ice-penetrating radar data, direct ice-temperature measurements, and analytical and numerical thermal modelling to improve understanding of ice temperature and associated thermal softening in ice streams.

As is the case elsewhere on an ice sheet, ice streams are warmest at the ice-bed interface, where the ice is most insulated from cold surface air temperatures. Conversely, unlike other areas of the ice sheet, ice streams may produce substantial heat throughout the ice column due to lateral shear and friction at the ice-sheet base associated with basal sliding (Cuffey & Paterson, 2010). Warm, even potentially temperate, ice is therefore expected in areas of high strain, such as an ice-stream shear margin (Meyer & Minchew, 2018). However, there are few direct ice-temperature measurements in shear margins due to the challenges of working in an area where crevasses are often present. Hence, understanding of ice temperature in shear margins has developed through data-informed thermal modelling using measurements of surface velocity (Suckale et al., 2014) and ice-temperature measurements from other areas of the ice sheets. Due to strain heating, thermal models often indicate thick temperate ice columns in shear margins, but observational verification has heretofore remained elusive.

Extensive field efforts using boreholes from hot-water drilling have yielded direct measurements of ice temperature throughout the Siple Coast (Engelhardt, 2004b; Harrison et al., 1998), at Jakobshavn Isbræ(Iken et al., 1993; M. Lüthi et al., 2002), and in the slower-flowing ice of western Greenland (e.g. Harrington et al., 2015; Hills et al., 2017; Law et al., 2021; M. P. Lüthi et al., 2015; Thomsen et al., 1991). For safety, these holes are generally drilled away from the crevassed shear margins, with the one exception being the south margin of the northern tributary of Whillans Ice

Stream, Dragon Shear Margin (Harrison et al., 1998). Unfortunately, hot-water drilling into this shear margin was impeded by the crevasses, so temperature measurements extend only halfway through the ice column where temperate ice is not expected. Those measurements from the upper half of the ice column are colder than was expected based on thermal models, likely the result of several processes including cold air pooling in surface crevasses (Harrison et al., 1998), potentially anomalous vertical advection patterns through the ice-stream shear margins (Holschuh et al., 2019), and longitudinal (downstream) advection of ice from colder upstream areas (e.g. Iken et al., 1993; M. Lüthi et al., 2002). Direct observations of thick temperate ice are limited to a few locations in western Greenland (e.g. Harrington et al., 2015), and this ice likely becomes temperate due to liquid water infiltration (M. P. Lüthi et al., 2015; Phillips et al., 2010) rather than strain heating.

Advances in ice-penetrating radar technology offer new insights into shear-margin processes because englacial radar-wave speed, attenuation, and reflectivity are sensitive to ice temperature, crystal-orientation fabric, and bed properties, and because radar data acquisition via aircraft avoids safety and logistical risks inherent to borehole temperature measurements in shear margins. Here we present ground-based radar-derived ice-temperature observations from four separate surveys, accompanied by a new thermal numerical modelling experiment. We revisit the measured ice temperatures from hot-water boreholes drilled along the Siple Coast (Engelhardt, 2004b; Harrison et al., 1998) and compare those observations to the published analytical solutions for ice temperature (Meyer & Minchew, 2018; Robin, 1955). Based on the radar attenuation results and the mismatch between those models and measurements, we add an approximation for longitudinal advection (Weertman, 1968) to an established thermal model (Hills, Christianson, Hoffman, et al., 2022) to estimate the heat sink associated with ice being sourced from cold upstream regions. While our modelling does not include a full physical treatment of the co-evolution of ice temperature, ice dynamics, and rheology, it demonstrates the need to consider advective heat sinks (i.e., past flow and upstream conditions) in ice-stream thermal modelling.

3.2 Radar Attenuation

Radar attenuation in ice is chemistry (sea salts and acids) and temperature dependent, following an Arrhenius relationship (Corr et al., 1993; MacGregor et al., 2007). Variations in ice chemistry

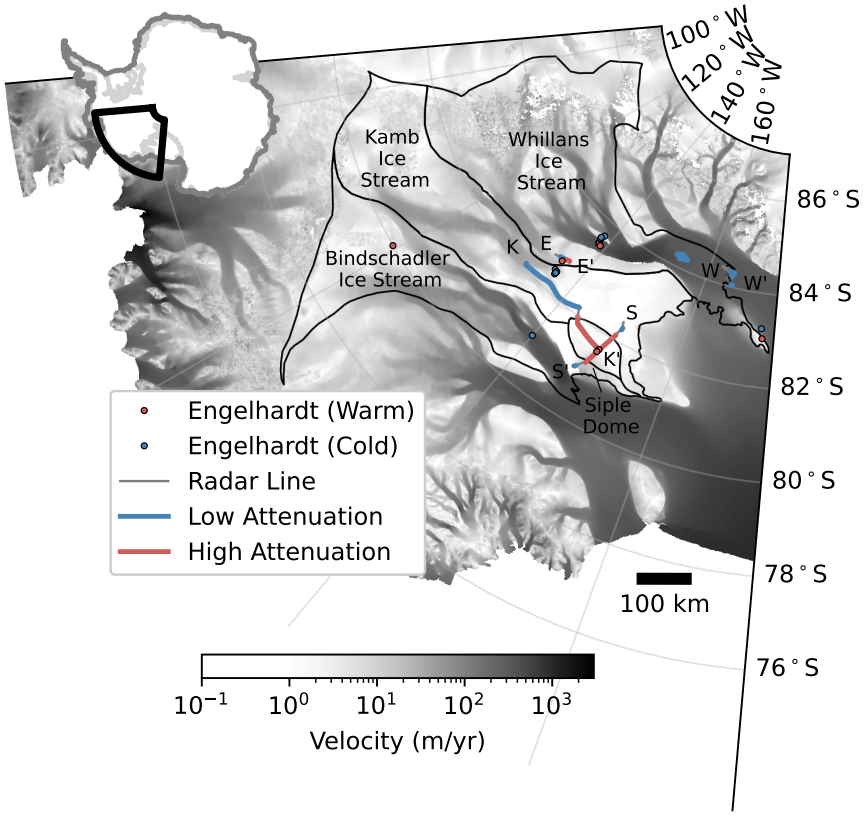

Figure 3.1: Ice surface velocity at West Antarctica's Siple Coast (Mouginot et al., 2019). Dots mark borehole drilling locations colored to indicate whether the borehole temperature profile is relatively cold (blue) or warm (red), based on the original classification (Engelhardt, 2004b). Lines correspond to the radar profiles shown in Figures 3.2 and 3.3. Drainage areas of the Bindschadler, Kamb, and Whillans ice streams (Rignot et al., 2013) are outlined in black, as is Siple Dome.

Table 3.1: Attenuation rates from selected prior studies at the Siple Coast.

Location	**One-Way Attenuation Rate (dB/km)**	**Reference**	**Effective Ice Temperature** (°C)
Siple Dome	29.5±0.3	(Jacobel et al., 2009)	-9
Siple Dome (common-midpoint survey)	26; 25.3±1.1	(Winebrenner et al., 2003) (MacGregor et al., 2007)	-11
Upstream Kamb	14.9±0.2	(Jacobel et al., 2009)	-19
Subglacial Lake Whillans	14	(Christianson et al., 2012)	-19
Whillans Grounding Zone	17.8±2.1	(Christianson et al., 2016)	-16

are due to synoptic-scale weather variability so act at spatial scales larger than typical radar surveys. Local lateral spatial variability in attenuation are therefore generally associated with ice-temperature changes (MacGregor, Li, et al., 2015; Schroeder, Seroussi, et al., 2016). Below, we assume that abrupt changes (within 10 km) in radar attenuation are primarily due to ice-temperature variability and ignore any spatial variation in ice chemistry.

We calculate englacial attenuation rates at four regions across the Siple Coast of West Antarctica (Figure 3.1): Siple Dome (SD); the two ice streams neighboring SD, Bindschadler Ice Stream (BIS) and Kamb Ice Stream (KIS); a tributary of Whillans Ice Stream (WIS) and nearby Engelhardt Ridge (ER); and the grounding zone of WIS. Englacial attenuation results were reported in prior publications, but here methodologies are standardized to allow self-consistent comparisons. For each radar profile, we migrate hyperbolic reflectors, correct for spherical spreading, and isolate bed-echo power using an open-source radar processing package, ImpDAR (Lilien et al., 2020). We choose to focus on representative lines from each survey due to their high quality and spatial continuity, but the trends discussed below are consistent with the breadth of ground-based radar data collected across the Siple Coast (see supplementary material). We note here that the radar instruments used are different for each survey, so direct power and attenuation comparisons between surveys is difficult.

Instead, we emphasize spatial variations within each survey and especially attenuation contrasts across ice-stream shear margins.

Data at SD are from two prior surveys (Gades et al., 2000; Jacobel et al., 2009). The range of ice thicknesses within the surveyed areas is large, so we calculate the attenuation rate by regressing the corrected power, P_c, against the ice thickness, H, using an error-in-variables linear regression (Appendix A).

The resulting englacial attenuation rates at SD (Figure 3.2) are broadly consistent, although lower in the first survey (24.2±0.4 dB/km) and higher in the second (30.2±0.3 dB/km). These attenuation rates are slightly higher than those from prior calculations due to the incorporation of uncertainties in equation A.1 through χ. Results are not statistically different for various subsamples of ice thicknesses and basal reflectivities along a given radar profile. Assuming constant salt (4.2 μMCl^{-}) and acid (1.3 μMH^{+}) content from the Siple Dome ice core, which are representative values for across the Siple Coast (MacGregor et al., 2007), the attenuation rates correspond to bulk ice temperatures of -11.9°C and -8.9°C for the first and second surveys, respectively. The interpreted bed reflector only spans part of the ice column, meaning that it is sampling the deepest and warmest ice. Thus, we expect a slight bias toward warmer ice for attenuation rates calculated this way (Appendix B).

Both above surveys extend off SD into the neighboring ice streams. The first reaches only slightly into both KIS and Siple Ice Stream, a currently inactive tributary of BIS. Following the procedure above, we calculate the attenuation rate by assuming that ice properties are consistent between the two ice streams and regressing the corrected bed-echo power against ice thickness across radar traces from both ice streams. We isolate segments of the radar profile in which englacial layers are visible (Figure 3.2A) since scattering in the crevassed shear margins would reduce the measured bed-echo power and obscure the attenuation properties of the ice. The resulting ice-stream attenuation rate is 14.6±0.7 dB/km (Figure 3.2B), corresponding to a depth-averaged temperature of -18.7°C. The second survey was focused on KIS (Jacobel et al., 2009) and extends far into what would have been streaming flow before the stagnation of KIS. Here, we calculate an attenuation rate of 15.2±0.2 dB/km (Figure 3.2D), which corresponds to an ice temperature -18.3°C.

Ice Stream C0 is a tributary of WIS, which was newly established since ice flow was redirected into WIS when KIS stagnated (Conway et al., 2002). The radar profile extends across the west-

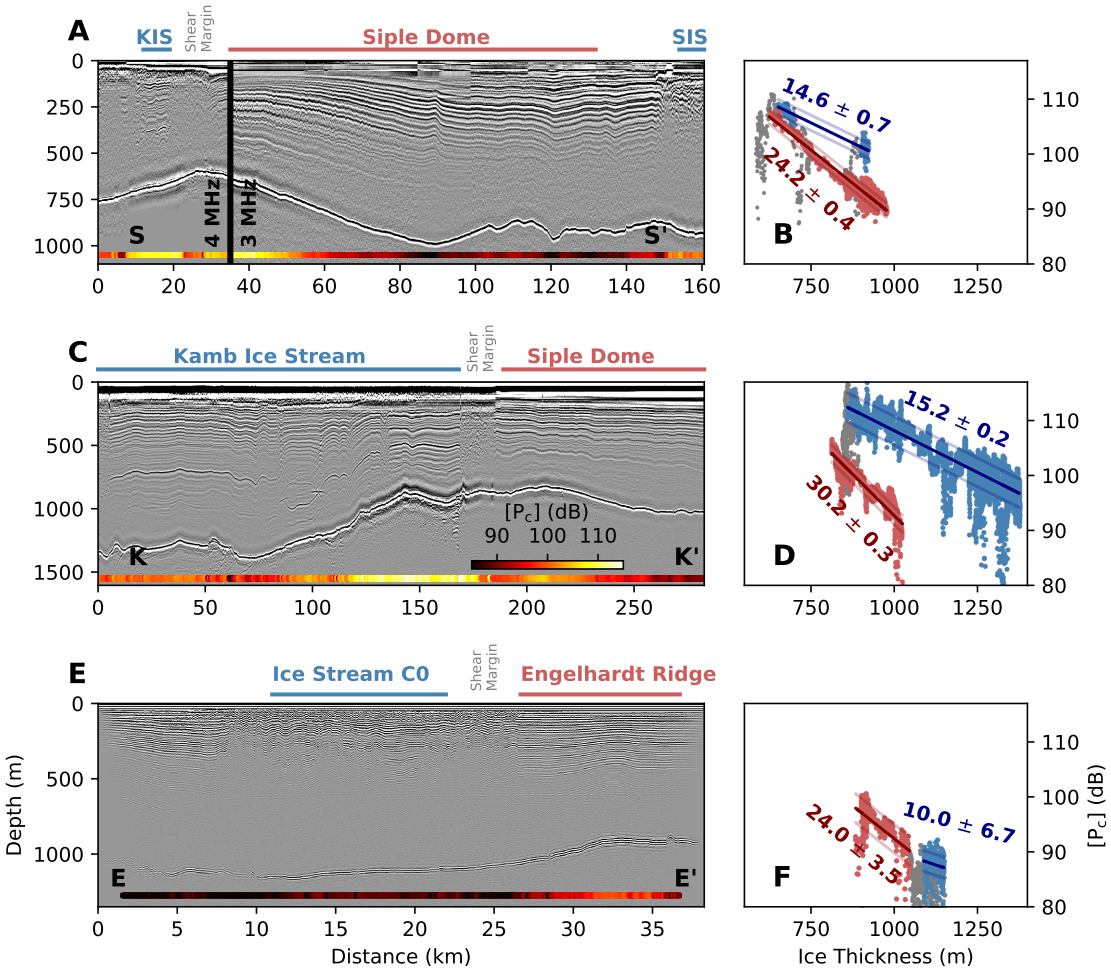

Figure 3.2: (A, C, E) Radar profiles corresponding to S-S' (Gades et al., 2000), K-K' (Jacobel et al., 2009), and E-E' (Conway et al., 2002), in Figure 3.1, respectively. Corrected bed-echo power is shown along the bottom of the image for each with the colorbar in (C) applying to all. (B, D, F) Corrected bed-echo power from (A, C, E) plotted against ice thickness to highlight the difference in attenuation between streaming ice (blue) and the neighboring ridge/dome (red). Siple Ice Stream (SIS) is a tributary of BIS, and Ice Stream C0 is a tributary of Whillans Ice Stream (Conway et al., 2002).

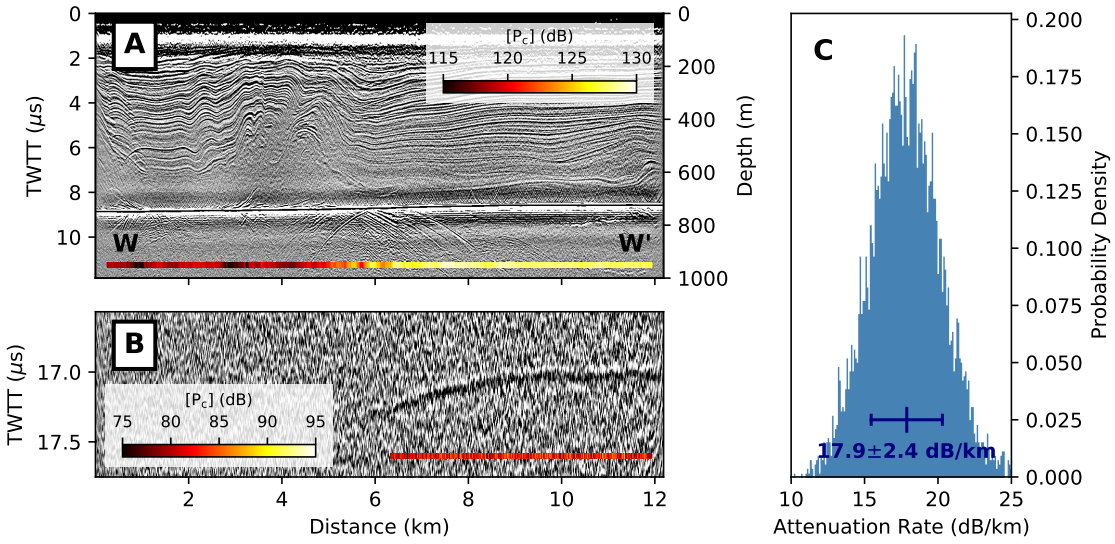

Figure 3.3: (A) Radar image corresponding to W-W' in Figure 3.1 (Christianson et al., 2016) with y-axes for both depth and two-way travel time. (B) Deeper (later travel time) radar image from the same profile as (A) to emphasize the first-multiple bed reflection. Corrected bed-echo power is shown along the bottom of (A) and first-multiple power along the bottom of (B). (C) Histogram of calculated attenuation rates for all traces using equation (2) with P_c from (A) and P_cm from (B). The histogram also includes traces from other similar profiles of the same survey (see Figure 3.1).

ern shear margin of the ice-stream tributary and onto ER (Figure 3.2E). The attenuation rates are 10.0±6.7 dB/km or -24.1°C inside the ice stream and 24.0±3.5 dB/km or -12.0°C on ER (Figure 3.2F). Uncertainties are higher in this survey than those above because the trace spacing is ∼10 times larger, so the total number of traces in the regression is much fewer. Unlike the results from KIS and BIS, bed-echo power within Ice Stream C0 is not elevated compared to the neighboring ridge.

Radar transects from the WIS grounding zone have less variation in ice thickness and more variation in ice-bed reflectivity (Figure 3.3) (Christianson et al., 2016). Here, we calculate attenuation rate by *Method 7* (Chapter 2.3). This calculation is done over the ice shelf where the basal reflectivity is uniformly bright, consistent with a smooth ice-seawater basal interface. The result over 5000 traces with a clear bed multiple is 17.9±2.4 dB/km which corresponds to an ice temperature of -16.0°C.

Attenuation results presented in this section are in broad agreement with previous measurements (Table 1). At SD, Winebrenner et al. (2003) measured attenuation with a different radar survey design but a similar empirical attenuation method, finding an attenuation rate of 26 dB/km (revised to 25.3±1.1 dB/km by MacGregor et al. (2007)). Jacobel et al. (2009) used the same data with a slightly different regression and found an attenuation rate of 29.5±0.3 dB/km at SD. Within ice streams, attenuation rates are generally lower. As above, Jacobel et al. (2009) found 14.9±0.2 dB/km at KIS. Christianson et al. (2016) found 17.8±2.1 dB/km using bed-echo multiples at the WIS grounding zone and 14 dB/km at the upstream Subglacial Lake Whillans site (Christianson et al., 2012). MacGregor et al. (2011) used a similar multiple-bed-echo method to calculate attenuation at the KIS grounding zone, finding an attenuation rate of ∼25 dB/km, but other results from earlier surveys showed significantly lower attenuation rates at the KIS grounding zone, from 13-17.3 dB/km (Bentley et al., 1998; Shabtaie et al., 1987).

The Siple Coast ground-based radar attenuation rates presented above fall into two broad categories: fast-moving (or recently stagnated) ice streams have low attenuation rates <20 dB/km and slow-moving ridges/domes have higher attenuation rates >20 dB/km. Again, ice chemistry should be spatially consistent across the Siple Coast (MacGregor et al., 2007), so attenuation variability at this spatial scale is associated with ice temperature. Although our attenuation calculations do not precisely define englacial temperatures, they do identify the temperature contrast between the slow-flowing ice ridges/domes and the ice streams. We hypothesize that this temperature contrast is a result of longitudinal advection of cold ice into regions of streaming (or recently streaming) flow. In the following section, we incorporate longitudinal advection into a thermal model to test this hypothesis.

3.3 Ice-Stream Temperature

Initial two-dimensional finite-element modelling of ice-stream temperature suggested that thermal softening is likely (Jacobson & Raymond, 1998). Since then, ice-stream and shear-margin thermal modelling has ranged from targeted analytical solutions to full three-dimensional thermomechanical numerical models. One-dimensional models (e.g. Meyer & Minchew, 2018; Perol & Rice, 2015) have focused on steady-state conditions, parameterizing lateral advection and ignoring longitudinal

ice flow. Similar one-dimensional models have been incorporated into more sophisticated ice dynamics and rheology treatments (Minchew et al., 2018). Recent two-dimensional models are usually defined on a cross-flow domain between the slow-flowing ridge and the ice stream. These models are similar in scope to the earlier work (Jacobson & Raymond, 1998), but have been optimized to explain the observed surface strain rates (Suckale et al., 2014), to consider basal melt water and lubrication (Elsworth & Suckale, 2016) and shear margin migration (Perol & Rice, 2015; Schoof et al., 2012), and to test parameter sensitivity under conditions with and without temperate ice (Hunter et al., 2021). While longitudinal advection has been considered in ice-sheet thermal modelling along flow (e.g. Dahl-Jensen, 1989; Weertman, 1968), it has only been briefly mentioned in the context of ice-stream shear margins (Jacobson & Raymond, 1998; Meyer & Minchew, 2018; Minchew et al., 2018), and, as far as we know, it has never been given any quantitative consideration. Here, we evaluate the effects of longitudinal ice advection on ice-stream and shear-margin temperature using both analytical and numerical approaches.

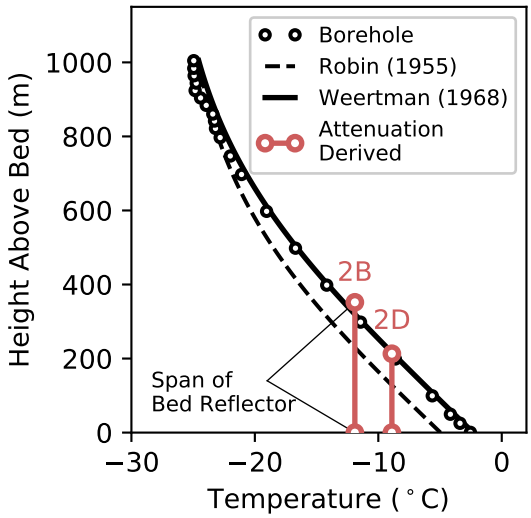

Figure 3.4: Measured and modelled ice temperatures at Siple Dome. Black dots are measured from a hot-water borehole (Engelhardt, 2004a). The Robin (1955) (black dashed) and Weertman (1968) (black solid) solutions are shown using boundary conditions from Table 2. Attenuation-derived temperatures (light red) for the locations at which radar data were collected (corresponding to Figures 3.2B and 3.2D), with the vertical span indicating the span of the bed reflector.

We assess ice temperatures for the same three regimes along the Siple Coast we considered in our observations above: slow divide flow at SD; streaming flow at BIS and KIS; and strong lateral shear at the Dragon Shear Margin (DSM) of WIS. Borehole temperature measurements have been made within each of these flow regimes (Figure 3.1) (Engelhardt, 2004b; Harrison et al., 1998).

The ice temperature at SD reflects mainly the local climate. There is a local precipitation anomaly at SD (confirmed by reanalysis and ice-core data (K. C. Taylor et al., 2004)); accumulation is orographically enhanced by a factor of two relative to nearby ice streams. BIS currently exhibits streaming flow with most ice being sourced from the upstream region near Byrd Station. KIS is currently the slowest-moving ice stream along the Siple Coast, having stagnated approximately 100 years ago (Catania et al., 2006; Ng & Conway, 2004; Retzlaff & Bentley, 1993). Like BIS, the ice at KIS has likely been sourced from higher elevations during past periods of streaming flow. DSM is the transition from slow flow on the Unicorn Ridge to fast flow in the northern tributary of WIS. Seven boreholes were drilled across DSM (Harrison et al., 1998). We use three different thermal models to simulate ice temperatures at these locations and compare simulation results with the borehole temperature-depth profiles. We begin with analytical models and then introduce a numerical model that includes additional ice-flow processes.

Table 3.2: Climate and ice-sheet parameters for calculation of the longitudinal advection heat sink. Accumulation and thickness gradients are displayed in both their respective units as well as their associated contribution to the temperature gradient (equation 6) in square brackets.
[†]Assumed steady-state flow speed is faster than present-day stagnant speed.

	q_{geo} $\left(\frac{\text{mW}}{\text{m}^2}\right)$	T_S **(°C)**	$\dot{a}$ **(cm/yr)**	H **(m)**	$\frac{\partial T_S}{\partial x}$ **(°C/km)**	$\frac{\partial \dot{a}}{\partial x}$ **(m/yr/km)** $[°\text{C/km}]$	$\frac{\partial H}{\partial x}$ **(m/km)** $[°\text{C/km}]$	u^* **(m/yr)**	$\dot{\mathscr{E}}_{xy}$ $\left(\text{yr}^{-1}\right)$
Siple Dome	65.3	-24.6	12.1	1005	N/A	N/A	N/A	0.0	0.0
Bindschadler Ice Stream	60.4	-24.4	11.1	1086	$10.1\text{x}10^{-3}$	$-0.15\text{x}10^{-3}$	-3.12	375	0.0
Kamb Ice Stream	66.3	-25.5	8.58	949	$13.4\text{x}10^{-3}$	$-0.27\text{x}10^{-3}$ $\left[6.50 \times 10^{-3}\right]$	-3.45 $\left[-7.50 \times 10^{-3}\right]$	300[†]	0.0
Dragon Shear Margin (WIS)	63.3	-26.0	6.98	1050	$12.1\text{x}10^{-3}$	$-0.31\text{x}10^{-3}$ $\left[21.5 \times 10^{-3}\right]$	-0.95 $\left[-4.37 \times 10^{-3}\right]$	180	0.048
Reference	(An et al., 2015)	(Harrison et al., 1998) (Engelhardt, 2004b)	(Hamilton, 2002) (Wang et al., 2021)	(Harrison et al., 1998) (Engelhardt, 2004b)	(Dixon, 2007)	(Wang et al., 2021)	(Morlighem et al., 2020)	(Mouginot et al., 2019)	(Perol & Rice, 2015)

First, the Robin (1955) model (see Section 2.2.2). Since this solution only considers the vertical dimension and heat sources at the boundaries, it is best suited for slow-flowing areas, such as ice divides (SD), and is less appropriate within streaming flow (KIS and BIS) or lateral shear (DSM). Steady-state model parameters are in Table 3.2, including accumulation rate (Hamilton, 2002; Wang et al., 2021), ice thickness from BedMachine Antarctica (Morlighem et al., 2020), mean annual surface temperature from firn cores (Dixon, 2007), and geothermal flux from seismic velocities (An et al., 2015). The Robin (1955) solution fit at SD is slightly colder than borehole measurements due to the linear vertical advection assumption (Figure 3.4) and at BIS and KIS is notably warmer. We do not apply this solution at DSM.

Second, the Meyer and Minchew (2018) model (see Section 2.2.3). Some notable approximations are made to extend this model to the continental scale, namely a constant vertical velocity and constant rate factor. Meyer and Minchew (2018) treat lateral advection as a parameterized heat sink described by a non-dimensional number, Λ (defined below). They argued that Λ is sufficiently small to be ignored, at least in the lateral, cross-margin case. We apply this model at DSM only, since model assumptions about lateral shear are most appropriate at this location. Again, we use input model parameters listed in Table 2, and several rate factors, A, with the softer end of the range appropriate for fully temperate ice ($2.47\text{x}10^{-24}$) and the stiffer end of the range being representative of the bulk ice temperature (average between surface and melting temperature as in Perol and Rice (2015)). In these cases, we set $\Lambda = 0$ for direct comparison to the result from (Meyer & Minchew, 2018). The resulting temperature profile is at the pressure-melting point through up to 22% and 49% of the ice column in the softer and stiffer cases, respectively. Both cases are notably warmer than the borehole temperatures measured at DSM although the limited borehole depth allows for comparison only in the uppermost $\sim$40% of the ice column. Still, the comparatively cold borehole temperatures suggest that a physical process may be missing from this analytical solution or that higher dimensional thermal effects may be at play in ice-stream shear margins.

Finally, we use a 1.5-dimensional numerical model (see Section 2.2.3). Ice temperatures modelled with the addition of longitudinal advection are considerably colder than results that do not consider advection, and, in some cases, even colder than the borehole measurements. For each location, we model temperature-depth profiles for an ensemble of scenarios from no advection, $\Lambda = 0$, to maximum advection based on the climate parameters in Table 2. Then, we assign a best-fit sce-

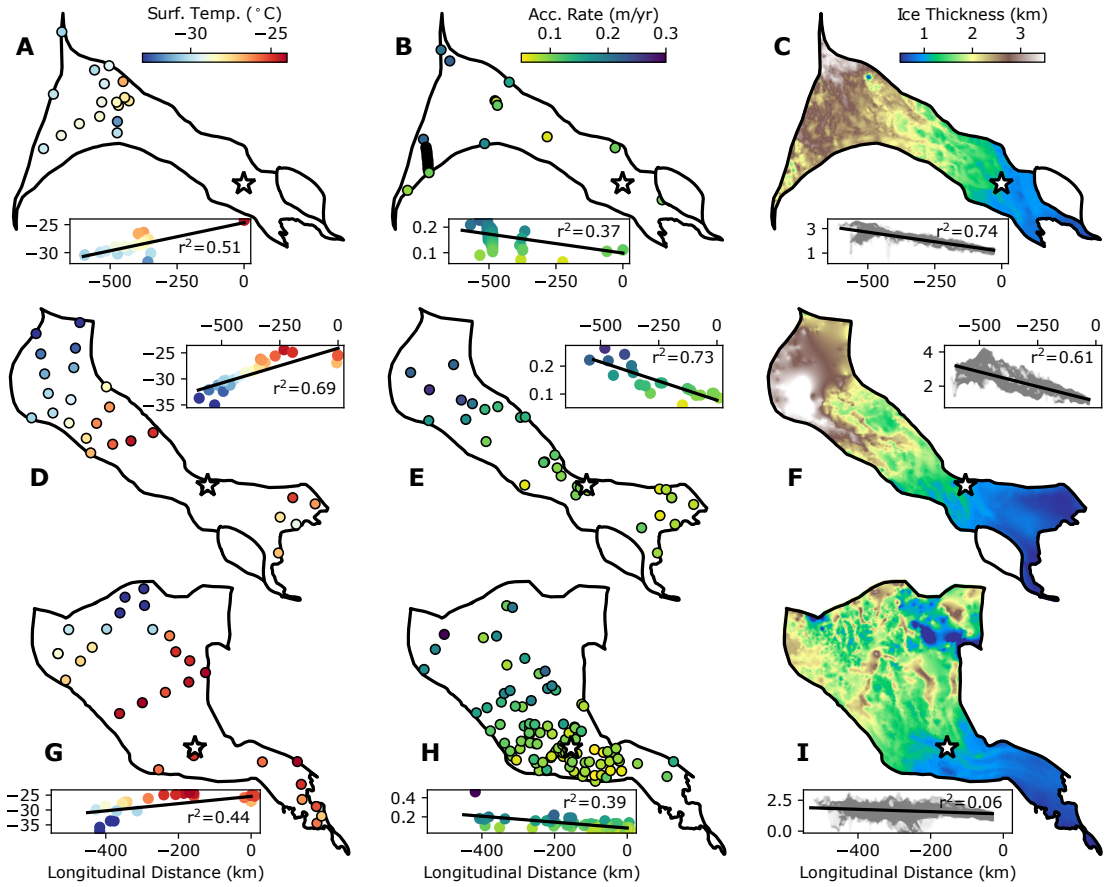

Figure 3.5: Present-day values and longitudinal gradients of surface temperature (Dixon, 2007), accumulation rate (Wang et al., 2021), and ice thickness (Morlighem et al., 2020) used in equation (6), for Bindschadler Ice Stream (A, B, C), Kamb Ice Stream (D, E, F), and Whillans Ice Stream (G, H, I). For each panel, a star is shown to indicate the borehole location for data plotted in Figures 3.6 and 3.7. Regression lines and associated r-squared values are shown in each inset panel.

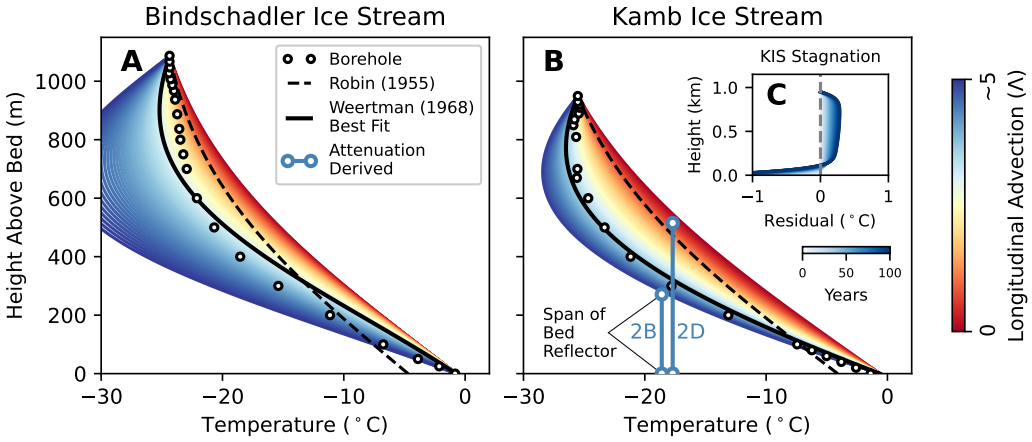

Figure 3.6: Measured and modelled ice temperatures at BIS (A) and KIS (B). Dots are measured from hot-water boreholes (Engelhardt, 2004b). The Robin (1955) solution is shown for each site (black dashed). Colored lines are numerical solutions to equation (5) (Weertman, 1968) over a range of plausible Λ's from 0 (red) to that derived from values in Table 2 (blue) for both BIS and KIS. Attenuation-derived temperatures are in light blue for the locations at which radar data were collected (corresponding to Figures 3.2B and 3.2D), with the vertical span indicating the span of the bed reflector. C) The thermal effect of KIS stagnation in a sequence of temperature profiles through time as a residual from steady state. Warming in the upper column is associated with softening of the longitudinal advection heat sink and cooling near the bed is associated with softening of the bed friction heat source.

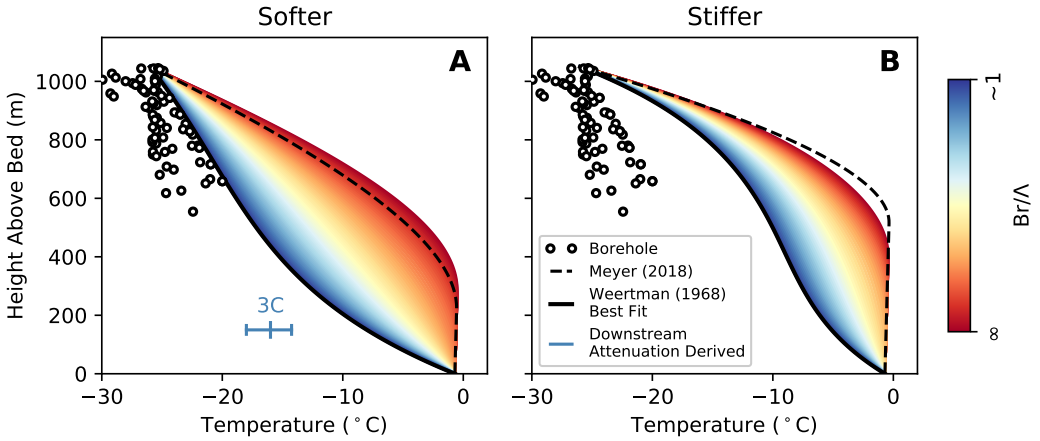

Figure 3.7: Measured and modelled ice temperatures at DSM. Borehole temperature measurements are from all boreholes drilled across the shear margin (Harrison et al., 1998), plotted the same in each panel. The Meyer and Minchew (2018) solution is shown (black dashed) for both the softer case (A) using the rate factor for temperate ice and the stiffer case (B) using that for the bulk ice temperature. Colored lines are numerical solutions to equation (5) (Weertman, 1968) over a range of plausible Λ's from 0 (red) to that derived from values in Table 2 for DSM (blue). The attenuation-derived temperatures, shown in light blue in (A), are from the most relevant ground-based radar survey, which is downstream of this shear margin at the WIS grounding zone (Figure 3.3C).

nario for the solution which most closely matches the borehole measurements. The reported value of Λ in the best-fit case is not meant to precisely quantify longitudinal advection alone, but rather to compare the plausible heat sink (which could come from longitudinal but also from lateral advection) to the competing value of Br in order to ascertain the likely presence of cold or warm ice streams and shear margins. At BIS (Figure 3.6A), the best-fit numerical solution is with $\Lambda = 1.6$, where the resulting temperature profile is on average 0.7°C colder than the Robin (1955) solution. At KIS (Figure 3.6B), the best-fit steady-state (pre-stagnation) numerical solution is with $\Lambda = 2.7$, with temperatures 2.7°C colder than the Robin (1955) solution. At DSM, even the strongest longitudinal advection results in temperature profiles warmer than those measured from boreholes (Figure 3.7). The coldest solution for the softer scenario is with $\Lambda = 5.3$, compare this with the heat source, $Br = 5.15$. For this softer scenario, the mean temperature is 8.2°C colder than the analytical solution. The coldest solution for the stiffer scenario is with $\Lambda = 6.8$, $Br = 10.2$, and ice is on average 6.2°C colder than the analytical solution. These modelled coolings correspond to stiffening in the lateral shear direction by 3.5 and 3.0 times, respectively.

Longitudinal advection is not a factor at Siple Dome. Still, the numerical model result at SD is slightly warmer, 1.7°C, than the Robin (1955) solution because the vertical velocity function is nonlinear in the numerical model (Figure 3.4). Divide flow, with nonlinear vertical velocity, is a better approximation of the ice dynamics at SD (Zumberge et al., 2002), so the better fit to data is not surprising.

3.4 Discussion

Near an ice divide, ice temperature is well studied and relatively simple. The relevant heat transfer processes are limited to vertical advection and vertical diffusion between the ice surface and bed. It is therefore most appropriate to consider ice-divide temperature using the non-dimensional *Peclet* number in the vertical,

$$Pe_z = \frac{\dot{a}H}{\alpha} \tag{3.1}$$

as is commonly done (e.g. Cuffey & Paterson, 2010, Figure 9.5). Vertical *Peclet* numbers at ice divides are of the order ~1-10. Both processes are slow at a divide, so much so that glacial cycles

are sometimes preserved within the ice temperature (Cuffey et al., 2016; Dahl-Jensen et al., 1998). For instance, we expect that the mismatch between measurements and our numerical model solution at BIS (Figure 3.6A) are related to historically and persistently cold temperatures in the source region (e.g. Gow et al., 1968). Away from the divides, ice flow is more complicated. Alternative heat transfer processes can affect and may even dominate the resulting temperature profile, as we have demonstrated. Below, we use non-dimensional numbers, such as *Pe*, as well as those discussed above, *Br* and Λ, to consider the thermal processes acting in the Siple Coast ice streams.

While thermal diffusion is relevant in the vertical, especially near an ice divide, it is rarely considered in the horizontal dimensions because horizontal temperature gradients are weak, and diffusion is too slow to act at the spatial scales of an ice sheet. Consider the longitudinal *Peclet* number,

$$Pe_{x^*} = \frac{u^* L}{\alpha} \tag{3.2}$$

Even in a slow-moving ice stream ($u^* \approx 50$ m/yr) and at a characteristic length scale, L, of $\sim$3-5 ice thicknesses ($\sim$5 km), longitudinal advection strongly outpaces diffusion ($Pe_{x^*} \approx 10^4$). For this reason, we argue that the $\sim$100-year stagnation of KIS is inconsequential to ice temperature analysis and interpretation. In Figure 3.6C, we demonstrate that stagnating the ice stream (i.e., turning off the advective heat sink) only leads to at most 0.3°C warming from the best-fit case. This is inconsequential compared to the advective cooling that had accumulated in the ice stream prior to stagnation, 4.5°C cooling on average. Put simply, 100 years is insufficient time for the longitudinal advection signal within the ice temperature at KIS to diffuse away. Since the recent stagnation has a minimal effect on ice temperature, both the observations and the modelling presented here indicate that ice streams, and to a slightly lesser degree shear margins, are cooled significantly via longitudinal ice advection. However, the stagnation has led to considerable thickening, which may eventually contribute toward reactivation by thawing the bed (Bougamont et al., 2015; Vogel et al., 2005); thus, it is not surprising that the KIS thickness gradient (Figure 3.5F) is significantly stronger than the gradient on WIS (Figure 3.5I). In the pre-stagnation state, the KIS thickness gradient would have been shallower and its inverse effect on longitudinal advection (thinning gradient reduces the heat sink) would be more muted, resulting an even stronger advective heat sink.

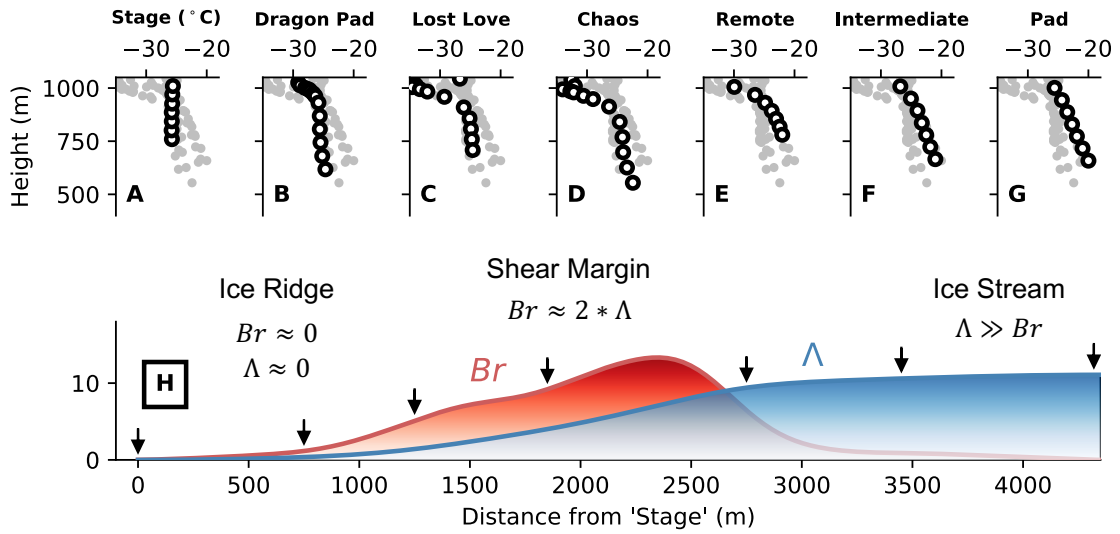

Figure 3.8: A-G) Borehole temperatures from DSM (Harrison et al., 1998) as in Figure 3.7 with the specific borehole measurements for each site as black circles and all other profiles across the shear margin as grey dots for reference. H) Dimensionless Brinkman number (red) and Λ (blue) calculated at DSM using the strain rate from surface velocity measurements (Mouginot et al., 2019) as well as temperature, accumulation, and thickness gradients from Table 2. Arrows correspond to borehole locations from (A-G) above.

In our model results, we demonstrate that the pre-stagnation state of KIS would have been comparatively cold in the ice stream itself ($Br < \Lambda$), with mid-depth ice temperatures colder than even the ice surface due to ice advection from higher elevations upstream. This is not surprising, as heat production within the ice stream is only from vertical shear, which is relatively weak; nor is this result new, as the importance of longitudinal advection has been previously discussed in thermal modelling along flow lines (e.g. Dahl-Jensen, 1989; Weertman, 1968). The observed advection process is fundamental to any ice stream where ice is sourced from colder regions. Borehole temperature measurements from Jakobshavn Isbræ (Iken et al., 1993) illustrate the advective cooling process, with a large cold core in the center of the ice column. In this end-member scenario, both Λ and Br are of order 100. Even here, any potential thickness of temperate ice is eliminated by the conveyor of cold ice from upstream.

We focus on the longitudinal component of Λ rather than the lateral component, not because it is

necessarily the dominant term, but since it has been underappreciated in recent studies and because the ground-based radar attenuation rates in Section 3.2 highlight the role of longitudinal advection. In fact, the persistent warm bias in our numerical results at DSM (Figure 3.7) are likely due to the missing heat sink associated with lateral advection. Again, we can demonstrate the relative strength of lateral advection to diffusion using a *Peclet* number,

$$Pe_{y^*} = \frac{v^* W}{\alpha} \tag{3.3}$$

where v^* is the lateral velocity and W is the width of the shear margin. A typical shear margin could be ~5 km across with cross-margin flow at $v^* \approx 10 m/yr$, so $Pe_{y^*} \approx 103$. The relative magnitude of Pe_{y^*} versus Pe_{x^*} does not imply that advection is more effective in one direction or another since the temperature gradient will be stronger across the shear margin than along it. Instead, we argue that the maximum Λ for the shear-margin scenario (Figure 3.7) should be considered a plausible heat sink, which could be amplified even further considering the possibility of strong lateral advection.

In the theoretical scenario where heat production greatly exceeds the longitudinal/lateral advective heat sinks ($Br \gg \Lambda$) ice-stream shear margins are excessively warm, hosting thick columns of temperate ice and a strong horizontal temperature gradient. Past studies which suggested the presence of significant temperate ice made this assumption, either implicitly or explicitly. In our case study at DSM (Figure 3.8), we find that Br and Λ are both small on the ice ridge, that they are on the same order of magnitude within the shear margin, and that $\Lambda \gg Br$ within the ice stream. We therefore argue that ice in an ice stream should generally be cold, even colder than the ice-surface temperature in some cases. Similarly, ice-stream shear margins should only be slightly warmer than slower flowing areas, with columns of temperate ice being reserved to areas with melt water injection through crevasses.

Our result of relatively cold ice in ice-stream shear margins contradicts prior studies and requires some other process explanation for shear softening necessary for the observed surface strain rates. Previous modelling studies have been optimized to the observed surface velocities (Suckale et al., 2014); that is, the shear margin must be soft enough for the observed lateral strain rates to be feasible. The natural first choice of mechanism for shear-margin softening is warm ice. However, other mechanisms can reduce stiffness as well. For example, ice-crystal grain size and orientation fabric

could allow more deformation at colder temperatures (Minchew et al., 2018; Ranganathan et al., 2021). Material damage in both surface and basal crevasses reduces the total number of molecular bonds, softening the ice to shear (Minchew et al., 2018). Some studies even show that in areas with extraordinarily high stress, such as in shear margins, the dominant mode of deformation could shift from dislocation glide along the basal plane to dislocation climb between planes (Goldsby & Kohlstedt, 2001), changing the creep exponent from $n = 3$ to 4, which would greatly reduce the associated heat production by softening the ice. We therefore argue that the softer case in Figure 3.7 may be more representative of shear-margin physics. Much like temperature, both the crystal fabric and material damage are advected by the ice stream, but these two fields can develop and evolve faster than ice temperature, especially in a high strain setting like an ice-stream shear margin.

In cases where $\Lambda > 0$, modelled temperature profiles at DSM have little to no temperate ice except at the ice-bed interface. However, there are locations where thick temperate ice columns have been directly observed. These sites are limited to western Greenland, where abundant surface melt water is available (Harrington et al., 2015; Iken et al., 1993; M. P. Lüthi et al., 2015). Temperate ice thickness extending upward from the bed within an ice-stream shear margin could also result from upward heat transfer by melt water infiltration through basal crevasses (McDowell et al., 2021), a process which is not included in our numerical model. This is a different mechanism than suggested by previous studies, which have indicated the possibility of significant temperate ice from strain heating.

Future investigations into shear softening in ice-stream shear margins should take an integrated multi-process approach (e.g. Minchew et al., 2018) instead of focusing solely on thermal softening, which has been common. Our results also highlight the importance of treating higher-dimensional heat transport processes, especially longitudinal and lateral advection, whereas much of the previous work has been limited to either solely the vertical dimension (Meyer & Minchew, 2018; Perol & Rice, 2015) or a cross section perpendicular to ice flow (Elsworth & Suckale, 2016; Hunter et al., 2021; Suckale et al., 2014). Fully partitioning shear-margin softening between thermal, material damage, crystal orientation fabric, and other effects would require three-dimensional modelling with solvers for each process and coupling to the stress balance calculation through a comprehensive ice rheology treatment.

3.5 Chapter Summary

In this study, we demonstrate a strong contrast in radar attenuation rates between Siple Dome and its neighboring ice streams. Ice temperature is the most likely attenuation-related variable that could vary spatially on the length scale of 10's to 100's of km considered here. We argue that the low attenuation rates measured in the three ice streams (BIS, KIS, and WIS) correspond to proportionally colder ice there, which is sourced from higher, colder upstream regions. We use a suite of 1+ dimensional thermal models to place our attenuation measurements within the context of direct borehole temperature measurements throughout the Siple Coast and theoretical understanding of ice physics and heat flow. Based on our measurements and model results, we argue that longitudinal advection acts to cool ice streams to a greater extent than has been considered in recent studies. This cooling equates to $\sim$3-3.5 times hardening in ice-stream shear margins. Additional work that considers the linked effects of higher strain rates on ice temperature, damage, and crystal-orientation fabric are necessary to advance our understanding of ice dynamics and stability of ice-stream shear margins.

Chapter 4

Radar Reflectivity at South Pole Lake Indicates a Regionally Thawed Bed and Consistency of Historical Ice Flow

Originally published in Geophysical Research Letters (Hills, Christianson, Hoffman, et al., 2022).

Chapter Abstract.

Subglacial lakes require a thawed bed either now or in the past; thus, their presence and stability have implications for current and past basal conditions, ice dynamics, and climate. Here, we present the most extensive geophysical exploration to date of a subglacial lake near the geographic South Pole, including radar-imaged stratigraphy, surface velocities, and englacial vertical velocities. We use a 1.5-dimensional temperature model, optimized with our geophysical dataset and nearby temperature measurements, to estimate past basal-melt rates. The ice geometry, reflected bed-echo power, surface and vertical velocities, and temperature model indicate that the ice-bed interface is regionally thawed, contradicting prior studies. Together with an earlier active-source seismic study, which showed a 30-m deep lake underlain by 150 m of sediment, our results suggest that the lake has been thermodynamically stable through at least the last 120,000 years and possibly much longer, making it a promising prospective site for sediment coring.

4.1 Introduction

The existence of a subglacial lake requires that the base of the ice sheet is, or has been, thawed. Lakes can thus provide windows into past regional ice dynamics and climate. South Pole Lake (SPL) is a subglacial lake in East Antarctica that was first identified in the Pensacola Pole Transect (Carter et al., 2007), though it had been imaged in earlier radar surveys (M. J. Siegert et al., 2005). This lake is only 10 km from the South Pole Ice Core, which provides well-constrained climate data over the last 50 thousand years (Kahle et al., 2021; Steig et al., 2021). There are 150 m of sediment beneath the lake (L. E. Peters et al., 2008). In this region of the East Antarctic interior, which has likely been glaciated for much of the last 35 million years (Deconto & Pollard, 2003; M. J. Siegert, 2008), such lake sediments could extend the recorded climate and geologic history far beyond the ~800 thousand year record preserved in ice cores, potentially to before Antarctic glaciation. Thus, this site is a promising target for sediment-core paleoclimate studies (Christoffersen et al., 2008; Kuhn et al., 2017; A. M. Smith et al., 2018).

The thermodynamic stability of SPL and the regional ice flow history play key roles in determining the sedimentation history beneath the lake. Nearby temperature measurements have been used to infer a regionally frozen bed (Price et al., 2002), supporting a hypothesis that SPL is a remnant of the past ice sheet and is freezing today (Beem et al., 2017). This hypothesis was based on radar evidence for a possible past upstream extension of Support Force Ice Stream towards the South Pole region that persisted until as recently as 10,000 years ago. The radar evidence for a paleo ice stream comes from two separate observations: disruptions in the englacial stratigraphy (Bingham et al., 2007), and higher submergence rates (Beem et al., 2017) within the inferred ice-stream extension.

Here, we present a new ground-based geophysical survey at SPL. Our survey constrains the current ice-sheet geometry, bed properties, and ice dynamics at higher resolution than previous work. With a more thorough description of the lake setting and newly acquired paleo climate constraints from the recently drilled and nearby South Pole Ice Core, we offer an updated hypothesis that SPL is in fact thermodynamically stable under current conditions.

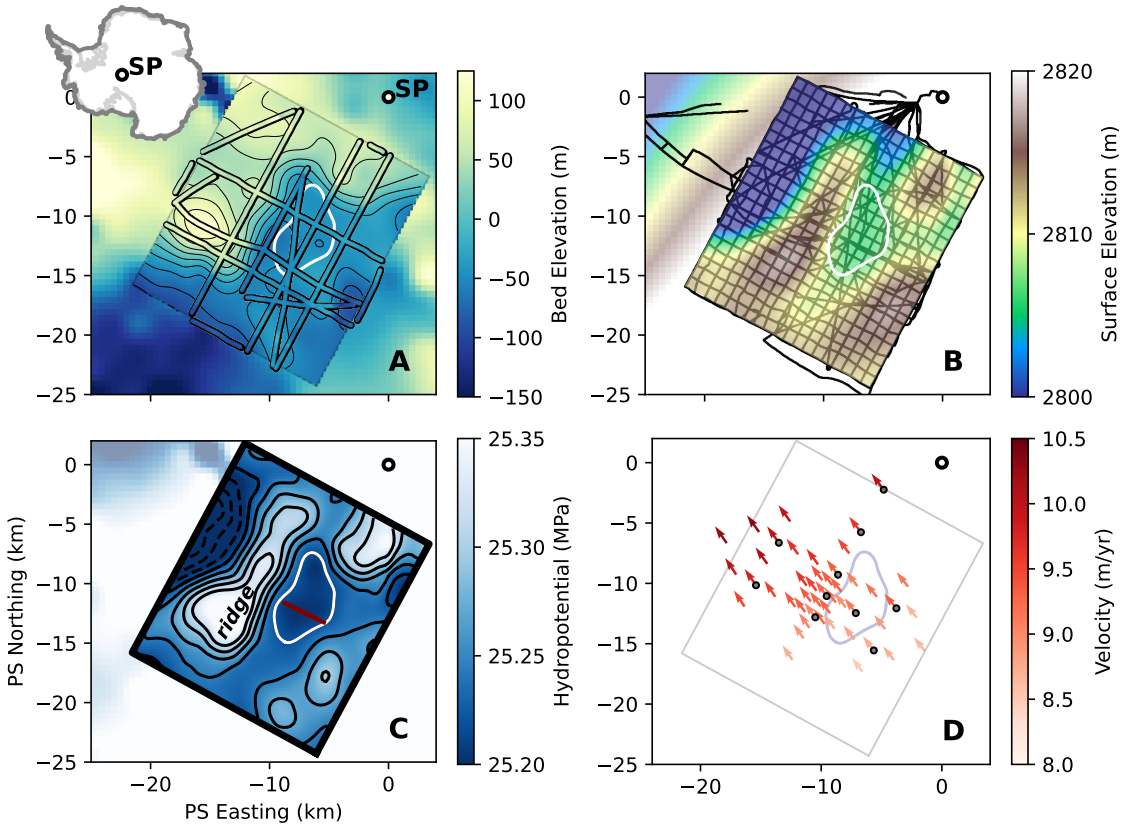

Figure 4.1: Maps of ice-sheet geometry at SPL (projection EPSG:3031) (black dot is the geographic South Pole). A) Bed geometry from deep-sounding radar. Colored lines are bed picks from the radar data presented in this study and the colored survey area is the interpolated bed elevation product. B) Surface geometry from kinematic GNSS data. The surveyed lines are in black, and the colored surface shows the interpolated surface elevation product. C) Hydropotential calculated from (A) and (B). Black contours correspond to the colormap in the surveyed area with dashed below the interpreted lake level (white) and solid above. The maroon line shows the active-seismic survey location. In panels (A), (B), and (C), fields plotted outside the surveyed area are from reference products, the BedMachine bed elevation model (Morlighem et al., 2020) and REMA surface elevation model (Howat et al., 2019). D) Surface velocity vectors measured with GNSS (red arrows) and sites of the 10 ApRES acquisitions (grey dots).

4.2 Geophysical Methods and Results

4.2.1 Ice Sheet and Lake Geometry

We collected 150 line km of ground-based 3-MHz impulse radar data (Figure 4.1). The processing was detailed in chapter 3. Generally, englacial layers are bed-conformal and nearly flat, but two features stand out. First, a shallow angular unconformity cross cuts layers between the surface and 300 m depth (Figure 4.2A). This unconformity dips in the direction of ice flow, to the grid northwest, with a slope 7.5 m/km (as expected, this is approximately equal to the accumulation rate divided by the downstream velocity). Second, we observe a synclinal depression with its fold axis oriented in the direction of ice flow along the grid southwest of the lake (Figure 4.2A). This feature is present in most profiles and has a consistent morphology; it is ~2 km wide and 200 m tall from ridge to trough. The syncline starts upstream of the lake, leading us to believe that it is not a lake feature, unlike past observations of lake-derived stratigraphy (e.g. Tikku et al., 2004).

Given the limited satellite elevation data near the South Pole, we also surveyed the surface elevation using Global Navigation Satellite System (GNSS) kinematic profiling. We collected approximately 1000 line km of dual-frequency GNSS data, using Septentrio Altus APS3G receivers sampling at 1 Hz along transects spaced 1 km apart. The antenna was mounted on an aluminum pole attached to a snowmobile that extended ~2 m above the snow surface. Position uncertainties are 5 cm or less in all dimensions.

We use spline interpolation between the radar and GNSS profiles to generate bed and surface elevation grids. We use our interpolated bed and surface elevation fields to calculate the glaciostatic hydropotential (Shreve, 1972). The hydropotential basin at the center of the surveyed area is the site of the subglacial lake. We define the exact lake boundary as the most conservative; that is, the lowest basin which encircles the liquid water imaged in the seismic data (L. E. Peters et al., 2008, Figure 3).

The center of SPL is 12 km to the grid south and 8 km to the grid west of the geographic South Pole along 150° W longitude. The bed elevation is depressed by 150 m at the site of the lake with an up-sloping bed to the grid west, north, and east. The bed depression extends to the grid southwest. The surface elevation is depressed at the lake site by 10 m. Opposite to the bed, the surface depression continues as a trough to the grid north, but it is bounded by surface highs to the

grid west, south, and east. The hydropotential shows a basin at the lake site with an upstream inlet to the grid east and outflow to the grid south, but a 100-kPa hydropotential barrier perpendicular to ice flow. We refer to this hydropotential barrier as 'the ridge'. Our data indicate that the lake overflow level at the southern outlet is 20 kPa above the conservative lake stand that we outlined (or ~2 m water equivalent). Small, currently active outflows may not be detected by this radar, since it has a large footprint (the first Fresnel zone is ~420 m wide at this ice thickness).

4.2.2 Bed-Echo Power

Beyond the radar processing described by Chapter 3, we apply additional corrections to the measured bed-echo power for attenuative losses using an Arrhenius model (MacGregor et al., 2007), which was tuned to match the empirically calculated attenuation rates (Hills et al., 2020). Bed-echo power over the surveyed area is normally distributed, showing no consistent spatial patterns (Figure 4.2). The difference between mean bed-echo power inside and outside the lake area is 1.0 dB. The standard deviation of power for returns outside the lake area is 3.6 dB, and for those inside is 1.8 dB. The bed-echo power within the lake is statistically indistinguishable from its surrounding area.

4.2.3 Ice Dynamics

Surface Velocity and Strain Rates

Satellite surface velocity measurements are limited near the South Pole. Thus, we collected surface velocity measurements at 46 sites over the surveyed area by differencing repeat GNSS acquisitions over a time interval of one year (Figure 4.1D). Measurement locations (monuments) were marked using an aluminum pole driven ~20-30 cm into the snow surface. At each location, the GNSS antenna was attached to the monument using a removable mount and data were collected for a minimum of 10 minutes. The monument position for each measurement is the mean of all position solutions calculated from the 10-minute measurement interval. Uncertainties are calculated as the standard deviation of the position solutions, which is ~2 cm in the horizontal dimensions. The mean velocity over the survey is 9.3 m/yr, with a slight increase from 8.5-10.3 m/yr in the direction of flow.

Using Delauney Triangulation, we grid the individual velocity measurements and calculate hor-

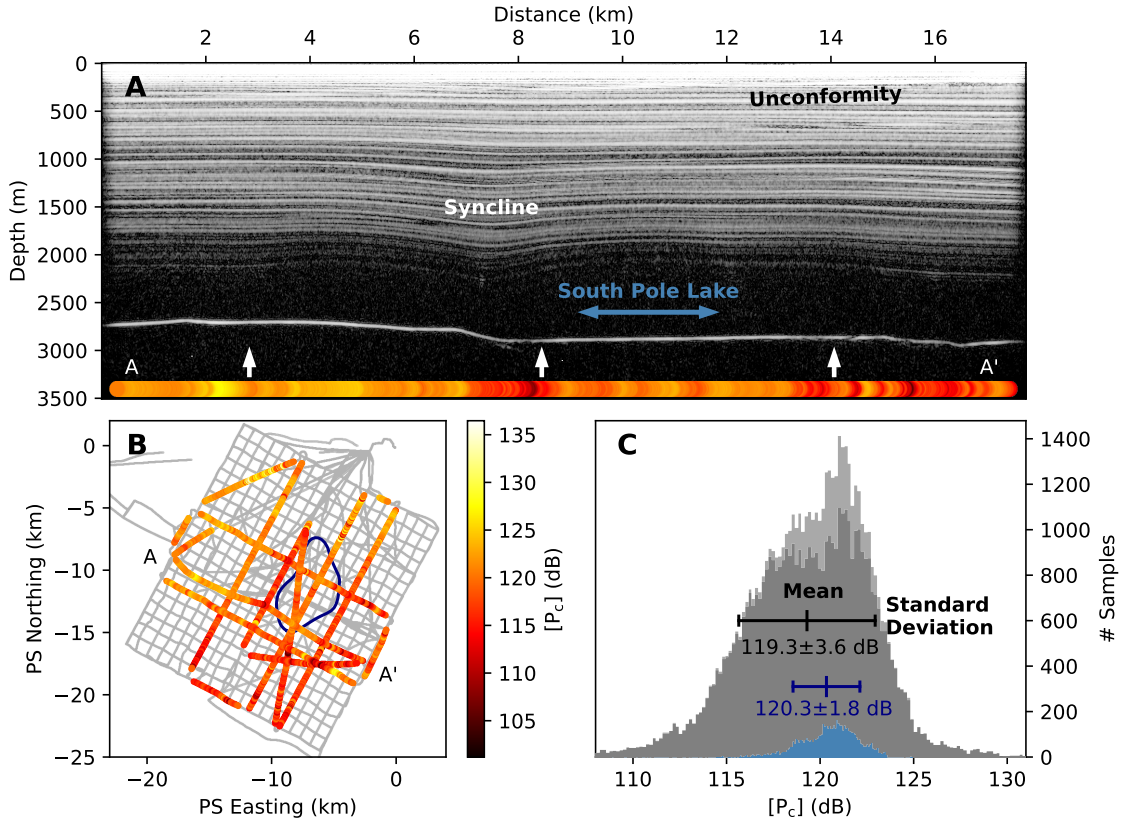

Figure 4.2: Deep-sounding radar power interpretation. A) Radar profile with location in the survey shown by A-A' in (B). Colored bar at the bottom shows the corrected bed power for this profile, with amplitudes corresponding to the colorbar shown in (B). White arrows show the location of ApRES acquisitions. B) Corrected bed power for all radar lines overlain on the kinematic GNSS survey (grey) and the interpreted lake outline (blue). C) Bed power for all traces over the radar survey (light grey), and for traces within (blue) and outside (dark grey) the interpreted lake area; mean (center hash mark) and standard deviation (edge hash marks) are shown for each.

izontal strain rates within each grid triangle (Jaeger, 1969; Shean et al., 2017). Tensile strain rates are as high as 2.5x10-4 yr^{-1}; compressive strain rates are slightly lower, up to 1.9x10-4 yr^{-1}. Measured surface strain is predominantly tensile along flow and compressive across flow. The highest tensile strain rates occur as ice flows over the ridge, and we do not distinguish any strong pattern in the strain rates associated with the lake boundary itself.

Englacial Vertical Velocity and Strain Rates

We calculate 10 vertical velocity profiles using repeat measurements from an Autonomous phase-sensitive Radio Echo Sounder (ApRES) (Nicholls et al., 2015) collected over a one-year interval. ApRES data are processed as described by Brennan et al. (2014) and implemented in ImpDAR (Lilien et al., 2020). For each acquisition, we stack at least 1000 raw chirps and do a range conversion using the known transmit signal. Following Kingslake et al. (2014), we calculate phase uncertainty using a median noise phasor associated with the noise floor for returns from below the bed reflector. The observed layer deflection is the phase difference between acquisitions after converting to distance using the center frequency of the transmitted signal (300 MHz).

Due to characteristic changes between profiles, vertical velocity results are grouped by those measurements taken away from the ridge and those taken on top of it (Figure 3). Profiles away from the ridge have an approximately linear velocity profile extending from no movement at the bed to the known accumulation rate (~8.7 cm/yr) at the surface, which is expected for slow-flowing ice. The signal vanishes for reflections below ~2000 m depth due to low phase coherence (<0.9) between acquisitions. Phase coherence is high (>0.9) at the bed reflection itself. Along the ridge, we observe about 2-3 times the vertical strain, with some variability between sites, and an apparent upward motion for deep reflections and the bed assuming the same accumulation rate as for sites off the ridge.

4.3 Ice Temperature Methods and Results

Next, we examine ice temperature using a 1.5-dimensional advection-diffusion model in which we parameterize longitudinal advection to account for colder temperatures originating upstream (for model details see Section 2.2.3). We assume a constant surface velocity (9.3 m/yr), geothermal flux

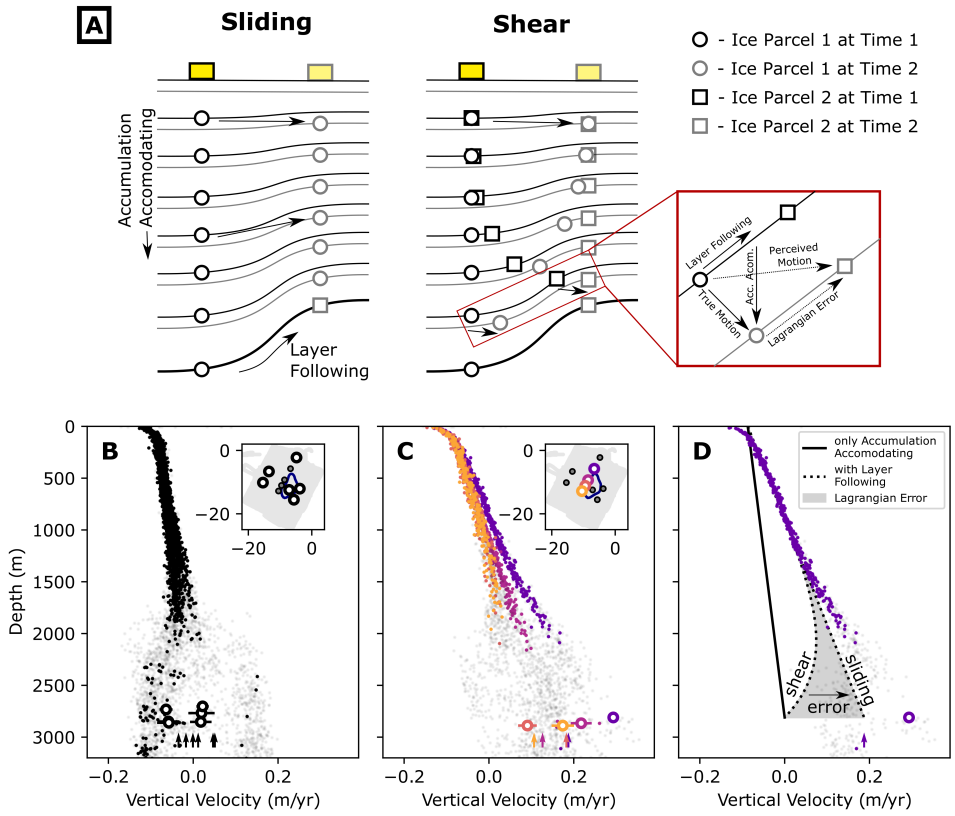

Figure 4.3: Vertical velocity interpretation. A) An illustration of ice moving over a bedrock bump with reflection surfaces (black at the first acquisition and grey at the second), imaged particles (circles), and the ApRES instrument (yellow box). In the shear case, the imaged particle only travels part of the distance that the instrument does, so a secondary particle is shown as a square. B) Vertical velocity profiles from six ApRES sites away from the ridge. Solid black dots show measured velocities for reflections with high coherence between acquisitions and faded black dots show those with lower coherence. Open circles show vertical velocity at the bed reflector with a horizontal line for uncertainty. Arrows show the inferred bed motion from the surface velocity against measured bed and surface slopes. The inset is an overview map with the lake outline and open circles at the six site locations. C) Same as (B) but for the four ApRES sites along the ridge. D) Vertical velocity at one site from (C), now with reference lines for the accumulation-accommodating and layer-following components of motion (Holschuh et al., 2017). Lagrangian error is only applicable in the shear case.

(60 mW/m^2), and ice geometry, ignoring any possible Holocene thickening (Lilien et al., 2018). We vary the surface temperature and accumulation rate over time. The chosen geothermal flux minimizes model-data misfit and is within the uncertainty for what has been estimated in this region (Martos et al., 2017; Shen et al., 2020; Stål et al., 2021).

To constrain the surface boundary condition, we use reconstructions of temperature and accumulation rate from the South Pole Ice Core (Kahle et al., 2021). Ice-core data extend to only 50 thousand years before present, and our testing showed that the initial condition is still somewhat persistent over that timescale. Therefore, we extend the paleoclimate record using air temperature and accumulation data from EPICA Dome C (Jouzel et al., 2007). We scale these parameters to match the data from South Pole Ice Core using a regression over that 50 thousand year period (Figures 4.1A and 4.1B). We initialize the model using a constant initial air temperature and accumulation rate (the initial value from each time series) and continue model iterations until the temperature profile converges to a steady state.

We first test the model against ice temperature measurements from the AMANDA/IceCube array (Price et al., 2002). Recent 7-MHz impulse radar data yields an ice thickness of approximately 2880 m within the IceCube array, about 70 m deeper than previous estimates (Price et al., 2002). The best model-data fit is for basal sliding, where the vertical velocity profile is linear (Lliboutry (1979) shape factor, $p = 1000$) and the shear stress is zero everywhere except the bed where it is approximated as equal to the driving stress. The resulting temperature profile matches the measurements to within ± 0.5°C and the ice-bed interface is thawed (Figure 4.4). In the internal shear case ($p \approx 10$), the heat source at the bed is weaker and shear heating in ice slightly above the bed is stronger, weakening the basal temperature gradient below what is observed. Hence, our model favors a velocity profile dominated by sliding rather than shear. Cooling from longitudinal advection is necessary to reproduce the observed temperatures; this is expected since the upstream temperatures are colder than those at South Pole (Fudge et al., 2020).

Next, we extend the modeling to the lake. We assume that horizontal temperature gradients between the site of measured temperatures at the IceCube array and the lake location are negligible, since strain rates are low and there is no liquid water present at the ice surface (c.f. Hills et al., 2017). The ice thickness estimates are 2852±10 m above the lake. Again, we assume that the ice thickness and velocity are constant in time and that velocity is dominated by sliding. The resulting melt rate

is positive through most of the reconstructed paleoclimate history with three brief exceptions during interglacial periods at 400, 320, and 120 thousand year. For some thinner areas around the lake, such as directly over the ridge, model results are colder and sometimes freezing at the bed. A small increase in the estimated geothermal flux (e.g. to 62 mW/m^2) thaws the bed here, and nearby studies show that there is large uncertainty, with a geothermal flux as high as 120 mW/m^2 in one case (T. A. Jordan et al., 2018).

4.4 Discussion

Below, we argue that the geophysical data and ice temperature modeling suggest a regionally thawed bed for the region around the South Pole. Although inconclusive individually, taken together our arguments are only consistent with an interpretation of a thawed bed. Our result contradicts prior studies, which suggested that the bed is frozen (Beem et al., 2017; Price et al., 2002). Where appropriate, we point out these differences and indicate specifically what additional data led to our contrasting hypothesis.

The SPL lake stand is currently within 2 m of its capacity. If regional freeze-on had been persistent for the last ~10 thousand years at rates of at least 3 mm/year, as suggested by Beem et al. (2017), we would expect the current lake level to be at least 30 m below its maximum capacity. A lake of a few meters depth would be at the limits of detectability (~2 m water depth) using active-seismic methods (Horgan et al., 2012), whereas this lake is clearly detectable with 32±10 m depth in active seismic data (L. E. Peters et al., 2008).

Bed reflections are bright throughout the survey. The difference in mean bed power between reflections from inside and outside the lake area (1.0 dB) is well within the standard deviation over the entire survey (3.5 dB). If the area outside of the lake were frozen, we would expect the reflected power to decrease by ~20 dB, which is the reflectivity difference between freshwater and frozen till/bedrock (Christianson et al., 2016; M. E. Peters et al., 2005). The bed power within the lake area has a slightly lower standard deviation than outside the lake, implying a more specular bed interface, which is expected for reflections from a likely smooth lake lid. A regionally bright bed is also consistent with radar data from the ITASE-2 traverse (Jacobel et al., 2010). Those data showed high bed-echo power in only two areas: Byrd Glacier and the last ~250 km approaching the South

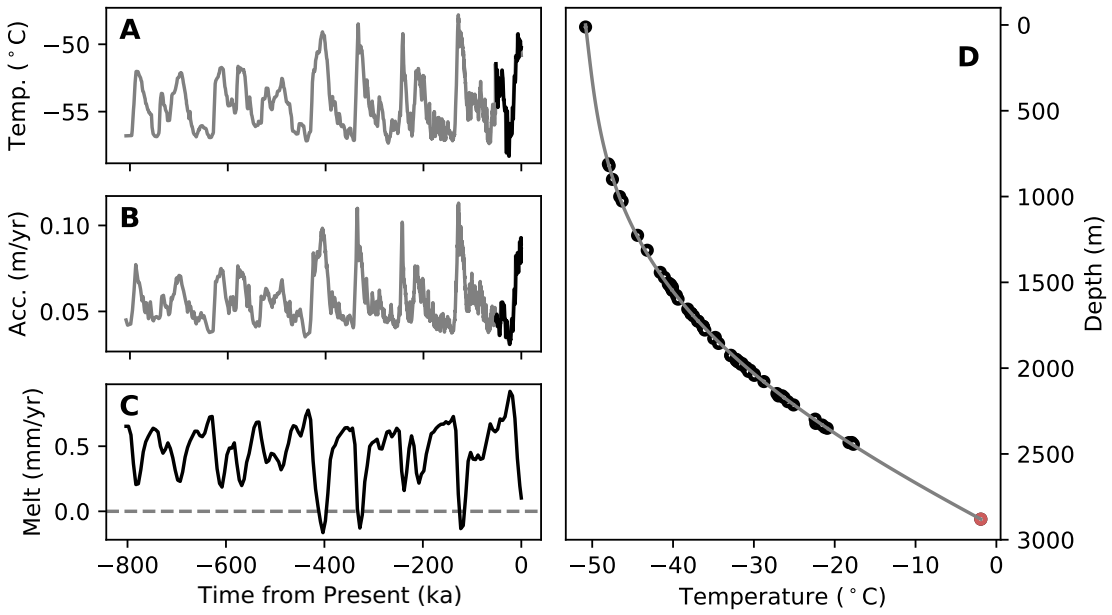

Figure 4.4: Temperature modeling data and results. A) Surface temperature reconstruction from South Pole Ice Core (black) (Kahle et al., 2021) and scaled from EPICA Dome C (grey) (Jouzel et al., 2007). B) Surface accumulation rate reconstructed from ice cores as in (A). C) Modeled melt rates at SPL with ice thickness of 2852 m (black) and a reference line at 0 mm/yr basal melt (grey dashed). D) Measured (black dots) and modeled (grey) ice temperature profiles. The shallowest data point is from nearby firn measurements (Giovineto, 1960) and the deepest point (displayed in red) is inferred at the pressure-melting point, assuming that the bed is thawed.

Pole. If the fast-flowing Byrd Glacier has a thawed bed, the implication is that the bed near the South Pole is also thawed, corroborating our interpretation.

The upward motion measured in the vertical velocity profiles corresponds to ice flow over an up-sloping bed at the ridge (Figure 4.3). To discuss these measurements, it is useful to separate the signal into three components: the accumulation-accommodating and the layer-following components of steady-state ice flow (Holschuh et al., 2017), and a Lagrangian error from horizontal motion of the ApRES instrument over a dipping reflector (i.e. the second acquisition images a different ice parcel along the same reflector). This error is only relevant in the shear case where velocities at depth are significantly slower than at the surface. Movement of the instrument itself over an upward dipping reflector leads to perceived upward motion. However, there is less bed parallel flow in this shear case, compensating for the error. Because of the Lagrangian error, we cannot directly distinguish between sliding and shear with any single vertical velocity profile, but together their uniformity and linearity suggest distributed sliding rather than discontinuous shear around the lake. There is also no substantial change in the surface strain rates across the lake boundary, which suggests that surface strain rates have minimal impact on spatial variability of vertical velocity.

Together, our temperature modeling and geophysical data interpretation suggest that for the present-day ice sheet: 1) sliding dominates over shear velocity; 2) the bed is currently thawed; and 3) the bed has been thawed for most of the past 800,000 years. The few times when modeled temperatures are close to or below freezing were during three brief interglacial periods with high accumulation. We have assumed that the higher accumulation was accommodated by additional vertical strain, but it is likely that the ice sheet thickened in response, which would decrease the amount of inferred freezing. All periods of modeled freezing were quickly followed by a rapid decline in the accumulation rate, which led to a return to basal melting.

The disagreement between previous studies (Beem et al., 2017; Price et al., 2002) and our temperature modeling is largely due to the updated ice thickness estimate of 2880 m within the IceCube array. A thicker ice column usually has a warmer bed because it is better insulated from the cold surface. Even accounting for measurement uncertainty (~¼ radar wavelength is 6 m at 7 MHz), this new, more direct ice-thickness measurement is still notably thicker than the previous estimates of 2810 m (Price et al., 2002) and 2800 m (Beem et al., 2017), which were based on the BedMap1 gridded product (Lythe & Vaughan, 2001). Since the best available ice thickness estimate

is compatible with both the 'cold' temperature measurements from IceCube and a thawed bed, our interpretation favors the simplest hypothesis; that is, the ice-sheet bed is currently thawed and is thermodynamically stable in its present configuration.

Finally, we note that the seismic survey of SPL imaged 150±60 m of sediment under the lake (L. E. Peters et al., 2008). The lake is therefore a viable drilling target for an East Antarctic sediment core, which could provide a paleoclimate record through many glacial cycles, as has been proposed for other subglacial lake sites (A. M. Smith et al., 2018). Sediments from a preserved Laurentide subglacial lake show that such a record could even persist between glaciations (Christoffersen et al., 2008). An ideal environment for an extended sediment record would be slow yet continuous deposition. While our data cannot guarantee the continuous presence of a thick water column, the modeled melt rates are positive through most of the 800 thousand year paleo reconstruction. Determining whether sediment deposition has been continuous, or if the lake has undergone periods of both deposition and erosion is beyond the scope of this work and would require more targeted geophysical surveys.

4.5 Chapter Summary

In this study, we present a geophysical survey at SPL. We find that the lake is currently full or nearly full of water to its maximum high stand given the current ice geometry, that the radar bed reflections are regionally bright, and that strain rates favor ice flow dominated by sliding as opposed to internal shear. Additionally, our temperature modeling, which is the most up-to-date model using high resolution estimates of ice thickness and the newly reconstructed paleo-climate variables from South Pole Ice Core, closely approximates the measured temperatures when assuming a sliding dominated velocity profile consistent with a thawed bed and some longitudinal advection. Based on these results, we argue that the ice-sheet bed is thawed in the area surrounding the South Pole and that SPL is therefore thermodynamically stable given the present-day ice-sheet geometry and climate. The deep sediment column, the apparent thermodynamic stability, and the basin's position on bedrock that would adjust to a surface well above sea-level in the absence of the East Antarctic Ice Sheet, establish the potential for the lake sediment to record a unique climate history potentially from the ice sheet's inception when SPL may have been open and exposed to the surface.

Chapter 5

Radar Interferometry and Polarimetry Indicate Local Divide Stability at Hercules Dome

In preparation for submission to Journal of Geophysical Research: Earth Surface.

Chapter Abstract.

Hercules Dome is a prospective ice-core drilling site due to its location in the bottleneck between East and West Antarctica. If ice from the last interglacial period has been preserved there, it could provide critical insight into the history of the West Antarctic Ice Sheet during that time in which the global climate was most recently similar to today. The likelihood of a continuous, well resolved, easily interpretable climate record preserved in ice extracted from Hercules Dome depends in part on the persistence of the divide location. Significant changes in ice draw down from the Ross or Ronne ice shelves can change the relative thickness of layers and the deposition environment represented in a prospective core. Paleo ice-sheet models predict that differential draw down from the Ross/Ronne could force divide migration at Hercules Dome by 10's of km; however these models are poorly constrained in this part of the East-Antarctic interior. Here, we constrain present-day and historical ice dynamics at Hercules Dome using ApRES interferometry and polarimetry, respectively. Repeated ApRES acquisitions (interferometry) show that the vertical velocity is consistent

with the ‘Raymond Effect’ expected at an ice divide. ApRES polarimetry is used to constrain the ice crystal orientation fabric (COF) for ice-flow history. COF develops over time as a result of cumulative strain, so it depends on both the nature of ice flow and the time over which that flow has been consistent. We also use a physical model to simulate COF evolution for both constant and variable strain scenarios. We find that the Hercules Dome summit has been stable in its current ice-flow configuration, at least during Holocene deglaciation. Divide stability has likely been due to a prominent bedrock ridge that had not been surveyed until now and was therefore not represented in the bed geometry of paleo ice-sheet models.

5.1 Introduction

Model results have shown that a hypothetical draw down of the West Antarctic Ice Sheet (WAIS) would change the regional atmospheric dynamics (Steig et al., 2015), forcing more warm air onto the edge of the East Antarctic Plateau which would be preserved in the ice at Hercules Dome as positive oxygen isotope anomalies (Dütsch et al., 2023). Therefore, if WAIS collapsed during the last interglacial period, as has been suggested by some ice-sheet models (DeConto & Pollard, 2016), Hercules Dome is uniquely situated to preserve the signal of that collapse. Still, the question remains whether the ice dynamic setting at Hercules Dome is suitable to preserve interglacial ice with uniform and continuous stratigraphy through the ice column in a way that would lead to an interpretable ice core.

As global air temperatures cooled into the last glacial period, the WAIS would have grown considerably, even if it did not fully collapse during the prior interglacial. Growth peaked at the Last Glacial Maximum (LGM), $\sim$14-20 thousand years ago. Ice-sheet modeling results show a considerably different ice sheet at the time, with different ice-stream behavior (Albrecht et al., 2020a, 2020b; DeConto & Pollard, 2016; Golledge et al., 2012). The ice-dynamic setting at Hercules Dome during LGM and through deglaciation into the Holocene would have depended, at least in part, on the relative evolution of the two downstream ice shelves, Ronne and Ross. If the divide position at Hercules Dome is primarily dependent on downstream effects the dynamic interplay between the ice shelves may have forced divide migration between them (i.e. at Hercules Dome). The precise growth and retreat behavior are unknown, but it is unlikely that the Ronne and Ross ice shelves underwent the same evolution with the same timing since they have different geometries and are exposed to different ocean currents. Therefore, considering these continental-scale processes, there is reason to consider that the divide at Hercules Dome *could* have migrated during deglaciation and into today's position, but an understanding of the local setting is necessary to determine whether that was the case in reality.

The dominant ice-flow regime at Hercules Dome is divergence by spreading in the polar stereographic ('grid') north-south direction. To the grid north, ice flows toward the Ronne Ice Shelf through Foundation Ice Stream. To the grid south, ice flows toward the Ross Ice Shelf through two drainages, van der Veen Ice Stream (a tributary of Whillans Ice Stream) and Reedy Glacier (a trib-

utary of Mercer Ice Stream). Hercules Dome can then be divided regionally based on this ice-flow regime and the ice geometry. The dome summit ('Summit') is at the grid-westernmost extent of the prominent north-south flow divide, with dome-like ice flow radially to the grid north, west, and south. A secondary rise in the surface topography ('East Dome') is further along the divide toward the grid-east. A topographic saddle (what we will call the 'Belt') connects the Summit and East Dome. Finally, an alternative divide ('South Ridge') extends to the grid-south from East Dome toward the Ross Ice Shelf. South Ridge forms the east-west surface divide with ice spreading toward Mercer Ice Stream to the grid east and toward Whillans Ice Stream to the grid west.

Prior work has identified large bedrock troughs in the region surrounding Hercules Dome which has been deemed the 'bottleneck' connecting East and West Antarctica (K. Winter et al., 2018). The bedrock troughs are bounded by tectonic activity, and were incised further by streaming ice flow during a time when the ice-sheet geometry was considerably different from today (Hoffman et al., in Review). However, evidence from radar stratigraphy indicates that the troughs continue to steer ice flow today, limiting draw down of ice from the higher East Antarctic Plateau and possibly controlling ice-sheet divide migration in the region (K. Winter et al., 2018).

In an initial geophysical survey at Hercules Dome, Jacobel et al. (2005) suggested ice-flow and divide stability based on preliminary evidence of the Raymond Effect (C. F. Raymond, 1983) seen in ice-penetrating radar stratigraphy. Subsequent work has made that initial radar stratigraphy interpretation of a true 'Raymond Arch' more ambiguous. Still, kinematic models of ice flow that consider advection and conduction of heat suggest that interglacial ice may be preserved at Hercules Dome, especially in the grid-western region which is the true dome summit (Fudge et al., 2022).

Here, we expand on those prior geophysical surveys by adding critical constraints to 1) the present-day ice dynamics through measurements of surface velocity and englacial vertical velocity, and 2) the historical ice dynamics through measurements of crystal orientation fabric (COF). We develop and discuss these new constraints in two parts. In part one, *Geophysical Methods and Results*, we focus on the ground-based observations collected at Hercules Dome. These include direct measurements of the three dimensional velocity structure; radar-derived COF orientation and strength which develops with the ice flow; and bed topography data collected with a variety of deep sounding radar systems. In part two, *Model Analysis*, we use the radar-derived COF results to motivate a series of model experiments. We describe and apply a model for COF development that

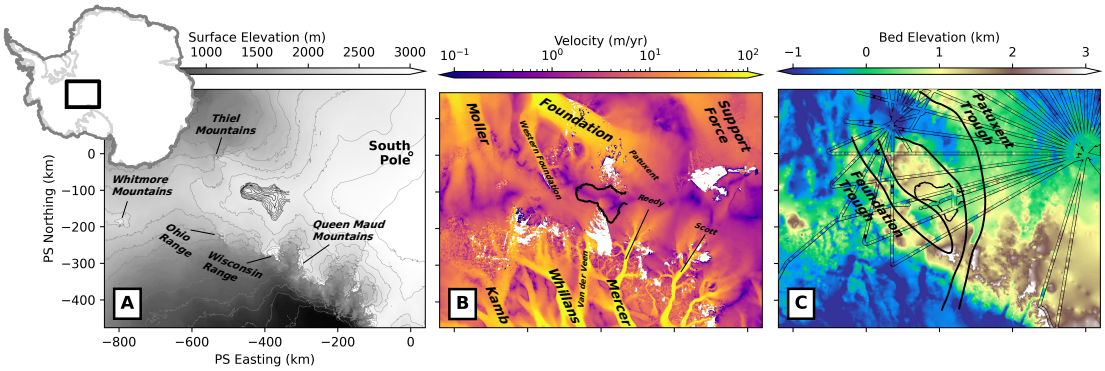

Figure 5.1: The ice-sheet setting near Hercules Dome. A) Ice surface elevation from the Reference Elevation Model of Antarctica (Howat et al., 2019). Contour spacing is 200 m away from Hercules Dome and 10 m at Hercules Dome. B) Ice surface velocity from various integrated satellite data products (Mouginot et al., 2019). C) Bed elevation from BedMachine Antarctica (Morlighem et al., 2020) and regional radar surveys (Jacobel et al., 2005; K. Winter et al., 2018).

we use to understand the history of strain represented in the measured COF signals. We then use this model with strain-rate histories informed by paleo ice-sheet model simulations of ice-sheet retreat and advance out of the LGM to evaluate whether the modeled strain of the last 10 thousand years is consistent with the COF signals encoded in our observations. We discuss our results, both measured and modeled, within the current understanding of ice-sheet history during Holocene deglaciation.

5.2 Geophysical Methods

5.2.1 GNSS

We surveyed the ice surface using the Global Navigation Satellite System (GNSS) for both kinematic profiling and static positioning. We used Septentrio Altus APS3G as well as Trimble NetR8 and NetRS receivers. For all receivers, we sampled at 1 Hz. We use the Canadian Spatial Reference System precise-point positioning (Tétreault et al., 2005) to convert from raw GNSS files to positions through time.

We collected ∼1800 line km of dual-frequency GNSS data along and between profiling radar lines. For this kinematic profiling, the antennas were mounted on conduit attached to a snowmo-

bile that extended ∼2 m above the snow surface. These data are used for spatial referencing and interpolation of the profiling radar data presented below.

Satellite-derived velocities are unreliable at low surface speed and especially near Hercules Dome where data coverage is sparse (Mouginot et al., 2019). Thus, we collected surface velocity measurements by differencing repeat static GNSS acquisitions. Due to some logistical constraints, not all sites were visited each field season and the time difference between repeat acquisitions varies from one to three years depending on the site. Measurement locations (monuments) were marked using conduit driven ∼20-30 cm into the snow surface. At each location, the GNSS antenna was attached to the monument using a removable mount and data were collected for a minimum of 10 minutes. The monument position for each measurement is the mean of all position solutions calculated from the 10-minute measurement interval. Uncertainties are calculated as the standard deviation of the position solutions, which is ∼2 cm in the horizontal dimensions. We measured surface velocity at a total of 26 sites laid out in 5 separate transects over the surveyed area. We calculate along-track strain rates by differencing the measured velocities between points along a given transect. Since velocities are slow relative to the position uncertainty, especially near the ice divide, the calculated strain-rate uncertainty is high.

5.2.2 Profiling Radar

We collected ∼750 line km of ground-based profiling radar data with two separate instruments and over 3 field seasons from January 2019 to January 2023. The radar survey is aligned with ice flow so that each line forms a transect across the ice divide. Since Hercules Dome is a triple divide, some of the radar lines are oriented north-south between the Foundation and Whillans drainages, and others are orientated east-west between the Whillans and Mercer drainages.

The first profiling radar instrument was a 3 MHz impulse radar (Welch & Jacobel, 2003) with which we profiled 537 line km. The transmitter for this system was a commercial pulse generator produced by Kentech Instruments that operates at a 1 kHz pulse-repetition frequency with a pulse amplitude of 4 kV. The receiver was a two-channel, 200 MHz, digitizing PCIe board made by GaGe Applied Electronics that was mounted in a ruggedized computer. Transmitter-receiver separation was ∼150 m. The antennas were resistively-loaded dipoles that were towed across the snow sur-

face. The data processing flow included a bandpass filter (fifth-order Butterworth filter from 1 to 5 MHz), time correction for antenna spacing and wave-speed variations through the firn column, interpolation to a standard trace spacing of 3 m, a horizontal de-meaning filter and two-dimensional time-wavenumber migration. The de-meaning filter subtracts a moving-averaged trace with a 100-trace window and scaled toward no correction below 500-m depth to emphasize the removal of horizontal artifacts near the surface. We then estimated the ice thickness by digitizing the bed reflection in each profile using a semi-automated routine built in the radar processing and interpretation package ImpDAR (Lilien et al., 2020). Absolute range uncertainty is roughly 1/4 wavelength ($\sim$14 m for the first radar instrument), while the relative uncertainty from crossover analysis is $\sim$1 m.

The second instrument was an FMCW radar with which we profiled 256 line km. This radar system has multiple antenna elements, capable of resolving off-nadir soundings (Hoffman et al., in Review). Processing steps for this system were through the standard CReSIS processing flow (CReSIS., 2021). The radar profiles and interpreted bed locations presented in this manuscript are for nadir-focused data only. For a more thorough description of the data processing and off-nadir capabilities see the original manuscript (Hoffman et al., in Review).

Ice surface elevation and receiver position were measured along each radar profile with a GNSS antenna as explained above. In select locations where the GNSS receiver died, surface elevation was interpolated using the Reference Elevation Model of Antarctica (REMA) (Howat et al., 2019). Elevation of the bedrock interface is estimated as the surface elevation minus interpreted ice thickness. We also present interpreted bed positions from three additional profiling radar systems, none of which are the focus of this investigation but each provide context for regional ice geometry and flow. The ITASE traverse from Byrd to South Pole Station and directly through Hercules Dome used the same ground-based radar as the first radar instrument above (Jacobel et al., 2005; Welch & Jacobel, 2003). Two airborne surveys have flown directly over Hercules Dome, first as a part of the broader PolarGap survey (K. Winter et al., 2018) and second with the High Capability Radar Sounder as a part of the surveying done in January 2023 for the Center for Oldest Ice Exploration. Each of these surveys use a separate algorithm to interpret the location of the ice-bed interface, we use that original bed interpretation for each.

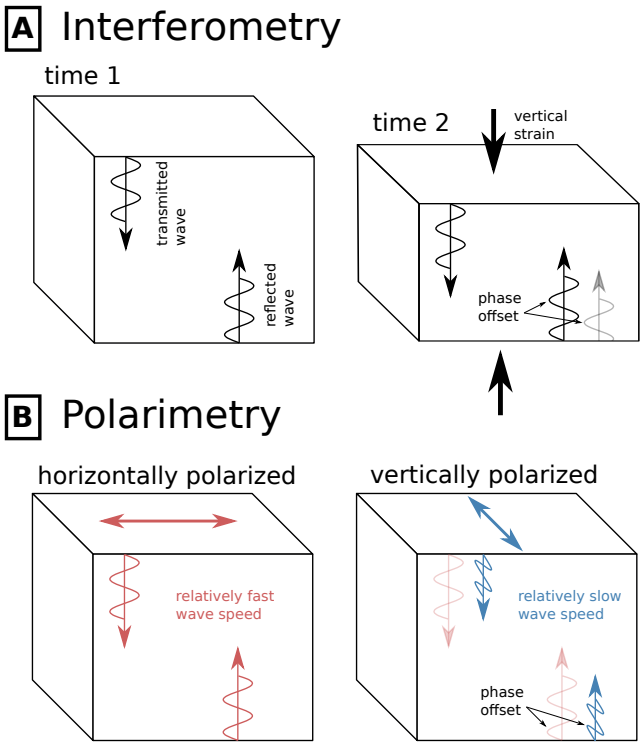

Figure 5.2: Illustration of the ApRES measurement techniques used in this study. A) Interferometry with a repeated acquisition in the same location but with some time separation, used to interpret vertical motion of reflecting interfaces relative to the instrument at the surface. B) Polarimetry with a repeated acquisition at the same time but with different antenna orientation (polarization) to interpret anisotropic crystal orientation fabric.

5.2.3 ApRES

We made Autonomous phase-sensitive Radio Echo Sounding (ApRES) (Nicholls et al., 2015) acquisitions at 36 sites spread regionally throughout Hercules Dome. At each site, the antennas were placed ∼10 m apart, oriented grid north-south. The acquisition location, including precise antenna locations, were flagged for reoccupation and measured with precision GNSS as described above. We use a single attenuator at 20 dB and -4 dB gain for a ramped chirp from 200 to 400 MHz (range resolution ∼0.4 m), and recorded 40,000 samples over 1 second. ApRES data are processed as described by Brennan et al. (2014) and implemented in ImpDAR (Lilien et al., 2020). For each acquisition, we stack at least 1000 raw chirps and do a range conversion using the known transmit signal. Following Kingslake et al. (2014), we calculate phase uncertainty using a median noise phasor associated with the noise floor for returns from below the bed reflector.

ApRES Interferometry

We repeat ApRES acquisitions for measurements of englacial vertical velocity (Fig. 5.2A) at 26 sites. Re-acquisitions were between one- and three-years time difference, again with logistical constraints on when individual sites were revisited. We compare the repeated acquisitions using cross correlation,

$$C_{12} = \frac{\sum_{i=1}^{N} \vartheta_{1,i} \cdot \vartheta_{2,i}^{*}}{\sqrt{\sum_{i=1}^{N} |\vartheta_{1,i}|^2} \sqrt{\sum_{i=1}^{N} |\vartheta_{2,i}|^2}} \tag{5.1}$$

where ϑ_1 and ϑ_2 are the first and second acquisitions to be compared. These are arrays of complex numbers over a set of range bins. We repeat this calculation over a moving window of samples where the window size, N, is some number of samples less than the total chirp length (in this case we use $N = 100$). The coherence between acquisitions over the given window is the real component of C_{12}, and the phase delay between acquisitions is

$$\Phi_{12} = arg(C_{12}) \tag{5.2}$$

We unwrap this phase delay profile, $\Phi_{12}(z)$, by adding or subtracting 2π at each wrap discontinuity. Then, the observed layer motion (in m/yr) is the phase difference between acquisitions after

converting to distance using the center frequency of the transmitted signal (f_c=300 MHz). Being a relative velocity, we align it with the approximate accumulation rate at the surface of 15 cm/yr ice equivalent (i.e. excluding firn compaction) (Horlings et al., in Prep) for consistency in figure axes. Finally, we isolate the range and power of the bed reflection as the deepest (furthest range) peak in measured power for both acquisitions, and confirm that this reflection has high coherence between acquisitions.

To compare between sites, we parameterize each measured velocity profile in two ways (Figure 5.3A). First, we calculate an upper-column vertical strain rate by linear regression of

$$\dot{\varepsilon}_{zz} = \frac{1}{\Delta t}\frac{\partial \Phi_{12}}{\partial z}\frac{c}{4\pi f_c \sqrt{\varepsilon}} \tag{5.3}$$

where Δt is the time between acquisitions, c is the vacuum wave speed, and ε is the permittivity of ice. We isolate this regression to the upper half of the ice column as has been done in prior studies (Kingslake et al., 2014). Second, we optimize the measured velocity profile to a Lliboutry (1979) shape factor,

$$w = \dot{a}\left(1 - \frac{p+2}{p+1}\zeta + \frac{1}{p+1}\zeta^{p+2}\right) \tag{5.4}$$

where ζ is the normalized depth below surface, $\frac{z}{H}$, H the full thickness of the ice column, $\dot{a}$ the accumulation rate at the surface, and p is the shape factor that we use for optimization. For both the strain rate calculation and the shape factor optimization, we discard the shallow range bins less than 200 m depth (firn compaction signal) and those with low coherence.

ApRES Polarimetry

Ice crystals have anisotropic permittivity (T. Matsuoka et al., 1997). Therefore, perpendicularly polarized waves exhibit some phase delay due to the difference in wave speed through the ice (Section 2.3.3). When the radar antennas are strategically polarized relative to the expected COF, measurable phase delays reveal information about COF strength and orientation. The effectiveness of such polarimetric radar experiments on glacier ice has been demonstrated in theory (Fujita et al., 2006) and applied across Antarctica and Greenland to understand fabric development and ice flow history

(Brisbourne et al., 2019; T. M. Jordan et al., 2022; T. M. Jordan et al., 2019; Young et al., 2021). Since it is logistically easiest to polarize the wave in the x/y directions, with the wave propagating downward in the z direction, the most directly measurable fabrics are those with some x/y variation. For example, a vertical girdle is measurable with x/y polarimetry, but a vertical pole is not (Rathmann et al., 2022). More sophisticated inverse methods which include reflectivity interpretation are one workaround for the vertically oriented COF (Ershadi et al., 2022).

We did x/y polarimetric ApRES acquisitions (Figure 2B) at 27 sites. Again, the antennas were oriented approximately grid north-south, and precise positions for both transmit and receive antennas were measured with GNSS. The azimuthal orientation of the antenna array is therefore accounted for in the polarimetric data processing. At each site, we stacked between 500-1000 chirps in both co-polarizations as well as at least one cross-polarization and sometimes both (in theory, the cross-polarized terms are identical, so only one needs to be measured). We use the polarization notation from the literature where 'H' indicates horizontally polarized (in line with the antenna array) and 'V' indicates vertically polarized (perpendicular to the antenna array), then the co-polarized acquisitions are HH or VV, and the cross-polarized are HV or VH (Young et al., 2021, Fig. 1).

The processing flow for polarimetric ApRES data is implemented in ImpDAR. We use all four acquisitions in a rotational transform to define azimuthal radar images for each

$$\mathcal{S}(\theta,z) = \mathbf{R}(\theta)\mathcal{S}_0(z)\mathbf{R}(-\theta) \tag{5.5}$$

where $\mathcal{S}_0 = \left[\begin{smallmatrix} \mathcal{S}_{hh} & \mathcal{S}_{hv} \\ \mathcal{S}_{vh} & \mathcal{S}_{vv} \end{smallmatrix}\right]$ is the measured waveform, $\mathbf{R}$ is the rotation matrix, and θ is the angle of azimuthal rotation. Each measurement acquisition is an array of range bins, so rotating through all azimuths gives a total of four 2-dimensional images, one for each polarization ($\mathcal{S}_{HH}$, $\mathcal{S}_{HV}$, $\mathcal{S}_{VH}$, $\mathcal{S}_{VV}$).

Alignment of the optical axis of the ApRES antenna with the bulk COF axis leads to two critical phenomena, both of which are encoded in the received signal. First, the cross-polarized acquisition measures minimal returned power (cross-polarized extinction; XPE) (Ershadi et al., 2022) because the wave does not 'depolarize' as it moves through the ice column. The H-polarized wave will stay H-polarized and not be measurable by the V-polarized receive antenna. The same is also true for V-transmit/H-receive. We can therefore estimate the orientation of x/y COF anisotropy (girdle

orientation) by searching for the XPE axis (the orientation with minimal returned power) for each range bin in the cross-polarized image

$$\theta_{xpe}(z) = min(\boldsymbol{\mathcal{S}}_{VH}(z)) \tag{5.6}$$

The cross-polarized image is symmetric at $\pi/2$, so we choose the XPE which is closest to the measurement axis.

The second measurable phenomenon is the phase delay between co-polarized terms which is related to the magnitude of x/y COF anisotropy. A wave polarized parallel to the COF maximum (i.e. in line with most crystal c axes) travels slower than its perpendicular counterpart. The parallel wave therefore arrives at the receive antenna slightly later than the perpendicular wave would, creating a phase delay which increases with propagation depth into the ice. In the same manner as in equation 5.1 above, we calculate phase delay using the coherence between the co-polarized images ($\boldsymbol{\mathcal{S}}_{HH}$ and $\boldsymbol{\mathcal{S}}_{VV}$),

$$C_{HHVV} = \frac{\sum_{i=1}^{N}\sum_{j=1}^{M} \boldsymbol{\mathcal{S}}_{HH,i,j} \cdot \boldsymbol{\mathcal{S}}^{*}_{VV,i,j}}{\sqrt{\sum_{i=1}^{N}\sum_{j=1}^{M} |\boldsymbol{\mathcal{S}}_{HH,i,j}|^2}\sqrt{\sum_{i=1}^{N}\sum_{j=1}^{M} |\boldsymbol{\mathcal{S}}_{VV,i,j}|^2}} \tag{5.7}$$

averaged over a moving 2-d window with some range span (size N) and some azimuth span (size M). The phase delay between co-polarized images is then calculated as in equation 5.2,

$$\Phi_{HHVV} = arg(C_{HHVV}) \tag{5.8}$$

The rate of change in phase delay with depth (the phase gradient) corresponds to the difference in wave velocity between H and V polarizations. This difference will be maximized at the XPE azimuth, so we extract the calculated phase delay along that axis, $\Phi_{xpe}(z)$. This phase gradient at XPE is then directly proportional to the girdle strength (T. M. Jordan et al., 2019),

$$\lambda_2 - \lambda_1 = \frac{\partial \Phi_{xpe}}{\partial z}\frac{2c\sqrt{\varepsilon}}{4\pi f_c \Delta\varepsilon} \tag{5.9}$$

where λ_2 and λ_1 are the principal eigenvalues (with the third pointing directly upward and not considered here). Since the measured phase delay is noisy, we unwrap the signal and apply a

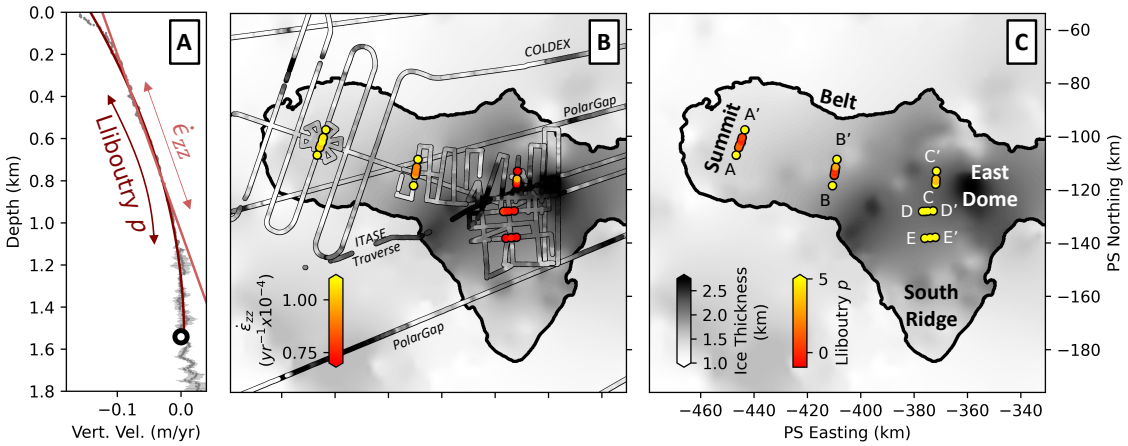

Figure 5.3: Regional overview of vertical velocity and ice thickness measurements. A) An example velocity profile with two parameterizations, linear for strain rate (equation 5.3) and the Lliboutry (1979) shape factor (equation 5.4). B) Vertical strain rate for each ApRES site (colored dots) and ice thickness measurements from profiling radar (grayscale). All profiling radar systems are shown, with labels for those not specific to this study. The base map is ice thickness from BedMachine (Morlighem et al., 2020). The thick outline is a surface elevation contour (same as in Figure 5.1). C) Lliboutry (1979) shape factor for each ApRES site. Low values of p indicate a divide effect. The base map is the same as (B).

Savitsky-Golay filter before calculating the gradient in depth. To compare the polarimetry results between sites, we parameterize each profile by extracting the maximum phase gradient within some depth span (we use 300 to 1100 m for every profile). Of course, not every profile can be well represented by a single gradient, but the data interpretations we present below are broad enough to be consistent with the dataset as a whole.

5.3 Geophysical Results

5.3.1 Ice Geometry

The regional surface topography is dominated by the two perpendicular ridges. The predominant ridge is from the Summit, through the Belt, to East Dome, and onward toward South Pole. That ridge is met by a grid southward extension from East Dome to South Ridge. The overall surface relief in the surveyed area spans from 2530-2620 m. At a smaller scale, the surface roughness has amplitude on the order of 10's of cm over wavelength of $\sim$10's of m.

Measured ice thicknesses range from 1400-2900 m (Figure 5.3). The thinnest and most uniform ice is at the Summit (total variation ∼400 m over the ∼200 km^2 radial survey). The thickest ice is in a large east-west trough at East Dome. South Ridge and the Belt are intermediate, both with thicker ice and more bed relief than the Summit but the only substantial trough in the bed geometry is the one identified at East Dome.

5.3.2 Surface Velocity and Strain Rate

Measured surface velocities are qualitatively aligned with the surface topography as expected. At the Summit, the surface velocities were only measured along one transect, oriented perpendicular to the regional divide. Along that transect, ice flow is north-south spreading. Measured speeds are from 0 m per year at the divide to 0.5 m per year at the transect ends, 5 km to the grid north/south. In other words, the ice is spreading at $\sim 10^{-4} yr^{-1}$. At the Belt, the surface velocity matches that of the Summit, although with more measurements. Again, the surface strain rate is $\sim 10^{-4} yr^{-1}$. At South Ridge, all flow vectors have some southward velocity component, but the predominant flow pattern is east-west spreading, although weaker than the Summit, $\sim 5 \times 10^{-5} yr^{-1}$. At East Dome, the surface velocity vectors are not aligned with the transect. Instead, ice flow is toward the grid east, aligned with the bedrock trough, even at what was originally thought to be the divide location.

5.3.3 ApRES Vertical Velocities

We measured a total of 26 vertical velocity profiles along 5 separate transects of Hercules Dome. Every velocity profile has the greatest downward speed at the ice surface, where new snow is deposited. The depth gradient, or vertical strain rate, is also greatest within the uppermost ∼200 m, the portion of the ice column subject to firn compaction. In the middle of the ice column the vertical velocity profiles are approximately linear (approximately uniform thinning). In this portion of the ice column with uniform-thinning, the magnitude of the strain rate is most strongly dependent on the ice thickness, with thin ice necessitating a higher strain rate for the same accumulation and outward spreading (Figure 5.3B). In the lower ice column, the measured velocity behavior is less consistent between profiles, even qualitatively. Some profiles approach zero velocity nonlinearly (small p), as would be expected in a region of divide flow (Fudge et al., 2022; Kingslake et al., 2014). Others,

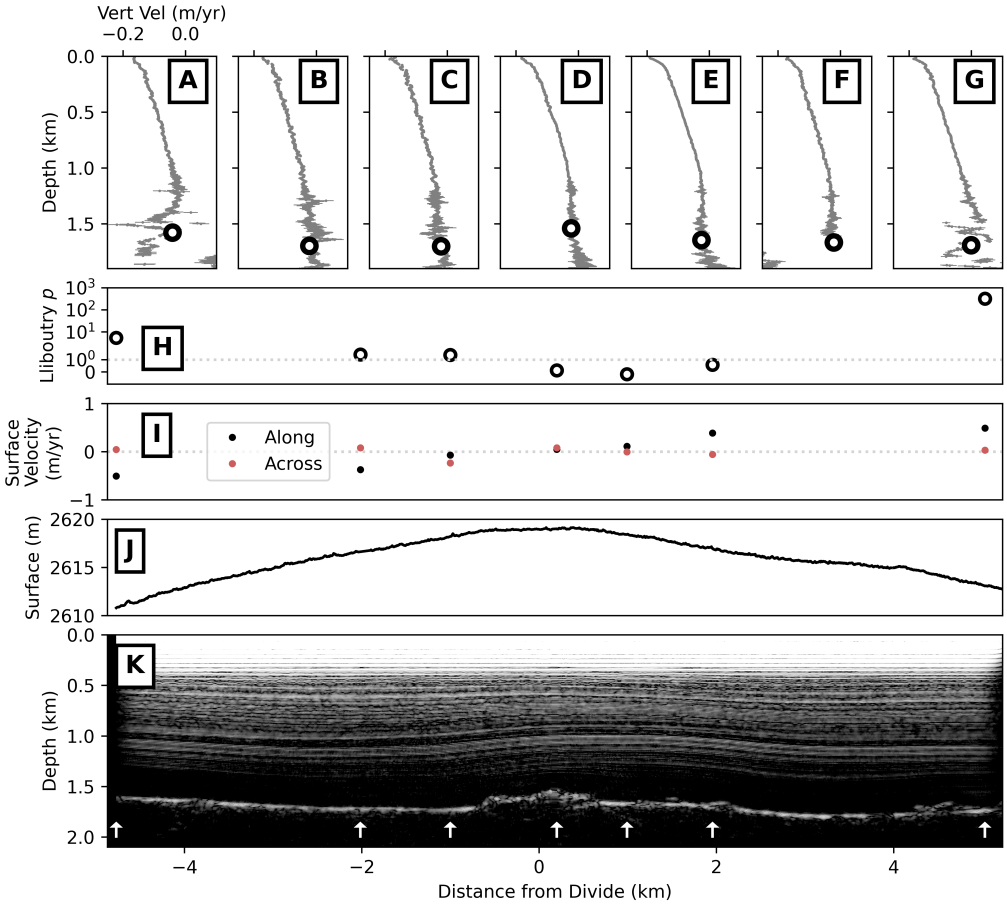

Figure 5.4: Hercules Dome Summit present-day ice dynamics and geometry measurements along profile A-A' in Figure 5.3. A-G) Vertical velocity profiles measured with ApRES at 7 sites. Gray dots represent a calculated velocity within a single range bin, with the associated horizontal line the uncertainty within that bin. The larger black dot is the vertical velocity of the interpreted bed reflector. Note that the ApRES phase offset measurement gives a relative velocity, which has been referenced to the surface accumulation rate as described in the text. H) Vertical velocity optimization to the Lliboutry (1979) p value (equation 5.4) for each ApRES profile (A-G). I) Surface velocity measured with repeat GNSS acquisition. J) Surface elevation profile measured with kinematic GNSS profiling. K) Ice-penetrating radar profile. White arrows correspond to ApRES site locations (A-G).

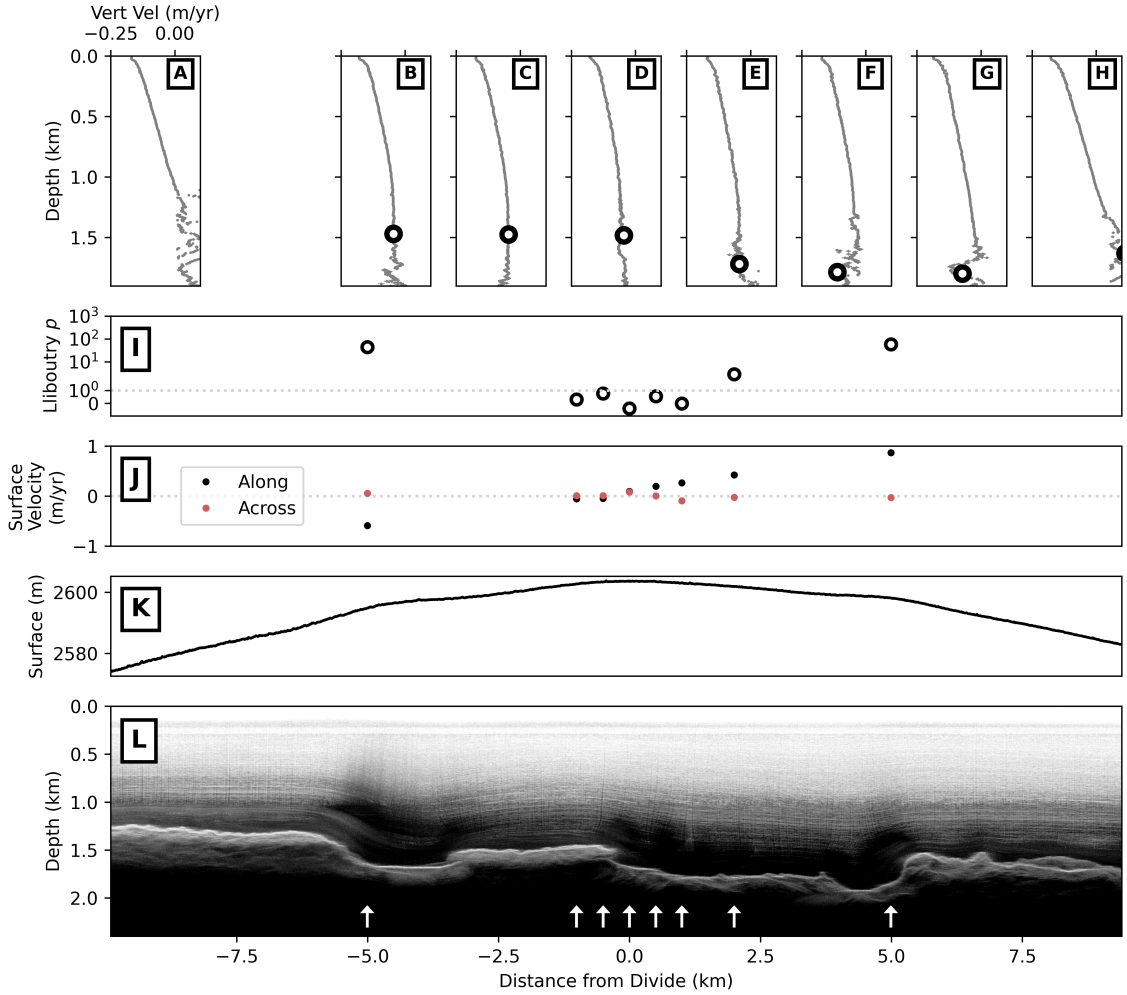

Figure 5.5: Hercules Dome Belt present-day ice dynamics and geometry measurements along profile B-B' in Figure 5.3. Figure layout and design are as in Figure 5.4.

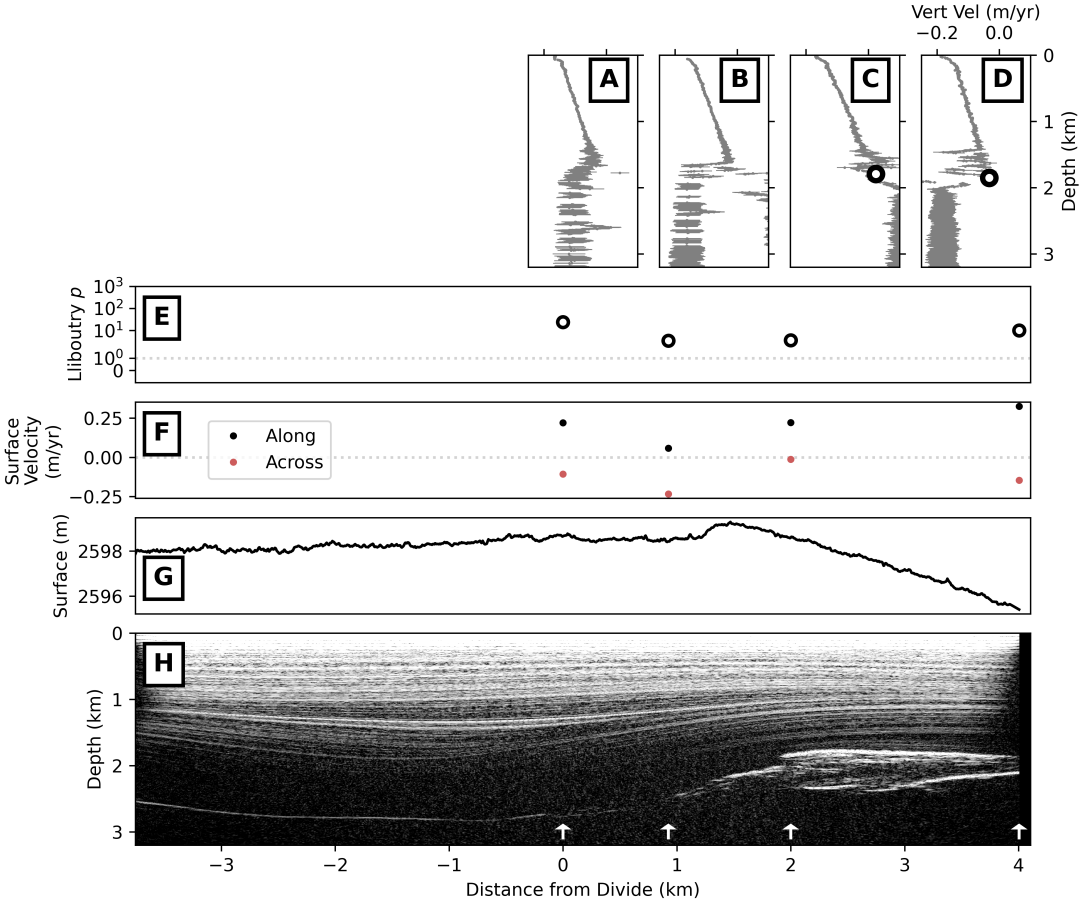

Figure 5.6: East Dome present-day ice dynamics and geometry measurements along profile C-C' in Figure 5.3. Figure layout and design are as in Figure 5.4.

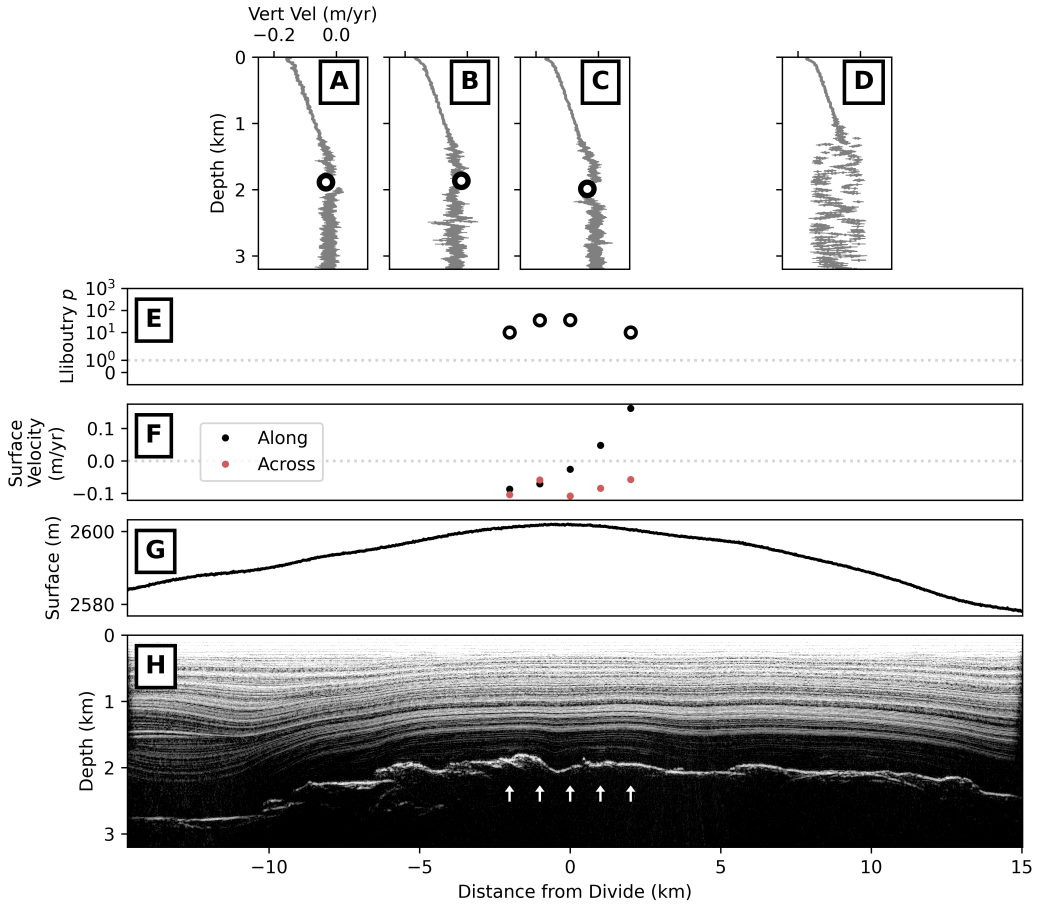

Figure 5.7: South Ridge present-day ice dynamics and geometry measurements along profile D-D' in Figure 5.3. Figure layout and design are as in Figure 5.4.

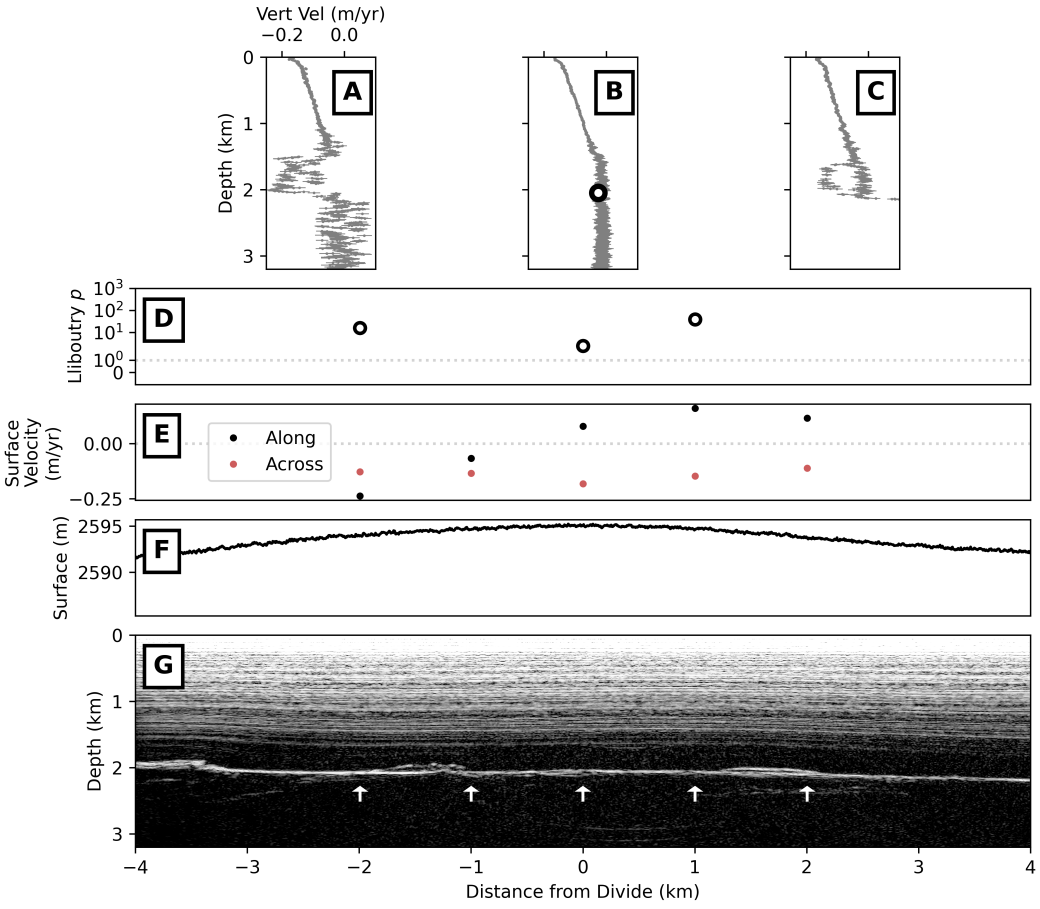

Figure 5.8: South Ridge present-day ice dynamics and geometry measurements along profile E-E' in Figure 5.3. Figure layout and design are as in Figure 5.4.

seem to be dominated by effects from a rough bed and dipping internal layers (Hills, Christianson, Hoffman, et al., 2022), and those in the thickest ice even lose coherence for deep reflectors, giving no interpretable vertical velocity for the lower ice column.

At the Summit, 7 vertical velocity profiles form a 10-kilometer transect across the divide (Figure 5.4). The 4 profiles from the divide and to the grid north were published with a preliminary interpretation in a prior study (Fudge et al., 2022). The additional 3 profiles to the grid south do not qualitatively change the original interpretation presented there. That is, the vertical velocity profiles are most linear ('flank-like' flow) away from the divide (Figures 5.4A and 5.4G) and most nonlinear ('divide-like' flow) toward the divide, especially slightly north of the divide (Figures 5.4D and 5.4E). This distinction is shown quantitatively in the optimized p values (Figure 5.4H) where the most nonlinear profiles (smallest p) are at and just north of the divide.

The Belt has similar vertical velocities to the Summit. Here, 8 profiles were measured, with closer site spacing (500-meter) near the divide than the transect at the Summit. The divide effect present in the Summit transect is also present here. All velocity profiles within 1 kilometer of the divide are similar, and all are nonlinear (Figures 5.5B-F). Any trend among those near-divide profiles is more likely associated with bed features (see Figure 5.5L) than a variation in the divide effect. Extending away from the divide, the profile at 2 km (Figure 5.5G) is trending toward linear, and those furthest from the divide (Figures 5.5A and 5.5H) are *super*linear. In other words, those two profiles have reversed curvature, with an increasing strain rate near the bed. This result is not physical (strain rate should not increase near the bed), rather we suggest that it is an artifact of the measurement technique as has been discussed previously (Hills, Christianson, Hoffman, et al., 2022), and that it indicates increased vertical shear at those locations.

The two transects along South Ridge are 6 km, shorter than at the Summit and Belt (extending only 2 km in either direction of the surface divide). Vertical velocity profiles here are more consistent with one another, all being approximately linear. The ice column is also thicker here, so deep reflections are lost due to low coherence between ApRES acquisitions. If there is a nonlinear effect of divide-like flow, it is not observable due to this loss of coherence.

At East Dome, vertical velocities are again approximately linear and again coherence is lost in the deepest layers of the thick ice column. Here, no divide effect is observed which is not surprising since the surface divide is weak. The greatest vertical strain rate is at the site 2 km to the grid north

of the surface divide, which is directly over the edge of the large bedrock trough.

5.3.4 ApRES Polarimetry

The general characteristics of each polarimetry acquisition are similar (Figure 5.9). The co-polarized phase delay is approximately 0 for near-surface reflections which is expected since it depends on the propagation distance through the ice. Phase gradients are also weak in the uppermost $\sim$500 m. Again, this is expected since snow is deposited randomly (isotropic) and near-surface ice has not been sufficiently strained to develop a girdle COF. At least one dipole node is observed in every acquisition, although the depth, orientation, magnitude, and directionality are different for each. For most acquisitions, the depth of the first co-polarized dipole node is $\sim$700-1200 m.

A striking qualitative difference in acquisitions is in the phase gradient directionality between sites to the grid west (Summit and Belt) and sites to the grid east (East Dome and South Ridge). While the interpreted XPE-axis orientation is approximately grid north-south for all, the phase gradient is opposite, implying a 90-degree rotation of the girdle. In other words, the H-polarization comes to be aligned with the maximum girdle axis (instead of the V-polarization as in the case at Summit), so H propagates slower than V and the HH-VV phase gradient is negative (positive in the case of the Summit). This observation is made clearer in Figure 5.10 where the interpreted girdle orientations are shown for each site across the surveyed area.

For the Summit and Belt regions, where most of the polarimetry experiments were conducted, the interpreted girdle orientations indicate fabric development and alignment consistent with north-south spreading perpendicular to the divide (Figures 5.10B and 5.10C). Differences between acquisitions within these regions are subtle and require a quantitative comparison (Figure 5.11). Seven sites form a transect across the divide at the Summit. From those sites, the strongest calculated girdle strengths are at the divide and 1 kilometer north of the divide, and the weakest girdles are at the sites furthest from the divide. Another seven sites form a transect along the divide at the Summit. These sites have more consistent phase gradients than the across-divide transect, with one prominent outlier to the grid east (toward the Belt). That location has a slight negative phase gradient in the near surface and a deeper dipole node with positive phase gradient. Finally, eight sites form a transect across the divide at the Belt. Overall, this transect is less characteristic of a divide effect

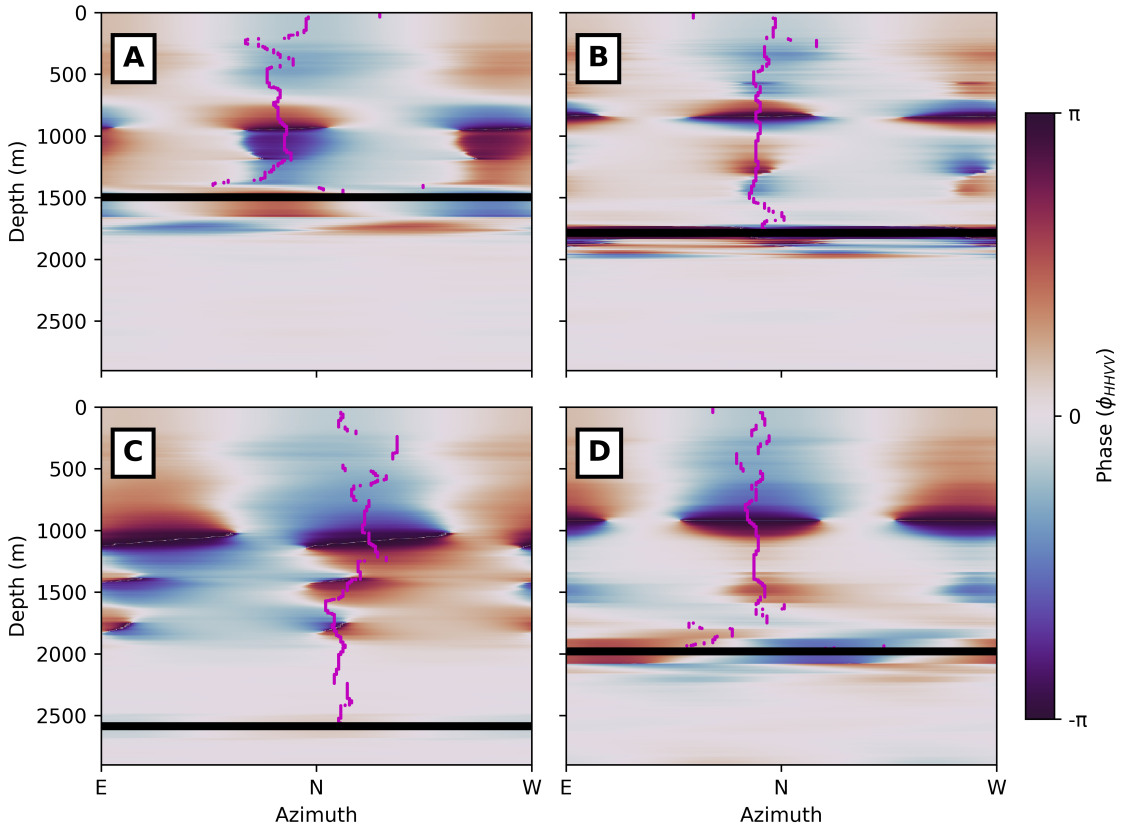

Figure 5.9: Polarimetric interferograms for each region: the Summit (A), the Belt (B), East Dome (C), and South Ridge (D). The colormap is the co-polarized phase delay, as calculated in equation 5.8. The magenta dots are the XPE axis orientation for each range bin, as calculated in equation 5.6.

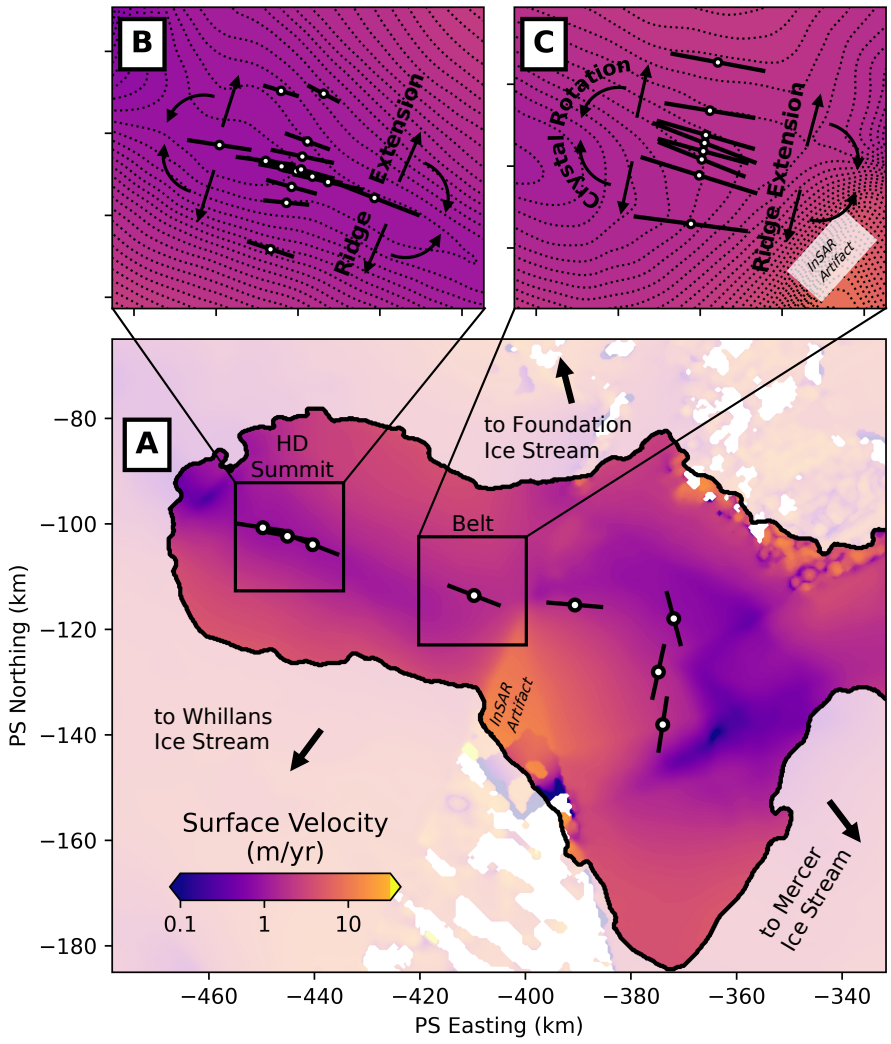

Figure 5.10: A map view of ApRES polarimetry results. Dots show polarimetry acquisition locations with lines indicating the inferred maximum girdle axis (line orientation) and representative girdle strength (line length). The base map is ice surface velocity (Mouginot et al., 2019). The surface velocities are shown here as a reference but should not be over interpreted, they are known to be problematic at these slow flow speeds as can be seen by the labeled InSAR Artifact.

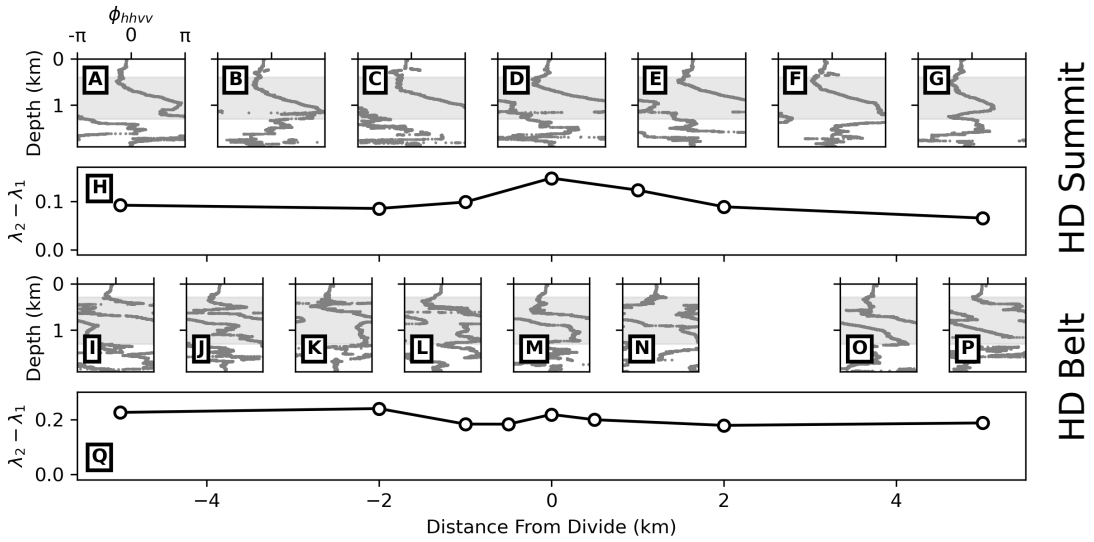

Figure 5.11: ApRES polarimetry results from individual sites forming two separate transects across the surface divide, first at the Summit (top 2 rows) and second at the Belt (bottom 2 rows). Co-polarized phase profiles are plotted for measured phase delay along the XPE axis at each location (A-G; I-P). Each gray dot represents a single phase calculation (equation 5.8) for a single range bin, and for the azimuth bin of the XPE. H and Q) Maximum girdle strength for each profile, calculated from the phase gradient (equation 5.9) within the depth range shown by the gray box in each panel.

than the transect at the summit. There is a slight increase in girdle strength at the divide, but even greater strength to the grid south. Additionally, the typical girdle strength here is ∼double that at the Summit (see the change in y-axis between Figure 5.11H and 5.11Q).

5.4 Model Analysis

In this section we contextualize the geophysical results with a mathematical model. This modeling enables us to relate measured strain rates (both vertical and surface strain) to COF results from polarimetry. We use it to simulate the timescales on which a vertical girdle could be established under the present-day strain regime at Hercules Dome, and how long it would take to overprint the COF from a historical strain regime. The primary COF results of interest here are: 1) the measured girdle strength at Summit as compared to the measured strain rates at summit; 2) the difference in girdle strength between the Summit transect and the Belt transect; and 3) the divide effect at Summit.

The model is a continuum representation of crystal *c* axes in spectral coordinates which evolves in time based on an input stress/strain regime (Rathmann et al., 2021; Rathmann & Lilien, 2021) (see Section 2.1.2 for details). We assume idealized dislocation glide along the basal plane, $\iota = 1$. In model experiment 1, we explore parameter space for the other two unconstrained model inputs, rotational diffusivity, Ω, and dynamic recrystallization rate factor, Γ_0, in an ensemble of simulations for the representative timescale to COF stabilization. In model experiment 2, we fix the values for Ω and Γ_0, representative at Hercules Dome, varying only the strain regime to compare with the measured girdle strength and divide effect.

5.4.1 Model Experiment 1 – COF Evolution Timescale

In order to extend the measured COF to an interpretation of past ice dynamics, we must first know the timescale on which COF evolves. COF is a result of cumulative strain, integrated over time. Lab results show that COF begins to effect ice deformation at approximately $\mathscr{E} = 0.1$ (Budd & Jacka, 1989), so a COF should be measurable at that stage. Given sufficient time in a steady strain regime, the COF will eventually converge onto some stable state. The time to stabilization depends on the strain rate as well as the two unconstrained model parameters that we are going to explore

here, Ω and Γ_0. For generalizability to many ice-sheet settings, we will discuss 'time' in terms of a characteristic time, $t = t \times \dot{\mathscr{E}}$.

For each model iteration in the parameter-sensitivity test, we start with an isotropic parcel of ice, applying a constant strain rate through time, and simulating how the COF develops (Figure 5.12). In the extreme case with no rotational recrystallization, $\Omega = 0$, and no dynamic recrystallization, $\Gamma_0 = 0$, The stable COF will have *all* crystals perfectly aligned with the applied strain regime. In any more realistic case, the COF converges onto some state where the rate of lattice rotation and the rate of recrystallization balance one another. We define the *characteristic stabilization time* as that characteristic time, t, at which the COF has developed to within $\frac{1}{e}$ of its stable state.

We run simulations from isotropic to steady COF for a range of parameter values, and in four separate strain regimes: confined compression, unconfined compression, unconfined extension, and simple shear (Figure 5.13). The resulting stabilization times range from 0.5-1.2. In the compression regimes, greater recrystallization leads to a faster stabilization time, but in extension and simple shear the opposite is true. Richards et al. (2021) showed that $\Omega \approx 0.15$ and does not have a strong temperature dependence. Assuming that is the case, the characteristic time for cold ice (small Γ_0) in compression (i.e. ice dome or divide) is ~0.9, or $t = \frac{0.9}{\dot{\mathscr{E}}}$. Unconfined extension is not a realistic ice-sheet setting so is not considered further. In Simple Shear, recrystallization strengthens the COF state, shifting toward more of a vertical pole and less of a girdle (instead of damping as in compression), so added recrystallization increases the time to stabilization. For cold ice in simple shear (i.e. vertical shear deformation over frozen bedrock) stabilization times will be lower, ~0.7. For warm or temperate ice in simple shear (i.e. horizontal shear in a shear margin) stabilization times are slightly higher, ~0.75.

5.4.2 Model Experiment 2 – Divide COF

As a second model experiment, we simulate COF evolution in a synthetic divide profile, with depth (age) in the vertical and distance from the divide (varying strain regime) in the horizontal. There are two objectives in this experiment, neither of which is to recreate the full strain history of an ice sample nor to perfectly match the results of our polarimetry measurements. The first objective is to test the difference in divide dynamics on COF between a confined divide with no radial spreading

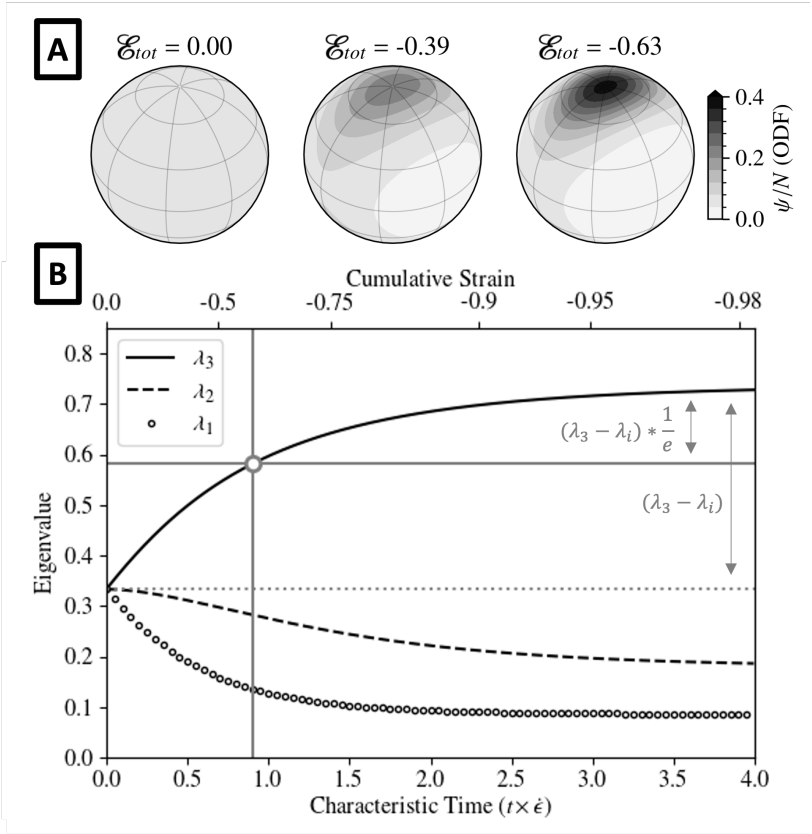

Figure 5.12: An example COF evolution for compression in the vertical, z, and confined in x. A) A series of ordinary distribution functions (ODF) in a spherical projection as the vertical girdle develops. B) Eigenvalues through the time evolution from isotropic to steady-state girdle. Here, time is plotted as the *characteristic time* (multiplied by the strain rate). The large grey dot shows the selected time to stabilization.

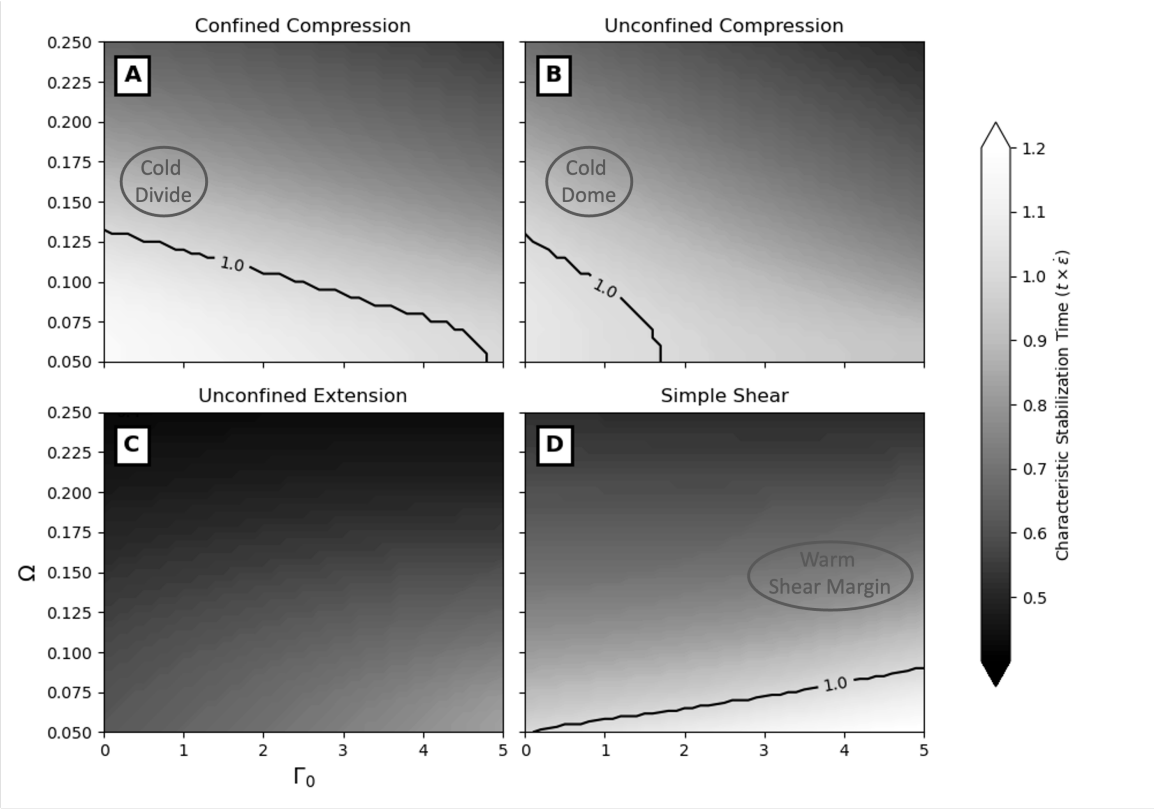

Figure 5.13: A parameter sensitivity test for time to stabilization in COF evolution. For each of the four strain regimes (confined compression (A); unconfined compression (B); unconfined extension (C); and simple shear (D)) we show the characteristic time to stabilization over a range of rotational diffusivities, Ω, and recrystallization rate factors, Γ_0.

(i.e. the Belt) and an unconfined divide (i.e. the Summit). The second objective is to test the timescale for COF evolution when the divide is migrating. In these experiments we fix the model parameters, Ω and Γ_0. We use the empirically-derived value for rotational diffusivity, $\Omega = 0.15$ (Richards et al., 2021). Based on the cold ice temperatures, -40 in the upper ice column (Fudge et al., 2022), we assume that the component of dynamic recrystallization is small, $\Gamma_0 = 0.5$ (Richards et al., 2021). For warm ice at depth, this term likely becomes dominant and is a point of discussion below.

For each of the stable divide (non migrating) scenarios, we assign a strain regime to a given location based on its distance from the divide. Importantly, we do not consider advective transport by ice flow away from the divide in this model, we only simulate the COF evolution over time based on the assigned strain regime (as in model experiment 1) then convert age to depth based on an established depth-age model (Fudge et al., 2022). For both stable cases, confined and unconfined, the longitudinal extension (along the profile) and vertical compression are constant, both in distance along the profile and in time. In the confined case, we only consider changes in vertical shear away from the divide which we increase linearly based on the measured surface velocities and the ice thickness (assuming ice is frozen to the bed). In the unconfined case, we include the linear increase in shear from before, but also another term for radial spreading. This term also increases linearly away from the divide based on the dome geometry. The simulated girdle strengths for these stable divide scenarios are shown in Figure 5.14. For the confined case, the increased shear away from the divide acts together with longitudinal extension to increase the girdle strength. For the unconfined case, the increasing radial extension acts to dampen the girdle away from the divide.

For the migrating divide scenario, we take a similar approach to the stable cases above but change the strain regime in time based on a moving divide position. Here, we consider an unconfined divide, so both shear and radial extension increase with distance away from the divide location. The COF state is initialized with a divide position 5 km away from the stable cases (i.e. the end of the simulated profile). We migrate the divide position to be coincident with the stable cases (i.e. at 0 km) over the time range between 7 and 3 thousand years ago, with the fastest migration rate at 5 thousand years ago. We choose this timing based on the paleo-ice-sheet model results which are described in the next section. In Figure 5.15 we show both the final state and the comparison between this state and its stable counterpart from Figure 5.14B. Even though the final strain regime

for the migrating divide scenario is identical to the strain regime for the stable scenario, there is a residual which persists from the pre-migrated state.

5.5 Discussion

5.5.1 Geophysical Measurement Trends and Outliers

At the Summit, Belt, and South Ridge, the present-day ice dynamics, as measured by repeat ApRES and repeat surface GNSS measurements, and COF girdle orientation and strength, as measured by ApRES polarimetry, are all generally consistent with the ice-surface geometry. These dynamic trends also correspond to the bed geometry, with the surface divide location commonly situated over a bedrock high (especially at the Summit). The measured surface velocities point away from the surface divide (Figures 5.4I and 5.5J). Vertical velocity profiles trend from sublinear (small p) at the surface divide toward linear away from the divide (as expected for divide-to-flank flow). The COF indicates a divide-aligned girdle (i.e. east-west girdle for sites at the Summit and Belt but north-south Girdle for sites at South Ridge). The magnitude and depth of the girdle varies slightly between sites, but the orientation is consistent with the divide orientation for every site. This COF result is consistent with the present-day dynamics since a divide-aligned girdle would develop under conditions where vertical thinning and cross-divide spreading are the dominant flow patterns. The observed girdle has greater magnitude at the Belt as compared to the Summit. This is also not surprising since the Belt is confined extension in a single direction (across the divide) whereas the Summit has a more dome-like shape so will have some amount of divide parallel spreading (especially for sites further from the divide).

The only significant outlier to the consistency between ice dynamics and ice geometry for sites at the Summit, Belt, and South Ridge are the two vertical velocity profiles in the ApRES transect at the Belt, those furthest from the divide at 5 km north/south. Those two profiles are *super*linear (opposite curvature from those profiles nearest the divide). We interpret these two sites as having a Lagrangian effect from dipping reflectors since they are both situated at the edge of a large bedrock bump, and they have a significantly faster surface velocity than sites nearer to the divide. As explained by Hills, Christianson, Hoffman, et al. (2022), vertical shear results in horizontal motion over dipping reflectors which causes an apparent vertical velocity.

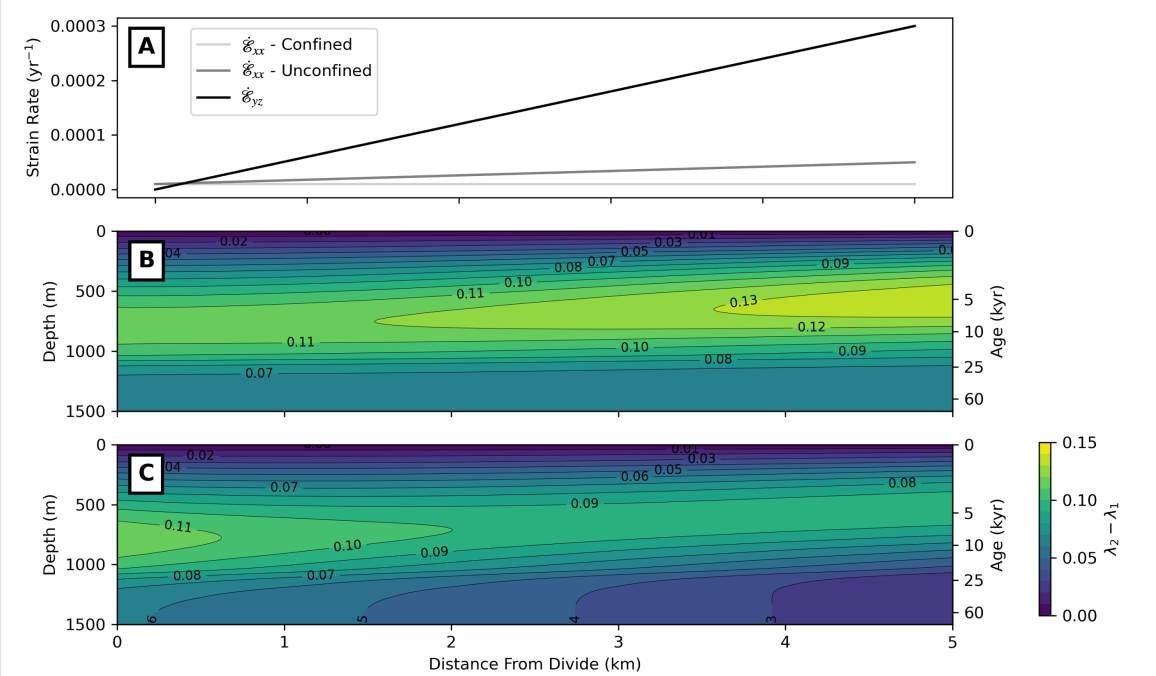

Figure 5.14: COF girdle strength in a divide profile for two distinct strain regimes. A) Variable strain rates for both regimes, vertical shear is the same in each. B) Confined divide with only vertical shear away from divide (no radial spreading). C) Unconfined divide with both vertical shear and radial spreading away from divide. This model does not include any ice flow outward from the divide.

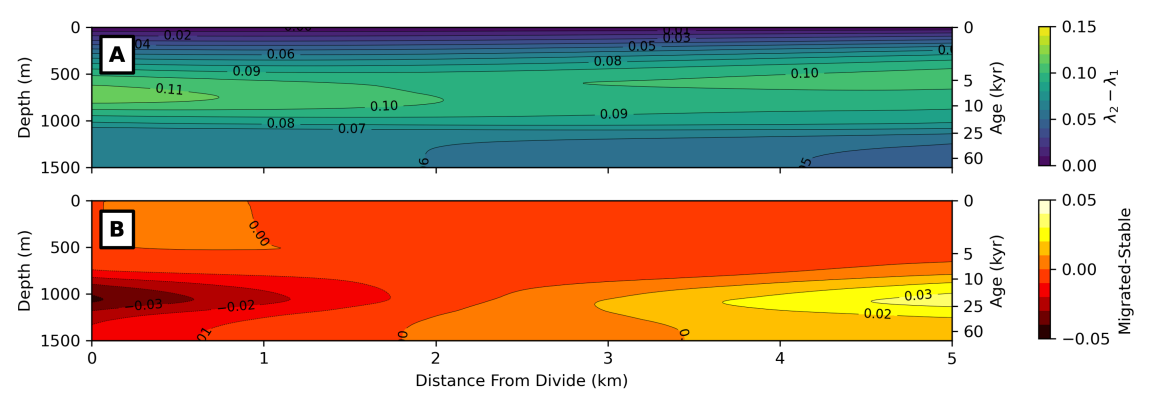

Figure 5.15: A) COF girdle strength (as in Fig. 5.14) after divide migration from 5-0 km (right to left) over a span 3-7 thousand years ago. B) Difference between migrated divide (A) and stable divide (Fig. 5.14B). This model does not include any ice flow outward from the divide.

The present and past ice dynamics at East Dome are not consistent with the ice-surface geometry in the way that the other three regions are. Ice surface velocity and englacial vertical velocity seem to be controlled by the bedrock trough. Surface velocities point along the trough, and the vertical strain rate is greatest at the trough edge. Only one polarimetry acquisition was taken at East Dome and that was directly over the trough. The resulting phase gradient at this site is more uniform with depth than at any other site, with three dipole nodes along the XPE axis (Figure 5.9C). The unmatched uniformity and deeper observed dipole nodes may be a result of this being the site with the thickest ice column. The girdle itself is aligned perpendicular to the trough axis which is consistent with longitudinal extension along the axis of the trough.

At the Summit, one feature stands out as reminiscent of the bedrock trough at East Dome. This feature is most prominent in the airborne radar profile to the grid northwest of Summit (Figure 5.3), but upstream indications of channelization into a bedrock trough are seen in both the ground-based profiling radar and as a subtle expression in the surface topography (Horlings et al., in Prep). The direction of the trough would be consistent with routing flow toward Western Foundation Ice Stream even though there is no obvious indication of that in the surface velocity measurements. There is also no indication of a shift in the girdle axis toward this western trough. In Section 5.5.3 we discuss the relevance of this trough in terms of the COF evolution timescales.

5.5.2 Interpreting Polarimetric Ice-Penetrating Radar

We limit our interpretation of the radar polarimetry measurements to a single characteristic girdle orientation (Figure 5.10) and a magnitude of the phase-depth gradient (Figure 5.11), both extracted from the middle of the ice column. More intricate interpretations of the polarimetric interferograms (as in Figure 5.9) are possible, including variations with depth through the ice column. For instance, prior studies have interpreted rotations of the vertical girdle (Brisbourne et al., 2019; T. M. Jordan et al., 2022) as well as effects from anisotropic scatterers (Drews et al., 2012). Since our measurements indicate a relatively simple vertical girdle, we do not pursue any additional analysis. Still, we discuss the nuance of such interpretations and how they can be made difficult by radar system characteristics, wave depolarization, phase decorrelation, and scattering versus path effects.

Girdle rotation through the ice column implies some change to the ice dynamics over time,

whether that be a macroscpic change in ice-sheet behavior (Brisbourne et al., 2019) or an ice parcel being advected into a new flow regime (T. M. Jordan et al., 2022). Precisely measuring a girdle rotation with radar polarimetry is made difficult since the wave received at the surface is an integration of path effects for all the ice through which it travelled. If the girdle rotation is not by *exactly* 90°, then the wave depolarizes with respect to the rotated girdle. Phase interpretation below the girdle rotation depends not only on the strength and orientation of the new girdle but also on the integrated effects from above. Model results from Ershadi et al. (2022) Figure 3 demonstrate this effect well, with the modeled XPE below 3000 m continuing to rotate even with a constant girdle axis. In this case, if the phase gradient were interpreted along the XPE (as we do in equation 5.9) it would repeatedly change sign, indicating rapid 90-degree girdle rotations.

We only consider anisotropic path effects (i.e. permittivity), but the scattering interfaces can be anisotropic as well. For example, if englacial bubbles or crystal grain boundaries are elongated in one direction over another they can cause a reflection to bias toward one polarization over another (Drews et al., 2012). Anisotropic scattering reduces the azimuthal spacing between dipole nodes in the polarimetric interferogram (Fujita et al., 2006) which we do not observe.

Our polarimetry acquisitions lose phase coherence deep in the ice column (below $\sim$1500 m). Several factors likely contribute to this loss of signal. Warm temperatures for the deepest ice could lead to increased recrystallization and a less interpretable COF. Alternatively, significant phase delay could eventually cause decorrelation across range bins, but the co-registration method (Zeising et al., 2023) did not improve our result. Instead, we argue that those deep reflections are sufficiently attenuated to no longer be comparable, especially since the time-based ApRES interference seems to lose coherence at a similar depth.

5.5.3 Glacial-to-Holocene Ice Dynamics

The persistence of Hercules Dome as a steady divide between the Ross and Ronne ice shelves depends on 1) the ice flux into the system by precipitation, 2) the ice flux out of the system, in this case mainly by melt and discharge in the Ross and Ronne ice shelves, and 3) the ice flux from the divide region toward the ice shelves, controlled by the underlying bedrock topography and mechanics of glacier sliding. When the ice sheet is in equilibrium these three fluxes equal one another and the

position of features like the ice divide remain fixed. When one of these fluxes change, for instance during the climate transition out of the LGM, the other fluxes change in response and the position of features like divides and the grounding zone of marine outlet glaciers can change. In this section, we look at how climate changes associated with the transition out of the LGM affect the ice sheet's interior flux response. We consider whether there was mismatch in deglaciation timing between the two ice shelves and whether that could have had an upstream effect, potentially shifting or rotating the divide at Hercules Dome.

Deglaciation of the Ross and Ronne Ice Shelves

At the LGM, sea level was $\sim$100 m lower than today (Spratt & Lisiecki, 2016). Ice likely filled the Ross and Weddell seas, and paleo-ice-sheet models predict that ice was grounded all the way to the continental shelf break (Golledge et al., 2012). As the global climate warmed into the Holocene, models and observations both show that the grounding line retreated toward today's position, but the precise timing and detailed characteristics of this retreat for both the Ronne and Ross Ice shelves are not well known. We briefly describe the history of retreat hypotheses formulated from models and observations before describing the simulated ice-sheet configurations we use to understand the strain histories modeled for Hercules Dome and how these modeled strain rates compare to the strain histories we construct from ApRES polarimetry observations.

Historical ice geometries and grounding-line locations can be constrained by a variety of measurements and proxies including exposure ages (Stone et al., 2003), sea level change and isostatic rebound (Mitrovica et al., 2001), subglacial sediments and geomorphology (Kingslake et al., 2018), englacial structures (Conway et al., 2002; M. Siegert et al., 2013), to name a few. From these observations of the past configuration of the ice sheet, we know that the Antarctic Ice Sheet was at least hundreds of m thicker during LGM, both in the Weddell Sea (Ronne) (Nichols et al., 2019) and in the Ross (Anderson et al., 2014). Some studies show quasi-steady and monotonic grounding line retreat through the Holocene and to today's position (Conway et al., 1999), but more recent work suggests that the maximum extent of retreat was actually further inland than today ('over-retreat') (Johnson et al., 2022). The extent of over-retreat and subsequent readvance is thought to be larger on the Ross side in the Siple Coast than the Ronne side (Kingslake et al., 2018). The bed geometry

of the Siple Coast ice streams is flat, so the grounding line can be expected to move relatively large distances even with only subtle changes in the ice dynamics or climate forcing.

Nearest to Hercules Dome, the best ice geometry constraints come from two sources, exposure ages and subglacial lake sediments. There are two dated sites with exposure ages, one in the mountains adjacent to Reedy Glacier (Todd et al., 2010) and another in the Pensacola Mountains adjacent to Foundation Ice Stream (Balco et al., 2016). Although with some inconsistencies, these two studies both show a peak thickness between $\sim$17-9 thousand years ago (depending on the specific outcrop) and the Ross side has slightly earlier onset of thinning, 13 ka at Quartz Hills (Todd et al., 2010) as opposed to 11 ka at Thomas and Williams Hills (Balco et al., 2016). Subglacial lake sediments were recovered from both Whillans and Mercer, the two ice stream drainages which form the grid east-west divide at South Ridge. Critically to the story of stability at South Ridge, dated sediments from these subglacial lakes both indicate grounding line retreat past their location to a maximum extent $\sim$7.5 thousand years ago followed by readvance (Venturelli et al., 2020).

Paleo-Ice-Sheet Model Output

Ice-sheet models are forced with paleo climate conditions to simulate past ice-sheet states. Since both the forcings and the model parameters are uncertain, there is a wide spread in modeled results, not only between models but also for a given parameter space within a single model. In particular for the the model output discussed here, the relatively coarse grid resolution does not adequately capture the relief that defines much of the subglacial landscapes beneath Hercules Dome. We do not interpret any model result as the truth of a past ice-sheet state. Rather, we use these model results to understand the downstream forcing from ice-shelf melting and discharge (i.e. the ice flux *out* of the system mentioned above). Specifically, we investigate the range in deglaciation scenarios for the Ross and Ronne ice shelves and use those to discuss draw down forcing and associated divide stability at Hercules Dome. In the next section, we will use our geophysical measurements and the COF model investigation from Section 5.4 to tie the draw down forcing (based on paleo model output) to the possibility of upstream impact felt at Hercules Dome.

As far as we know, there are three paleo-Antarctic-Ice-Sheet model investigations which have simulated continental-scale paleo-ice dynamics. The first is static in time for the ice dynamic state

at the LGM (Golledge et al., 2012). They showed that ice-dynamic effects were important for the deglaciation history out of LGM. The second is the full dynamic history of the Antarctic Ice Sheet since the last interglacial period (DeConto & Pollard, 2016). The third, and most recent, is a two-part study with the first a full dynamic history spanning two glacial cycles (Albrecht et al., 2020a) and the second a 256-member ensemble for deglaciation into the Holocene (Albrecht et al., 2020b). Their model ensemble spans a range of physically plausible values for four unknown model parameters: ice-flow enhancement (viscosity), basal-sliding plasticity, precipitation forcing, and mantle viscosity (for isostatic rebound). They selected a 'best-fit' ensemble member based on misfit to measurements of both present-day and paleo conditions.

We use the model output from Albrecht et al. (2020b) to interpret ice-dynamic conditions between the Ross and Ronne ice shelves as a framing for interpretation of draw down and associated divide stability at Hercules Dome. We focus on their parameter ensemble analysis during the Holocene deglaciation (Albrecht et al., 2020b) as opposed to the model forcing from earlier glacial cycles (Albrecht et al., 2020a). For each of the model ensemble members and at every time snapshot we use the ice-surface geometry to extract a surface divide location between ice that flows into the Ross Ice Shelf and ice that flows into the Ronne Ice Shelf (Figure 5.16). Between 20-10 thousand years ago, the majority of ensemble members have a divide position within 2 grid cells of the best-fit case and stable through time. Into the Holocene, after 10 thousand years ago, the ensemble spread of divide positions increases, and even the best-fit case moves in time by 10's of km (Figures 5.16D and 5.16E). Next, we extract an ice-sheet cross section along flow lines from Hercules Dome into the Ronne and Ross Ice shelves. We plot the cross-section geometry for every ensemble member to highlight the relative retreat times of the two ice shelves (Figure 5.16F). In most cases, the Ross Ice Shelf retreats from its LGM state *before* the Ronne. In many cases, including the best-fit ensemble member, the Ross retreats beyond its present-day position, to readvance from $\sim$5 thousand years ago to now. This result agrees with the exposure dating (Balco et al., 2016; Todd et al., 2010) and geochemical evidence from subglacial lakes (e.g. Venturelli et al., 2020) discussed above.

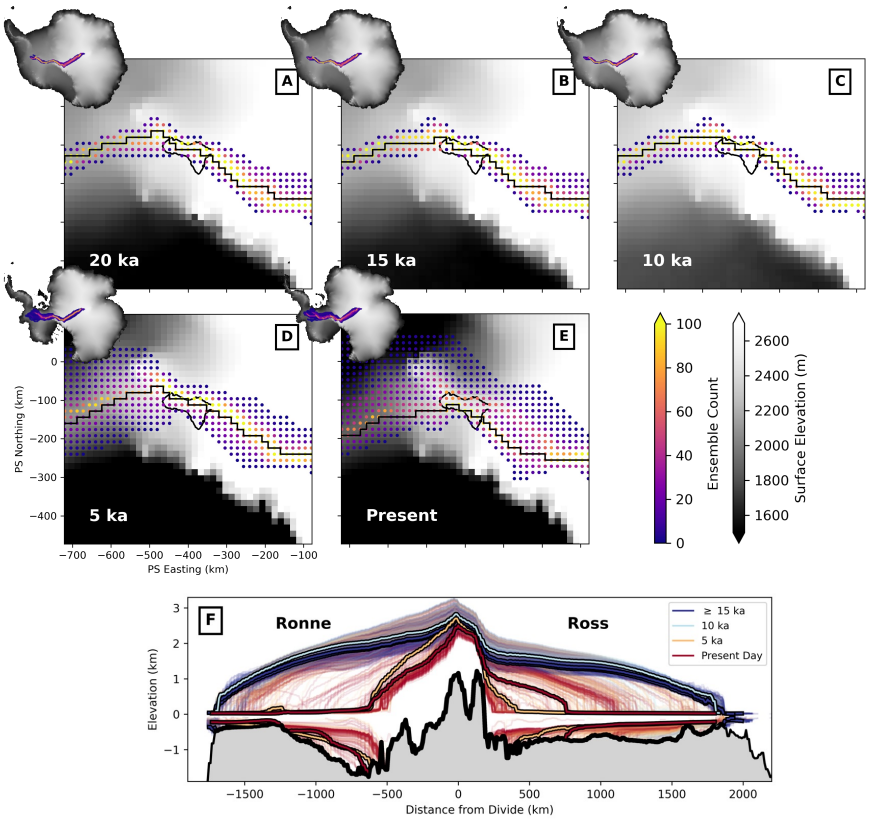

Figure 5.16: Ice geometry and divide migration from a deglaciation model ensemble (Albrecht et al., 2020b). A-E) Modeled 'best-fit' surface elevation at Hercules Dome (frame) and for the Antarctic Continent (inset) at the time shown. Colored dots show the number of model ensemble members with their surface divide position at that location, again for the time shown, and the black line is the 'best-fit' divide. F) Modeled ice-sheet cross sections along flow lines centered at Hercules Dome and extending onto the Ronne and Ross ice shelves. The full model ensemble is shown, with the 'best-fit' solution in bold lines. Gray is bedrock.

Measured and Modeled COF

Based on the paleo-ice-sheet model output interpreted above, Hercules Dome divide migration and rotation are *plausible* during deglaciation out of LGM based on differential timing of retreat in the Ross and Ronne ice shelves. However, the timing of those interpreted dynamic changes are within the COF evolution timescales that we model in Section 5.4, using the measured present-day strain rates at Hercules Dome. We argue that timescale is order $1/\dot{\mathscr{E}}$, or $\sim$10 thousand years at Hercules Dome. Therefore, we expect the present-day COF to preserve a signal from the deglaciation history, including any potential divide rotation or migration. We would expect dynamic changes to be observable in the ApRES polarimetry measurements, but our results at the Summit indicate consistent ice flow and divide stability. We argue that the divide position is stabilized by the underlying bedrock ridge which is significantly smaller than the spatial resolution of the paleo-ice-sheet model.

Of course, based on a COF timescale of $\sim$10 thousand years we cannot make any explicit claim on stability into the last glacial period or earlier. Instead, we argue our result lends to a process interpretation, that the Hercules Dome Summit position is stabilized by bed roughness, and see no reason why that interpretation should not be extended to longer timescales. Moreover, this interpretation is consistent with recent findings that the bed geometry in the broader 'bottleneck' area has a strong influence on ice flow (K. Winter et al., 2018).

The difference in divide dynamics between the Summit (unconfined divide or 'dome') and the Belt (confined divide) are evident in the polarimetry measurements and shown to be reproducible by the divide profile modeling experiment. Since the confined divide is only subject to changes in shear, it should not be expected to have a more prominent girdle at the divide itself than away from it. Therefore, changes in the divide position would not be measurable in the COF either. The unconfined divide, on the other hand, does show a prominent divide effect in the polarimetry measurements and divide migration should therefore be measurable. A similar divide effect was observed in a transect of polarimetry acquisitions at Dome C (Ershadi et al., 2022).

The ApRES polarimetry result from East Dome indicates consistent extension along the axis of the bedrock trough. The trough has therefore steered ice flow at least through deglaciation and continues to do so today. The same is not true of the trough-like feature to the grid northwest of the Summit. The polarimetry acquisition nearest to that trough does not indicate any influence by the

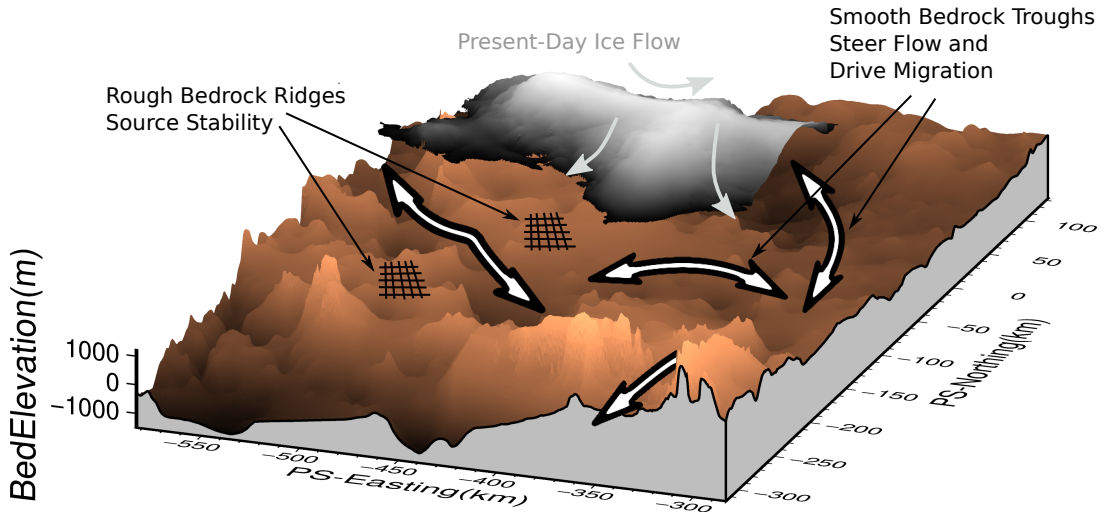

Figure 5.17: An illustration of how bed topography drives ice dynamics in the bottleneck. The extruded bed and surface topography are from BedMachine Antarctica (Morlighem et al., 2020).

trough on ice flow. The girdle at that location is oriented approximately east-west, in line with the regional polarimetry results and interpreted north-south spreading at the Summit.

5.5.4 Toward an Ice-Core Drilling Site

To constrain the state of the WAIS during the last interglacial period using an ice core at Hercules Dome, interglacial ice must have been preserved at this location and hopefully in a uniform manner for ease of the depth-age interpretation. A drilling location with little to no vertical shear and with maximal steadiness through time is desirable. Prior work constrained the thermodynamic setting (Fudge et al., 2022) in order to rule out sites which may be melting and losing the oldest ice from the base. Here, we aimed to further constrain the ice-dynamic history in order to select a site with the simplest and most easily interpretable ice-flow history.

East Dome is defined by the large bedrock trough which is known to have redirected ice flow in the deep past, ∼millions of years ago (Hoffman et al., in Review). Our surface velocity and ApRES vertical velocity results imply that the trough is still steering ice flow today. The prominent girdle aligned perpendicular to the trough implies along-trough extension which has been at least

quasi-steady through the Holocene. Moreover, the thickest ice in the surveyed area is at East Dome which means it is the most likely to have a melting bed at least in isolated locations if not more regionally. While basal melt does not strictly rule out the persistence of interglacial ice, it decreases the likelihood and spatial variability in melting could lead to additional complications in the ice flow. For all of these reasons, East Dome is not a good location to recover interpretable interglacial ice.

The Belt and South Ridge are both extensional ridges, with South Ridge having some down-ridge (southward) flow component. While neither of these sites has any obvious criteria for exclusion in the way that East Dome does, they also do not stand out as optimal candidates for an ice-core drilling site. Both are underlain by some bed roughness, but rather than a discrete bedrock ridge coincident with the surface divide, the underlying peaks and valleys span multiple ice thicknesses from the divide. ApRES vertical velocities are approximately uniform in the case of South Ridge, and seemingly bed-controlled at the Belt. The measured girdle orientations are consistently divide aligned at both locations, and stronger than at the Summit, but do not exhibit the divide effect that those at the Summit do (i.e. gradually decreasing girdle strength away from the divide).

Of the HD subregions discussed here, the Summit is the most optimal as an ice-core drilling site. The underlying bedrock ridge is narrow and directly underneath the surface divide, implying that it pins the divide location. The measured vertical velocity profiles demonstrate a progression from divide-like to flank-like flow, and that signal is dominant over any bed-controlled effect. The measured girdle orientations are uniform across the region and aligned with present-day ice flow. Our modeling demonstrates that if the divide had rotated at this site, which could have been inferred from the paleo ice-sheet models, that signal would have been preserved within today's COF.

5.6 Chapter Summary

In this study, we used geophysical measurements to constrain the past and present ice-flow dynamics at Hercules Dome. We use our results as constraints for models of COF evolution and electromagnetic wave propagation. We find that the measured COF is in line with the present-day ice flow that is largely controlled by the bed geometry. The COF evolution timescale under present-day strain rates is approximately 10 thousand years, so any significant change to the divide orientation or po-

sition can be ruled out. As in prior work, we argue that the bed geometry largely controls ice flow at Hercules Dome, especially the Foundation and Patuxent troughs as well as one large trough running through East Dome. Here though, we find that more subtle bed topography, $\sim$100 m of relief over $\sim$1 kilometer, pins the surface divide in a way that continental-scale ice-sheet models could not have predicted. In total, our geophysical results and model experiments indicate that the Summit is the maximally stable region at Hercules Dome and is most suitable for ice-core drilling.

Chapter 6

Conclusion and Outlook

The broad motivation for this dissertation was to contribute toward the body of knowledge which places ever-improving constraints on the uncertainty of future sea-level rise. Specifically, I do this by studying past ice-sheet states and contextualizing them within the current understanding of ice physics and ice-sheet dynamics. While none of the research studies presented here directly assign any new quantitative update to the uncertainty for future sea-level projections, each adds insight into how ice-sheets change, the processes that govern their thermal and physical structure, and the specific historical behavior for several glacier systems across Antarctica. Moreover, this work is a part of the broader effort to extend what we can measure with ice-penetrating radar. More sophisticated measurements will eventually lead to better constraints on ice properties and ice dynamics at the continental scale as I explore below.

6.1 Review of Study Findings

In Chapter 3, we found that ice streams and their shear margins are colder than previously thought, corresponding to thermal shear hardening by 3-3.5 times. In order to accommodate the observed ice velocities, some other shear-softening mechanism must be effective in ice-stream shear margins (e.g. material damage or COF softening). The timescale for thermal evolution is long, but damage and COF can evolve much faster, especially in a high-stress/strain environment like an ice-stream shear margin. We therefore argue that shear margins are less stable and more susceptible to migration than previously thought.

In Chapter 4, we found that the regional ice dynamics near South Pole are stable in their current configuration, contradicting prior work which had suggested an upstream extension of Support Force Ice Stream during the Last Glacial Maximum. Our argument here is mainly driven by two findings. First, that the ice-bed interface is regionally 'bright' in terms of its radar reflectivity, both on and off South Pole Lake, implying that the ice-bed interface is thawed everywhere. Second, we improved the state of ice temperature modeling for this region, adding a better estimate of the ice thickness, the newly reconstructed paleo-climate variables from South Pole Ice Core, and a process effect in the downstream advective heat sink. With an improved temperature model, we find that the measured ice temperatures from the ICECUBE array (Price et al., 2002) are in fact consistent with the subglacial lake 15 km away (previously thought inconsistent). For this region, far inland away from the ice-sheet margin, we find that the ice dynamics are stable. Ice flow and thermodynamic stability both indicate that the sediment under South Pole Lake could be a strong candidate for coring to sample climate history for a time period to which ice cores do not extend.

In Chapter 5, we found that the surface-divide position at Hercules Dome Summit aligns with a divide effect in the present-day englacial ice velocities and that the divide effect has been consistent during Holocene deglaciation. In contrast with paleo-ice-sheet model output, which implied divide migration by 10's of km, our geophysical measurements indicate that the present and past flow are consistent with a stable divide position. Both vertical velocities (from ApRES interferometry) and COF (from ApRES polarimetry) indicate a divide effect, or 'Raymond Effect', and our COF modeling demonstrated that the effect would have taken approximately 10 thousand years of consistent divide location to become established in this way. We therefore argue that the subtle bed roughness at Hercules Dome Summit has led to relative stability during deglaciation, while prior work has shown that ice flow in the nearby bedrock troughs may be what accommodates differential draw down (K. Winter et al., 2018). As before, these results suggest *more* dynamic behavior within the relatively fast-flowing areas and *less* dynamic behavior at the inland locations.

For this body of work overall, I found that the dynamic areas are susceptible to faster changes than currently predicted, and that the inland slower-flowing areas change slowly even more so than what has been argued in other studies. We can use these findings to make an argument for future change in ice-sheet geometry and subsequent sea-level rise. The susceptibility of shear margins to fast-evolving processes (e.g. COF over temperature) leads to the argument that areas which are

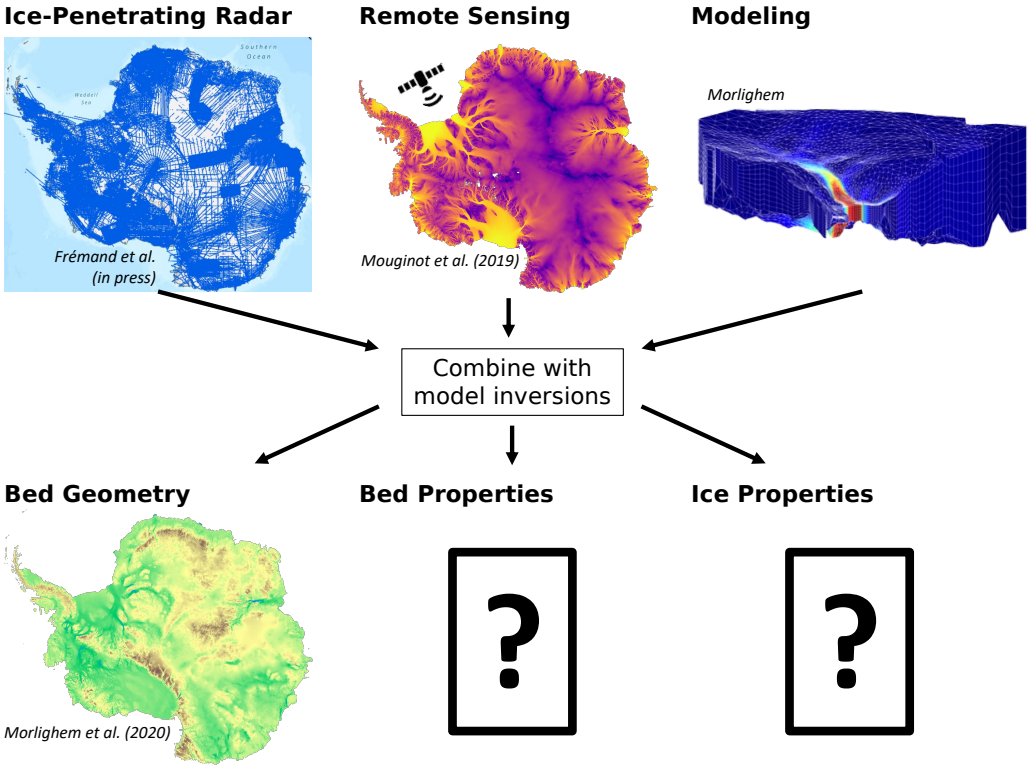

Figure 6.1: A schematic of my outlook for future research in physical glaciology. Ice-penetrating radar can be used together with remote-sensing data in a paired model inversion to infer distributed data products. We have seen this work well for bed-geometry products (Morlighem et al., 2020). Future work will include more sophisticated radar measurements, like those presented in this dissertation (e.g. radar power and phase interpretations), again coupled with remote-sensing data to build out continental-scale products for bed properties (e.g. geology and hydrology) and internal ice properties (e.g. temperature and COF).

already susceptible to collapse (e.g. Thwaites glacier and much of West Antarctica) may be able to migrate inland and collapse the region faster since 'soft' shear margins could be setup faster than with temperature alone as a softening mechanism. Conversely, our findings of inland stability in East Antarctica suggest that those high divides are more dependent on local and possibly upstream effects than on the ice streams drawing at them from below. The evidence that we find for dramatic change in these areas are on more like geologic timescales (i.e. tens to hundreds of thousands of years).

6.2 Looking Forward in Physical Glaciology

A theme in this dissertation has been to use novel measurement techniques in ice-penetrating radar, those beyond the geometric interpretation from timing of radio echos. In Chapter 3, I used radar attenuation, Chapter 4 radar reflectivity, and Chapter 5 radar interferometry and polarimetry. I am not alone in doing so, much of the radio glaciology community is innovating on what can be measured with the radar instrument (Schroeder, 2023). To close, I want to briefly discuss how I believe these types of measurements will be used in the near future for more comprehensive constraints on continental-scale ice-dynamic interpretation and sea-level projections.

To frame this discussion, it is useful to first look at a recent example of how *conventional* radar data (i.e. bed-reflection timing for ice thickness) is now being used together with remote-sensing data in paired model inversions. *BedMachine* (Morlighem et al., 2020; Morlighem et al., 2017) is a project which uses the aggregated ice thickness measurements from ice-penetrating radar, *BedMap* (Fretwell et al., 2013; Lythe & Vaughan, 2001), and satellite measurements of ice-surface velocity (Mouginot et al., 2019) together in a numerical model inversion using the Ice-Sheet System Model (ISSM) (Figure 6.1). The *BedMachine* model inversions leverage the incompressibility of ice and mass conservation (Morlighem et al., 2011) to estimate the bed geometry, even in areas which it has not been directly measured. The result is a continent-wide data product for bed geometry which gives the most precise estimates to date of total ice volume and potential sea-level rise from the two ice sheets.

One idea for an analogous model inversion would be in using the imaged englacial stratigraphy. Holschuh et al. (2017) showed that the slope of englacial layers is tied to both present-day and his-

torical ice dynamics, sometimes in ways that are not measurable at the ice-sheet surface. As with the bed geometry, measured layer slopes could be used alongside satellite remote-sensing observations in a paired model inversion for ice-dynamic interpretation.

Future work in physical glaciology will bring all the radar measurements explored in this dissertation (radar timing, power, and phase) into model inversions like those above. Radar timing maps ice geometry and englacial stratigraphy, both used to infer ice flow. Significant innovations are underway in how precisely we can map the ice-bed interface (Holschuh et al., 2020). Reflected radar power is associated with reflector properties, such as wetness at the ice-sheet bed, and will be used to map subglacial geology and hydrology. Power is also dependent on internal properties (mainly temperature) through attenuation which will be disentangled from the reflector properties using these model inversions. Continental-scale radar phase interpretations will take more measurements, but radar instruments being deployed today are generally phase capable (Li et al., 2022; Miller et al., 2020). Eventually, we will be able to map vertical motion, crystal orientation fabric, and more throughout the Antarctic and Greenland ice sheets. Again, those measurements will be coupled to satellite remote sensing and used in multivariate model inversions. All these efforts will directly lead to constraints on past, present, and future ice flow, as well as projections for future sea-level rise.

References

Albrecht, T., Winkelmann, R., & Levermann, A. (2020a). Glacial-cycle simulations of the Antarctic Ice Sheet with the Parallel Ice Sheet Model (PISM)-Part 1: Boundary conditions and climatic forcing. *Cryosphere*, *14*(2), 599–632. https://doi.org/10.5194/tc-14-599-2020

Albrecht, T., Winkelmann, R., & Levermann, A. (2020b). Glacial-cycle simulations of the Antarctic Ice Sheet with the Parallel Ice Sheet Model (PISM)-Part 2: Parameter ensemble analysis. *Cryosphere*, *14*(2), 633–656. https://doi.org/10.5194/tc-14-633-2020

Alley, R. B. (1988). Fabrics in Polar Ice Sheets: Development and Prediction. *Science*, *240*(4851), 493–495.

Alley, R. B. (1992). Flow-law hypotheses for ice-sheet modeling. *Journal of Glaciology*, *38*(129).

Alley, R. B., Gow, A. J., & Meese, D. A. (1995). Mapping c-axis fabrics to study physical processes in ice. *Journal of Glaciology*, *41*(137), 197–203. https://doi.org/10.1017/S0022143000017895

An, M., Wiens, D. A., Zhao, Y., Feng, M., Nyblade, A., Kanao, M., Li, Y., Maggi, A., & Lévêque, J. J. (2015). Temperature, lithosphere-asthenosphere boundary, and heat flux beneath the Antarctic Plate inferred from seismic velocities. *Journal of Geophysical Research: Solid Earth*, *120*(12), 8720–8742. https://doi.org/10.1002/2015JB011917

Anderson, J. B., Conway, H., Bart, P. J., Witus, A. E., Greenwood, S. L., McKay, R. M., Hall, B. L., Ackert, R. P., Licht, K., Jakobsson, M., & Stone, J. O. (2014). Ross Sea paleo-ice sheet drainage and deglacial history during and since the LGM. *Quaternary Science Reviews*, *100*, 31–54. https://doi.org/10.1016/j.quascirev.2013.08.020

Archer, D., Kheshgi, H., & Maier-Reimer, E. (1997). Multiple timescales for neutralization of fossil fuel CO2. *Geophysical Research Letters*, *24*(4), 405–408.

Arcone, S. A. (1995). Numerical studies of the radiation patterns of resistively loaded dipoles. *Journal of Applied Geophysics*, *33*(1-3), 39–52. https://doi.org/10.1016/0926-9851(95)90028-4

Ashmore, D. W., Bingham, R. G., Ross, N., Siegert, M. J., Jordan, T. A., & Mair, D. W. (2020). Englacial Architecture and Age-Depth Constraints Across the West Antarctic Ice Sheet. *Geophysical Research Letters*, *47*(6), 1–11. https://doi.org/10.1029/2019GL086663

Balco, G., Todd, C., Huybers, K., Campbell, S., Vermeulen, M., Hegland, M., Goehring, B. M., & Hillebrand, T. R. (2016). Cosmogenic-nuclide exposure ages from the Pensacola Mountains adjacent to the foundation ice stream, Antarctica. *American Journal of Science*, *316*(6), 542–577. https://doi.org/10.2475/06.2016.02

Bassis, J. N., Berg, B., Crawford, A. J., & Benn, D. I. (2021). Transition to marine ice cliff instability controlled by ice thickness gradients and velocity. *Science*, *372*(6548), 1342–1344. https://doi.org/10.1126/science.abf6271

Beem, L. H., Cavitte, M. G. P., Blankenship, D. D., Carter, S. P., Young, D. A., Muldoon, G. R., Jackson, C. S., & Siegert, M. J. (2017). Ice-flow reorganization within the East Antarctic Ice Sheet deep interior. *Geological Society London Special Publications*, *461*(1). https://doi.org/10.1144/SP461.14

Bentley, C. R., Lord, N., & Liu, C. (1998). Radar reflections reveal a wet bed beneath stagnant Ice Stream G and a frozen bed beneath ridge BG5 West Antarctica. *Journal of Glaciology*, *44*(146), 149–156. https://doi.org/10.1017/S0022143000002434

Bernal, J. D., & Fowler, R. H. (1933). A theory of water and ionic solution, with particular reference to hydrogen and hydroxyl ions. *The Journal of Chemical Physics*, *1*(8), 515–548.

Bingham, R. G., & Siegert, M. J. (2007). Radio-Echo Sounding Over Polar Ice Masses. *Journal of Environmental & Engineering Geophysics*, *12*(1), 47–62. https://doi.org/10.2113/JEEG12.1.47

Bingham, R. G., Siegert, M. J., Young, D. A., & Blankenship, D. D. (2007). Organized flow from the South Pole to the Filchner-Ronne ice shelf: An assessment of balance velocities in interior East Antarctica using radio echo sounding data. *Journal of Geophysical Research: Earth Surface*, *112*(3), 1–11. https://doi.org/10.1029/2006JF000556

Bintanja, R., Van De Wal, R. S., & Oerlemans, J. (2005). Modelled atmospheric temperatures and global sea levels over the past million years. *Nature*, *437*(7055), 125–128. https://doi.org/10.1038/nature03975

Bjerrum, N. (1951). *Structure and Properties of Ice*. https://books.google.com/books?id=XfknzwEACAAJ

Bogorodsky, V., Bentley, C., & Gudmandsen, P. (1985). *Radioglaciology*. D. Reidel Publishing Company.

Bougamont, M., Christoffersen, P., Price, S. F., Fricker, H. A., Tulaczyk, S., & Carter, S. P. (2015). Reactivation of Kamb Ice Stream tributaries triggers century-scale reorganization of Siple Coast ice flow in West Antarctica. *Geophysical Research Letters*, *42*(20), 8471–8480. https://doi.org/10.1002/2015GL065782

Brennan, P. V., Lok, L. B., Nicholls, K., & Corr, H. (2014). Phase-sensitive FMCW radar system for high-precision antarctic ice shelf profile monitoring. *IET Radar, Sonar and Navigation*, *8*(7), 776–786. https://doi.org/10.1049/iet-rsn.2013.0053

Brisbourne, A. M., Martín, C., Smith, A. M., Baird, A. F., Kendall, J. M., & Kingslake, J. (2019). Constraining Recent Ice Flow History at Korff Ice Rise, West Antarctica, Using Radar and Seismic Measurements of Ice Fabric. *Journal of Geophysical Research: Earth Surface*, *124*(1), 175–194. https://doi.org/10.1029/2018JF004776

Budd, W., & Jacka, T. (1989). A review of ice rheology for ice sheet modelling.

Budyko, M. I. (1969). The effect of solar radiation variations on the climate of the Earth. *Tellus A: Dynamic Meteorology and Oceanography*, *21*(5), 611. https://doi.org/10.3402/tellusa.v21i5.10109

Carslaw, H., & Jaeger, J. (1959). *Conduction of Heat in Solids* (Second). Oxford University Press.

Carter, S. P., Blankenship, D. D., Peters, M. E., Young, D. A., Holt, J. W., & Morse, D. L. (2007). Radar-based subglacial lake classification in Antarctica. *Geochemistry Geophysics Geosystems*, *8*(3), 1–20. https://doi.org/10.1029/2006GC001408

Casella, G., & Berger, R. L. (2002). *Statistical Inference* (Second). Wadsworth Group.

Catania, G. A., Scambos, T. A., Conway, H., & Raymond, C. F. (2006). Sequential stagnation of Kamb Ice Stream, West Antarctica. *Geophysical Research Letters*, *33*(14), 2–5. https://doi.org/10.1029/2006GL026430

Christianson, K., Jacobel, R. W., Horgan, H. J., Alley, R. B., Anandakrishnan, S., Holland, D. M., & Dallasanta, K. J. (2016). Basal conditions at the grounding zone of Whillans Ice Stream, West Antarctica, from ice-penetrating radar. *Journal of Geophysical Research: Earth Surface*, *121*, 1954–1983. https://doi.org/10.1002/2015JF003806

Christianson, K., Jacobel, R. W., Horgan, H. J., Anandakrishnan, S., & Alley, R. B. (2012). Subglacial Lake Whillans - Ice-penetrating radar and GPS observations of a shallow active reservoir beneath a West Antarctic ice stream. *Earth and Planetary Science Letters*, *331-332*, 237–245. https://doi.org/10.1016/j.epsl.2012.03.013

Christianson, K., Peters, L. E., Alley, R. B., Anandakrishnan, S., Jacobel, R. W., Riverman, K. L., Muto, A., & Keisling, B. A. (2014). Dilatant till facilitates ice-stream flow in northeast Greenland. *Earth and Planetary Science Letters*, *401*, 57–69. https://doi.org/10.1016/j.epsl.2014.05.060

Christoffersen, P., Tulaczyk, S., Wattrus, N. J., Peterson, J., Quintana-Krupinski, N., Clark, C. D., & Sjunneskog, C. (2008). Large subglacial lake beneath the Laurentide Ice Sheet inferred from sedimentary sequences. *Geology*, *36*(7), 563–566. https://doi.org/10.1130/G24628A.1

Colgan, W., Sommers, A., Rajaram, H., Abdalati, W., & Frahm, J. (2015). Earth's future considering thermal-viscous collapse of the Greenland ice sheet. *Earth's Future*, *3*, 252–267. https://doi.org/10.1002/2015EF000301.Abstract

Conway, H., Catania, G., Raymond, C. F., Gades, A. M., Scambos, T. A., & Engelhardt, H. (2002). Switch of flow direction in an antarctic ice stream. *Nature*, *419*(6906), 465–467. https://doi.org/10.1038/nature01081

Conway, H., Hall, B. L., Denton, G. H., Gades, A. M., & Waddington, E. D. (1999). Past and future grounding-line retreat of the West Antarctic Ice Sheet. *Science*, *286*(5438), 280–283. https://doi.org/10.1126/science.286.5438.280

Corr, H., Moore, J. C., & Nicholls, K. W. (1993). Radar absorption due to impurities in Antarctic ice. *Geophysical Research Letters*, *20*(11), 1071–1074. https://doi.org/10.1029/93GL01395

CReSIS. (2021). cresis-toolbox (Version 3.0.1).

Cuffey, K. M., & Paterson, W. (2010). *The physics of glaciers*. https://doi.org/10.1016/0016-7185(71)90086-8

Cuffey, K. M., Clow, G. D., Alley, R. B., Stuiver, M., Waddington, E. D., & Saltus, R. W. (2016). Large Arctic Temperature Change at the Wisconsin-Holocene Glacial Transition. *Science*, *270*(5235), 455–458. https://doi.org/10.1126/science.270.5235.455

Dahl-Jensen, D. (1989). Steady thermomechanical flow along two-dimensional flow lines in large grounded ice sheets. *Journal of Geophysical Research*, *94*(B8), 355–362. https://doi.org/10.1029/JB094iB08p10355

Dahl-Jensen, D., & Johnsen, S. J. (1986). Paleotemperatures still exist in the Greenland ice sheet. *Nature*, *320*, 250–252. https://doi.org/10.1038/320129a0

Dahl-Jensen, D., Mosegaard, K., Gundestrup, N., Clow, G. D., Johnsen, S. J., Hansen, A. W., & Balling, N. (1998). Past temperatures directly from the Greenland Ice Sheet. *Science*, *282*(5387), 268–271. https://doi.org/10.1126/science.282.5387.268

DeConto, R. M., & Pollard, D. (2016). Contribution of Antarctica to past and future sea-level rise. *Nature*, *531*(7596), 591–597. https://doi.org/10.1038/nature17145

Deconto, R. M., & Pollard, D. (2003). Rapid Cenozoic glaciation of Antarctica induced by declining atmospheric CO2. *Nature*, *421*, 245–249. https://doi.org/https://doi.org/10.1038/nature01290

Dixon, D. A. (2007). Antarctic Mean Annual Temperature Map. *U.S. Antarctic Program (USAP) Data Center*. https://doi.org/https://doi.org/10.7265/N51C1TTV.

Dowdeswell, J. A., & Evans, S. (2004). Investigations of the form and flow of ice sheets and glaciers using radio-echo sounding. *Reports on Progress in Physics*, *67*(10), 1821–1861. https://doi.org/10.1088/0034-4885/67/10/R03

Drews, R., Eisen, O., Steinhage, D., Weikusat, I., Kipfstuhl, S., & Wilhelms, F. (2012). Potential mechanisms for anisotropy in ice-penetrating radar data. *Journal of Glaciology*, *58*(209), 613–624. https://doi.org/10.3189/2012JoG11J114

Dütsch, M., Steig, E. J., Blossey, P. N., & Pauling, A. G. (2023). Response of water isotopes in precipitation to a collapse of the West Antarctic Ice Sheet in high-resolution simulations with the Weather Research and Forecasting Model. *Journal of Climate*. https://doi.org/10.1175/JCLI

Eisen, O., Wilhelms, F., Nixdorf, U., & Miller, H. (2003a). Identifying isochrones in GPR profiles from DEP-based forward modeling. *Annals of Glaciology*, *37*, 344–350. https://doi.org/doi:10.3189/172756403781816068

Eisen, O., Wilhelms, F., Nixdorf, U., & Miller, H. (2003b). Revealing the nature of radar reflections in ice: DEP-based FDTD forward modeling. *Geophysical Research Letters*, *30*(5). https://doi.org/10.1029/2002GL016403

Eisen, O., Wilhelms, F., Steinhage, D., & Schwander, J. (2006). Improved method to determine radio-echo sounding reflector depths from ice-core profiles of permittivity and conductivity. *Journal of Glaciology*, *52*(177), 299–310. https://doi.org/10.3189/172756506781828674

Elderfield, H., Ferretti, P., Greaves, M., Crowhurst, S., McCave, I. N., Hodell, D., & Piotrowski, A. M. (2012). Evolution of ocean temperature and ice volume through the mid-Pleistocene climate transition. *Science*, *337*(6095), 704–709. https://doi.org/10.1126/science.1221294

Elsworth, C. W., & Suckale, J. (2016). Rapid ice flow rearrangement induced by subglacial drainage in West Antarctica. *Geophysical Research Letters*, *43*(22), 697–11. https://doi.org/10.1002/2016GL070430

Engelhardt, H. (2004a). Ice temperature and high geothermal flux at Siple Dome, West Antarctica, from borehole measurements. *Journal of Glaciology*, *50*(169), 251–256. https://doi.org/10.3189/172756504781830105

Engelhardt, H. (2004b). Thermal regime and dynamics of the West Antarctic ice sheet. *Annals of Glaciology, Vol 39, 2005*, *39*, 85–92. https://doi.org/10.3189/172756404781814203

Epifanio, J. A., Brook, E. J., Buizert, C., Edwards, J. S., Sowers, T. A., Kahle, E. C., Severinghaus, J. P., Steig, E. J., Winski, D. A., Osterberg, E. C., Fudge, T. J., Aydin, M., Hood, E., Kalk, M., Kreutz, K. J., Ferris, D. G., & Kennedy, J. A. (2020). The SP19 chronology for the South Pole Ice Core - Part 2: Gas chronology, Δage, and smoothing of atmospheric records. *Climate of the Past*, *16*(6), 2431–2444. https://doi.org/10.5194/cp-16-2431-2020

Ershadi, M. R., Drews, R., Martín, C., Eisen, O., Ritz, C., Corr, H., Christmann, J., Zeising, O., Humbert, A., & Mulvaney, R. (2021). Polarimetric radar reveals the spatial distribution of ice fabric at domes in East Antarctica. *The Cryosphere Discussions*, (January), 1–34.

Ershadi, M. R., Drews, R., Martín, C., Eisen, O., Ritz, C., Corr, H., Christmann, J., Zeising, O., Humbert, A., & Mulvaney, R. (2022). Polarimetric radar reveals the spatial distribution of ice fabric at domes and divides in East Antarctica. *Cryosphere*, *16*(5), 1719–1739. https://doi.org/10.5194/tc-16-1719-2022

Farinotti, D., Huss, M., Fürst, J. J., Landmann, J., Machguth, H., Maussion, F., & Pandit, A. (2019). A consensus estimate for the ice thickness distribution of all glaciers on Earth. *Nature Geoscience*, *12*(3), 168–173. https://doi.org/10.1038/s41561-019-0300-3

Fitzpatrick, J. J., Voigt, D. E., Fegyveresi, J. M., Stevens, N. T., Spencer, M. K., Cole-Dai, J., Alley, R. B., Jardine, G. E., Cravens, E. D., Wilen, L. A., Fudge, T. J., & McConnell, J. R. (2014). Physical properties of the WAIS divide ice core. *Journal of Glaciology*, *60*(224), 1140–1154. https://doi.org/10.3189/2014JoG14J100

Fletcher, N. H. (1970). *The Chemical Physics of Ice*. Cambridge University Press.

Fox-Kemper, B., Hewitt, H. T., Xiao, C., Aðalgeirsdóttir, G., Drijfhout, S. S., Edwards, T. L., & Hemer, M. (2021). *Ocean, Cryosphere and Sea Level Change. In Climate Change 2021: The Physical Science Basis. AR6* (tech. rep.). Cambridge, United Kingdom, New York, NY, USA. https://doi.org/10.1017/9781009157896.011

Frederikse, T., Landerer, F., Caron, L., Adhikari, S., Parkes, D., Humphrey, V. W., Dangendorf, S., Hogarth, P., Zanna, L., Cheng, L., & Wu, Y. H. (2020). The causes of sea-level rise since 1900. *Nature*, *584*(7821), 393–397. https://doi.org/10.1038/s41586-020-2591-3

Fretwell, P., Pritchard, H. D., Vaughan, D. G., Bamber, J. L., Barrand, N. E., Bell, R., Bianchi, C., Bingham, R. G., Blankenship, D. D., Casassa, G., Catania, G., Callens, D., Conway, H., Cook, A. J., Corr, H. F., Damaske, D., Damm, V., Ferraccioli, F., Forsberg, R., … Zirizzotti, A. (2013). Bedmap2: Improved ice bed, surface and thickness datasets for Antarctica. *Cryosphere*, *7*(1), 375–393. https://doi.org/10.5194/tc-7-375-2013

Fudge, T. J., Hills, B. H., Horlings, A. N., Holschuh, N., Christian, J. E., Davidge, L., Hoffman, A. O., O'Connor, G. K., Christianson, K., & Steig, E. J. (2022). A site for deep ice coring at West Hercules Dome : results from ground-based geophysics and modeling. *Journal of Glaciology*, 1–13.

Fudge, T. J., Lilien, D. A., Koutnik, M., Conway, H., Max Stevens, C., Waddington, E. D., Steig, E. J., Schauer, A. J., & Holschuh, N. (2020). Advection and non-climate impacts on the South Pole Ice Core. *Climate of the Past*, *16*(3), 819–832. https://doi.org/10.5194/cp-16-819-2020

Fujita, S., Mae, S., & Matsuoka, T. (1993). Dielectric anisotropy in ice Ih at 9.7 GHz. *Annals of Glaciology*, *17*, 276–280. https://doi.org/10.3189/s0260305500012969

Fujita, S., Maeno, H., & Matsuoka, K. (2006). Radio-wave depolarization and scattering within ice sheets: A matrix-based model to link radar and ice-core measurements and its application. *Journal of Glaciology*, *52*(178), 407–424. https://doi.org/10.3189/172756506781828548

Fujita, S., Matsuoka, T., Ishida, T., Matsuoka, K., & Mae, S. (2000). A summary of the complex dielectric permittivity of ice in the megahertz range and its applications for radar sounding of polar ice sheets. *Physics of Ice Core Records*, 185–212.

Gades, A. M., Raymond, C. F., Conway, H., & Jacobel, R. W. (2000). Bed properties of Siple Dome and adjacent ice streams, West Antarctica, inferred from radio-echo sounding measurements. *Journal of Glaciology*, *46*(152), 88–94. https://doi.org/10.3189/172756500781833467

Giovineto, M. (1960). *South Pole Shallow Firn Annual Cycle Temperatures, USNC-IGY Antarctic Glaciological Data, Field Work 1958 and 1959, Report 825-2-Part IV, April 1960* (tech. rep.).

Glen, J. W. (1955). The Creep of Polycrystalline Ice. *Proceedings of the Royal Society of London A: Mathematical, Physical and Engineering Sciences*, *228*(1175), 519–538. https://doi.org/10.1098/rspa.1955.0066

Gleser, L. J., & Hwang, J. T. (1987). The nonexistence of 100(1-α)% confidence sets of finite expected diameter errors-in-variables and related models. *The Annals of Statistics*, *15*(4), 1351–1362. https://doi.org/10.1214/aos/1176348654

Gödert, G., & Hutter, K. (1998). Induced anisotropy in large ice shields: Theory and its homogenization. *Continuum Mechanics and Thermodynamics*, *10*(5), 293–318. https://doi.org/10.1007/s001610050095

Goldsby, D. L., & Kohlstedt, D. L. (2001). Superplastic deformation of ice: Experimental observations. *Journal of Geophysical Research*, *106*(B6), 11017–11030. https://doi.org/10.1029/2000JB900336

Golledge, N. R., Fogwill, C. J., Mackintosh, A. N., & Buckley, K. M. (2012). Dynamics of the last glacial maximum Antarctic ice-sheet and its response to ocean forcing. *Proceedings of the National Academy of Sciences of the United States of America*, *109*(40), 16052–16056. https://doi.org/10.1073/pnas.1205385109

Gow, A. J., Ueda, H. T., & Garfield, D. E. (1968). Antarctic ice sheet: Preliminary results of first core hole to bedrock. *Science*, *161*(3845), 1011–1013. https://doi.org/10.1126/science.161.3845.1011

Hamilton, G. S. (2002). Mass balance and accumulation rate across Siple Dome, West Antarctica. *Annals of Glaciology*, *35*(December 1998), 102–106. https://doi.org/10.3189/172756402781816609

Hanna, E., Navarro, F. J., Pattyn, F., Domingues, C. M., Fettweis, X., Ivins, E. R., Nicholls, R. J., Ritz, C., Smith, B., Tulaczyk, S., Whitehouse, P. L., & Jay Zwally, H. (2013). Ice-sheet mass balance and climate change. *Nature*, *498*(7452), 51–59. https://doi.org/10.1038/nature12238

Hansen, T. C. (2021). The everlasting hunt for new ice phases. *Nature Communications*, *12*(1), 10–12. https://doi.org/10.1038/s41467-021-23403-6

Harland, W. B. (1964). Critical evidence for a great infra-Cambrian glaciation. *Geologische Rundschau*, *54*(1), 45–61. https://doi.org/10.1007/BF01821169

Harper, J., & Dorn, J. E. (1957). Viscous creep of aluminum near its melting temperature. *Acta Metallurgica*, *5*(11), 654–665. https://doi.org/10.1016/0001-6160(57)90112-8

Harrington, J. a., Humphrey, N. F., & Harper, J. T. (2015). Temperature distribution and thermal anomalies along a flowline of the Greenland Ice Sheet. *Annals of Glaciology*, *56*(70), 98–104. https://doi.org/10.3189/2015AoG70A945

Harrison, W. D., Echelmeyer, K. A., & Larsen, C. F. (1998). Measurement of temperature in a margin of Ice Stream B, Antarctica: implications for margin migration and lateral drag. *Journal of Glaciology*, *44*(148), 615–624. https://doi.org/10.3189/S0022143000002112

Hills, B. H., Christianson, K., Jacobel, R. W., Conway, H., & Petersson, R. (2022). Radar attenuation demonstrates advective cooling at the Siple Coast ice streams. Journal of Glaciology. *Journal of Glaciology*.

Hills, B. H., Christianson, K., Hoffman, A. O., Fudge, T. J., Holschuh, N., Kahle, E. C., Conway, H., Christian, J. E., Horlings, A. N., O'Connor, G. K., & Steig, E. J. (2022). Geophysics and Thermodynamics at South Pole Lake Indicate Stability and a Regionally Thawed Bed. *Geophysical Research Letters*, *49*(2), 1–10. https://doi.org/10.1029/2021GL096218

Hills, B. H., Christianson, K., & Holschuh, N. (2020). A framework for attenuation method selection evaluated with ice-penetrating radar data at South Pole Lake. *Annals of Glaciology*, *61*(81), 1–12. https://doi.org/10.1017/aog.2020.32

Hills, B. H., Harper, J. T., Humphrey, N. F., & Meierbachtol, T. W. (2017). Measured horizontal temperature gradients constrain heat transfer mechanisms in Greenland ice. *Geophysical Research Letters*, *44*, 9778–9785. https://doi.org/10.1002/2017GL074917

Hindmarsh, R. C. A., Leysinger Vieli, G. J. M. C., Raymond, M. J., & Gudmundsson, G. H. (2006). Draping or overriding: The effect of horizontal stress gradients on internal layer architecture in ice sheets. *Journal of Geophysical Research: Earth Surface*, *111*(2). https://doi.org/10.1029/2005JF000309

Hoffman, A., Holschuh, N., Mueller, M., Paden, J. D., Muto, A., Ariho, G., Brigham, C., Christian, J. E., Davidge, L., Heitmann, E., Hills, B., Horlings, A., Morey, S., O'Connor, G., Fudge, T., Steig, E., & Christianson, K. (in Review). Scars of tectonism promote ice-sheet nucleation from Hercules Dome into West Antarctica. *Nature Geoscience*.

Holschuh, N., Christianson, K., Paden, J., Alley, R. B., & Anandakrishnan, S. (2020). Linking postglacial landscapes to glacier dynamics using swath radar at Thwaites glacier, Antarctica. *Geology*, *48*(3), 268–272. https://doi.org/10.1130/G46772.1

Holschuh, N., Christianson, K., & Anandakrishnan, S. (2014). Power loss in dipping internal reflectors, imaged using ice-penetrating radar. *Annals of Glaciology*, *55*(67), 49–56. https://doi.org/10.3189/2014AoG67A005

Holschuh, N., Christianson, K., Anandakrishnan, S., Alley, R. B., & Jacobel, R. W. (2016). Constraining attenuation uncertainty in common midpoint radar surveys of ice sheets. *Journal of Geophysical Research F: Earth Surface*, *121*(10), 1876–1890. https://doi.org/10.1002/2016JF003942

Holschuh, N., Lilien, D. A., & Christianson, K. (2019). Thermal Weakening, Convergent Flow, and Vertical Heat Transport in the Northeast Greenland Ice Stream Shear Margins. *Geophysical Research Letters*, 8184–8193. https://doi.org/10.1029/2019gl083436

Holschuh, N., Parizek, B. R., Alley, R. B., & Anandakrishnan, S. (2017). Decoding ice sheet behavior using englacial layer slopes. *Geophysical Research Letters*, *44*(11), 5561–5570. https://doi.org/10.1002/2017GL073417

Hooijer, A., & Vernimmen, R. (2021). Global LiDAR land elevation data reveal greatest sea-level rise vulnerability in the tropics. *Nature Communications*, *12*(1), 1–7. https://doi.org/10.1038/s41467-021-23810-9

Hooke, R. L. (1976). Near-surface temperatures in the superimposed ice zone and lower part of the soaked zone of polar ice sheets. *Journal of Glaciology*, *16*(74), 302–304.

Horgan, H. J., Anandakrishnan, S., Jacobel, R. W., Christianson, K., Alley, R. B., Heeszel, D. S., Picotti, S., & Walter, J. I. (2012). Subglacial Lake Whillans - Seismic observations of a shallow active reservoir beneath a West Antarctic ice stream. *Earth and Planetary Science Letters*, *331-332*, 201–209. https://doi.org/10.1016/j.epsl.2012.02.023

Horlings, A. N., Davidge, L., Erwin, E., Hills, B. H., Hoffman, A., Holschuh, N., Reusch, D., Kirkpatrick, L., Fudge, T., Steig, E. J., & Christianson, K. (in Prep). Snow accumulation at Hercules Dome, Antarctica during the last 420 years. *Geophysical Research Letters*.

Howat, I. M., Porter, C., Smith, B. E., Noh, M.-J., & Morin, P. (2019). The Reference Elevation Model of Antarctica. *The Cryosphere*, (September 2018), 1–16. https://doi.org/10.5194/tc-2018-240

Hunter, P., Meyer, C., Minchew, B., Haseloff, M., & Rempel, A. (2021). Thermal controls on ice stream shear margins. *Journal of Glaciology*, 1–15. https://doi.org/10.1017/jog.2020.118

Iken, A., Echelmeyer, K., Harrison, W., & Funk, M. (1993). Mechanisms of fast flow in Jakobshavns Isbrae, West Greenland: Part I. Measurements of temperature and water level in deep boreholes. *Journal of Glaciology*, *39*(131), 15–25. https://doi.org/10.3189/S0022143000015689

Imbrie, J., & Imbrie, J. Z. (1980). Modeling the climatic response to orbital variations. *Science*, *207*(4434), 943–953. https://doi.org/10.1126/science.207.4434.943

Jackson, J. D. (1999). *Classical Electrodynamics*. John Wiley & Sons.

Jackson, M., & Kamb, B. (1997). The marginal shear stress of Ice Stream B, West Antarctica. *Journal of Glaciology*, *43*(145), 415–426.

Jacobel, R. W., Lapo, K. E., Stamp, J. R., Youngblood, B. W., Welch, B. C., & Bamber, J. L. (2010). A comparison of basal reflectivity and ice velocity in East Antarctica. *Cryosphere*, *4*(4), 447–452. https://doi.org/10.5194/tc-4-447-2010

Jacobel, R. W., Welch, B. C., Osterhouse, D., Pettersson, R., & Macgregor, J. A. (2009). Spatial variation of radar-derived basal conditions on Kamb Ice Stream, West Antarctica. *Annals of Glaciology*, *50*(51), 10–16. https://doi.org/10.3189/172756409789097504

Jacobel, R. W., Welch, B. C., Steig, E. J., & Schneider, D. P. (2005). Glaciological and climatic significance of Hercules Dome, Antarctica: An optimal site for deep ice core drilling. *Journal of Geophysical Research: Earth Surface*, *110*(1), 1–9. https://doi.org/10.1029/2004JF000188

Jacobson, H. P., & Raymond, C. F. (1998). Thermal effects on the location of ice stream margins. *Journal of Geophysical Research*, *103*. https://doi.org/10.1029/98JB00574

Jaeger, J. (1969). *Elasticity, Fracture and Flow*.

Johannesson, T., Raymond, C., & Waddington, E. (1989). Time-scale for adjustment of glaciers to change in mass balance. *Journal of Glaciology*, *35*(121), 355–369. https://doi.org/10.3189/S002214300000928X

Johnson, J. S., Venturelli, R. A., Balco, G., Allen, C. S., Braddock, S., Campbell, S., Goehring, B. M., Hall, B. L., Neff, P. D., Nichols, K. A., Rood, D. H., Thomas, E. R., & Woodward, J. (2022). Review article: Existing and potential evidence for Holocene grounding line retreat and readvance in Antarctica. *Cryosphere*, *16*(5), 1543–1562. https://doi.org/10.5194/tc-16-1543-2022

Jordan, T. A., Martin, C., Ferraccioli, F., Matsuoka, K., Corr, H., Forsberg, R., Olesen, A., & Siegert, M. (2018). Anomalously high geothermal flux near the South Pole. *Scientific Reports*, *8*(1), 1–8. https://doi.org/10.1038/s41598-018-35182-0

Jordan, T. M., Bamber, J. L., Williams, C. N., Paden, J. D., Siegert, M. J., Huybrechts, P., Gagliardini, O., & Gillet-Chaulet, F. (2016). An ice-sheet-wide framework for englacial attenuation from ice-penetrating radar data. *Cryosphere*, *10*(4), 1547–1570. https://doi.org/10.5194/tc-10-1547-2016

Jordan, T. M., Cooper, M. A., Schroeder, D. M., Williams, C. N., Paden, J. D., Siegert, M. J., & Bamber, J. L. (2017). Self-affine subglacial roughness: Consequences for radar scattering and basal water discrimination in northern Greenland. *Cryosphere*, *11*(3), 1247–1264. https://doi.org/10.5194/tc-11-1247-2017

Jordan, T. M., Martín, C., Brisbourne, A. M., Schroeder, D. M., & Smith, A. M. (2022). Radar Characterization of Ice Crystal Orientation Fabric and Anisotropic Viscosity Within an Antarctic Ice Stream. *Journal of Geophysical Research: Earth Surface*, *127*(6), 1–24. https://doi.org/10.1029/2022JF006673

Jordan, T. M., Schroeder, D. M., Castelletti, D., Li, J., & Dall, J. (2019). A Polarimetric Coherence Method to Determine Ice Crystal Orientation Fabric from Radar Sounding: Application to the NEEM Ice Core Region. *IEEE Transactions on Geoscience and Remote Sensing*, *57*(11), 8641–8657. https://doi.org/10.1109/TGRS.2019.2921980

Joughin, I., Smith, B. E., & Howat, I. M. (2018). A complete map of Greenland ice velocity derived from satellite data collected over 20 years. *Journal of Glaciology*, *64*(243), 1–11. https://doi.org/10.1017/jog.2017.73

Journaux, B., Chauve, T., Montagnat, M., Tommasi, A., Barou, F., Mainprice, D., & Gest, L. (2019). Recrystallization processes, microstructure and crystallographic preferred orientation evolution in polycrystalline ice during high-temperature simple shear. *Cryosphere*, *13*(5), 1495–1511. https://doi.org/10.5194/tc-13-1495-2019

Jouzel, J., Masson-Delmotte, V., Cattani, O., Dreyfus, G., Falourd, S., Hoffmann, G., Minster, B., Nouet, J., Barnola, J. M., Chappellaz, J., Fischer, H., Gallet, J. C., Johnsen, S., Leuenberger, M., Loulergue, L., Luethi, D., Oerter, H., Parrenin, F., Raisbeck, G., … Wolff, E. W. (2007). Orbital and millennial antarctic climate variability over the past 800,000 years. *Science*, *317*(5839), 793–796. https://doi.org/10.1126/science.1141038

Kahle, E. C., Steig, E. J., Jones, T. R., Fudge, T. J., Koutnik, M. R., Morris, V. A., Vaughn, B. H., Schauer, A. J., Stevens, C. M., Conway, H., Waddington, E. D., Buizert, C., Epifanio, J., & White, J. W. C. (2021). Reconstruction of Temperature, Accumulation Rate, and Layer Thinning From an Ice Core at South Pole, Using a Statistical Inverse Method. *Journal of Geophysical Research: Atmospheres*, *126*(13), 1–20. https://doi.org/10.1029/2020jd033300

Karlsson, N. B., Dahl-Jensen, D., Gogineni, S. P., & Paden, J. D. (2013). Tracing the depth of the Holocene ice in North Greenland from radio-echo sounding data. *Annals of Glaciology*, *54*(64), 44–50. https://doi.org/10.3189/2013AoG64A057

Kingslake, J., Scherer, R. P., Albrecht, T., Coenen, J., Powell, R. D., Reese, R., Stansell, N. D., Tulaczyk, S., Wearing, M. G., & Whitehouse, P. L. (2018). Extensive retreat and re-advance of the West Antarctic Ice Sheet during the Holocene. *Nature*, *558*(7710), 430–434. https://doi.org/10.1038/s41586-018-0208-x

Kingslake, J., Hindmarsh, R. C. A., Aðalgeirsdóttir, G., Conway, H., Corr, H. F. J., Gillet-Chaulet, F., Martin, C., King, E. C., Mulvaney, R., & Pritchard, H. D. (2014). Full-depth englacial vertical ice sheet velocities measured using phase-sensitive radar. *Journal of Geophysical Research F: Earth Surface*, *119*, 2604–2618. https://doi.org/10.1002/2014JF003275

Kopp, R. E., Simons, F. J., Mitrovica, J. X., Maloof, A. C., & Oppenheimer, M. (2009). Probabilistic assessment of sea level during the last interglacial stage. *Nature*, *462*(7275), 863–867. https://doi.org/10.1038/nature08686

Kuhn, G., Hillenbrand, C. D., Kasten, S., Smith, J. A., Nitsche, F. O., Frederichs, T., Wiers, S., Ehrmann, W., Klages, J. P., & Mogollón, J. M. (2017). Evidence for a palaeo-subglacial lake on the Antarctic continental shelf. *Nature Communications*, *8*, 1–10. https://doi.org/10.1038/ncomms15591

Kulp, S. A., & Strauss, B. H. (2019). New elevation data triple estimates of global vulnerability to sea-level rise and coastal flooding. *Nature Communications*, *10*(1). https://doi.org/10.1038/s41467-019-12808-z

Law, R., Christoffersen, P., Hubbard, B., Doyle, S. H., Chudley, T. R., Schoonman, C. M., Bougamont, M., des Tombe, B., Schilperoort, B., Kechavarzi, C., Booth, A., & Young, T. J. (2021). Thermodynamics of a fast-moving Greenlandic outlet glacier revealed by fiber-optic distributed temperature sensing. *Science Advances*, *7*(20), 1–12. https://doi.org/10.1126/sciadv.abe7136

Li, L., Wattal, S., Nunn, J., Paden, J., & Yan, J. B. (2022). Development of a MIMO VHF Radar for the Search of the Oldest Ice in Antarctica. *IEEE Geoscience and Remote Sensing Letters*, *19*. https://doi.org/10.1109/LGRS.2022.3176287

Lilien, D. A., Fudge, T. J., Koutnik, M. R., & Conway, H. (2018). Holocene Ice-Flow Speedup in the Vicinity of the South Pole. *Geophysical Research Letters*, *45*, 6557–6565. https://doi.org/10.1029/2018GL078253

Lilien, D. A., Hills, B. H., Driscol, J., Jacobel, R., & Christianson, K. (2020). ImpDAR: An open-source impulse radar processor. *Annals of Glaciology*, *61*(81), 114–123. https://doi.org/10.1017/aog.2020.44

Lliboutry, L. (1979). A critical review of analytical approximate solutions for steady state velocities and temperatures in cold ice-sheets. *Gletscherkd. Glazialgeol.*, *15*(2), 135–148.

Lüthi, M. P., Ryser, C., Andrews, L. C., Catania, G. a., Funk, M., Hawley, R. L., Hoffman, M. J., & Neumann, T. a. (2015). Heat sources within the Greenland Ice Sheet: dissipation, temperate paleo-firn and cryo-hydrologic warming. *The Cryosphere*, *9*(1), 245–253. https://doi.org/10.5194/tc-9-245-2015

Lüthi, M., Funk, M., Iken, A., Gogineni, S., & Truffer, M. (2002). Mechanisms of fast flow in Jakobshavns Isbrae, West Greenland: Part III. measurements of ice deformation, temperature and cross-borehole conductivity in boreholes to the bedrock. *Journal of Glaciology*, *48*(162), 369–385. https://doi.org/10.3189/172756502781831322

Lythe, M. B., & Vaughan, D. G. (2001). BEDMAP: A new ice thickness and subglacial topographic model of Antarctica. *Journal of Geophysical Research: Solid Earth*, *106*(B6), 11335–11351. https://doi.org/10.1029/2000jb900449

MacGregor, J. A., Anandakrishnan, S., Catania, G. A., & Winebrenner, D. P. (2011). The grounding zone of the Ross Ice Shelf, West Antarctica, from ice-penetrating radar. *Journal of Glaciology*, *57*(205), 917–928. https://doi.org/10.3189/002214311798043780

MacGregor, J. A., Fahnestock, M. A., Catania, G. A., Paden, J. D., Gogineni, S. P., Young, S. K., Rybarski, S. C., Mabrey, A. N., Wagman, B. M., & Morlighem, M. (2015). Radiostratigraphy and age structure of the Greenland Ice Sheet. *Journal of Geophysical Research: Earth Surface*, *120*, 212–241. https://doi.org/10.1002/2014JF003215. Received

MacGregor, J. A., Li, J., Paden, J. D., Catania, G. a., Clow, G. D., Fahnestock, M. a., Gogineni, S. P., Grimm, R. E., Morlighem, M., Nandi, S., Seroussi, H., & Stillman, D. E. (2015). Radar attenuation and temperature within the Greenland Ice Sheet. *Journal of Geophysical Research: Earth Surface*, *120*, 983–1008. https://doi.org/10.1002/2014JF003418

MacGregor, J. A., Matsuoka, K., & Studinger, M. (2009). Radar detection of accreted ice over Lake Vostok, Antarctica. *Earth and Planetary Science Letters*, *282*(1-4), 222–233. https://doi.org/10.1016/j.epsl.2009.03.018

MacGregor, J. A., Winebrenner, D. P., Conway, H., Matsuoka, K., Mayewski, P. A., & Clow, G. D. (2007). Modeling englacial radar attenuation at Siple Dome, West Antarctica, using ice chemistry and temperature data. *Journal of Geophysical Research: Earth Surface*, *112*(3), 1–14. https://doi.org/10.1029/2006JF000717

Martos, Y. M., Catalán, M., Jordan, T. A., Golynsky, A., Golynsky, D., Eagles, G., & Vaughan, D. G. (2017). Heat Flux Distribution of Antarctica Unveiled. *Geophysical Research Letters*, *44*(22), 417–11. https://doi.org/10.1002/2017GL075609

Matsuoka, K., MacGregor, J. A., & Pattyn, F. (2010). Using englacial radar attenuation to better diagnose the subglacial environment: A review. *Proceedings of the 13th Internarional Conference on Ground Penetrating Radar, GPR 2010*, 1–5. https://doi.org/10.1109/ICGPR.2010.5550161

Matsuoka, K., MacGregor, J. A., & Pattyn, F. (2012). Predicting radar attenuation within the Antarctic ice sheet. *Earth and Planetary Science Letters*, *359-360*, 173–183. https://doi.org/10.1016/j.epsl.2012.10.018

Matsuoka, K., Morse, D. L., & Raymond, C. F. (2010). Estimating englacial radar attenuation using depth profiles of the returned power, central West Antarctica. *Journal of Geophysical Research: Earth Surface*, *115*. https://doi.org/10.1029/2009JF001496

Matsuoka, K., Wilen, L., Hurley, S. P., & Raymond, C. F. (2009). Effects of birefringence within ice sheets on obliquely propagating radio waves. *IEEE Transactions on Geoscience and Remote Sensing*, *47*(5), 1429–1443. https://doi.org/10.1109/TGRS.2008.2005201

Matsuoka, T., Fujita, S., Morishima, S., & Mae, S. (1997). Precise measurement of dielectric anisotropy in ice Ih at 39 GHz. *Journal of Applied Physics*, *81*(5), 2344–2348. https://doi.org/10.1063/1.364238

McDowell, I. E., Humphrey, N. F., Harper, J. T., & Meierbachtol, T. W. (2021). The cooling signature of basal crevasses in a hard-bedded region of the Greenland Ice Sheet. *Cryosphere*, *15*(2), 897–907. https://doi.org/10.5194/tc-15-897-2021

Meyer, C. R., & Minchew, B. M. (2018). Temperate ice in the shear margins of the Antarctic Ice Sheet: Controlling processes and preliminary locations. *Earth and Planetary Science Letters*, *498*, 17–26. https://doi.org/10.1016/j.epsl.2018.06.028

Miller, B., Ariho, G., Paden, J., & Arnold, E. (2020). Multipass SAR Processing for Radar Depth Sounder Clutter Suppression, Tomographic Processing, and Displacement Measurements. *International Geoscience and Remote Sensing Symposium (IGARSS)*, 822–825. https://doi.org/10.1109/IGARSS39084.2020.9324498

Millstein, J. D., Minchew, B. M., & Pegler, S. S. (2022). Ice viscosity is more sensitive to stress than commonly assumed. *Communications Earth and Environment*, *3*(1), 1–7. https://doi.org/10.1038/s43247-022-00385-x

Minchew, B. M., Meyer, C. R., Robel, A. A., Gudmundsson, G. H., & Simons, M. (2018). Processes controlling the downstream evolution of ice rheology in glacier shear margins : case study on Rutford Ice Stream , West Antarctica, 1–12. https://doi.org/10.1017/jog.2018.47

Mitrovica, J. X., Tamisiea, M. E., Davis, J. L., & Milne, G. A. (2001). Recent mass balance of polar ice sheets inferred from patterns of global sea-level change. *Nature*, *409*(February), 4–7.

Morlighem, M., Rignot, E., Seroussi, H., Larour, E., Ben Dhia, H., & Aubry, D. (2011). A mass conservation approach for mapping glacier ice thickness. *Geophysical Research Letters*, *38*(19), 1–6. https://doi.org/10.1029/2011GL048659

Morlighem, M., Rignot, E., Binder, T., Blankenship, D., Drews, R., Eagles, G., Eisen, O., Ferraccioli, F., Forsberg, R., Fretwell, P., Goel, V., Greenbaum, J. S., Gudmundsson, H., Guo, J., Helm, V., Hofstede, C., Howat, I., Humbert, A., Jokat, W., … Young, D. A. (2020). Deep glacial troughs and stabilizing ridges unveiled beneath the margins of the Antarctic ice sheet. *Nature Geoscience*, *13*(2), 132–137. https://doi.org/10.1038/s41561-019-0510-8

Morlighem, M., Williams, C. N., Rignot, E., An, L., Arndt, J. E., Bamber, J. L., Catania, G., Chauché, N., Dowdeswell, J. A., Dorschel, B., Fenty, I., Hogan, K., Howat, I., Hubbard, A., Jakobsson, M., Jordan, T. M., Kjeldsen, K. K., Millan, R., Mayer, L., … Zinglersen, K. B. (2017). BedMachine v3: Complete Bed Topography and Ocean Bathymetry Mapping of Greenland From Multibeam Echo Sounding Combined With Mass Conservation. *Geophysical Research Letters*, *44*(21), 051–11. https://doi.org/10.1002/2017GL074954

Mouginot, J., Rignot, E., & Scheuchl, B. (2019). Continent-Wide, Interferometric SAR Phase, Mapping of Antarctic Ice Velocity. *Geophysical Research Letters*, *46*(16), 9710–9718. https://doi.org/10.1029/2019GL083826

Ng, F., & Conway, H. (2004). Fast-flow signature in the stagnated Kamb Ice Stream, West Antarctica. *Geology*, *32*(6), 481–484. https://doi.org/10.1130/G20317.1

Nicholls, K. W., Corr, H. F., Stewart, C. L., Lok, L. B., Brennan, P. V., & Vaughan, D. G. (2015). Instruments and methods: A ground-based radar for measuring vertical strain rates and time-varying basal melt rates in ice sheets and shelves. *Journal of Glaciology*, *61*(230), 1079–1087. https://doi.org/10.3189/2015JoG15J073

Nichols, K. A., Goehring, B. M., Balco, G., Johnson, J. S., Hein, A. S., & Todd, C. (2019). New Last Glacial Maximum ice thickness constraints for the Weddell Sea Embayment, Antarctica. *Cryosphere*, *13*(11), 2935–2951. https://doi.org/10.5194/tc-13-2935-2019

Nye, J. F. (1960). The response of glaciers and ice-sheets to seasonal and climatic changes. *Proceedings of the Royal Society A: Mathematical, Physical and Engineering Sciences*, (986). http://rstb.royalsocietypublishing.org/content/royptb/338/1285/299.full.pdf

Ogilvy, J. A. (1991). *Theory of Wave Scattering From Random Rough Surfaces* (Vol. 90). Institute of Physics Publishing. https://doi.org/10.1121/1.401410

Oswald, G. K., & Gogineni, S. P. (2008). Recovery of subglacial water extent from Greenland radar survey data. *Journal of Glaciology*, *54*(184), 94–106. https://doi.org/10.3189/002214308784409107

Parrenin, F., Dreyfus, G., Durand, G., Fujita, S., Gagliardini, O., Gillet, F., Jouze, J., Kawamura, K., Lhomme, N., Masson-Delmotte, V., Ritz, C., Schwander, J., Shoji, H., Uemura, R., Watanabe, O., & Yoshida, N. (2007). 1-D-ice flow modelling at EPICA Dome C and Dome Fuji, East Antarctica. *Climate of the Past*, *3*(2), 243–259. https://doi.org/10.5194/cp-3-243-2007

Perol, T., & Rice, J. R. (2015). Shear heating and weakening of the margins of Western Antarctic ice streams. *Geophysical Research Letters*, *42*, 3406–3413. https://doi.org/10.1002/2015GL063638.Received

Peters, L. E., Anandakrishnan, S., Alley, R. B., & Voigt, D. E. (2012). Seismic attenuation in glacial ice: A proxy for englacial temperature. *Journal of Geophysical Research: Earth Surface*, *117*(2), 1–10. https://doi.org/10.1029/2011JF002201

Peters, L. E., Anandakrishnan, S., Holland, C. W., Horgan, H. J., Blankenship, D. D., & Voigt, D. E. (2008). Seismic detection of a subglacial lake near the South Pole , Antarctica. *Geophysical Research Letters*, *35*, 1–5. https://doi.org/10.1029/2008GL035704

Peters, M. E., Blankenship, D. D., & Morse, D. L. (2005). Analysis techniques for coherent airborne radar sounding: Application to West Antarctic ice streams. *Journal of Geophysical Research B: Solid Earth*, *110*(6), 1–17. https://doi.org/10.1029/2004JB003222

Petrenko, V. F., & Whitworth, R. W. (1999). *Physics of Ice*. Oxford University Press.

Phillips, T., Rajaram, H., & Steffen, K. (2010). Cryo-hydrologic warming: A potential mechanism for rapid thermal response of ice sheets. *Geophysical Research Letters*, *37*(20), 1–5. https://doi.org/10.1029/2010GL044397

Placidi, L., Greve, R., Seddik, H., & Faria, S. H. (2010). Continuum-mechanical, Anisotropic Flow model for polar ice masses, based on an anisotropic Flow Enhancement factor. *Continuum Mechanics and Thermodynamics*, *22*(3), 221–237. https://doi.org/10.1007/s00161-009-0126-0

Placidi, L., Hutter, K., & Faria, H. (2006). A critical review of the mechanics of polycrystalline polar Ice. *GAMM-Mitteilungen*, *29*(1), 80–117.

Price, P. B., Nagornov, O. V., Bay, R., Chirkin, D., He, Y., Miocinovic, P., Richards, A., Woschnagg, K., Koci, B., & Zagorodnov, V. (2002). Temperature profile for glacial ice at the South Pole : Implications for life in a nearby subglacial lake. *Proceedings of the National Academy of Sciences*, *99*(12), 7844–7847. https://doi.org/10.1073/pnas.082238999

Qi, C., Prior, D. J., Craw, L., Fan, S., Llorens, M. G., Griera, A., Negrini, M., Bons, P. D., & Goldsby, D. L. (2019). Crystallographic preferred orientations of ice deformed in direct-shear experiments at low temperatures. *Cryosphere*, *13*(1), 351–371. https://doi.org/10.5194/tc-13-351-2019

Ranganathan, M., Minchew, B., Meyer, C. R., & Peč, M. (2021). Recrystallization of ice enhances the creep and vulnerability to fracture of ice shelves. *Earth and Planetary Science Letters*, *576*. https://doi.org/10.1016/j.epsl.2021.117219

Rathmann, N. M., Hvidberg, C. S., Grinsted, A., Lilien, D. A., & Dahl-Jensen, D. (2021). Effect of an orientation-dependent non-linear grain fluidity on bulk directional enhancement factors. *Journal of Glaciology*, *67*(263), 569–575. https://doi.org/10.1017/jog.2020.117

Rathmann, N. M., & Lilien, D. A. (2021). Inferred basal friction and mass flux affected by crystal-orientation fabrics. *Journal of Glaciology*. https://doi.org/10.1017/jog.2021.88

Rathmann, N. M., Lilien, D. A., Grinsted, A., Gerber, T. A., Young, T. J., & Dahl-Jensen, D. (2022). On the Limitations of Using Polarimetric Radar Sounding to Infer the Crystal Orientation Fabric of Ice Masses. *Geophysical Research Letters*, *49*(1), 1–11. https://doi.org/10.1029/2021GL096244

Raymond, C. (1996). Shear margins in glaciers and ice sheets. *Program*, *42*(140), 90–102. https://doi.org/10.3198/1996JoG42-140-90-102

Raymond, C. F. (1983). Deformation in the vicinity of ice divides. *Journal of Glaciology*, *29*(103), 357–373. https://doi.org/10.3189/S0022143000030288

Retzlaff, R., & Bentley, C. R. (1993). Timing of stagnation of ice stream C, West Antarctica, from short- pulse radar studies of buried surface crevasses. *Journal of Glaciology*, *39*(133), 553–561. https://doi.org/10.1017/S0022143000016440

Rezvanbehbahani, S., van der Veen, C. J., & Stearns, L. A. (2019). An Improved Analytical Solution for the Temperature Profile of Ice Sheets. *Journal of Geophysical Research: Earth Surface*, *124*(2), 271–286. https://doi.org/10.1029/2018JF004774

Richards, D. H., Pegler, S. S., Piazolo, S., & Harlen, O. G. (2021). The evolution of ice fabrics: A continuum modelling approach validated against laboratory experiments. *Earth and Planetary Science Letters*, *556*, 116718. https://doi.org/10.1016/j.epsl.2020.116718

Rignot, E., Jacobs, S., Mouginot, J., & Scheuchl, B. (2013). Ice-shelf melting around antarctica. *Science*, *341*(6143), 266–270. https://doi.org/10.1126/science.1235798

Rignot, E., Mouginot, J., & Scheuchl, B. (2011). Antarctic grounding line mapping from differential satellite radar interferometry. *Geophysical Research Letters*, *38*(10), 1–6. https://doi.org/10.1029/2011GL047109

Robin, G. d. Q. (1955). Ice movement and temperature distribution in glaciers and ice sheets. *Journal of Glaciology*, *2*(18), 523–532. https://doi.org/10.3189/002214355793702028

Ryser, C., Lüthi, M., Blindow, N., Suckro, S., Funk, M., & Bauder, A. (2013). Cold ice in the ablation zone: Its relation to glacier hydrology and ice water content. *Journal of Geophysical Research: Earth Surface*, *118*(2), 693–705. https://doi.org/10.1029/2012JF002526

Schoof, C., Hewitt, I., & Werder, M. A. (2012). Flotation and free surface flow in a model for subglacial drainage . Part 1 . Distributed drainage. *Journal of Fluid Mechanics*, *702*, 126–156. https://doi.org/10.1017/jfm.2012.165

Schroeder, D. M. (2023). Paths forward in radioglaciology. *Annals of Glaciology*, 1–5. https://doi.org/10.1017/aog.2023.3

Schroeder, D. M., Blankenship, d. D., Raney, R. K., & Grima, C. (2015). Estimating Subglacial Water Geometry Using Radar Bed Echo Specularity : Application. *IEEE Geoscience and Remote Sensing Letters*, *12*(3), 443–447. https://doi.org/10.1109/LGRS.2014.2337878

Schroeder, D. M., Blankenship, D. D., Young, D. A., Witus, A. E., & Anderson, J. B. (2014). Airborne radar sounding evidence for deformable sediments and outcropping bedrock beneath Thwaites Glacier, West Antarctica. *Geophysical Research Letters*, *41*(20), 7200–7208. https://doi.org/10.1002/2014GL061645

Schroeder, D. M., Grima, C., & Blankenship, D. D. (2016). Evidence for variable grounding-zone and shear-margin basal conditions across Thwaites Glacier, West Antarctica. *Geophysics*, *81*(1), WA35–WA43. https://doi.org/10.1190/geo2015-0122.1

Schroeder, D. M., Seroussi, H., Chu, W., & Young, D. A. (2016). Adaptively constraining radar attenuation and temperature across the Thwaites Glacier catchment using bed echoes. *Journal of Glaciology*, *62*(236), 1075–1082. https://doi.org/10.1017/jog.2016.100

Schwerdtfeger. (1963). Theoretical derivation of the thermal conductivity and diffusivity of snow. *International Association of Scientific Hydrology*, *61*, 75–81.

Shabtaie, S., Whillans, I. M., & Bentley, C. R. (1987). The morphology of ice streams A, B, and C, West Antarctica, and their environs. *Journal of Geophysical Research*, *92*(B9), 8865–8883. https://doi.org/10.1029/JB092iB09p08865

Shean, D. E., Christianson, K., Larson, K. M., Ligtenberg, S. R., Joughin, I. R., Smith, B. E., Max Stevens, C., Bushuk, M., & Holland, D. M. (2017). GPS-derived estimates of surface mass balance and ocean-induced basal melt for Pine Island Glacier ice shelf, Antarctica. *Cryosphere*, *11*(6), 2655–2674. https://doi.org/10.5194/tc-11-2655-2017

Shen, W., Wiens, D. A., Lloyd, A. J., & Nyblade, A. A. (2020). A Geothermal Heat Flux Map of Antarctica Empirically Constrained by Seismic Structure. *Geophysical Research Letters*, *47*(14), 1–8. https://doi.org/10.1029/2020GL086955

Shoji, H., & Langway, C. (1988). Flow-Law Parameters of the Dye 3, Greenland, Deep Ice Core. *Annals of Glaciology*, *10*, 146–150. https://doi.org/10.3189/s026030550000433x

Shreve, R. L. (1972). Movement of water in glaciers. *Journal of Glaciology*, *11*(62), 205–214. https://doi.org/10.3189/S002214300002219X

Siegert, M., Ross, N., Corr, H., Kingslake, J., & Hindmarsh, R. (2013). Late Holocene ice-flow reconfiguration in the Weddell Sea sector of West Antarctica. *Quaternary Science Reviews*, *78*, 98–107. https://doi.org/10.1016/j.quascirev.2013.08.003

Siegert, M. J. (2008). Antarctic subglacial topography and ice-sheet evolution. *Earth Surface Processes and Landforms*, *33*, 646–660. https://doi.org/10.1002/esp

Siegert, M. J., Carter, S., Tabacco, I., Popov, S., & Blankenship, D. D. (2005). A revised inventory of Antarctic subglacial lakes. *Antarctic Science*, *17*(3), 453–460. https://doi.org/10.1017/S0954102005002889

Siegert, M. J., Hodgkins, R., & Dowdeswell, J. A. (1998). A chronology for the Dome C deep ice-core site through radio-echo layer correlation with the Vostok ice core, Antarctica. *Geophysical Research Letters*, *25*(7), 1019–1022. https://doi.org/10.1029/98GL00718

Smith, A. M., Woodward, J., Ross, N., Bentley, M. J., Hodgson, D. A., Siegert, M. J., & King, E. C. (2018). Evidence for the long-term sedimentary environment in an Antarctic subglacial lake. *Earth and Planetary Science Letters*, *504*, 139–151. https://doi.org/10.1016/j.epsl.2018.10.011

Smith, E. C., Baird, A. F., Kendall, J. M., Martín, C., White, R. S., Brisbourne, A. M., & Smith, A. M. (2017). Ice fabric in an Antarctic ice stream interpreted from seismic anisotropy. *Geophysical Research Letters*, *44*(8), 3710–3718. https://doi.org/10.1002/2016GL072093

Spratt, R. M., & Lisiecki, L. E. (2016). A Late Pleistocene sea level stack. *Climate of the Past*, *12*(4), 1079–1092. https://doi.org/10.5194/cp-12-1079-2016

Stål, T., Reading, A. M., Halpin, J. A., & Whittaker, J. M. (2021). Antarctic Geothermal Heat Flow Model: Aq1. *Geochemistry, Geophysics, Geosystems*, *22*(2), 1–22. https://doi.org/10.1029/2020GC009428

Steig, E. J., Huybers, K., Singh, H. A., Steiger, N. J., Ding, Q., Frierson, D. M. W., Popp, T., & White, J. W. C. (2015). Influence of West Antarctic Ice Sheet collapse on Antarctic surface climate. https://doi.org/10.1002/2015GL063861.Abstract

Steig, E. J., Jones, T. R., Schauer, A. J., Kahle, E. C., Morris, V. A., Vaughn, B. H., Davidge, L., & White, J. W. (2021). Continuous-Flow Analysis of δ 17O, δ 18O, and δD of H2O on an Ice Core from the South Pole. *Frontiers in Earth Science*, *9*(March), 1–14. https://doi.org/10.3389/feart.2021.640292

Stone, J., Balco, G., Sugden, D., Caffee, M., Sass III, L., Cowdery, S., & Siddoway, C. (2003). Holocene Deglaciation of Marie Byrd Land , West Antarctica. *Science*, *299*(January), 99–102.

Suckale, J., Platt, J. D., Perol, T., & Rice, J. R. (2014). Earth Surface Deformation-induced melting in the margins of the West Antarctic ice streams. *Journal of Geophysical Research: Earth Surface*, *119*(May), 1004–1025. https://doi.org/10.1002/2013JF003008.Flow

Svendsen, B., & Hutter, K. (1996). A continuum approach for modelling induced anisotropy in glaciers and ice sheets. *Annals of Glaciology*, *23*. https://doi.org/10.1017/s0260305500013525

Talalay, P., Li, Y., Augustin, L., Clow, G. D., Hong, J., Lefebvre, E., Markov, A., Motoyama, H., & Ritz, C. (2020). Geothermal heat flux from measured temperature profiles in deep ice boreholes in Antarctica. *Cryosphere*, *14*(11), 4021–4037. https://doi.org/10.5194/tc-14-4021-2020

Taylor, K. (1992). Ice-core dating and chemistry by direct-current electrical conductivity. *Journal of Glaciology*, *38*(130), 325–332. https://doi.org/10.1017/S0022143000002215

Taylor, K. C., Alley, R. B., Meese, D. A., Spencer, M. K., Brook, E. J., Dunbar, N. W., Finkel, R. C., Gow, A. J., Kurbatov, A. V., Lamorey, G. W., Mayewski, P. A., Meyerson, E. A., Nishiizumi, K., & Zielisnki, G. A. (2004). Dating the Siple Dome (Antarctica) ice core by manual and computer interpretation of annual layering. *Journal of Glaciology*, *50*(170), 453–461. https://doi.org/10.3189/172756504781829864

Tétreault, P., Kouba, J., Héroux, P., & Legree, P. (2005). CSRS-PPP: AN INTERNET SERVICE FOR GPS USER ACCESS TO THE CANADIAN SPATIAL REFERENCE FRAME. *GEOMATICA*, *59*(1), 17–28. https://doi.org/10.5623/geomat-2005-0004

Thomsen, H. H., Olesen, O. B., Braithwaite, R. J., & Bøggild, C. E. (1991). Ice drilling and mass balance at Pakitsoq, Jakobshavn, central West Greenland. *Report of the Geological Survey of Greenland*, *152*, 80–84.

Tikku, A. A., Bell, R. E., Studinger, M., & Clarke, G. K. (2004). Ice flow field over Lake Vostok, East Antarctica inferred by structure tracking. *Earth and Planetary Science Letters*, *227*(3-4), 249–261. https://doi.org/10.1016/j.epsl.2004.09.021

Todd, C., Stone, J., Conway, H., Hall, B., & Bromley, G. (2010). Late Quaternary evolution of Reedy Glacier, Antarctica. *Quaternary Science Reviews*, *29*(11-12), 1328–1341. https://doi.org/10.1016/j.quascirev.2010.02.001

United Nations. (2015). The Paris Agreement: Framework Convention on Climate Change.

van der Veen, C. (2013). *Fundamentals of Glacier Dynamics* (Second). CRC Press.

Venturelli, R. A., Siegfried, M. R., Roush, K. A., Li, W., Burnett, J., Zook, R., Fricker, H. A., Priscu, J. C., Leventer, A., & Rosenheim, B. E. (2020). Mid-Holocene Grounding Line Retreat and Readvance at Whillans Ice Stream, West Antarctica. *Geophysical Research Letters*, *47*(15). https://doi.org/10.1029/2020GL088476

Vogel, S. W., Tulaczyk, S., Kamb, B., Engelhardt, H., Carsey, F. D., Behar, A. E., Lane, A. L., & Joughin, I. (2005). Subglacial conditions during and after stoppage of an Antarctic Ice Stream: Is reactivation imminent? *Geophysical Research Letters*, *32*(14), 1–4. https://doi.org/10.1029/2005GL022563

Voigt, D. E. (2017). c-Axis Fabric of the South Pole Ice Core, SPC14. https://doi.org/https://doi.org/10.15784/601057

Wang, Y., Ding, M., Reijmer, C. H., Smeets, P. C., Hou, S., & Xiao, C. (2021). The AntSMB dataset: A comprehensive compilation of surface mass balance field observations over the Antarctic Ice Sheet. *Earth System Science Data*, *13*(6), 3057–3074. https://doi.org/10.5194/essd-13-3057-2021

Warren, S. G. (2019). Optical properties of ice and snow. *Philosophical Transactions of the Royal Society A: Mathematical, Physical and Engineering Sciences*, *377*(2146). https://doi.org/10.1098/rsta.2018.0161

Weertman, J. (1957). On the sliding of glaciers. *Journal of Glaciology*, *3*(21), 33–38. https://doi.org/10.3189/S002214300002470

Weertman, J. (1968). Comparison between Measured and Theoretical Temperature Profiles of the Camp Century, Greenland, Borehole. *Journal of Geophysical Research*, *73*(8), 2691–2700. https://doi.org/10.1029/JB073i008p02691

Weertman, J. (1974). Stability of the Junction of an Ice Sheet and an Ice Shelf. *Journal of Glaciology*, *13*(67), 3–11. https://doi.org/10.3189/S0022143000023327

Weertman, J., & Weertman, J. R. (1964). *Elementary Dislocation Theory*. Macmillan.

Welch, B. C., & Jacobel, R. W. (2003). Analysis of deep-penetrating radar surveys of West Antarctica, US-ITASE 2001. *Geophysical Research Letters*, *30*(8), 1–4. https://doi.org/10.1029/2003GL017210

Welch, B. C., & Jacobel, R. W. (2005). Bedrock topography and wind erosion sites in East Antarctica: Observations from the 2002 US-ITASE traverse. *Annals of Glaciology*, *41*, 92–96. https://doi.org/10.3189/172756405781813258

Winebrenner, D., Smith, B., Catania, G., Conway, H., & Raymond, C. (2003). Radio frequency attenuation beneath Siple dome, West antarctica, from wide angle and profiling radar observations. *Annals of Glaciology*, *37*, 1–7. https://doi.org/10.3189/172756403781815483

Winter, A., Steinhage, D., Creyts, T. T., Kleiner, T., & Eisen, O. (2019). Age stratigraphy in the East Antarctic Ice Sheet inferred from radio-echo sounding horizons. *Earth System Science Data*, *11*(3), 1069–1081. https://doi.org/10.5194/essd-11-1069-2019

Winter, K., Ross, N., Ferraccioli, F., Jordan, T. A., Corr, H. F., Forsberg, R., Matsuoka, K., Olesen, A. V., & Casal, T. G. (2018). Topographic Steering of Enhanced Ice Flow at the Bottleneck Between East and West Antarctica. *Geophysical Research Letters*, *45*(10), 4899–4907. https://doi.org/10.1029/2018GL077504

Young, T. J., Schroeder, D. M., Jordan, T. M., Christoffersen, P., Tulaczyk, S. M., Culberg, R., & Bienert, N. L. (2021). Inferring Ice Fabric From Birefringence Loss in Airborne Radargrams: Application to the Eastern Shear Margin of Thwaites Glacier, West Antarctica. *Journal of Geophysical Research: Earth Surface*, *126*(5), 1–26. https://doi.org/10.1029/2020JF006023

Young, T., Martín, C., Christoffersen, P., Schroeder, D., Tulaczyk, S. M., & Dawson, E. J. (2021). Rapid and accurate polarimetric radar measurements of ice crystal fabric orientation at the Western Antarctic Ice Sheet (WAIS) Divide ice core site. *Cryosphere*, *15*(8), 4117–4133. https://doi.org/10.5194/tc-15-4117-2021

Zeising, O., Gerber, T. A., Eisen, O., Ershadi, M. R., Stoll, N., & Weikusat, I. (2023). Improved estimation of the bulk ice crystal fabric asymmetry from polarimetric phase co-registration, 1097–1105.

Zumberge, M. A., Elsberg, D. H., Harrison, W. D., Husmann, E., Morack, J. L., Pettit, E. C., & Waddington, E. D. (2002). Measurement of vertical strain and velocity at Siple Dome, Antarctica, with optical sensors. *Journal of Glaciology*, *48*(161), 217–225. https://doi.org/10.3189/172756502781831421

Appendix A

Incorporating Uncertainty into Radar Power Regressions

Originally published as an appendix in Annals of Glaciology (Hills et al., 2020).

Unlike the ordinary or weighted least squares implemented in a simple linear regression, a regression with errors in variables (EIV) is used in cases where both the regressor and the regressand variables are observed and subject to independent uncertainty. In our case, both the measured depth and measured power of a radar return are known only to finite precision. As in the simple linear regression case, we assume a functional relationship (equation 2.60). Then, following Casella and Berger (2002, sec. 12.2) we solve for attenuation by the regression slope,

$$\hat{N} = \frac{\sqrt{(SS_{zz} - \chi SS_{P_cP_c}) + 4\chi SS_{zP_c}^2} - (SS_{zz} - \chi SS_{P_cP_c})}{2\chi SS_{zP_c}} \tag{A.1}$$

where $\hat{}$ represents a regression result, SS is a sum-of-squares (e.g. $SS_{zP_c} = \sum_{i=1}^{n}(z_i - \bar{z})(P_{ci} - \bar{P}_c)$), and $\chi = \frac{\sigma_z^2}{\sigma_{P_c}^2}$ is the ratio of uncertainty variances for the regressor and regressand variables. A normal distribution of uncertainty is assumed for both variables. There are a variety of EIV regressions, but we choose to follow the Deming regression where is known and fixed by the calculated uncertainty at locations where radar profiles cross one another. Next, the regression variance for attenuation is defined,

$$\hat{\sigma}_N^2 = \frac{(1+\chi\hat{N}^2)^2(SS_{zz}SS_{P_cP_c} - SS_{zP_c}^2)}{(SS_{zz} - \chi SS_{P_cP_c})^2 + 4\chi SS_{zP_c}^2} \tag{A.2}$$

Finally, the formal uncertainty is reported at the 95% confidence interval using the t-statistic and Gleser's modification (Gleser & Hwang, 1987),

$$\hat{N} - \frac{t_{.95,n-2}\hat{\sigma}_N}{\sqrt{n-2}} \leq N \leq \hat{N} + \frac{t_{.95,n-2}\hat{\sigma}_N}{\sqrt{n-2}} \tag{A.3}$$

where $t_{.95,n}$ is the two-tail t-statistic at 95% confidence, and n is the number of points in the regression (i.e. degrees of freedom), and the uncertainty value reported in this study is $\tilde{N} = \frac{t_{.95,n-2}\hat{\sigma}_N}{\sqrt{n-2}}$.

Appendix B

Interval versus Depth-Averaged Attenuation-Rate Calculations

Originally published as supplementary material in Annals of Glaciology (Hills et al., 2020)

In describing the attenuation framework (Section 2.3.2) and associated results (Appendices D and G), we refer to single-reflector attenuation rates as an interval result, implying that they are representative of only the ice depth range which the reflector spans. Prior studies generally have discussed single-reflector attenuation rates as a depth-averaged result, representing all ice above the reflector (ice through which the radar wave travels) (Jacobel et al., 2009; Schroeder, Seroussi, et al., 2016). Here, we argue that under the implied assumptions for single-reflector methods (i.e. that $\left|\frac{\partial[R]}{\partial z}\right| \ll \left|\frac{\partial[P_c]}{\partial z}\right|$ and that $\left|\frac{\partial N}{\partial x}\right| \ll 0$) (see Section 2.3.2), the only well-posed problem is that of pure conduction. In this well-posed case, attenuative losses above the shallowest reflection are spatially uniform, and the regression is exactly equal to the interval attenuation rate over the depth range which the reflector spans. In any more realistic case, vertical and horizontal advection as well as heat generation create horizontal temperature gradients in the ice which violate the assumptions, creating an ill-posed problem, and possibly bias the calculated attenuation rate. Having said that, the bias is not necessarily toward the depth-averaged value, the direction of the bias depends on the direction of the temperature gradient.

In order to illustrate this problem more quantitatively, we create a synthetic glacier profile and

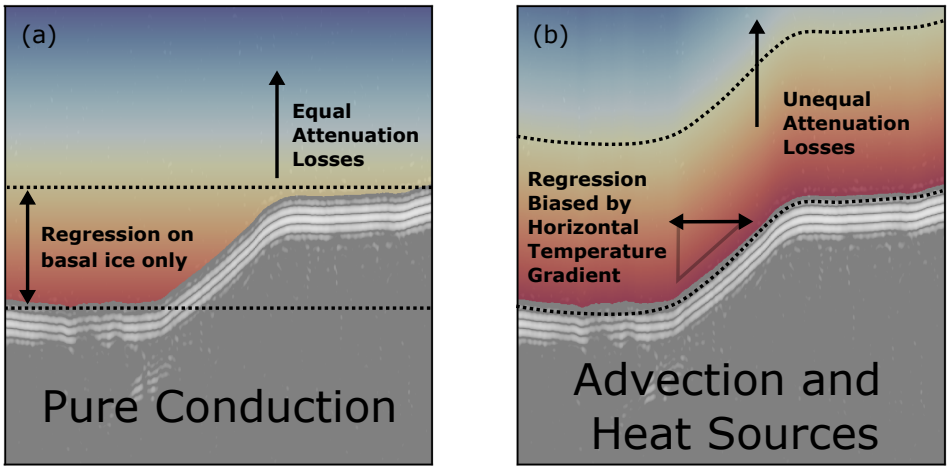

Figure B.1: A thought experiment for single-reflector attenuation calculations under two scenarios. In each, the temperature-dependent instantaneous attenuation rate (colormap) is overlain on a portion of the bed reflector from the radar image at South Pole Lake. a) Pure conduction controls the ice temperature while the surface temperature and geothermal flux are uniform. In this scenario, there is no horizontal temperature gradient, so temperature-related attenuative losses are identical between traces, and the depth-power regression on the bed reflector represents characteristics of the basal ice only (i.e. between the dotted lines). b) Additional heat transfer processes create a horizontal temperature gradient which can bias the regression in either direction (toward or away from the depth-averaged attenuation rate).

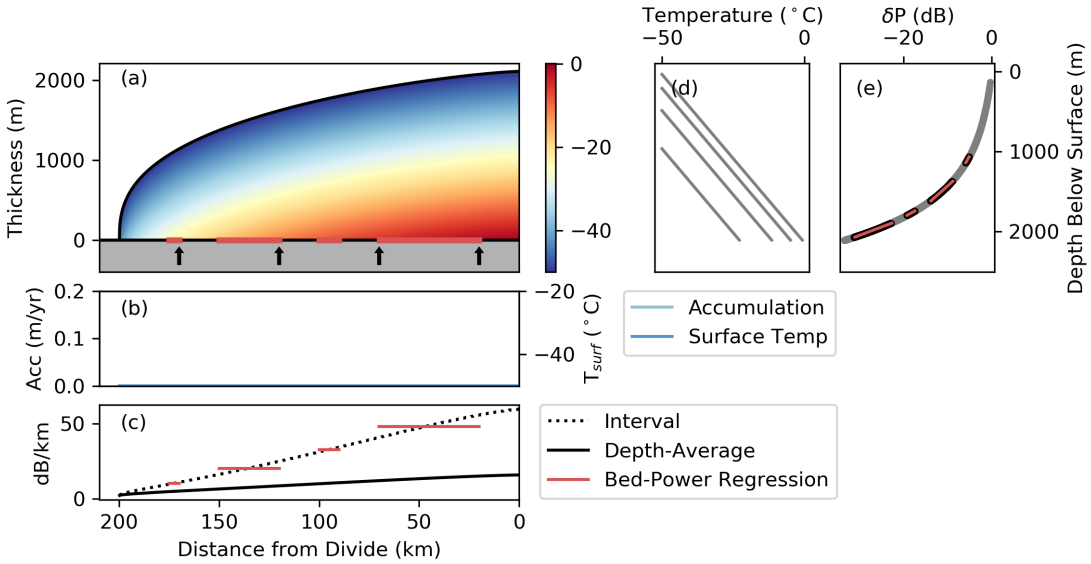

Figure B.2: Synthetic attenuation calculations using *Method 1* (bed reflector). For this case, the accumulation rate is zero, the air temperature is constant (-50°C), and the geothermal flux is constant (50 $\frac{mW}{m^2}$). a) Glacier thickness profile with the colormap showing ice temperature, grey is bedrock. The arrows show locations where temperature profiles are plotted in (d). The red sections along the bed reflector are where attenuation is calculated and correspond to red lines in (c) and (e). b) Accumulation and air temperature profiles. c) Attenuation profiles where the solid line is averaged over the ice thickness, the dotted line is the instantaneous value at the bed, and the red lines are regressions. d) Temperature profiles corresponding to arrow locations in (a). e) The power differential at the bed reflector associated with attenuative losses through the column.

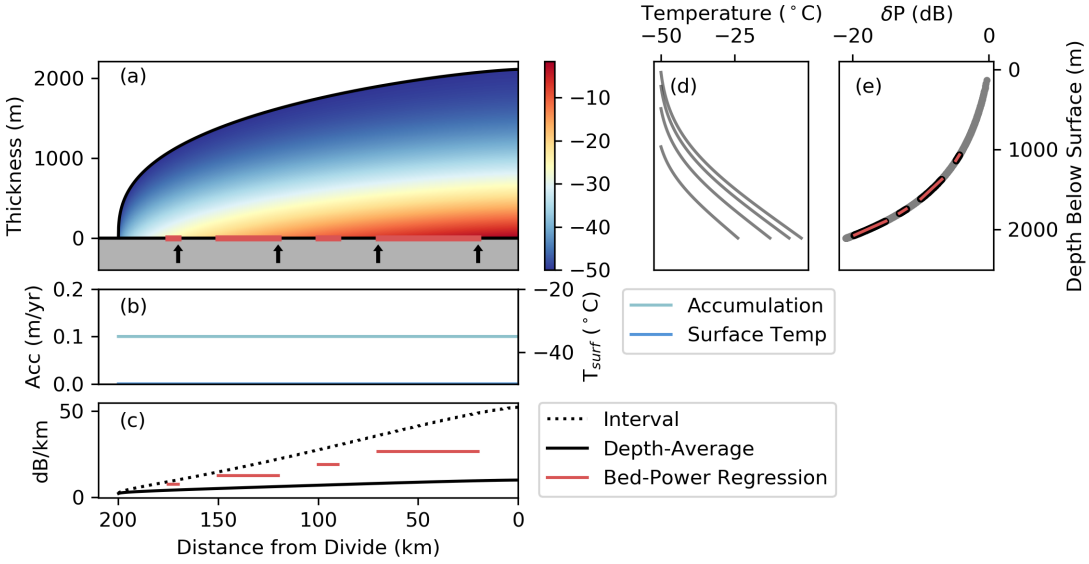

Figure B.3: Same as Figure B.2 but with uniform non-zero accumulation (10 cm/yr).

calculate synthetic attenuation rates below. The examples are not designed to precisely model any 'real' glaciological setting, but are intended to demonstrate the various possible biases in single-reflector attenuation calculations. We define the glacier thickness profile using the Vialov equation (Cuffey & Paterson, 2010). This equation assumes no sliding, a flat bed, a constant flow-band width, constant accumulation of 10 cm/yr, and a constant rate factor, $A = 3.5 \times 10^{-25} s^{-1} Pa^{-3}$. Ice temperature is defined using a 1-dimensional analytical solution that allows nonlinear vertical velocity (Rezvanbehbahani et al., 2019). For each trace, we optimize the exponent on the vertical velocity profile based on a logarithmic regression with the *Peclet* Number (Rezvanbehbahani et al., 2019, Sec. 3). Heat production associated with xz-strain in the column is added by increasing the geothermal flux term (Rezvanbehbahani et al., 2019, Sec. 3).

The instantaneous attenuation rate is calculated at all depths of the temperature profile using a temperature- and chemistry-dependent Arrhenius model (MacGregor et al., 2007). We use constant acidity ($1.3 \mu M H^+$) and constant sea salts ($4.2 \mu M ss Cl^-$). For each trace, we integrate the instantaneous attenuation rate over the ice column to calculate the power losses at the bed. Then, the *Method 1* attenuation rate is calculated at the bed reflector using the EIV regression (Appendix A).

In the case of pure conduction (Figure B.2), the single-reflector attenuation rate is exactly equal to the interval attenuation rate. Adding a constant accumulation (Figure B.3) biases the result lower (i.e. toward the depth-averaged result). Additional model scenarios were included in the original publication but are only briefly noted here. Adding heat production from xz-shear biases the result high, bringing it back toward the interval rate. In the case where we define air temperature and accumulation with a lapse rate, the attenuation rate is biased lower than even the depth-averaged value. When we impose a linear gradient in the geothermal flux, increasing toward the ice divide, the attenuation rate is biased slightly high. Finally, switching to the temperate-ice model biases the result very high until the basal ice is temperate, then the result exactly represents that of the interval attenuation rate.

For all cases, the single-reflector attenuation rate is only biased away from the interval value when the ice has a horizontal temperature gradient with respect to the cold surface boundary. The strongest horizontal gradients arise when there is some variation in heat production (e.g. near an ice stream shear margin (Holschuh et al., 2019)). However, more subtle gradients arise in almost any setting (Hills et al., 2017). For example, in the case of a spatially uniform accumulation rate

(with the vertical velocity varying only in the vertical) thickness variations create a subtle horizontal temperature gradient (Figure B.3). Unfortunately though, it is difficult to know exactly which way the single-reflector attenuation rate calculation will be biased without knowing the ice temperature, and in that case the attenuation could be modeled confidently.

Appendix C

South Pole Lake - Supplementary Measurements of Ice Dynamics

Originally published as supplementary material in Geophysical Research Letters (Hills, Christianson, Hoffman, et al., 2022).

Here we present additional ice dynamics calculations. We use Delauney Triangulation to grid the locations where velocities were measured. We calculate strain rates along each line of the grid and then principal strain rates for each triangular cell following (Jaeger, 1969; Shean et al., 2017)

$$\dot{\varepsilon}_i = \frac{1}{2}(\dot{\varepsilon}_{11} + \dot{\varepsilon}_{22}) + \frac{1}{2}(\dot{\varepsilon}_{11} - \dot{\varepsilon}_{22})\, cos(2(\theta_i - \Theta)) \tag{C.1}$$

where $\dot{\varepsilon}_i$ is the strain rate along the i^{th} side of a given triangle, $\dot{\varepsilon}_{11}$ is the first principal strain, $\dot{\varepsilon}_{22}$ is the second principal strain, θ_i is the azimuth of the i^{th} triangle edge, and Θ is the azimuth of the principal angle.

Next, we isolate the location of each ApRES acquisition to show the measured englacial dynamics at that site. For each ApRES site, we re-grid the Delauney triangulation for the four triangles immediately surrounding the site. The representative principal strain rates and principal angle are the mean values from those four triangles. We calculate an inferred bed motion by taking the dot product of the measured surface velocity at the site with the reflector slope in the direction of motion. Specifically for the bed, this is the gradient of the basal reflector minus that of the surface.

ApRES data in the figures shown below are analogous to profiles plotted in Figure 4.3C, 4.3D, and 4.3E.

Unfortunately, low coherence deep in the ice column makes it difficult to adequately assess the ice dynamics in a conclusive way. Most measurable distinction in dynamic process, between sliding and shear, will be observed at the greatest depths, exactly where we lose coherence. A more comprehensive ApRES study should be done at a shallower site where the processes we outline in Figure 3 can be adequately constrained. Ideally, this site would have a high surface velocity (100's of m per year), with some partitioning between sliding and shear, and high relief in the basal topography.

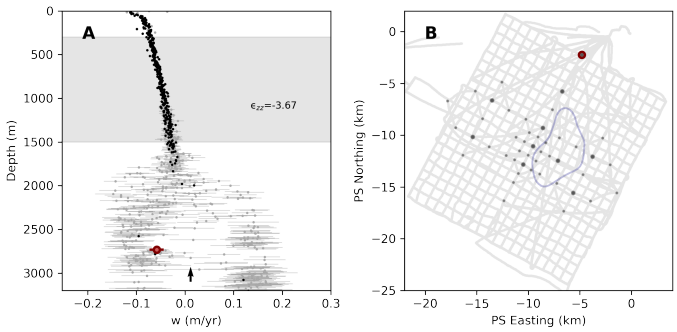

Figure C.1: A single ApRES acquisition as in Figure 4.3C. A) Measured vertical velocities and the calculated vertical strain rate ($\times 10^{-5}\text{yr}^{-1}$) by linear regression of the solid black dots within the grey region. The reported value for vertical strain rate ($\dot{\varepsilon}_{zz}$) is negative (compressive). The arrow shows the apparent bed motion, i.e., the dot product of the surface velocity with the depth (surface minus bed) gradient of the basal reflector. B) The survey map with the specific ApRES acquisition location (red dot), other ApRES sites (large grey dots), and all the velocity acquisition sites (small grey dots).

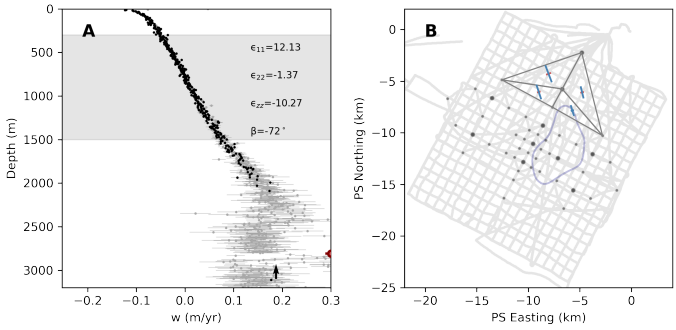

Figure C.2: A single ApRES acquisition as in Figure C.1, but with more surface strain information. For this location, four velocity measurements surround the acquisition location (triangles on the map), so strain rate calculations are shown as red and blue lines in as in Figure S9. The calculated values are printed on the profile in (A) for the mean strain rate. The first principal strain rate ($\dot{\varepsilon}_{11}$) is the most tensile, and the second ($\dot{\varepsilon}_{22}$) is the most compressive (again $\times 10^{-5}\text{yr}^{-1}$). The mean azimuth ($\Theta$) is also printed on the left panel.

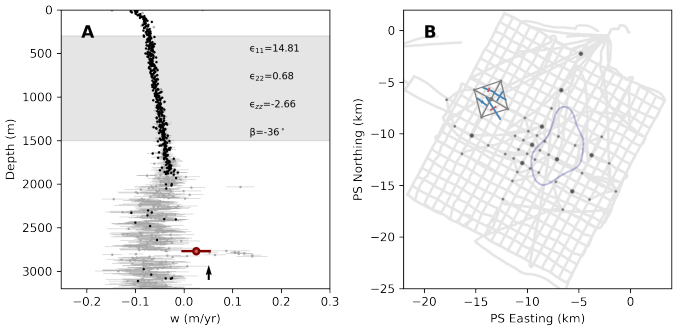
A
ϵ_{11}=14.81
ϵ_{22}=0.68
ϵ_{zz}=-2.66
β=-36°
Depth (m)
w (m/yr)
B
PS Northing (km)
PS Easting (km)

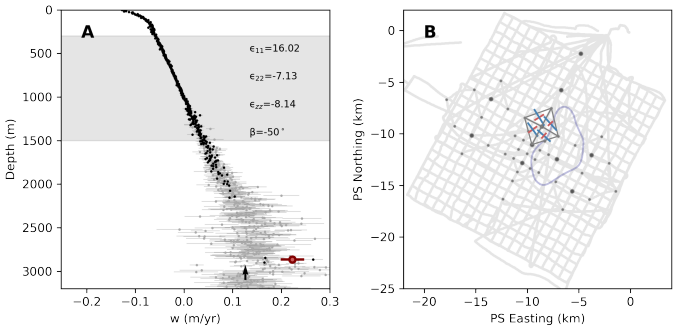
A
ϵ_{11}=16.02
ϵ_{22}=-7.13
ϵ_{zz}=-8.14
β=-50°
Depth (m)
w (m/yr)
B
PS Northing (km)
PS Easting (km)

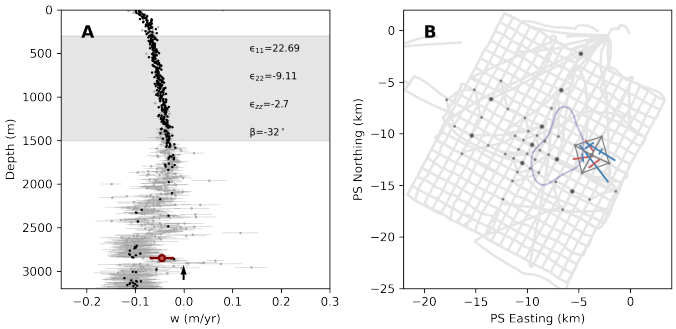
A
ϵ_{11}=22.69
ϵ_{22}=-9.11
ϵ_{zz}=-2.7
β=-32°
Depth (m)
w (m/yr)
B
PS Northing (km)
PS Easting (km)

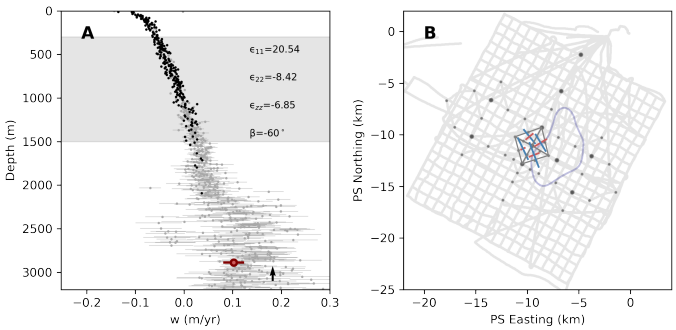
A
ϵ_{11}=20.54
ϵ_{22}=-8.42
ϵ_{zz}=-6.85
β=-60°
Depth (m)
w (m/yr)
B
PS Northing (km)
PS Easting (km)

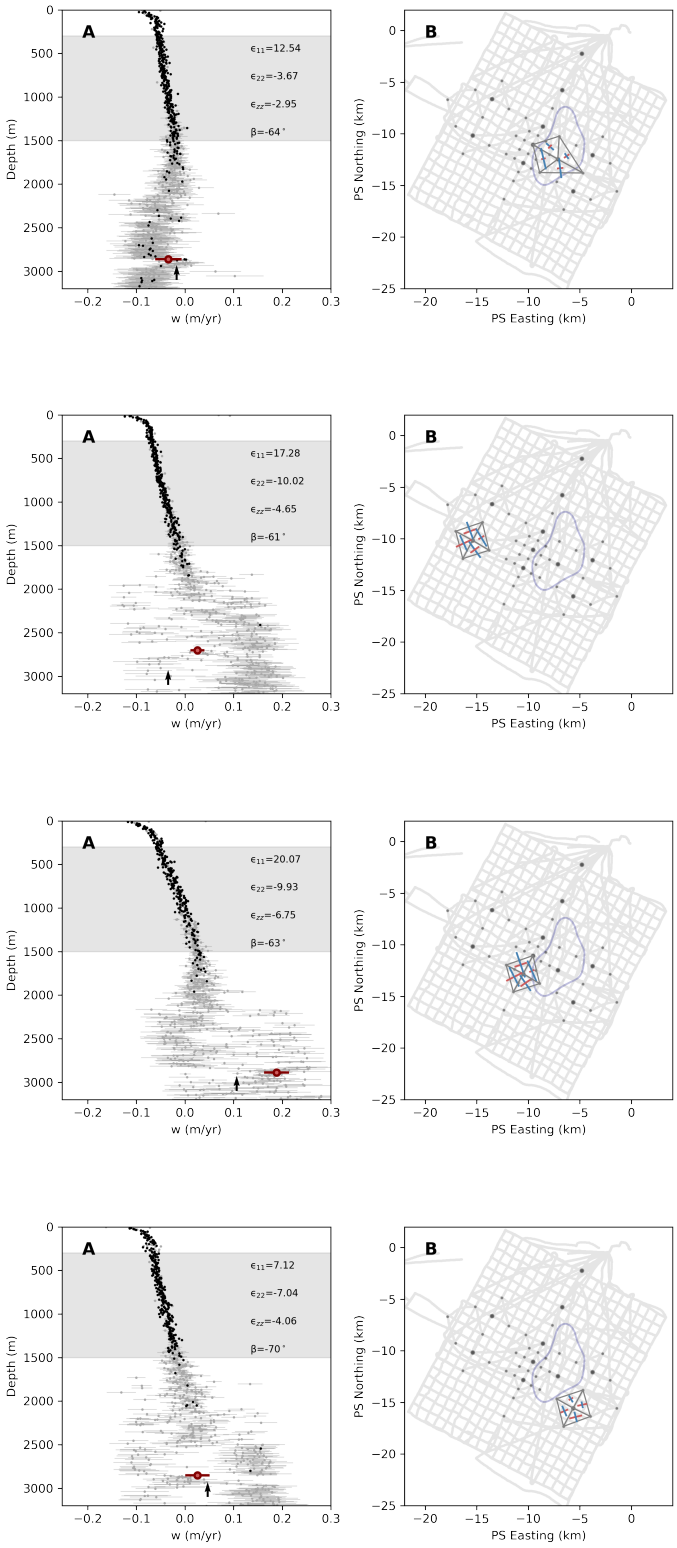
A
B
ϵ_{11}=12.54
ϵ_{22}=-3.67
ϵ_{zz}=-2.95
β=-64°
ϵ_{11}=17.28
ϵ_{22}=-10.02
ϵ_{zz}=-4.65
β=-61°
ϵ_{11}=20.07
ϵ_{22}=-9.93
ϵ_{zz}=-6.75
β=-63°
ϵ_{11}=7.12
ϵ_{22}=-7.04
ϵ_{zz}=-4.06
β=-70°
Depth (m)
w (m/yr)
PS Northing (km)
PS Easting (km)

Appendix D

South Pole Lake - Attenuation Intercomparison

This is an excerpt from a manuscript which was originally published in Annals of Glaciology (Hills et al., 2020). Here, we use the attenuation framework described in Section 2.3.2 to calculate attenuation rates for the radar survey at South Pole Lake (i.e. Chapter 4). For more detailed results from each method, see the original manuscript.

We digitized *every* observed englacial reflector for the radar dataset at South Pole Lake using ImpDAR (Lilien et al., 2020). Layers are then matched between profiles at their crossover locations. The power of an identified wavelet is calculated from the root-mean-square (RMS) amplitude between the two troughs of the wavelet. After isolating bright reflections, the measured power is corrected for known physical effects (equation 2.57) including spherical spreading, refractive focusing, roughness (by Kirchhoff theory). Uncertainty in measured power (σ_{P_c}) is defined layer-by-layer, using the mean difference between crossing profiles within one Fresnel zone of the cross-over locations. Relative uncertainty in reflector depth is defined in the same way ($\sigma_z = 1$ meter) although this value is admittedly difficult to know precisely. With measured power and uncertainty from all interpreted reflectors, we carry out all the empirical attenuation methods for this survey.

Methods 1 and *2* give the attenuation rate for each interpreted reflector. The plotted attenuation rate is representative of ice over the depth range that the reflector spans. The resulting attenuation

rates generally increase with depth but with high variability. Curiously, we observe many negative attenuation rates, especially near the ice surface; this result is nonphysical. Of the reflectors that meet our uncertainty criteria (i.e. below 0.3 dB/km), the bed (*Method 1*) shows the highest attenuation rate, 16.7 $\pm$ 0.2 dB/km, and the lowest attenuation rate is -20.9 $\pm$ 0.3 dB/km from a reflector at 800 m depth. The calculated uncertainty is highest for the shallowest reflectors (up to $\sim$2 dB/km), but rapidly decreases toward lower uncertainty with depth and is generally less than 0.3 dB/km for reflectors deeper than 1 km.

Method 5 gives trace-by-trace attenuation rates from both RMS power and threshold samples. The results using RMS power are normally distributed around 3.5 $\pm$ 1.1 dB/km. The threshold samples give slightly higher attenuation rates and lower uncertainty, 4.4 $\pm$ 0.3 dB/km. The standard deviation for reported attenuation rates is within the calculated uncertainty for RMS power (0.5 dB/km) and only slightly greater than the calculated uncertainty for threshold samples (0.6 dB/km). As expected, the total range in reported values from *Method 5* (i.e. the spatial variation in attenuation over SPL) is minimal ($\sim$2 dB/km).

Method 6 gives depth-resolved attenuation rates using multiple reflectors from both RMS power and threshold samples. Low and sometimes negative attenuation is observed near the surface, with the lowest result for RMS power 0.2 $\pm$ 0.01 dB/km and for threshold samples -0.5 $\pm$ 0.05 dB/km. The calculated attenuation rates climb as the fitting window moves toward the bed. This continues until the window gets to $\sim$2 km depth, below which there are not continuous coherent reflectors to implement this method. At the deepest window, the calculated attenuation rate by RMS power is 7.9 $\pm$ 0.01 dB/km and by threshold samples is 9.1 $\pm$ 0.05 dB/km. Both the variation in attenuation and the calculated uncertainty are greatly reduced with increasing window size (values reported in the text are using the 15-wavelength window).

We tested two different techniques for isolating 'bright' reflectors, one by calculating the RMS amplitude of an isolated wavelet and another by thresholding bright samples within a window of the trace. Both give similar depth and power for the bright reflectors. The attenuation rates are also similar for each, but with slightly higher uncertainty in the RMS case.

Even though we observe some discrepancy between the attenuation methods applied here, after discarding the results which do not meet our uncertainty criteria, the calculated attenuation rates approximately agree with what is expected based on the predicted attenuation from a chemistry-

dependent Arrhenius model (MacGregor et al., 2007). Single-reflector methods (i.e. *Methods 1* and *2*) result in a highly variable attenuation-depth profile that loosely represents the modeled profile but only for the deepest reflectors. The bed reflector (*Method 1*) gives the highest reported attenuation rate, which is expected because it is sampling the deepest and warmest ice. Multiple-reflector methods (i.e. *Methods 5* and *6*) are characteristic of the ice column in a bulk sense, but tend to misrepresent attenuation rates near the surface and bed.

For the survey presented here, spatial variation in attenuation rates are expected to be exceedingly small. There is no hydrologic or ice-dynamic feature that would cause a spatial gradient in ice temperature (Hills et al., 2017; Holschuh et al., 2019), and the impurity concentration should predominantly vary in the vertical, even at the ice-sheet scale (K. Matsuoka et al., 2012; M. J. Siegert et al., 1998). Hence, it was unsurprising that the trace-by-trace attenuation results were normally distributed with a standard deviation close to the calculated uncertainty. Perhaps more interesting is the agreement to within one standard deviation between RMS power results (which require semi-automated interpretation) and threshold sample results (which can be extracted automatically). Manually interpreting reflectors is time intensive. Our result points out that this manual interpretation could potentially be avoided in some studies, as long as the SNR for reflectors is high: that is, above the noise floor for reflectors shallower than $\sim$.85 of the ice thickness.

Depth-resolved attenuation results (*Methods 2* and *6*) show increasing attenuation rate with depth which is expected based on the strong temperature dependence. This result is encouraging given that prior attempts to resolve attenuation measurements with depth have shown the opposite result (i.e. decreasing attenuation with depth) (Holschuh et al., 2016; K. Matsuoka, Morse, et al., 2010). On the other hand, results from *Method 2* are significantly lower than expected (even negative) for most of the reflectors close to the surface, and there is high variance between results for all layers throughout the ice column. *Method 2* is an adaptation from the common-midpoint method outlined by Holschuh et al. (2016). Admittedly, it did not work well for this common-offset survey; however, results are more encouraging at other locations even with the same radar system (i.e. data from Northeast Greenland Ice Stream (Christianson et al., 2014) and unpublished data from Hercules Dome). One obvious explanation for the counter intuitive results from *Method 2* is that the reflectors are too flat near the surface, so using a regression to calculate attenuation is inappropriate because there is insufficient depth variation. This effect can be seen by the increasing uncertainty

Figure D.1: A comparison of all attenuation calculations and corresponding uncertainty calculated in this study. a) Attenuation results replotted from *Methods 1* and *2*, *Method 5*, and *Method 6*. The vertical lines represent the mean values from *Method 5* over the depth interval which the interpreted reflectors span. Only results from the 15-wavelength window are shown for *Method 6*. The black dashed line is the modeled profile from a temperature- and chemistry-dependent Arrhenius model (MacGregor et al., 2007) with uncertainty in the grey shaded region. Temperature input for the model is a Robin (1955) solution with air temperature -51.5°C, accumulation 8 cm/yr, and geothermal flux 75±10 mW/m^2, which generally approximates the nearest measured temperature profile (Price et al., 2002). Approximate ion concentrations are used for the entire ice column: the ice acidity $[H^+] = 1 \pm 0.5M$; and the sea salt concentration $[ssCl^-] = 3 \pm 0.5M$ (MacGregor et al., 2009; MacGregor et al., 2007; K. Matsuoka, MacGregor, et al., 2010). b) Regression uncertainty plotted against the degrees of freedom (number of points in the regression) for each of the methods implemented in this study (dots) and a profile of the uncertainty coefficient from equation A.3 to show that the number of measured points in the regression strongly controls the reported uncertainty.

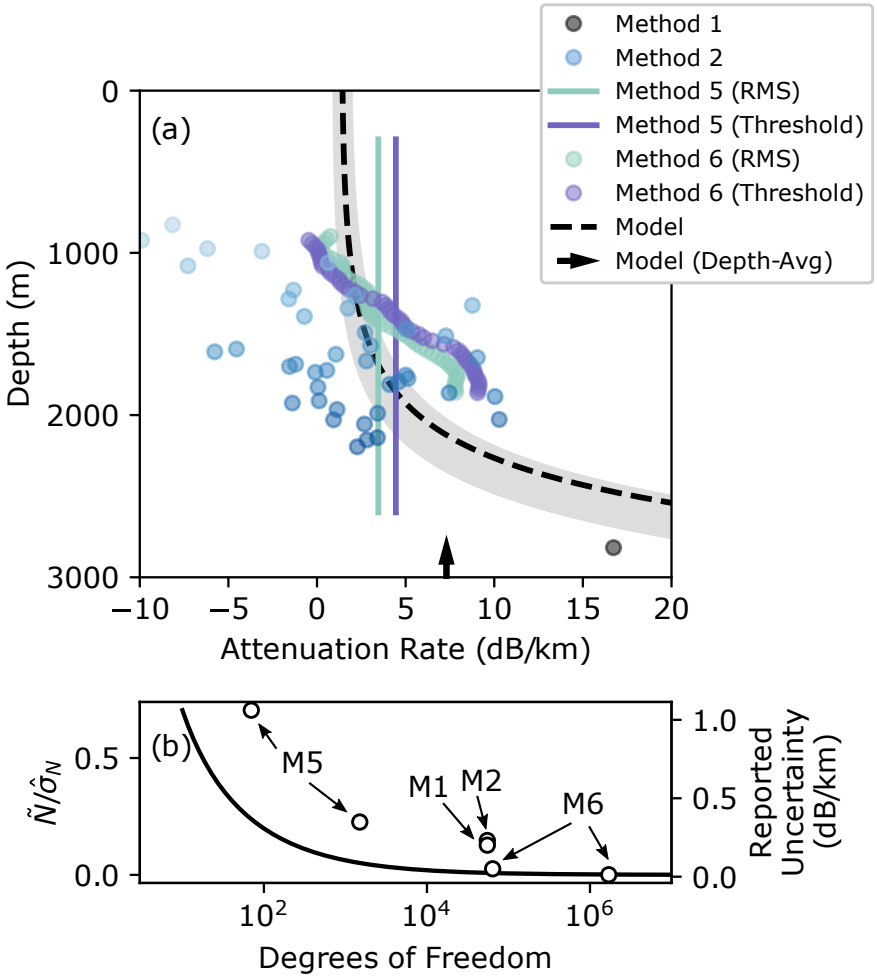
Method 1
Method 2
Method 5 (RMS)
Method 5 (Threshold)
Method 6 (RMS)
Method 6 (Threshold)
Model
Model (Depth-Avg)
(a)
Depth (m)
0
1000
2000
3000
−10
−5
0
5
10
15
20
Attenuation Rate (dB/km)
(b)
$\tilde{N}/\hat{\sigma}_N$
0.5
0.0
M5
M1
M2
M6
1.0
0.5
0.0
Reported Uncertainty (dB/km)
10^2
10^4
10^6
Degrees of Freedom

for near-surface layers. However, we also see that the power between reflectors is near-constant for the first ∼1000 m below the surface, causing slightly negative attenuation rates even from the multiple-reflector methods. An alternative explanation is that there are reflectivity changes between reflectors, which violates the assumption that $\frac{\partial[R]}{\partial z} \approx 0$. While it would be tempting to make reflectivity corrections using dielectric profiling data from nearby ice cores (MacGregor, Li, et al., 2015, Appendix A), prior efforts to do so at other locations have proven challenging (Eisen et al., 2003a, 2003b; Eisen et al., 2006). Moreover, these dielectric profiling experiments have not yet been done for the South Pole Ice Core.

The reported uncertainty is much lower than expected. In many cases the uncertainty for a given method is less than the variance observed between results for that same method; this is especially apparent in *Method 2*. Where this is true, some violation of the assumption, $\left|\frac{\partial[R]}{\partial z}\right| \ll \left|\frac{\partial[P_c]}{\partial z}\right|$, must be introducing a hidden bias in the regression that is not represented in the uncertainty calculation. Instead, the uncertainty is most strongly dependent on the number of measurements included in the regression (Figure D.1B). As an alternative uncertainty metric, Schroeder, Seroussi, et al. (2016) scale their fitting statistics to the attenuation cross-over error, although this value will still be subject to the same hidden biases.

The primary advantage of radar sounding is that it can infer subsurface properties without direct sampling. Because radar attenuation in ice is so strongly dependent on temperature, one somewhat elusive goal has been to measure temperature with radar. While depth-averaged temperature results have been reported (MacGregor, Li, et al., 2015), published results for depth-resolved attenuation and corresponding ice temperature have given counter intuitive or nonphysical results (Holschuh et al., 2016; K. Matsuoka, Morse, et al., 2010). Initial attempts with seismic data have been more promising (L. E. Peters et al., 2012). Unfortunately, seismic data acquisition requires intensive ground activities, and it is thus not suitable to apply at the ice-sheet scale in the way that radar methods are. Theoretical considerations suggest that radar methods are likely to be as capable as seismic methods with proper experimental design, especially when accounting for ice chemistry (MacGregor et al., 2007). Looking forward, it is important to assess how precisely we can measure attenuation (and associated temperature changes) for a given empirical method.

Prior attenuation studies use variations on the methods described here, both to calculate the attenuation and to constrain uncertainty (Table 2.2). Published attenuation uncertainty ranges from

$\sim$0-8 dB/km, with a few outliers up to 89.9 dB/km. The uncertainty in the associated ice temperature is up to $\sim$15°C for pure ice at ~-30°C. The reported uncertainty from our study is on the lower end of this range, 0.01-1.6 dB/km, as are most that report uncertainty from a regression result. It should be noted though, that the regression is often calculated using thousands of points (as is done here), and that many studies only report the regression uncertainty with no direct consideration of uncertainty in the regressor variables, both of which lead to erroneously low uncertainty estimates. If any of the sources of uncertainty discussed within our outline of the attenuation framework act to violate the assumption that $\left|\frac{\partial[R]}{\partial z}\right| \ll \left|\frac{\partial[P_c]}{\partial z}\right|$, the resulting uncertainty can be significantly greater than predicted by the regression, and even lead to a nonphysical results as we show in Figure D.1. Any direct interpretation of ice temperature should come only after careful correction for any possible hidden biases.

Appendix E

South Pole Lake - Radar Polarimetry

A single radar polarimetry acquisition was collected from the down-glacier edge of South Pole Lake in December 2018. These results have not been published, but they are a useful test of the polarimetry method since physical properties (including COF) were measured in the nearby ($\sim$15 km away) South Pole Ice Core (Voigt, 2017). Here, I step through the same processing flow as for the polarimetry acquisitions from Hercules Dome (see Chapter 5 and Appendix H), comparing the radar-derived girdle fabric to that directly sampled from the ice core (Figure E.1).

In the uppermost 1000 m, the radar derived girdle strength matches that from the ice core well. Below 1000 m, the CPE locks onto a single azimuth and what look like possible dipole nodes in the interferogram are not nearly as clean as above. The calculated phase gradient for this deeper ice is too small to match the ice-core results. There are several possible explanations for a loss of consistency with the ice core below 1000 m. Phase coherency drops with depth into the ice column due to attenuation. While the more typical depth loss of phase coherence is closer to 1500 m, attenuation is likely a contributing factor (Hills, Christianson, Hoffman, et al., 2022, Supplement). In addition, rotation of the girdle can make the interferogram difficult to interpret (see Section 2.3.3). Finally, since the girdle is significantly stronger here than at Hercules Dome, it is possible that the phase is delayed by more than an entire range bin and that an alternative processing flow would be more appropriate for this dataset (Zeising et al., 2023). Despite the inconsistency for deeper ice, I find the match to ice core COF in the upper ice column to be promising and argue that it supports interpretation of the polarimetry data at Hercules Dome.

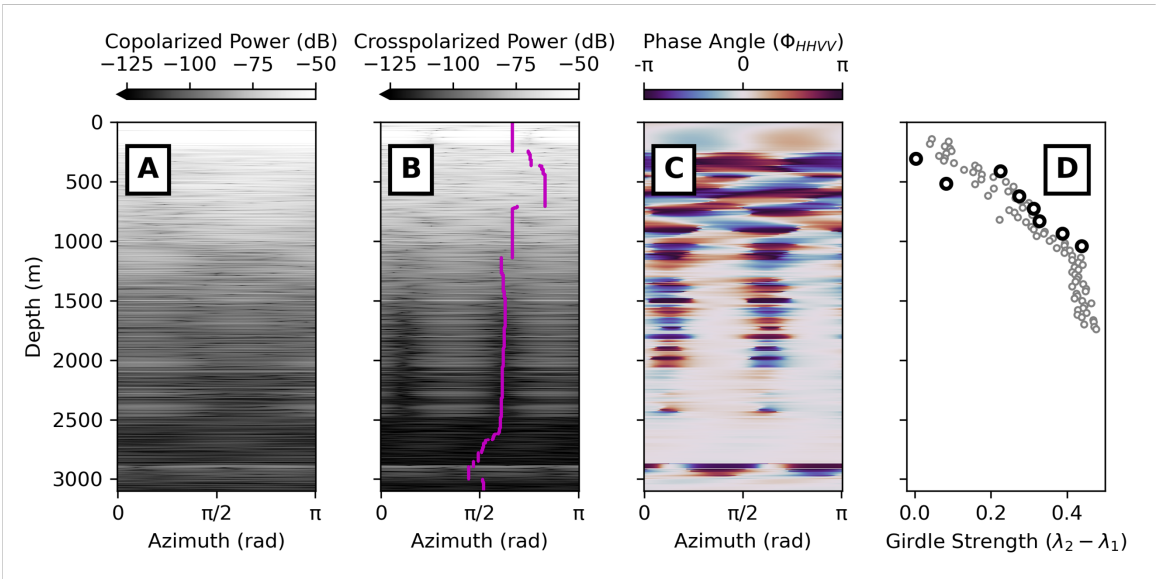

Figure E.1: A single radar polarimetry acquisition from South Pole Lake. A) Co-polarized (HH) power. B) Cross-polarized (HV) power and the selected CPE axis (magenta). C) Co-polarized phase delay. D) Strength of the vertical girdle, both directly from the ice core (grey) and derived from the measured phase gradient along CPE (black).

Appendix F

Hercules Dome - Englacial Layer Dating

Here, we estimate the depth-age relationship at Hercules Dome Summit by matching reflection horizons in the imaged radar stratigraphy between South Pole and Hercules Dome. We start by interpreting layer ages in the survey at South Pole Lake (Chapter 4) using the ages from South Pole Ice Core (Epifanio et al., 2020). We match those layers to stratigraphy in the ITASE traverse (Welch & Jacobel, 2003) at a location where those two surveys cross (Figure F.1). Then, we match those layers onto the survey at Hercules Dome (Chapter 5).

Unfortunately, the ground-based survey at Hercules Dome is not continuous between East Dome (where the ITASE traverse crosses) and HD Summit (the most likely ice-core drilling location). Instead of direct layer matching at a crossover location, we match layers based on the similarities in the reflected power profile. (Figure F.2). The interpreted layer ages are within the uncertainty of the modeled depth-age scale (Fudge et al., 2022) although with a slight bias toward older ages.

Based on the above layer matching to South Pole Ice Core, the deepest continuous layer at HD Summit was deposited at the ice surface 49 thousand years ago. In Figure F.2E we show the height of that deepest layer above the ice-bed interface. The higher that layer is above the bed in a given location, the more room for older ice there is in the deep ice column. While this is not the only important indicator for a good ice-core location, it does suggest that sites to the grid north of the surface divide are potentially holding older ice than those to the grid south.

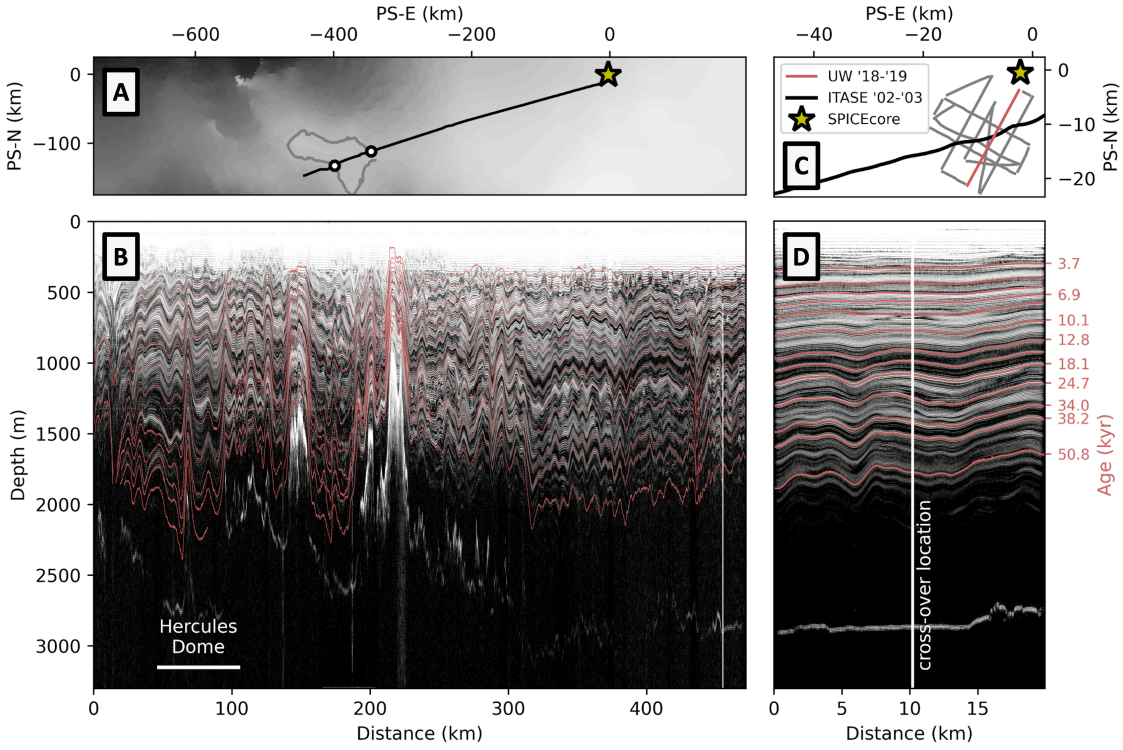

Figure F.1: Englacial layer matching and dating to South Pole Ice Core. (A and B) Reference map and radar profile from the ITASE traverse (Welch & Jacobel, 2005) with interpreted englacial reflectors in red. (C and D) Reference map and radar profile from South Pole Lake (Hills, Christianson, Hoffman, et al., 2022).

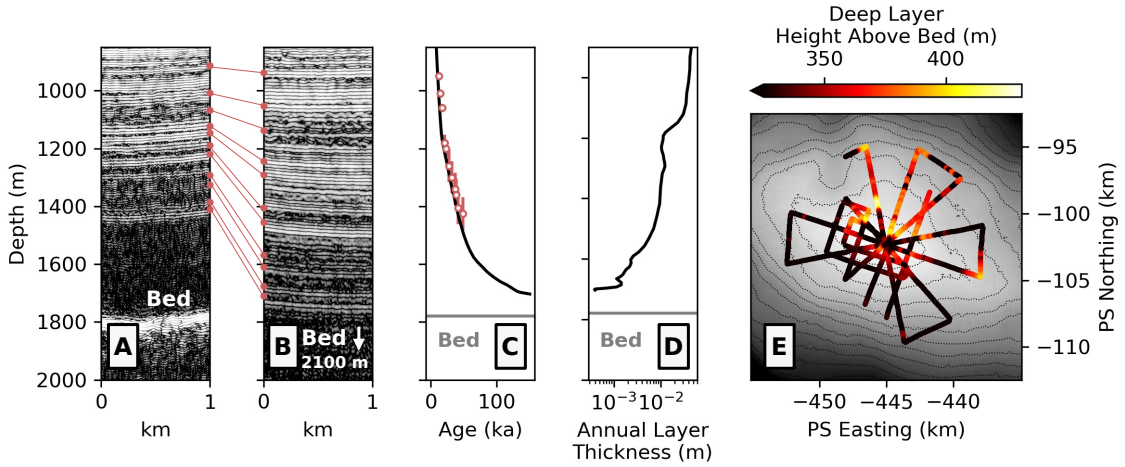

Figure F.2: Layer dating and matching between western and eastern Hercules Dome. A) Radar profile segment from the Hercules Dome summit. B) Radar profile segment from eastern Hercules Dome (East Dome) (collected in the 2019-20 season) with interpreted layers (red) directly traced from South Pole Ice Core. C) Depth-age scale for modeled (gray region) and radar-derived (red dots) ages. D) Modeled annual layer thickness (derivative of depth-age scale in (C)). E) Height above the bed for the deepest interpretable englacial layer.

Appendix G

Hercules Dome - Attenuation Intercomparison

This appendix is analogous to Appendix D but for the radar survey from Hercules Dome (i.e. Chapter 5).

Here, we use interpreted radar reflections for two profiles from the ground-based survey at Hercules Dome (Chapter 5), the first from HD Summit (i.e. Figure 5.4) and the second from East Dome (i.e. Figure 5.6). Reflected power is extracted from each interpreted layer using ImpDAR (Lilien et al., 2020) and calculated from the root-mean-square amplitude between the two troughs of the wavelet. For both profiles, we pick all of the observed layers. We calculate attenuation by two different methods described below.

First, we use *Method 2* from the attenuation framework (Section 2.3.2) to calculate attenuation rates for each interpreted layer in each profile (Figure G.1). As was true for the attenuation results from South Pole Lake (Appendix D) some of the resulting attenuation rates calculated by *Method 2* are negative (nonphysical) especially those near the surface. As before, we suggest that the depth relief of those near-surface layers is insufficient for the attenuation regression, leading to a nonphysical result. For both profiles, deeper layers have increasing attenuation rates, likely a result of the increasing ice temperature near the bed.

Second, we use *Method 6* to calculate attenuation rates in a depth profile, here only for the profile from HD Summit (Figure G.2). We match those calculated attenuation rates to a depth-temperature

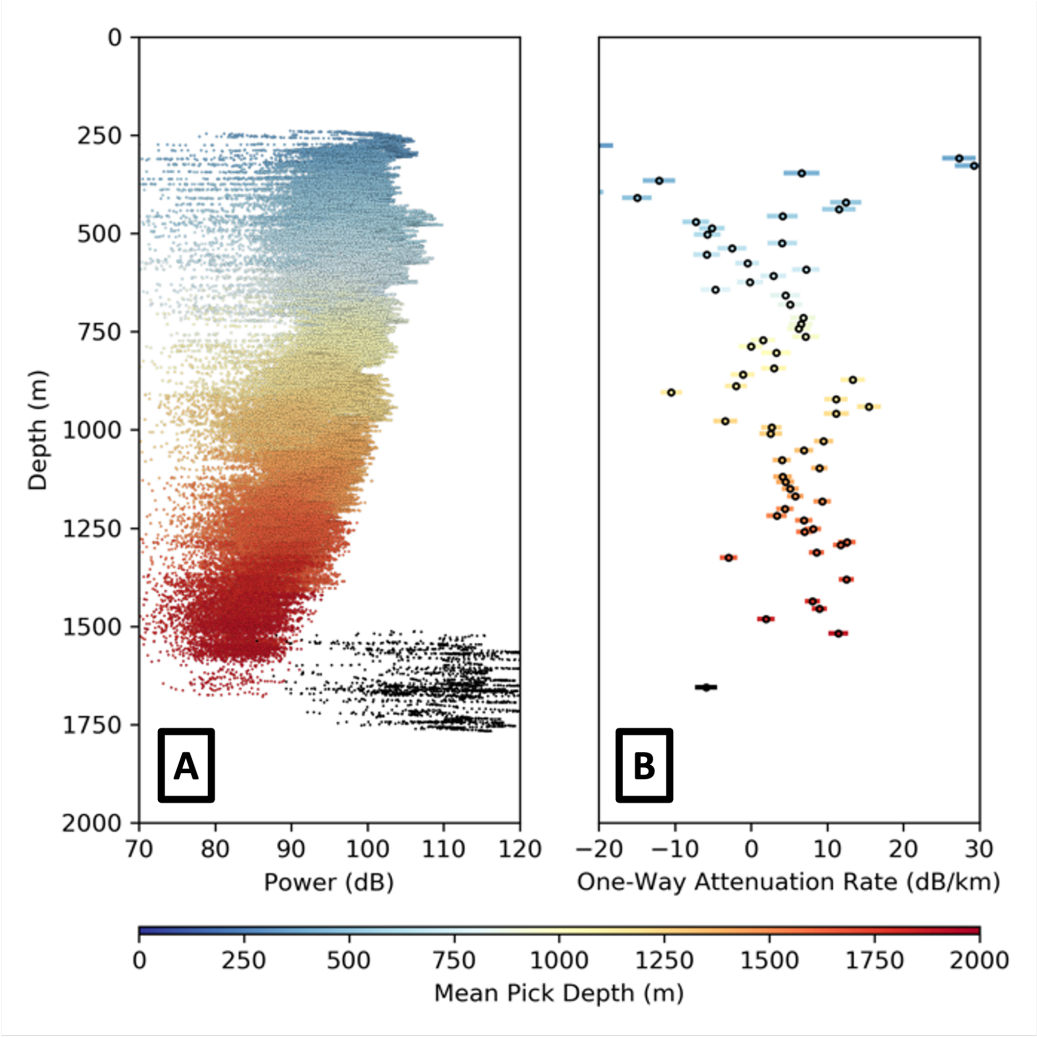

Figure G.1: Measured radar power (A) and attenuation rate by *Method 2* (B) at the Hercules Dome Summit.

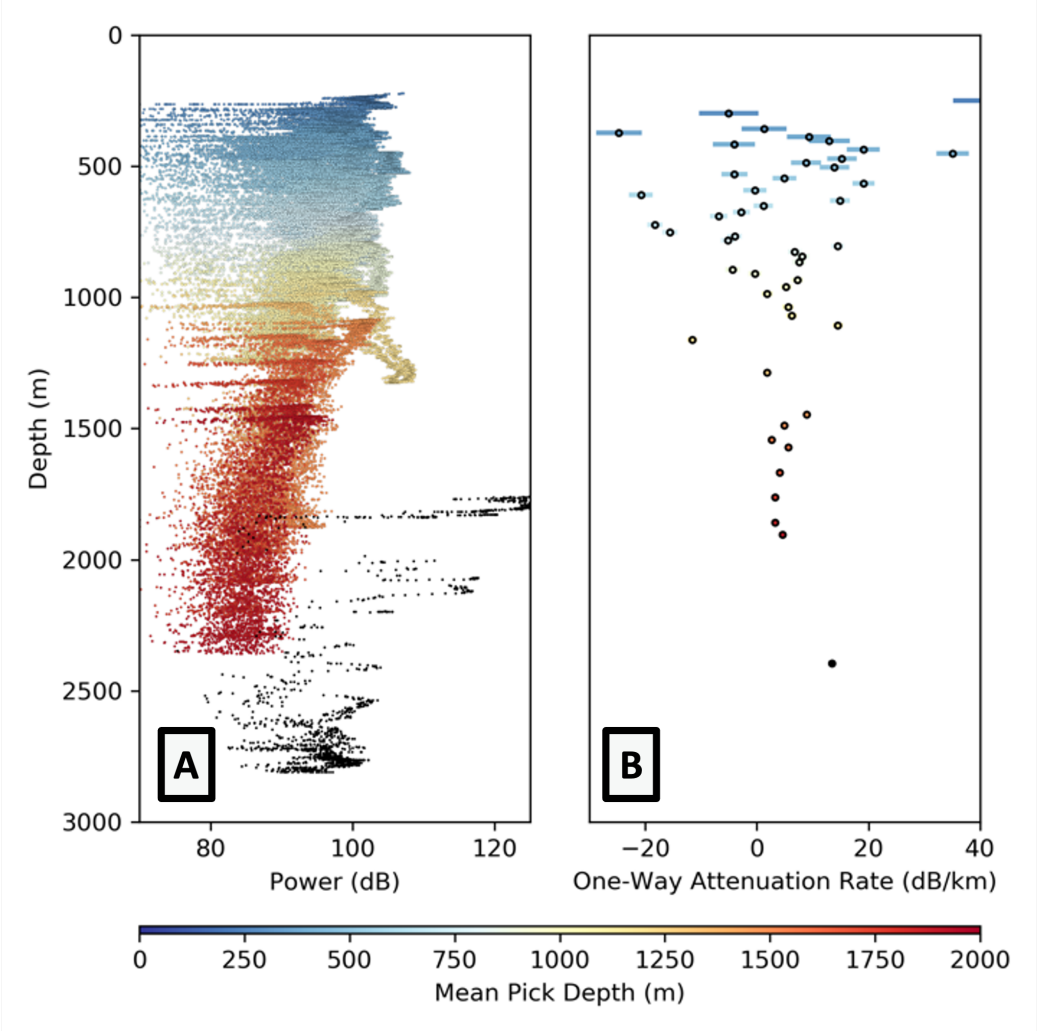

Figure G.2: Same as Figure G.1 but for the neighboring East Dome.

profile (Robin (1955) Solution) with varying geothermal flux and accumulation rate. We find that the calculated attenuation rates most closely match the temperature profiles which are frozen at the ice-bed interface.

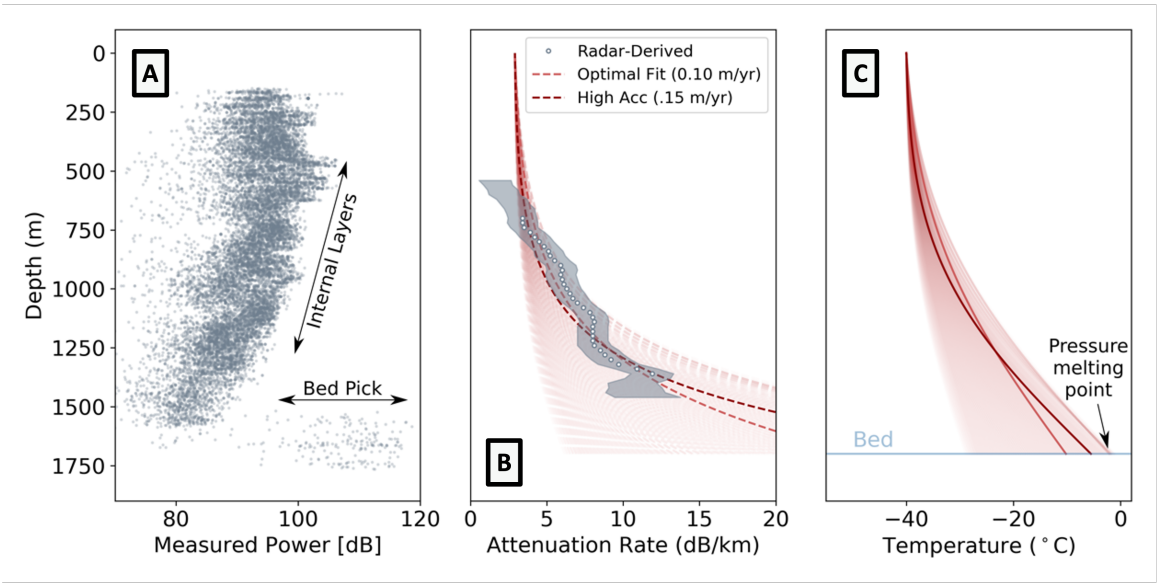

Figure G.3: Measured radar power (A), calculated (*Method 6*) and modeled attenuation rates (B), and modeled temperature profiles (C) (using the Robin (1955) Solution, Section 2.2) for Hercules Dome Summit.

Appendix H

Hercules Dome - Radar Polarimetry

Chapter 5 presented all the ApRES data from Hercules Dome, both time-based interferometry and polarimetry. That chapter focused on the interpretation for divide migration and left out some tangential analysis. Here, I add some detail for one acquisition in particular, from above the bedrock trough at East Dome. I also plot all the measured interferograms for completeness sake.

As stated in Chapter 5, the interpreted girdle orientation for the polarimetry acquisition above the trough is perpendicular to the trough axis (Figure H.1). This result indicates either extension, vertical shear, or both, along the length of the trough. There are three prominent dipole nodes (the most of any acquisition at Hercules Dome) between $\sim$900-1800 m depth. Those depths are dated to pre-Holocene (the upper layer is 10.1 thousand years old), which is longer than the timescale for COF evolution at the measured strain rates. Given the relatively short timescale, I argue that any COF derived from the polarimetry result is indicative of ice dynamics within the Holocene, likely consistent with present-day ice flow.

I now use the measured vertical strain rate from ApRES, and an estimated along-trough strain rate, as input to a model experiment to test the reproducibility of the above polarimetry result (Figure H.2). The non-uniform strain rate (zero at the surface and increasing linearly with depth to 500 m) is necessary to move the first node down to where it is measured. This is not surprising, as the strain rate near the surface is driven by firn compaction and will therefore be less associated with lattice rotation. The measured dipole nodes are slightly out of line, so as a final test I rotate the girdle in depth. I also add some anisotropy to the reflectivity in this test to decrease the width of the nodes

as is observed. It is also possible that coherence loss because of attenuation is driving the decay in node size with depth.

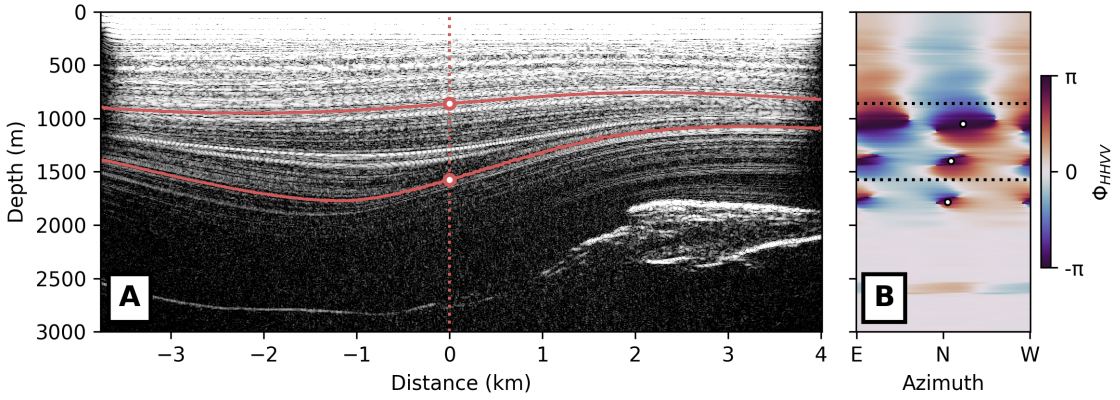

Figure H.1: Radar results from the trough beneath East Dome at Hercules Dome. A) Deep-sounding radar profiling with distance away from the site of the polarimetry acquisition. The two interpreted layers are dated to 10.1 and 24.7 thousand years ago. B) Polarimetric interferogram for an acquisition taken above the trough. Black dashed lines are the depth of the interpreted reflectors in (A). Dots mark the center of the dipole nodes used for comparison to model results in Figure H.2.

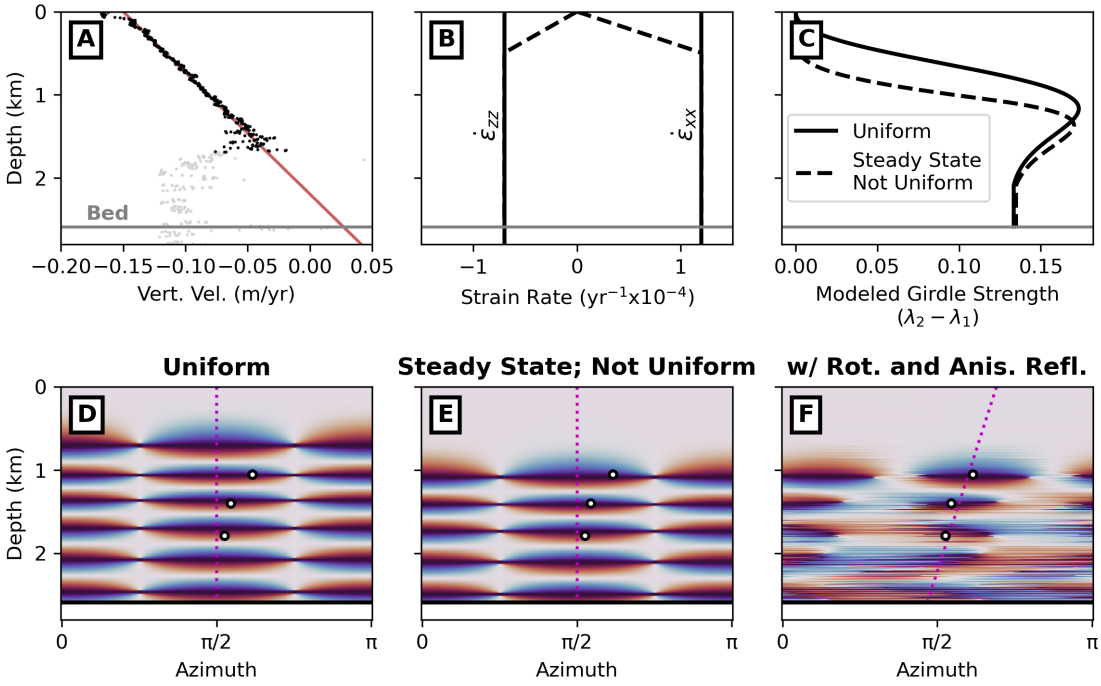

Figure H.2: COF and effective medium modeling for the trough location. A) Measured vertical velocity from the trough ApRES acquisition site for input to the COF model. B) Strain rates for input to the model, with $\dot{\varepsilon}_{zz}$ calculated from (A) and $\dot{\varepsilon}_{xx}$ estimated to match the measured radar polarimetry. C) Modeled girdle strength. D) Modeled co-polarized phase offset for a uniform strain rate (constant in depth). E) Modeled phase offset for increasing strain rate with depth (dashed in (B)). F) Same as (E) but with a girdle rotation (orientation axis along magenta line).

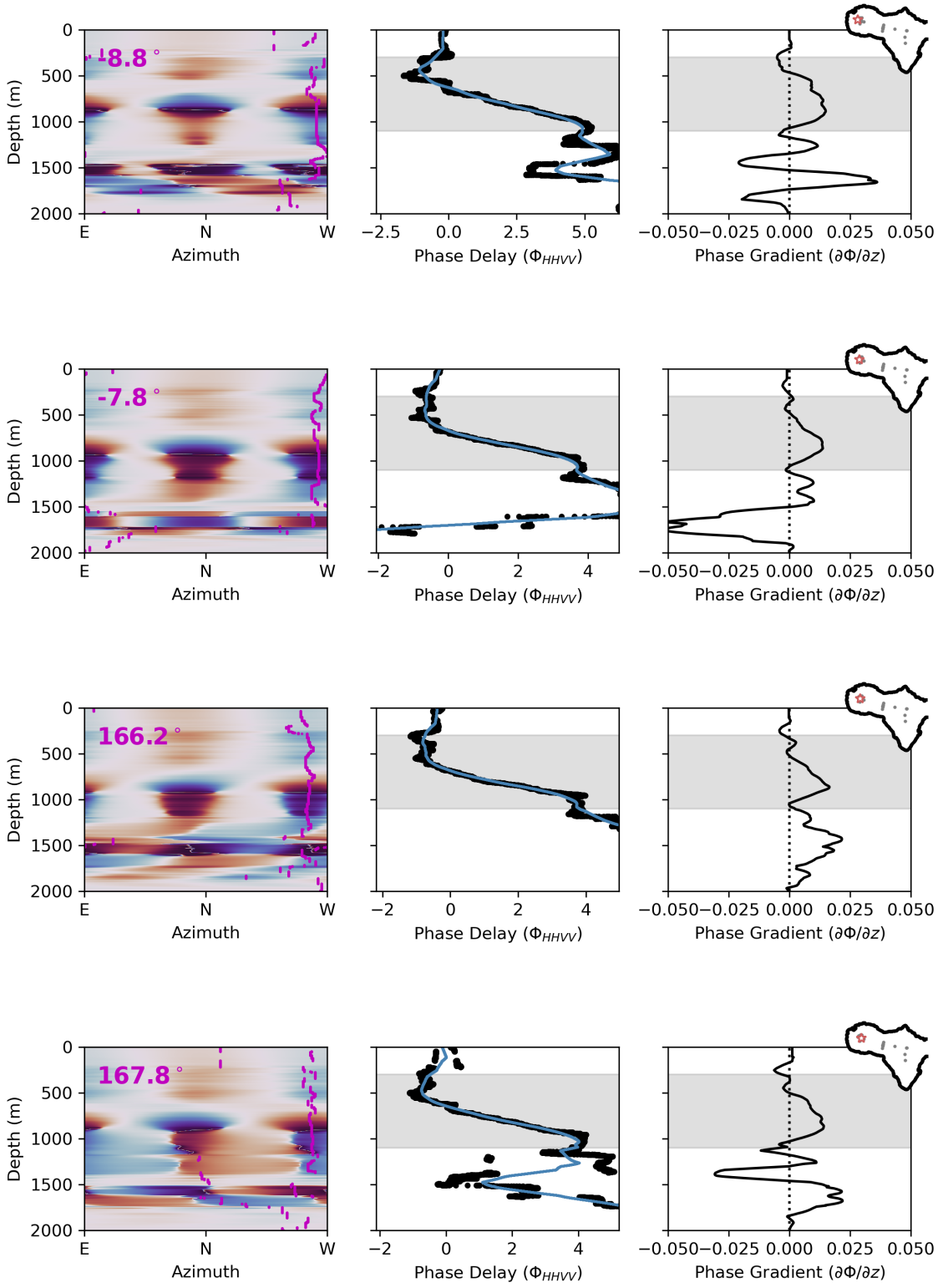
8.8 °
-7.8 °
166.2 °
167.8 °
Depth (m)
0
500
1000
1500
2000
E
N
W
Azimuth
−2.5
0.0
2.5
5.0
−2
0
2
4
Phase Delay (Φ_{HHVV})
−0.050
−0.025
0.000
0.025
0.050
Phase Gradient ($\partial\Phi/\partial z$)

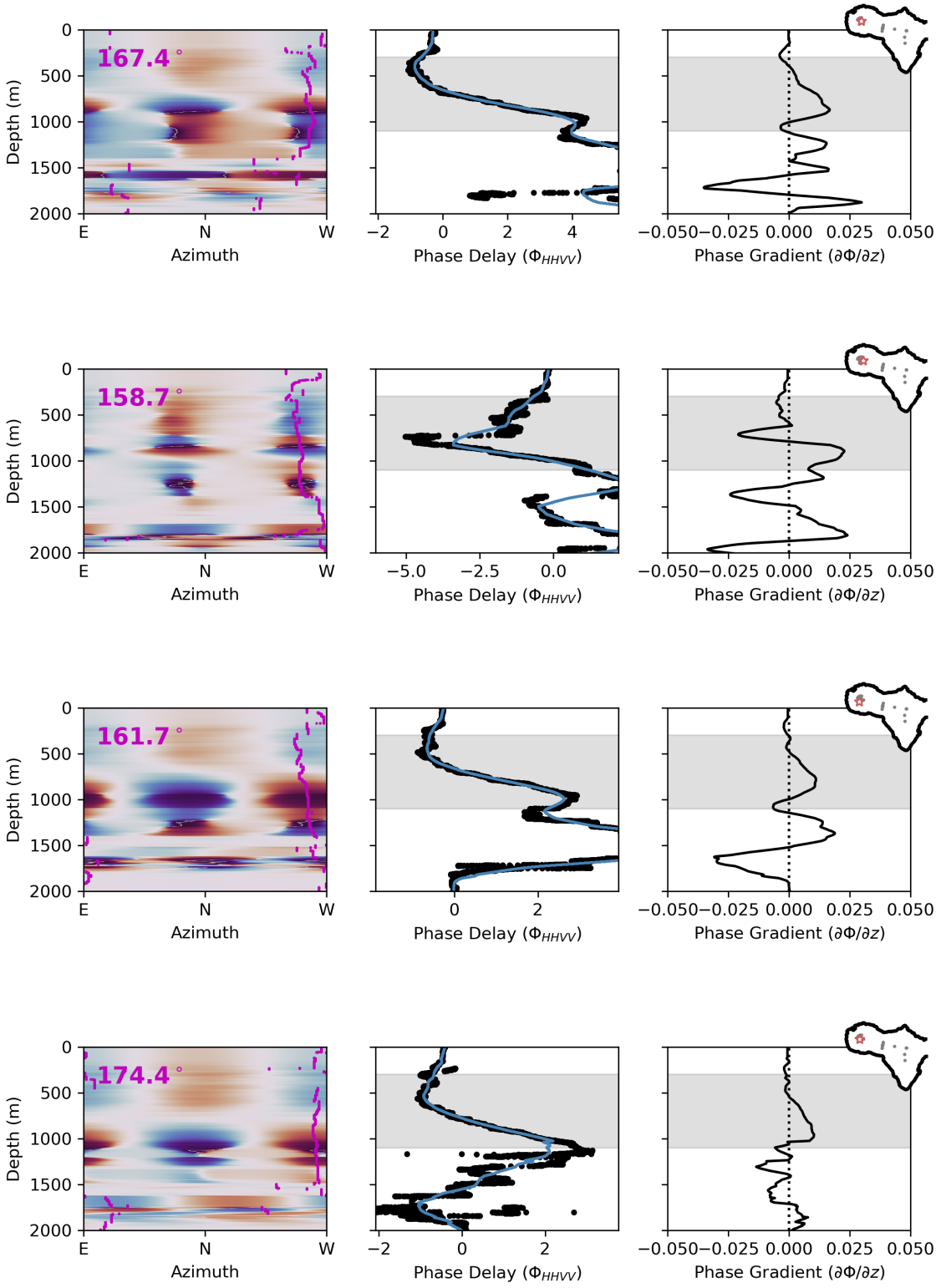
167.4°
158.7°
161.7°
174.4°
Depth (m)
0
500
1000
1500
2000
E
N
W
Azimuth
Phase Delay (Φ_{HHVV})
Phase Gradient ($\partial\Phi/\partial z$)
−0.050
−0.025
0.000
0.025
0.050

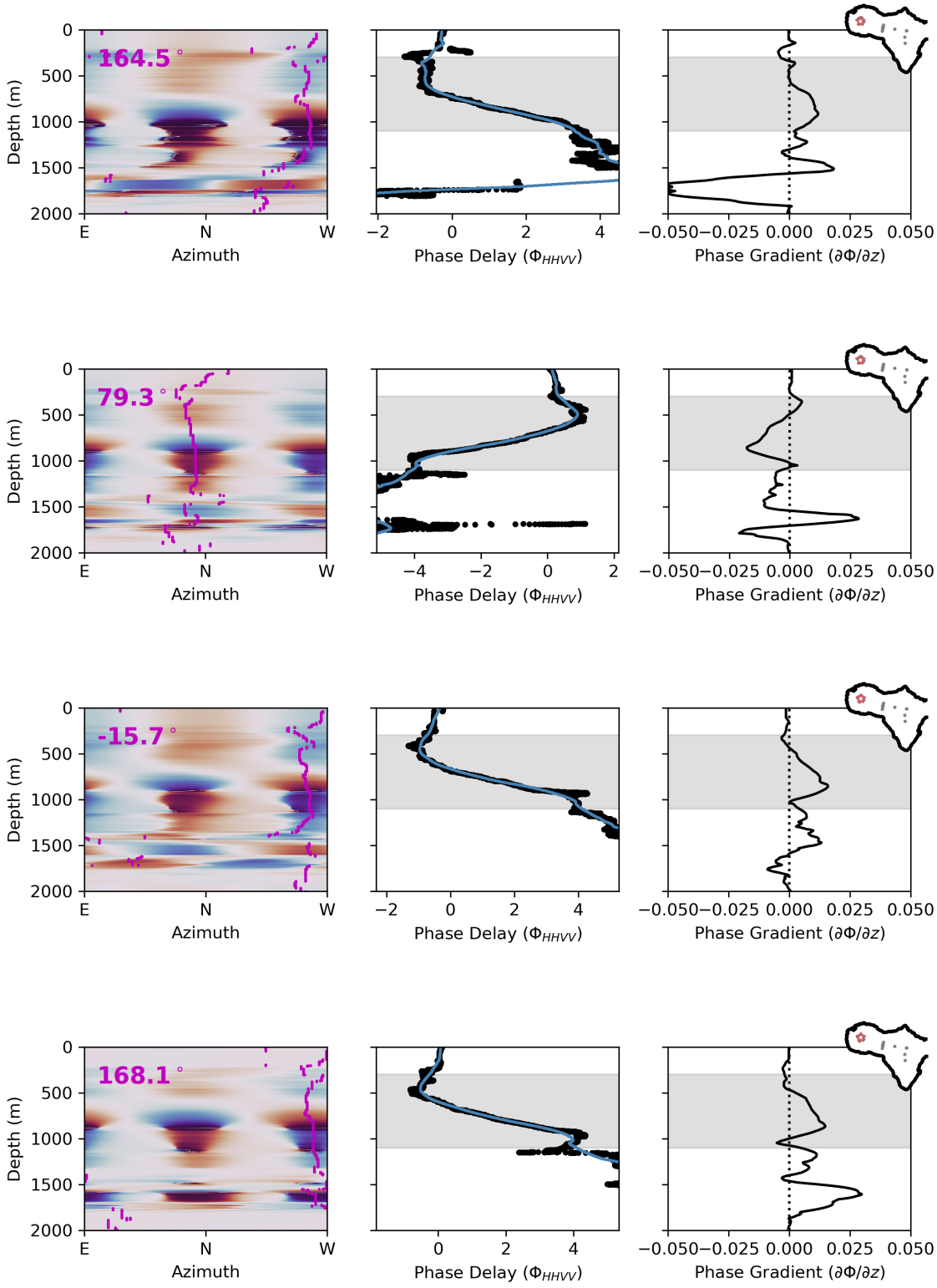
164.5 °
79.3 °
-15.7 °
168.1 °
Depth (m)
0
500
1000
1500
2000
E
N
W
Azimuth
Phase Delay (Φ_{HHVV})
Phase Gradient ($\partial\Phi/\partial z$)
−0.050
−0.025
0.000
0.025
0.050

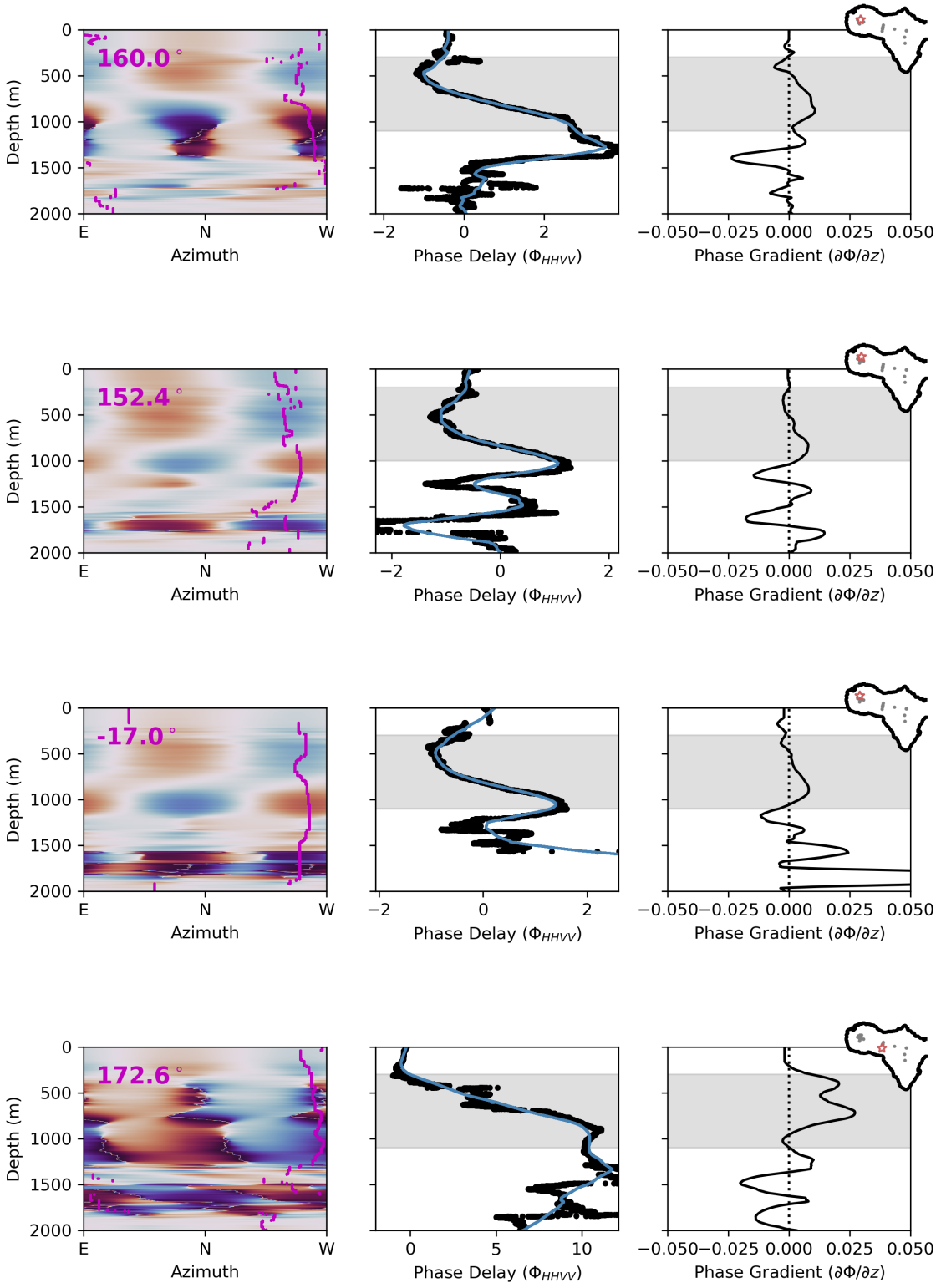
160.0°
152.4°
-17.0°
172.6°
Depth (m)
0
500
1000
1500
2000
E
N
W
Azimuth
−2
0
2
0
5
10
Phase Delay (Φ_{HHVV})
−0.050
−0.025
0.000
0.025
0.050
Phase Gradient ($\partial\Phi/\partial z$)

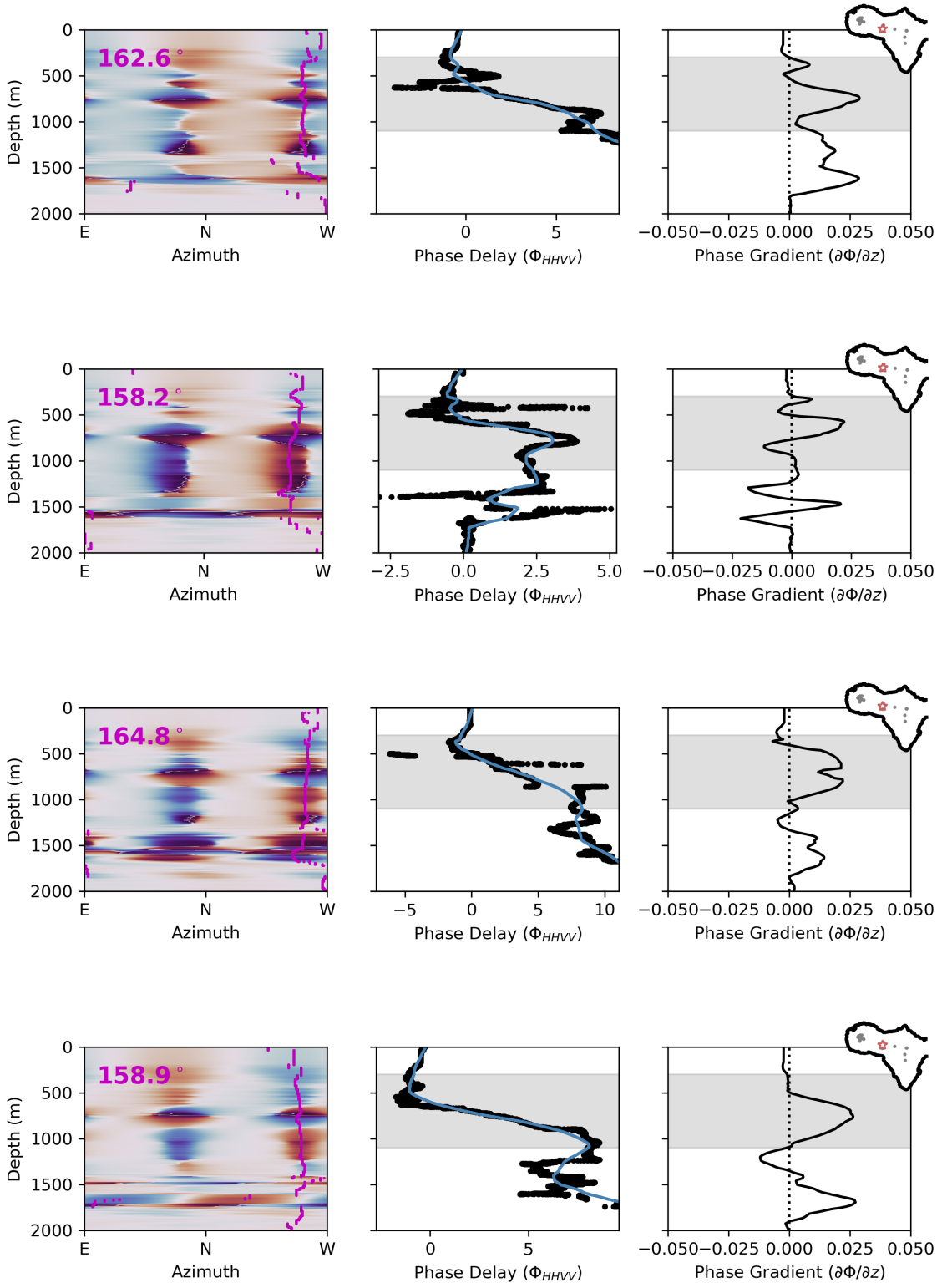
162.6°
158.2°
164.8°
158.9°
Depth (m)
0
500
1000
1500
2000
E
N
W
Azimuth
Phase Delay (Φ_{HHVV})
Phase Gradient ($\partial\Phi/\partial z$)
−0.050
−0.025
0.000
0.025
0.050
−2.5
0.0
2.5
5.0
−5
0
5
10

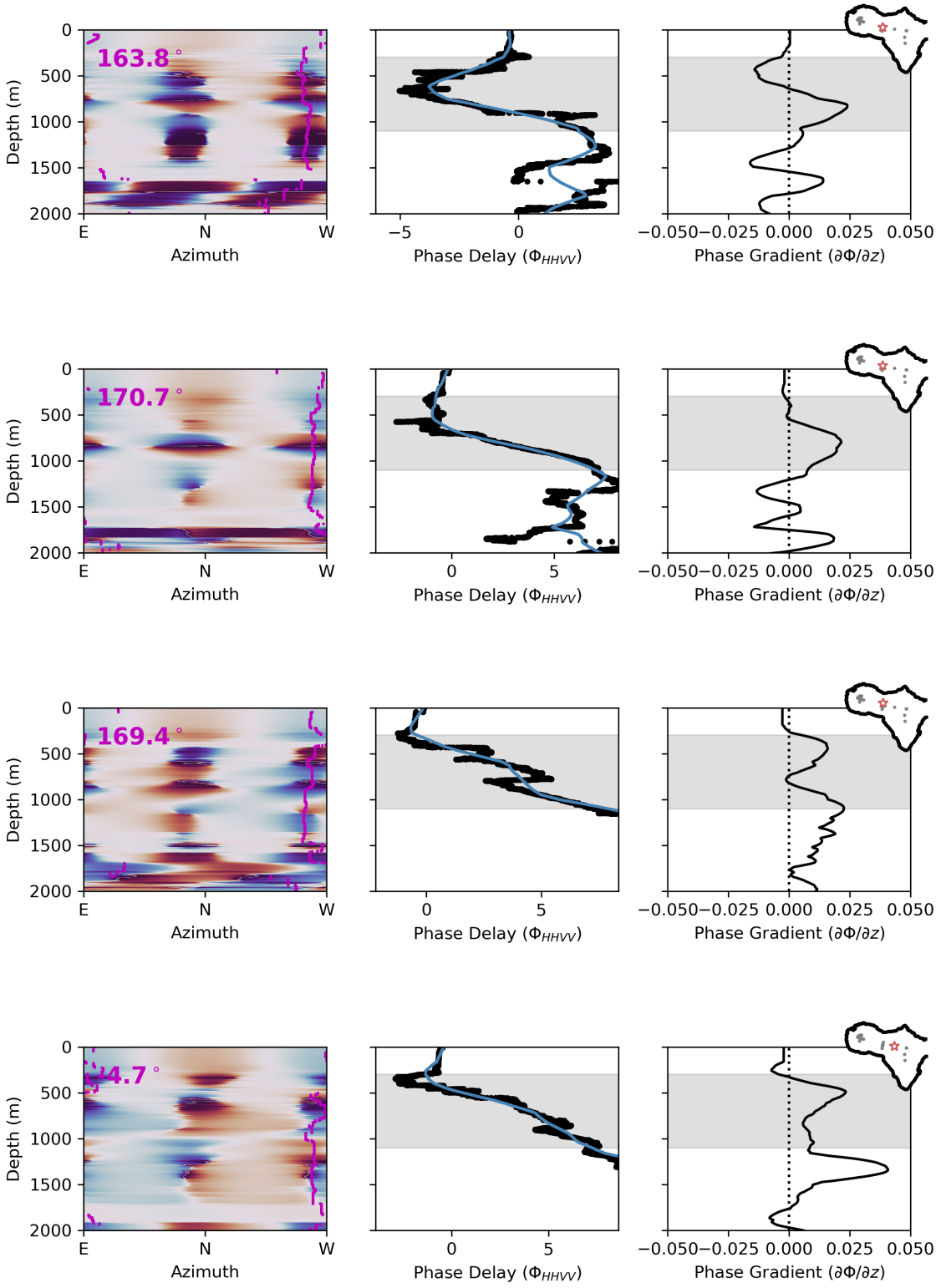
163.8°
170.7°
169.4°
14.7°
Depth (m)
0
500
1000
1500
2000
E
N
W
Azimuth
−5
0
5
Phase Delay (Φ_{HHVV})
−0.050
−0.025
0.000
0.025
0.050
Phase Gradient ($\partial\Phi/\partial z$)

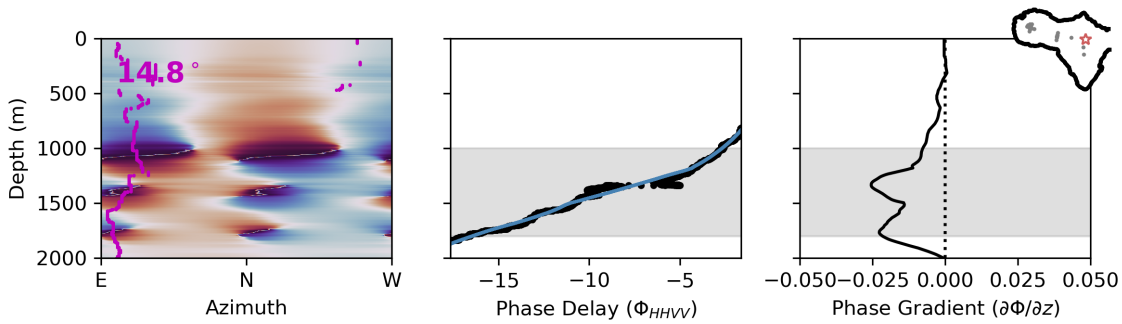
14.8°
Depth (m)
0
500
1000
1500
2000
E
N
W
Azimuth
−15
−10
−5
Phase Delay (Φ_{HHVV})
−0.050
−0.025
0.000
0.025
0.050
Phase Gradient ($\partial\Phi/\partial z$)

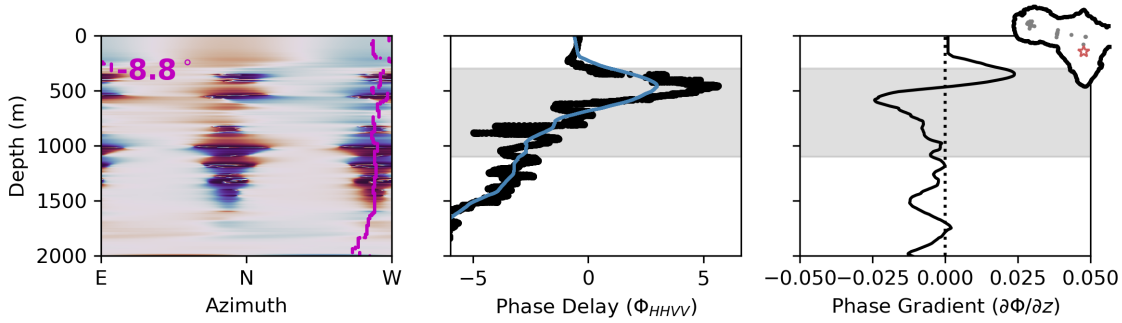
-8.8°
Depth (m)
0
500
1000
1500
2000
E
N
W
Azimuth
−5
0
5
Phase Delay (Φ_{HHVV})
−0.050
−0.025
0.000
0.025
0.050
Phase Gradient ($\partial\Phi/\partial z$)

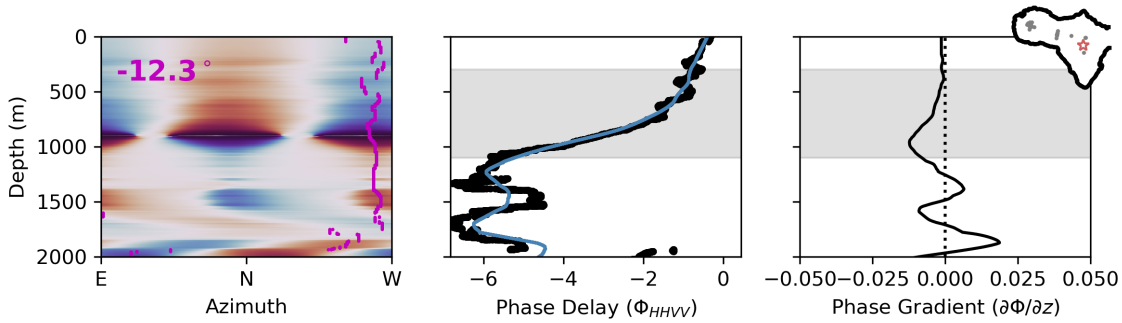
-12.3°
Depth (m)
0
500
1000
1500
2000
E
N
W
Azimuth
−6
−4
−2
0
Phase Delay (Φ_{HHVV})
−0.050
−0.025
0.000
0.025
0.050
Phase Gradient ($\partial\Phi/\partial z$)